The mobility of oxygen containing species (OCS*) over Pt-based catalyst surfaces:

Impact on the oxygen reduction reaction (ORR) activity

by

Thobani G. Gambu

MSc. Eng. (UCT 2015)

Thesis presented to the University of Cape Town in fulfilment of the requirements for the degree of Doctor of Philosophy

Catalysis Institute

Department of Chemical Engineering

University of Cape Town

Rondebosch, 7701

South Africa

(February 2020)

(Back of a cover page)

Declaration

I, Thobani G. Gambu, hereby declare that the work presented in this thesis is my sole and original work, in concept and in execution, and that no part of this work has been or is being or will be submitted to any university for another degree. All published and unpublished works is appropriately cited. I authorize the University of Cape Town and Professor Eric van Steen to reproduce the contents of this work for any academic and research purpose.

Signature: Signed by candidate Date: February 10, 2020

Acknowledgements

I would like to acknowledge a number of individuals and institutions whose guidance and support has not only been critical in the success of this project but has also had an immense impact in my academic and personal growth over the past several years:

Professor Eric van Steen, in this long journey you have been the best supervisor, promoter and mentor I could have ever hoped for. I cannot imagine who I would have become without your kind support. Since our first meeting in late 2012, your influence has created, in me, a capacity to think and reason in a very unique manner. Through your support, I have met and learnt from many others as well. Thank you for taking on a daunting task of training me both as master and doctoral student. Indeed, walking into your office with a question has been akin to starting a nuclear reactor, the only difference is one has questions for neutrons, you walk in with one and come out with many new questions—like in a nuclear reactor, this process sustained my interest in research. Your questions have kept the light on for many years, and when I think of the future, I am comforted by the idea of making you proud by carrying on the '*nuclear torch'* you have lit in me. Thank you for your patience and for believing in me—you have always seen the best in me. Because of you, *I will go on to bash my head on many walls of the world until a door emerges*.

I am also grateful for the team of supervisors you put together to nurture a young and impressionable novice that walked into your office so many years ago into who I am today. In particular, thank you for introducing me to Doctor Melissa Petersen whom as a co-supervisor has also had a big influence on me.

Dr Melissa Petersen, it is impossible to completely describe the impact and contribution you have made in the success of this research project and my training. From your very thoughtful and thorough feedback to consistent and reliable advice, you have truly been an important contributor to my academic development. Thank you for the innumerous hours you spent, earlier on teaching me basics of molecular modelling and later discussing the future. During the writing of this thesis, your support and encouragement became a fuel that saw me through this journey. I cannot imagine what my postgraduate training would have been without your involvement. Thank you for the time you invested in my development.

Dr Glenn Jones, thank you very much for playing a part in my postgraduate training. I appreciate all the discussions we had over the years and the insightful thoughts you shared ever so effortlessly. Thank you for introducing me to many of your colleagues and network. Your involvement in this project

brought many opportunities all of which I am eternally grateful for. I would like to acknowledge all Johnson Matthey (JM) researchers I have met, during the many JM meetings and also during my visit to Sonning Common, for being available to share advice and knowledge with me. Particularly, thanks to Dr Alex Martinez Bonastre, Dr Crina Corbos and Dr Frederic Pelletier for training and assisting me with various experimental techniques.

Professor Nora de Leeuw, thank you for inviting me to Cardiff University and also for enabling various research visits to other UK institutions. You provided me with a very important opportunity which resulted in many friendships with people inside and outside your research group. Particularly, thanks to Dr David Santos-Carballal and Dr Umberto Terranova, for introducing me to molecular dynamics and for a successful collaboration. You have a brilliant, friendly and supportive research team, one I am very lucky to have had an opportunity to be part of. I should mention Dr Qamreen Parker who went an extra mile to ensure that our exchange to the UK was smooth, comfortable and a success. Thank you very much Qam.

Dr Michail Stamatakis, thank you for welcoming me to your research group to learn the principles of kinetic Monte Carlo simulations, in particular your versatile kMC code (Zacros). Every single member of your group was friendly and shared generously. I look forward to visiting in the future. In particular, I would like to thank Konstantinos Papanikolaou (Kostas) and Dr Matthew Thomas Darby who spent time discussing the specific of the Zacros code with me.

Dr Miomir B. Vukmirovic, thank you for inviting me to Brookhaven National Laboratory and also for taking the time out to show me around. I am particularly grateful to have had the opportunity to meet Professor Radoslav Adzic. Thank you for the various electrochemical demonstrations you prepared for me during this visit.

Dr Santiago J. A. Figueroa, thank you for the many discussion we had during our beamtime at Laboratório Nacional de Luz Síncrotron (LNLS) over the last few years. You are very kind and generous with your time, knowledge and experiences. For this I am extremely grateful to have met and worked with you over the years.

There are many other individuals I would like to acknowledge. Students and postdocs within Professor van Steen's group. Thank you very much for the experiences we shared together. Sandeeran Govender and Tracey van Heerden, thank you both for a very nice working relationship we developed over the years. In particular, thanks to Sandeeran for always being ready with suggestions and ideas. Everyone within the Catalysis Institute and the rest of the Chemical Engineering department, I consider a friend and I am grateful for your friendship and the memories we shared. Thanks to Dr Rhiyaad Mohamed

for being a friend and a collaborator. Your interesting ideas will surely payback in the end, thank you for affording me the opportunity to explore theoretical methods further and beyond my PhD project.

This project benefited from the generous financial support from various organisations. The financial assistance of the National Research Foundation (NRF) towards this research is hereby acknowledged. Opinions expressed and conclusions arrived at, are those of the author and are not necessarily to be attributed to the NRF.

Furthermore, financial support from the Harry Crossley Foundation, Johnson Matthey and the University of Cape Town is also greatly acknowledged. Additional funding from the Catalysis Society of South Africa (CATSA), the NRF and grants provided by UK Engineering and Physical Research Council (grant nos. EP/K016288/1 and EP/K009567/2) and UK Economic and Social Research Council (grant no. ES/N013867/1) through a cooperation with NRF enabled various research travels including a conference in North America, multiple laboratory visits in North America and UK and access to advanced characterisation techniques at the Brazilian Light Source (LNLS). All this funding and support is greatly appreciated.

This research benefited from access to high performance computing facilities primarily provided by the Centre for High Performance Computing (CHPC), South Africa, University of Cape Town's high performance computing facility, Supercomputing Wales (and its predecessor, HPCWales), Wales, and the Engineering and Built Environment's computing cluster, Chimera. Without these resources this work would not have been possible. I would like to also thank the various system administrators of these HPC facilities for the kind, friendly and excellent support. In particular, I would like to thank Anton Lopis and Krishna Govender of the CHPC, Andrew Lewis of the UCT HPC and last but not least Graham Inggs for always going an extra mile to ensure that my HPC challenges were resolved timely and effectively.

Last but not least, I would like to also thank my family, my mother Sibongile Gambu, my sisters Thuthukile Gambu and Lindiwe Zondi and my brothers Mlekeleli, Mathemahle and Sakhile Gambu, and nephew Ntuthuko Gambu, *amaphupho ami afezeka-nje, yingenxa yenu!* I would not be able to name every single person who took interest and ensured that I get to where I am today, there are so many of you! I want you to know, I am grateful for your support and love.

This work is dedicated to my mother who risked everything for her children to have a life and dreams. It also honours the memory of those I have lost over the years, especially my grandmother Victoria Shabalala, may her soul rest forever in peace.

Friends and Colleagues **<3**

Abstract

The growing need to curb greenhouse gas emissions has made low-temperature proton exchange membrane fuel cells (PEMFCs) more attractive for automotive application. One of the major problems facing PEMFCs is the sluggish kinetics of the oxygen reduction reaction (ORR). To further enable wide-scale commercialisation of PEMFCs for automotive applications, major improvements in the ORR catalyst are therefore needed.

An in depth understanding of the ORR mechanism over Pt surfaces can enable rational approaches in the search for more active ORR catalysts. The ORR occurs over multi-faceted Pt nanoparticles which predominantly expose Pt{111} and Pt{100} facets. Most studies have modelled the overall ORR activity over multi-faceted surface assuming that the Pt{111} and Pt{100} facets are kinetically isolated.

Density functional theory (DFT) studies have shown that Pt(111) surfaces can efficiently facilitate OH* hydrogenation to H_2O* but not the hydrogenation of O* to OH*, whereas Pt(100) surfaces can facilitate O* hydrogenation to OH* better than OH* hydrogenation to H_2O*. If O* intermediates can readily diffuse from Pt{111} to Pt{100} facets and OH* from Pt{100} to Pt{111} facets, the ORR activity on Pt{111} and Pt{100} facets of multi-faceted surfaces may no longer be limited by O* and OH* hydrogenation steps, respectively.

This study uses DFT and microkinetic models to investigate the nature of inter-facet cooperation and how it influences the ORR activity under dry conditions, i.e. catalyst surface exposed to a gas mixture of 33% O_2 and 67% H_2 at 1 bar. Under these conditions, it is assumed that the Langmuir-Hinshelwood kinetics are dominant.

Using DFT, the adsorption, diffusion and reaction energetics of various reaction intermediates and reaction steps were calculated. The Pt{111} and Pt{100} facets were modelled as Pt(111)-*p*(3x3) and Pt(100)-*p*(3x3) slabs, respectively. The edge was modelled using a rhombic nanowire model with alternating Pt{111} and Pt{100} facets. Edge sites were found to adsorb oxygen containing species strongly. Consequently, the diffusion barriers of O* and OH* from edge sites towards terrace sites were much higher than the diffusion on the terraces and even higher than the activation barrier for reaction in the ORR. Replacing the edge Pt atoms with Au and Ag atoms weakens the adsorption of both O* and OH* on edge sites.

Microkinetic analyses of ORR requires the inclusion of lateral interactions, since otherwise a full coverage of the surface with O* is predicted. Higher ORR rates are obtained on Pt(100) surfaces and

Pt{100} facets than on Pt(111) surfaces and Pt{111} facets. The ORR activity on Pt(111) and Pt(100) is limited by O* hydrogenation at T < 480 K and O_2* dissociation at high temperatures. The ORR pathway varies greatly over these surfaces. On Pt(111), the ORR follows a peroxyl pathway at T < 500 K and a dissociative pathway at T > 700 K. On Pt(100) surface H_2O* is formed via O* hydrogenation to OH* followed by 2OH* coupling to H_2O* and O*. The ORR activity on multi-faceted Pt surfaces was shown to be dependent on the ratio of edge sites to Pt{111} sites

Modelling the inter-facet exchange of ORR intermediates based on data generated using Au and Ag modified nanowires could improve inter-facet cooperation. The most interesting case was Ag modified systems where inter-facet exchange of OH* occurs at temperatures as low as 360 K. On these systems, the ORR pathway on Pt{111} involves OH* diffusion from edge followed by OH* hydrogenation to H_2O*. No O_2 adsorbs on the Pt{111} facet. Edge modification has the ability to selectively enable inter-facet exchange of some reaction intermediates whilst inhibiting others. Therefore, it should be explored in rational catalyst design.

Table of contents

List of figures

List of tables

CHAPTER 1: Introduction and Literature Review

1.1 Background

Mitigation of anthropogenic greenhouse gas (GHG) emission remains one of the most pressing challenges facing today's world; its link to global warming threatens the sustainability of human civilization [1]. About 78% of all GHG emissions is due to CO_2 from fossil fuel combustion and other industrial processes [1]. Utilisation of renewable energy resources can help reduce GHG emissions, particularly from energy related applications. The hydrogen economy, in particular, envisages a future where among other developments, transportation systems are supported by hydrogen fuel cell technology—utilising renewable energy to generate and distribute hydrogen [2]. In this way the hydrogen economy will be sustainable and environmentally benign.

Currently, the transportation industry is heavily dependent on fossil fuels; a wide-scale commercialisation of proton exchange membrane fuel cell (PEMFC) technology can help to reduce anthropogenic CO_2 emissions from this sector [1,2]. This may further be enabled by the higher theoretical fuel utilisation efficiency than heat engines at practical temperatures [3,4]. The present challenge is that in practice theoretical efficiencies are not achieved—partly due to (i) ohmic resistance affecting proton and electron conduction, (ii) mass transport limitation affecting reactant availability at the catalyst surface and (iii) reaction activation losses [3,5,6]. This lowering in efficiency is observed as a decrease in cell voltage with increasing current drawn from a PEMFC. Reaction activation losses are primarily due to slow oxygen reduction reaction (ORR) kinetics; under automotive testing conditions, the ORR accounts for over two-thirds of the total voltage drop [5,6]. This voltage drop due to ORR activation occurs despite the use of the most ORR active pure metal catalyst, platinum [7,8]. Therefore, to achieve higher power outputs per PEMFC at a given cell voltage requires more platinum in addition to higher fuel and oxidant feed rates. This among other factors limits the wide-scale commercialisation of PEMFCs for mobile application. To successfully deploy PEMFCs in the automotive industry, improved ORR catalysts are needed. This requires an extensive understanding of the ORR process over catalyst surfaces and its various bottlenecks.

1.2 Oxygen reduction reaction in PEMFCs

Proton exchange membrane fuel cells exploit the potential difference between the hydrogen oxidation reaction (HOR) at the anode electrode and oxygen reduction reaction (ORR) at the cathode electrode. Figure 1.1 presents an illustration of a PEMFC indicating the different electrodes and associated reactions. Whilst the HOR is simple and catalysed efficiently by a platinum catalyst, [8] the ORR is more complex and can occur via a $4e^-$ transfer reaction resulting in the formation of two H_2O molecules,

$$O_2(g, 1\ bar) + 4H^+(aq, 1\ M) + 4e^- \rightarrow 2H_2O(g, 1\ bar), \qquad \Delta E = 1.23\ V\ @\ T=298.15\ K \qquad 1.1$$

or a $2e^-$ transfer reaction resulting in the formation of one H_2O_2 molecule,

$$O_2(g, 1b\ bar) + 2H^+(aq, 1\ M) + 2e^- \rightarrow H_2O_2(g.\ 1\ bar), \qquad \Delta E = 0.624\ V\ @\ T=298.15\ K \qquad 1.2$$

$$H_2(g, 1b\ bar) \rightarrow 2H^+(aq, 1\ M) + 2e^-, \qquad \Delta E = 0.000\ V\ @\ T=298.15\ K \qquad 1.3$$

where ΔE represents the theoretical potential difference between the HOR (equation 1.3) and ORR half reactions at standard conditions [9]. The extent of each of these reactions is dependent on reaction conditions and catalyst surface and is associated with high overpotentials even over the most active catalyst surfaces [4,8,10]. The anode and cathode electrodes are separated by a proton conducting polymer membrane and are connected to each other via an external circuit—protons and electrons generated from the HOR are conducted via the polymer membrane and external circuit, respectively. Consequently, due to internal resistances associated with electron and proton conduction the measured cell voltage deviates from the theoretical voltage [6]. Furthermore, mass transfer limitations, associated with the transport of H_2/O_2 to the catalyst surface at high current densities, result in an additional drop in cell voltage [6]. This decrease in cell voltage, also known as polarization loss, is equivalent to a decrease in cell efficiency. As stated above, the slow ORR kinetics are responsible for most of the losses in cell voltage; at current densities up to 1.5 $A.cm^{-2}$, over 67% of the measured voltage drop is due to the ORR [5,6]. Therefore, it is clear that improvements in ORR catalysis should result in a substantial improvement in PEMFC performance.

In practice, platinum nanoparticles supported on carbon (Pt/C) are used as PEMFC electro-catalysts [3,5]. This means that multiple surface regions, which include, terraces, edges and corners are exposed [11]. According to the Wulff Construction theorem, [12] equilibrated Pt nanoparticles (NPs) will be predominantly enclosed by Pt{111}, Pt{100} and Pt{110} surface terminations—as these terminations have the lowest surface energies [11,13–15]. The measured ORR surface area specific activity over Pt/C catalysts has been reported to decrease with a decrease in Pt NP size [16,17]. This has been

attributed to an increase in the density of edge and corner sites, which are said to be less active than terrace sites [16–18]. Mesoporous (with 3D pore structures) and nanowire/nanorod structures have also been investigated as catalysts for ORR [18,19]. Their improved ORR activities relative to Pt NPs have been attributed to having fewer under-coordinated sites, i.e. steps, edges and corners [18,19]. Given the importance of the ORR, it is necessary to understand its mechanism and activity over model surfaces in order to elucidate the causes of the above behaviour and to rationally design better catalysts.

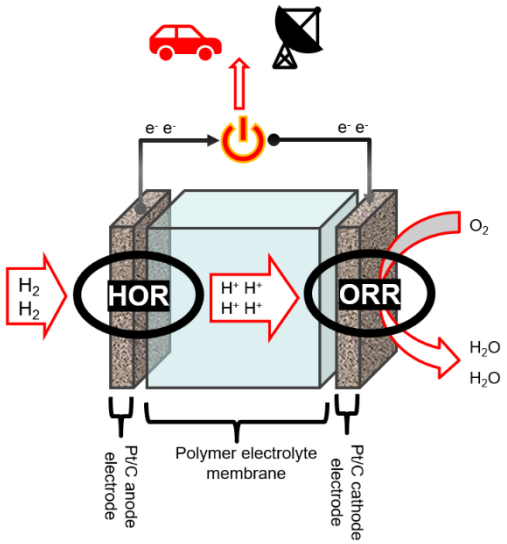

Figure 1.1: Schematic illustration of a PEM fuel cell.

1.3 ORR activity over low-Miller index Pt planes

1.3.1 Experimental studies

It has long been known that Pt is the most active pure metal for the ORR catalyst [7,10,16,20]. Early model studies utilising rotating disk electrode (RDE) experiments† were able to elucidate that the ORR activity over Pt surfaces is structure sensitive [10]. RDE experiments have shown that different Pt(hkl) surfaces exhibit different ORR activities and the ORR activity over each surface is strongly influenced by electrolyte-surface interactions [10,20–24]. For example, in a nonadsorbing electrolyte such as $HClO_4$, the ORR activity increases in the order Pt(100) < Pt(110) ≈ Pt(111) whilst in H_2SO_4 the activity order is somewhat reversed, viz. Pt(111) << Pt(100) < Pt(110) with Pt(110) two orders of magnitude more activity than Pt(111) [10,21,23,25]. This structure sensitivity of the ORR activity is related to

† The use of RDE in a three-electrode electrochemical cell has enabled significant progress towards the discovery of highly active catalyst materials. Unlike the laborious in-situ catalyst testing stations, which require large amounts of catalyst materials for membrane electrode assembly (MEA) fabrication, RDE experiments require only a small amount of catalyst material and enables activity measurement in the absence of other factors such as mass transport limitation or water flooding [10].

reaction pathways and electrolyte-surface interactions [10,20]. In $HClO_4$, the Pt(111) surface is most active whilst the Pt(100) shows the lowest activity. This trend worsens in a KOH electrolyte as the strong interaction of OH with Pt(100) surface sites results in poisoning of the surface by adsorbed OH species [10]. The latter argument seems reasonable considering that theoretical calculations have also shown that over a Pt(100) surface OH removal has the highest activation energy of all reaction steps involved in the ORR mechanism [26,27]. Moreover, the same calculations show that OH adsorption on Pt(100) bridge sites is ca. 0.55 eV more exothermic than adsorption over Pt(111) sites [26–28]. The extremely low ORR activity over the Pt(111) surface in H_2SO_4 was also rationalised based on a more favourable adsorption of SO_4^{2-} and HSO_4^- anions over Pt(111) surface compared to the other low-Miller index surfaces [10]. As result of anion adsorption, catalytic sites on the Pt(111) surface are blocked lowering the ORR activity.

The seminal work of Stamenkovic *et al.* [22] also showed that the ORR activity over low-Miller index surface of Pt_3Ni alloy varied in a similar way to Pt surfaces. They reported a segregation of Pt atoms to the surface resulting in what they termed Pt_3Ni(*hkl*)-skin surfaces. The activity measurements in $HClO_4$ revealed a 10-fold increase in the ORR activity over Pt_3Ni(111)-skin surface compared to the equivalent Pt(111) surface—consequently, the Pt_3Ni(111)-skin surface was argued to result in a 90-fold activity enhancement compared to state-of-the-art Pt/C catalysts [22]. The activity improvement was attributed to the weakening of OH adsorption (compared to Pt(111) surface) and consequently an increase in available sites for O_2 adsorption. Another interesting result was reported by Kondo *et al.* [23] who found that the ORR activity over low-Miller index surface of Pd increased in a completely opposite order to equivalent Pt surfaces under the same testing conditions. They found that under $HClO_4$ the Pd(100) surface was the most active low-index surface. This points to a complex behaviour of the ORR not only over Pt based surfaces but also other surfaces as well.

1.3.2 Theoretical studies

Density functional theory (DFT) methods have also been used to investigate the ORR activity over different low-index surfaces. Nørskov *et al*. [7,29] investigated the ORR activity over Pt(111), Pt(100) and Pt(211) surfaces aided by DFT calculations. They proposed a simple kinetic model based on the assumption that the ORR activation free energy will at least be equal to the reaction free energy of the most endergonic elementary step in a given reaction mechanism/pathway. Using this model, they were able generate a volcano curve describing the ORR activity of various metals as a function of the binding strength of O and OH intermediates. In this case their model was able explain observed trends and the effects of alloying, further suggesting that the optimal ORR catalyst should bind OH ca. 0.1 eV weaker than Pt(111) [7].

Other DFT studies have focused on investigating the ORR mechanism over different surfaces (see Table 1.1)—mapping the preferred reaction pathway based on relative activation energies of individual elementary steps [26–28,30]. Figure 1.2 presents the ORR pathway over different Pt and Pt-skin surfaces. Duan and Wang [26] compared the ORR reaction energetics over pure Pt surfaces, i.e. Pt(111) and Pt(100) slab surfaces, and Ni modified surfaces where Pt atoms of the subsurface layer of each Pt slab were replaced with Ni atoms resulting in Pt-skin surfaces, i.e. Pt/Ni(111) and Pt/Ni(100). Over unmodified Pt(111) and Pt(100) surfaces the ORR was argued to follow the peroxyl and dissociative pathway, respectively as shown in Figure 1.2. Modifying the Pt(111) with Ni results in a peroxide pathway with a highest activation energy of 0.15 eV (cf. 0.79 eV for the peroxyl pathway over a Pt(111) surface) whilst the modification of Pt(100) with Ni did not change the ORR pathway or highest activation energy. Li *et al.* [27] considered Cu modification instead of Ni and reported that over Cu modified Pt(111) the ORR followed a peroxide mechanism with a highest activation energy of 0.40 eV whilst the Cu modified Pt(100) surface favoured a dissociative pathway with a slightly higher activation energy of 0.85 eV. Moreover, the adsorption strength of O and OH over Pt/M(111), where *M* = Ni, Co, Fe, Cu, was found to be weaker than over Pt(111) surface [26–28]. This result together with the Nørskov model [7] is in good agreement with experimental trends [31].

Table 1.1: Commonly investigated ORR mechanism over Pt surfaces [26–28,30].

Dissociative mechanism	**Peroxyl mechanism**	**Hydrogen peroxide mechanism**
Adsorption/desorption	Adsorption/desorption	Adsorption/desorption
$O_2 + * \rightarrow O_2*$	$O_2 + * \rightarrow O_2*$	$O_2 + * \rightarrow O_2*$
$H_2 + 2* \rightarrow 2H*$	$H_2 + 2* \rightarrow 2H*$	$H_2 + 2* \rightarrow 2H*$
$H_2O* \rightarrow H_2O + *$	$H_2O* \rightarrow H_2O + *$	$H_2O* \rightarrow H_2O + *$
		$H_2O_2* \rightarrow H_2O_2 + *$
Surface reactions	Surface reactions	Surface reactions
$O_2* + * \rightarrow 2O*$	$O_2* + H* \rightarrow OOH* + *$	$O_2* + H* \rightarrow OOH* + *$
$O* + *H \rightarrow OH* + *$	$OOH* + * \rightarrow O* + OH*$	$OOH* + H* \rightarrow H_2O_2* + *$
$OH* + H* \rightarrow H_2O* + *$	$O* + H* \rightarrow OH* + *$	$H_2O_2* + * \rightarrow 2OH*$
$2OH* \rightarrow H_2O* + O*$	$OH* + H* \rightarrow H_2O* + *$	$OH* + H* \rightarrow H_2O*$
	$2OH* \rightarrow H_2O* + O*$	$2OH* \rightarrow H_2O* + O*$

*X** and * respectively denote an adsorbed species and an empty surface site

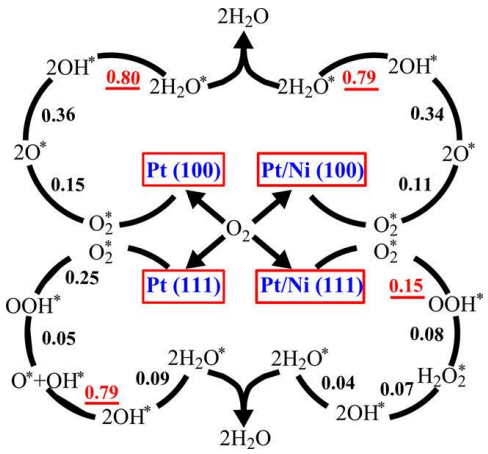

Figure 1.2: ORR pathway over unmodified and Ni modified Pt surfaces; activation energies are reported in electronvolts for each elementary step (and energetically difficult steps highlighted in red) [26].

A brief analysis of the reaction mechanisms (see Figure 1.2) shows that improvement of the ORR activity over Pt(111) and Pt(100) surfaces, assuming no change in the reaction pathway, would require a decrease in the activation energy of O* and OH* hydrogenation reactions, respectively. Modified (111) surfaces are able to improve the ORR activity by enabling the peroxide mechanism which does not result in any O* intermediates. Since the generation of OH over (100) surfaces cannot be avoided alternative pathways for its removal are of interest.

1.4 ORR activity over high-Miller index Pt planes

The ORR activity over single crystal Pt *n*(111)-(111), Pt *n*(111)-(100), Pt *n*(100)-(111) and Pt *n*(100)-(110) surfaces has also been investigated using the RDE technique [24,32,33]. These faceted single crystals have *n* atomic rows along the terraces and a single atomic step. In the case of Pt *n*(111)-(111) and Pt *n*(111)-(100), the ORR activity was found to increase with increasing step density, i.e. decreasing *n*, with a maximum around $n = 4$ [24,32,33]. Bandarenka *et al.* [32] argued that the observed improvement with increasing step density in Pt *n*(111)-(111) and Pt *n*(111)-(100) was due to the weakening of the binding energy of ORR intermediates, via a disruption of H-bonding networks, relative to Pt(111) surfaces. On the other hand, the ORR activity over Pt *n*(100)-(111) and Pt *n*(100)-(110) surfaces was independent of the step density [24]. This suggests that changing the (100) terrace length has no effect on the crucial factors determining the ORR activity over Pt(100) facets. Surprisingly, over Pd *n*(100)-(111) and Pd *n*(100)-(110) the activity was reported to increase with decreasing step density [23]. This inverse behaviour between Pt and Pd surfaces was also noted by Kondo *et al.* [23]. Whilst these studies investigate systems with varying terraces sizes, the step size is kept constant.

In an earlier study, Komanicky *et al.* [34,35] prepared (111)-(100) nanofaceted Pt surfaces, with larger and alternating {111} and {100} terraces, and compared their ORR activity to that of flat Pt(111) and Pt(100) surfaces, under H_2SO_4 and $HClO_4$ electrolytes. They found that the ORR activity of nanofaceted Pt surfaces was higher than a simple weighted average of the ORR activity of Pt(111) and Pt(100) surfaces. To rationalize their observation, they suggested a cooperative behaviour of adjacent Pt{111} and Pt{100} terraces involving the exchange of adsorbed O_2 and OH intermediates between the different facets. The same cooperative behaviour was also argued in their follow-up study which measured the ORR activity of arrayed cuboctahedral Pt NPs [36]. Unfortunately, this notion was not pursued further in later studies. Recent studies still consider the ORR activity of multifaceted surfaces simply as a linear combination of activities of constituent facets [15,25,37].

1.5 ORR catalyst development

The development of next-generation Pt-lean and highly active ORR catalysts has seen a lot of success, and as a result several review papers have been published on this topic [11,18,20,38–45]. Briefly, the different approaches applied are based on a common idea that surfaces which adsorb oxygen containing species (*OCS**) less strongly than Pt would be closer to the activity optimum [7]. Alloying Pt with 3d metals [31,46–48] and lanthanides [49] has confirmed that significant improvements in ORR activity can be obtained from the manipulation of the electronic structure of surface sites. In the so-called Pt-skin structures, where in a PtM alloy Pt segregates towards the surface forming a Pt monolayer, the ligand effect is believed to be responsible for the downward shift in the d-band center which occurs simultaneously with the weakening in adsorption strength of *OCS** [22,31]. The latter weakening as a result of modification with transition metals has been confirmed by several DFT studies [26–28].

On the other hand, alloying Pt with lanthanides resulted in the contraction of Pt-Pt bond lengths, simultaneously weakening the adsorption of H and OH on the catalyst surface [49]. It has been constantly argued that the formation of Pt-skin on these alloyed structures not only improves the catalytic activity further but also improves the catalyst durability by forming a protective Pt layer preventing the leaching of the alloying metal. Therefore, even in these next-generation catalysts, it is anticipated that platinum is still the active catalyst surface, albeit with modified electronic properties [22,31,49,50].

1.6 Aims of this study

ORR is a critical reaction in PEMFCs, and the improvement of its activity will bring the PEMFCs closer to commercialisation. Several studies have investigated the ORR mechanism over various

metallic surfaces, particularly over the most active metal surface, Pt and its alloys. The success of these studies, both experimental and theoretical, has resulted in a number of improved catalyst concepts and explanation of how to obtain further improvements. Despite this progress, very little has been done in order to understand the overall ORR activity over multifaceted surfaces. Whilst some experimental studies have suggested that there exists a synergistic behaviour between adjacent Pt{111} and Pt{100} terraces, most model studies tend to treat these terraces as isolated.

This study aims to investigate the ORR activity over multifaceted surfaces with adjacent Pt{111} and Pt{100} terraces in order to elucidate their potential cooperative behaviour, and the implications for the overall ORR activity and pathway over Pt based multifaceted catalysts.

Although alloying Pt with other elements seems to give the largest improvements in ORR activity, these modified surfaces have been argued to be covered by at least a monolayer of Pt. Therefore, even on these surfaces, the understanding of the cooperative behaviour of adjacent surface is still relevant.

Hypothesis 1

The cooperative behaviour of adjacent Pt{111} and Pt{100} facets over multi-faceted surfaces will improve the ORR activity by facilitating the inter-facet exchange of O* (Pt{111} → Pt{100}) and OH* (Pt{100} → Pt{111}). This exchange enables an alternative pathway for the rate-limiting O* and OH* hydrogenation steps over Pt(111) and Pt(100) surfaces, respectively. Despite strong adsorption of both O* and OH* over edge sites, the repulsive lateral interactions will improve inter-facet diffusion by weakening the differential adsorption strength of O*/OH* on a covered edge.

Key questions

- How mobile are O*, OH* and other ORR intermediates over Pt(111), Pt(100) and edge sites?
- Is there significant diffusion of O* and OH* between Pt{111} and Pt{100} over multi-faceted surfaces?
- What is the ORR mechanism over Pt{111} and Pt{100} facets on a multi-faceted Pt surface?
- How does the inter-facet connectivity of the Pt{111} and Pt{100} facet influence their intrinsic ORR activities compared to isolated Pt(111) and Pt(100) surfaces?
- Does inclusion of lateral interactions improve the inter-facet connectivity via diffusion of O* and OH*?

Hypothesis 2

Modification of Pt nanowires (NW) edge sites with Au and Ag will improve the inter-facet cooperation between adjacent Pt{111} and Pt{100} terraces since both O* and OH* interact weakly with Au and Ag surfaces [29,30]—as a result the potential energy surface for diffusion over the edge will flatten enabling faster diffusion properties.

Key questions

- What are the diffusion barriers of ORR intermediates over Au and Ag modified Pt NW surfaces?
- Is the ORR activity higher as a result of edge modification with Au and Ag?
- What is the ORR mechanism over modified multifaceted Pt surfaces? How does it compare to unmodified multifaceted surfaces?

1.7 Project scope

The above hypotheses are investigated using first principles methods in order to gain further mechanistic understanding of the ORR over multi-faceted surfaces. The ORR is a very complex process involving multiple reaction events some of which involve charge transfer. This complexity makes it very difficult to accurately model the ORR process completely from first principles—albeit various improvements in the recent years. Both the electrolyte and electrode potential effects are complex aspects of the electrochemical reduction of oxygen. In addition to these phenomena there are also difficulties associated with accounting for intermediate interactions on the surface.

This PhD study acknowledges the above complexity of the ORR process under potential bias and consider a relatively simple system as a proxy for the more complex picture. The considered system involves the ORR at the gas/solid interface. This simple model is then used to investigate the inter-facet cooperation and its impact on the ORR activity over multifaceted Pt surfaces. The effects of surface coverage are incorporated based on different mean-field approaches. Furthermore, avenues for improving the ORR activity are discussed—this is centred around the manipulation of inter-facet exchange of reaction intermediates on catalyst surfaces bounded by Pt{111} and Pt{100} facets. This study may also be used in the future as a basis for extending to include electrolyte and electrode potential effects.

CHAPTER 2: Theoretical Framework

2.1 Introduction

The complexity of heterogenous catalytic processes is well known. It includes questions such as the nature of the active sites, active intermediate, reaction pathway, etc. Until the development of first principles methods, these complex questions had remained relatively elusive to chemists and engineers alike. In recent years, density functional theory (DFT) has enabled the development of an atomistic view into the complex nature of heterogenous catalytic processes [7,8,27–30]. The application of the Sabatier principle together with DFT enabled rapid screening of alloys and prediction of optimum catalysts [7,8,29]. Moreover, the study of complex reaction networks is possible through the application of DFT together with microkinetic models [51–53]. This Chapter will present a brief discussion on DFT and its application (Section 2.2), surface models used to model ORR energetics (Section 2.3) and microkinetic models used to model the ORR activity (Section 2.4).

2.2 Density functional theory

In principle, the time-independent Schrödinger equation (TISE) can describe all electronic structure properties of a system with an arbitrary number of electrons and nuclei [54]. According to the Born-Oppenheimer Approximation, the electronic energy of a system of *N* isolated electrons can be described as,

$$\hat{H}\Psi = E\Psi \tag{2.1}$$

where Ψ is the electronic wavefunction, E is the total electronic energy and $\hat{H}$ is the Hamiltonian of the system.

$$\hat{H} = \sum_{i=1}^{N}\left(-\frac{1}{2}\nabla_i^2\right) + \sum_{i=1}^{N} v(\boldsymbol{r}_i) + \sum_{i<j}^{N}\frac{1}{\boldsymbol{r}_{ij}} \tag{2.2}$$

where $\boldsymbol{r}_{ij}$ is the distance between electrons i and j, and $v(\boldsymbol{r}_i)$ is the potential of nuclei acting on electron i at point $\boldsymbol{r}_i$ and is given by,

$$v(\boldsymbol{r}_i) = -\sum_{\boldsymbol{\alpha}}\frac{Z_\alpha}{\boldsymbol{r}_{i\alpha}} \tag{2.3}$$

with $\boldsymbol{r}_{i\alpha}$ being the distance between electron i and the nucleus α of charge Z_α. The electronic wavefunction, Ψ, depends on 4N variables, i.e. 3N spatial coordinates for each electron and N spin coordinates. The total energy (W) is therefore calculated as the sum of electronic energy (E) and the nucleus-nucleus repulsion energy.

$$W = E + V_{nn} = E + \sum_{\alpha<\beta} \frac{Z_\alpha Z_\beta}{R_{\alpha\beta}} \qquad 2.4$$

Whilst an analytical solution does not exist, except in very simple systems (e.g. hydrogen atom), numerical procedures such as the ones implemented in the Hatree-Fock (HF) method enable calculation of electronic properties of multi-electron systems. The HF method considers a system of N independent electrons in an effective potential due to nuclei and the averaged potential of other electrons in the system. This method explicitly treats the exchange energy; however, the only treatment of the correlation energy is through the enforcement of the Pauli Exclusion Principle, by the construction of the Slater determinantal matrix [55].

Building from the Thomas-Fermi model and the more successful $X\alpha$ method, DFT also replaces the 4N dimensional wavefunction with a much simpler 3 dimensional electron density function, $\rho(\boldsymbol{r})$ [54–56]. Whilst the Thomas-Fermi model predicts atoms very well, it also predicts that all molecular bonds are unstable [54,57]. The $X\alpha$ method was more successful in predicting both atoms and solids—and has also been used for molecules [55]. In 1964 Hohenberg and Kohn [58] published two theorems which founded modern DFT methods. From the first theorem, it follows that there is a functional which when operated on the ground state electron density function, $\rho_0(\boldsymbol{r})$, gives the total ground state energy (E_0) for any system with an arbitrary number of interacting particles,

$$E_0 = F[\rho_0(\boldsymbol{r})] = E_{v(\boldsymbol{r})}[\rho_0(\boldsymbol{r})] \qquad 2.5$$

where $E_{v(\boldsymbol{r})}$ is the energy functional which gives the ground state energy when operated on a ground state electron density. The second theorem proves that the variational principle applies to the electron density, i.e. the density that minimises the energy is the true ground state of the system,

$$E_v[\rho_t] \geq E_0 \qquad 2.6$$

where ρ_t is a trial density function satisfying the following conditions for any system of N electrons,

$$\int \rho_t(\boldsymbol{r}) d\boldsymbol{r} = N \text{ and } \rho_t(\boldsymbol{r}) \geq 0 \qquad 2.7$$

Although very powerful in providing an *a priori* guarantee of the variational principle in DFT, Hohenberg and Kohn did not provide how such a functional could be constructed. As a result, present DFT methods are based on approximate functionals built on the foundation laid by Kohn and Sham [59]. Kohn and Sham [59] considered a reference system of noninteracting electrons (quasi-electrons), whose ground state electron density function (ρ_r) equals to the ground state electron density function of a real system of interacting electrons, in an effective potential. This allowed for the partitioning of the electronic energy into terms which can be treated exactly without the use of DFT and a relatively smaller term which required a functional [55]. The total ground state electronic energy can be written as the sum of kinetic, nucleus-electron attraction potential and electron-electron repulsion potential energies as follows,

$$E_o = T[\rho_0(\boldsymbol{r})] + V_{ne}[\rho_0(\boldsymbol{r})] + V_{ee}[\rho_0(\boldsymbol{r})] \quad 2.8$$

where the kinetic energy is given by,

$$T[\rho_0(\boldsymbol{r})] = T[\rho_0(\boldsymbol{r})]_{\text{ref}} + \Delta T[\rho_0(\boldsymbol{r})] \quad 2.9$$

with $T[\rho_0(\boldsymbol{r})]_{\text{ref}}$ and $\Delta T[\rho_0(\boldsymbol{r})]$ being the kinetic energy of the fictitious reference system of quasi-electrons and the deviation of the real electronic kinetic energy from this reference system, respectively. The third term of equation 2.8 represents the electron-electron potential energy and is given by,

$$V_{ee}[\rho_0(\boldsymbol{r})] = \frac{1}{2}\iint \frac{\rho_0(\boldsymbol{r}_1)\rho_0(\boldsymbol{r}_2)}{\boldsymbol{r}_{12}} d\boldsymbol{r}_1 d\boldsymbol{r}_2 + \Delta V_{ee}[\rho_0(\boldsymbol{r})] \quad 2.10$$

with the first term being the classical Coulombic repulsion energy and the deviation from this of the real electron-electron repulsion energy given by $\Delta V_{ee}[\rho_0(\boldsymbol{r})]$. $\rho_0(\boldsymbol{r}_1)$ and $\rho_0(\boldsymbol{r}_2)$ represent the density volume elements located at position $\boldsymbol{r}_1$ and $\boldsymbol{r}_2$ and separated by a distance $\boldsymbol{r}_{12}$. For a given external potential, $v(\boldsymbol{r})$, the second term in equation 2.8 can be calculated as follows,

$$V_{ne}[\rho_0(\boldsymbol{r})] = \int \rho_0(\boldsymbol{r}) v(\boldsymbol{r}) d\boldsymbol{r} \quad 2.11$$

Substituting equations 2.9, 2.10 and 2.11 into equation 2.8 gives the total ground state energy (2.12).

$$E_o = T[\rho_0(\boldsymbol{r})]_{\text{ref}} + \Delta T[\rho_0(\boldsymbol{r})] + \int \rho_0(\boldsymbol{r}) v(\boldsymbol{r}) d\boldsymbol{r} + \frac{1}{2}\iint \frac{\rho_0(\boldsymbol{r}_1)\rho_0(\boldsymbol{r}_2)}{\boldsymbol{r}_{12}} d\boldsymbol{r}_1 d\boldsymbol{r}_2 + \Delta V_{ee}[\rho_0(\boldsymbol{r})] \quad 2.12$$

Only the two deviation terms, i.e. $\Delta T[\rho_0(\boldsymbol{r})]$ and $\Delta V_{ee}[\rho_0(\boldsymbol{r})]$ are unknown. Within the Kohn-Sham approach the sum of these terms is equivalent to the exchange-correlation energy,

$$E_{XC}[\rho_0(\boldsymbol{r})] \equiv \Delta T[\rho_0(\boldsymbol{r})] + \Delta V_{ee}[\rho_0(\boldsymbol{r})] \quad 2.13$$

The Kohn-Sham approach then provides a way to calculate all unknown terms in 2.12 including the electronic kinetic energy of the reference system which is given by,

$$T[\rho_0(\boldsymbol{r})]_{\text{ref}} = \left\langle \Psi_r \middle| -\frac{1}{2}\nabla^2 \middle| \Psi_r \right\rangle \quad 2.14$$

where Ψ_r is the ground state wavefunction of a reference system of N quasi-electrons [54]. Ψ_r is determined exactly as a Slater determinant of occupied spin orbitals whose elements are calculated as products of Kohn-Sham spatial orbitals, ψ_i^{KS}, of the reference system and spin function. The Slater-Condon rules allows for 2.14 to be reduced to,

$$T[\rho_0(\boldsymbol{r})]_{\text{ref}} = -\frac{1}{2}\sum_{i=1}^{N}\left\langle \psi_i^{KS} \middle| \nabla_i^2 \middle| \psi_i^{KS} \right\rangle \quad 2.15$$

The Kohn-Sham spatial orbitals can be calculated using basis functions ϕ,

$$\psi_i^{KS} = \sum_{s=1}^{m} c_{si}\phi_s \quad 2.16$$

with m and c_{si} being the number of basis functions in a set and expansion coefficients. With all the terms now known, the only remaining difficulty is the nature of the exchange-correlation energy functional ($E_{\text{xc}}[\rho(\boldsymbol{r})]$). From the Kohn-Sham equations, the relationship between the exchange-correlation energy functional and potential (υ_{xc}) is given by,

$$\upsilon_{\text{xc}} = \frac{\delta E_{\text{xc}}[\rho(\boldsymbol{r})]}{\delta\rho(\boldsymbol{r})} \quad 2.17$$

Various functionals have been proposed and developed over the years. The earlier was the so-called local density approximation (LDA) which is based on the uniform electron gas approximation of the exchange-correlation energy ($\varepsilon_{\text{xc}}^{\text{unif}}$) [54,57]. The exchange-correlation functional within the LDA level of theory is given by,

$$E_{\text{xc}}^{LDA}[\rho(\boldsymbol{r})] = \int \rho(\boldsymbol{r})\, \varepsilon_{\text{xc}}^{\text{unif}}\big(\rho(\boldsymbol{r})\big)\, d\boldsymbol{r} \quad 2.18$$

Whilst the LDA functional has been able to accurately describe solids and their surfaces, it gives a poor prediction of chemical bonds, overestimating the ground state energy and atomisation energy

whilst underestimating the lattice parameters [60]. In general, the LDA method has been argued to overestimate the correlation energy [61]. The next level of theory is the generalized gradient approximation (GGA). Unlike the LDA which only considers the local electron density at a point, GGA functionals incorporates non-local effects by approximating the exchange-correlation energy as a function of both electron density at a point and its first derivative with respect to spatial coordinates, i.e. $\nabla\rho(\boldsymbol{r})$. A mathematical description of GGA functionals is given by,

$$E_{\mathrm{xc}}^{GGA}[\rho(\boldsymbol{r})] = \int \rho(\boldsymbol{r})\, \varepsilon_{\mathrm{xc}}^{\mathrm{GGA}}\big(\rho(\boldsymbol{r}), \nabla\rho(\boldsymbol{r})\big)\, d\boldsymbol{r} \qquad 2.19$$

where $\varepsilon_{\mathrm{xc}}^{\mathrm{GGA}}\big(\rho(\boldsymbol{r}), \nabla\rho(\boldsymbol{r})\big)$ is the exchange-correlation energy function per differential volume of an electron gas. The GGA functionals predict atomization energies of molecules and adsorption energies at surfaces better than the LDA functional [61]. The most commonly used functionals in computational catalysis are the Perdew, Burke and Ernzerhof (PBE) [62], the Perdew-Wang from 1991 (PW91) [63], and the revised PBE (RPBE) [64]. The RPBE functional is based on the PBE functional and was proposed as a way to improve the atomisation energies of small molecules and their chemisorption on metal surfaces [64]. Other more accurate functionals have also been developed, however these also come with higher computational costs [65–69]. For computational catalysis applications, the improvement seen from the later methods does not justify the associated computational cost [60,66,70,71]. Therefore, surface reaction studies are almost exclusively based on the GGA methods. Furthermore, recent surface science studies now routinely include van der Waals interactions, which are not correctly described by standard local and semi-local exchange-correlation functionals, by application of various methods [72,73]. These methods include the DFT-D methods of Grimme [74,75], the TS-vdW methods of Tkatchenko and Scheffler [76], the vdW-DF methods proposed by Dion *et al*. [77–79] and the vdW-DF2 methods of Langreth and Lundqvist groups [80]. In general, the inclusion of van der Waals interactions leads to stronger adsorption of molecules on metal surfaces [72,73]. Moreover, the choice of method for van der Waals correction differs and may be system specific [73].

2.2.1 Solving Kohn-Sham equations

The derivation of Kohn-Sham equations is given in detail in Parr and Yang [54]. Briefly, the ground state electron density function is given by,

$$\rho_0(\boldsymbol{r}) = \rho_r(\boldsymbol{r}) = \sum_{i=1}^{N} \left|\psi_i^{KS}(1)\right|^2 \qquad 2.20$$

where $\psi_i^{KS}(n)$ is the Kohn-Sham wavefunction of electron i at the nth iteration step. Substituting 2.20 in 2.12 and differentiating with respect to ψ_i^{KS} gives the Kohn-Sham equivalence of the wave equation [54,55],

$$\hat{h}^{KS}\psi_i^{KS}(1) = \varepsilon_i^{KS}\psi_i^{KS}(1) \qquad 2.21$$

where the Kohn-Sham operator, $\hat{h}^{KS}$, is given by,

$$\hat{h}^{KS} = \left[-\frac{1}{2}\nabla_i^2 - \sum_{nuclei\ \alpha}\frac{Z_\alpha}{\boldsymbol{r}_{1\alpha}} + \int\frac{\rho(\boldsymbol{r}_2)}{\boldsymbol{r}_{12}}d\boldsymbol{r}_2 + v_{\mathrm{xc}}(1)\right] \qquad 2.22$$

The solution procedure in Kohn-Sham methods involves solving equations 2.21, 2.20 and 2.17 using the *self-consistent-field procedure* (SCF), akin to the HF approach. The following steps have been adapted from Lewars [55]:

a) Specify nuclei positions and charge
b) Specify an appropriate basis set $\{\phi\}$
c) Calculate the initial guess for the ground state electron density function, $\rho_0(1)$, for an N electron system
d) With $\rho_0(1)$ calculate $v_{\mathrm{xc}}(1)$ from equation 2.17 and the chosen exchange-correlation functional, i.e. LDA (2.18) or GGA (2.19)
e) Using $\rho_0(1)$ and $v_{\mathrm{xc}}(1)$, solve the wave equation (2.21)
f) Using the calculated $\hat{h}^{KS}$ and the specified basis function calculate the Kohn-Sham matrix elements (h_{rs}),
$$h_{rs} = \langle\phi_r|\hat{h}^{KS}|\phi_s\rangle \qquad 2.23$$
g) Orthogonalize the Kohn-Sham matrix and diagonalize to obtain Kohn-Sham energy levels and a matrix of c_{si}. The latter is used in equation 2.16 to calculate Kohn-Sham orbitals
h) Using Kohn-Sham orbitals and equation 2.20, calculate a new estimate of the ground state electron density function, $\rho_0(2)$
i) Using $\rho_0(2)$ and equation 2.12, calculate a new total energy of the system, E
j) Repeat steps d) to i) each time checking if the difference between successive E, i.e. ΔE, is less than the desired energy convergence criterion, $\Delta\epsilon$. In each repeat a new electron density is used in step d)

Once convergence is achieved, the loop is exited and the ground state energy for a given nuclei geometry and charge is obtained. In the case of geometry optimisation calculations, after each SCF

cycle the nuclei are moved in the direction of residual forces in an external loop which is repeated until residual forces acting on relaxed nuclei are within a specified convergence criterion.

2.2.2 Application of DFT in the present study

Modelling setup

Various computational codes have been developed for solving Kohn-Sham equations. In this study, spin-polarized periodic DFT calculations were conducted using the Vienna *ab initio* Simulation Package (VASP) [81–84]. All calculations were performed using the GGA-PBE exchange-correlation functional [62] with the projector augmented wave (PAW) method of Blöchl [85,86]. The difference in the accuracy between this combination and others was earlier found to be minimal [87].

VASP is a plane-wave periodic DFT code; it applies Bloch's theorem which proves that the wavefunctions of a periodic system can be expressed as a product of a plane wave and a function with the same periodicity as the system. From Bloch's theorem the problem of an infinite number of electron states is mapped onto a finite number of occupied states at an infinite number of **k**-points (wave-vectors) [61,88,89]; the properties of the system can then be obtained to a good approximation by replacing integration over an infinite number of **k**-points with summation over a finite set of **k**-points [88], as motivated by Monkhorst and Pack [90] or Chadi and Cohen [91].

At each wave-vector an infinite basis set of discrete plane-waves is required to describe electronic wavefunctions. For chemical processes, which concern mainly valence electrons, only the plane waves with lower kinetic energies, below a specified kinetic energy cut-off, are important [88]. The computational effort scales with the number of both wave-vectors and plane-waves. Therefore, it is important that both k-points and kinetic cut-off energy are optimized to within the desired convergence level.

Geometry optimisation and Vibrational analysis

In the present study, DFT is applied in (1) geometry optimization, (2) vibrational analysis and (3) transition state search calculations. All of these involve multiple electronic structure optimisation steps nested in between ionic movements. Self-consistency loops for electronic structure optimisation were converged to within 10^{-5} eV using a second order Methfessel-Paxton scheme [92] with a smearing width of 0.1 eV; total energies were extrapolated to 0 K. Ionic relaxation was based on a conjugate gradient method [88] to obtain local minima by moving ions until the residual forces acting on relaxed ions were below 0.02 eV/Å. Vibrational analysis calculations apply the finite difference method in order to determine the second derivative of the energy function with respect to atomic position (i.e.

Hessian matrix). An atomic displacement of 0.02 Å was considered—decreasing this value to 0.015 Å did not significantly affect calculated vibrational modes. The above parameters are in accordance with previous literature [93–95].

Adsorption energy

The adsorption energy of O_xH_y (E_{ads,O_xH_y}) was calculated from the total energies of adsorbed states and gas phase H_2O and H_2 as follows,

$$E_{ads,O_xH_y} = E_{surf.+O_xH_y} - E_{surf.} - xE_{H_2O} + \left(\frac{2x-y}{2}\right)E_{H_2} \qquad 2.23$$

where $E_{surf.+O_xH_y}$, $E_{surf.}$, E_{H_2O} and E_{H_2} are total energies of adsorbed adsorbate O_xH_y, clean surface, and gas phase H_2O and H_2, respectively. All reported adsorption energies in this study do not include zero-point energy and thermal corrections. However, these thermodynamic corrections were incorporated in all microkinetic models.

Transition state search

The climbing image nudged elastic band (CI-NEB) method [96] with four interpolating images connected by a spring (with spring constant of 5 eV/Å^2) was used to search for transition states between two energy minima on the potential energy surface (PES). All band forces were converged to within 0.05 eV/Å and the located transition state was further optimized to a residual force criterion of 0.02 eV/Å. The optimized transition state was then verified using vibrational analysis—only one imaginary mode in the direction of the band is expected in a true transition state. The activation energy was then calculated as the difference between the energy of the optimized transition state and the initial state.

2.3 Surface Models

Based on the Wulff construction theorem [12], several studies have argued that model Pt NPs should either be cuboctahedral [13,16,25] or truncated octahedral [15,37] in shape. These model shapes are predominantly enclosed by Pt{111} and Pt{100} facets (see Figure 2.1). In addition to Pt{111} and Pt{100} facets, finite NPs have (111)x(100) and (111)x(111) edges formed at the intersection of Pt{111} and Pt{100} facets. Figure 2.1a-c presents the distribution of atoms belonging to different surface sites on cuboctahedral, truncated octahedral and hexagonal nanowire models as a function of diameter. This change in surface type distribution with particle size has been used to rationalize the size dependency of the ORR activity [15–17,25,37].

To elucidate the role of inter-facet cooperation on the overall ORR activity over multifaceted Pt surfaces, this study models the Pt{111} and Pt{100} facets as Pt(111)-*p*(3x3) and Pt(100)-*p*(3x3) slab

surfaces, respectively. The edge region formed at the intersection of Pt{111} and Pt{100} facets is modelled using a Pt NW model in order to isolate edge effects from corner effects present on Pt NP models.

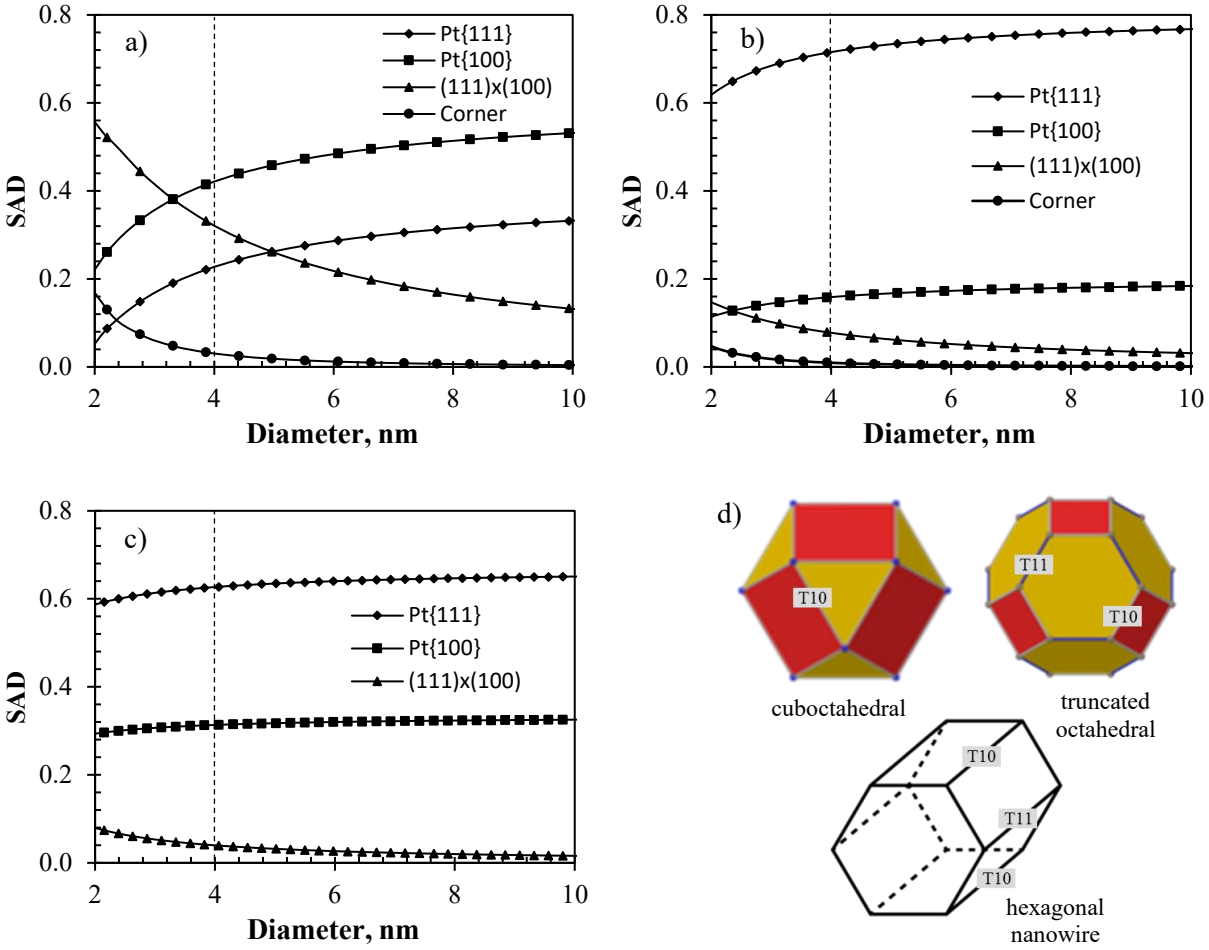

Figure 2.1: Averaged distribution of surface atoms on Pt{111}, Pt{100}, corner, (111)x(100) edge (T10) and (111)x(111) edge (T11) sites in (a) cuboctahedral and (b) truncated octahedral NP and (c) hexagonal NW models.

2.3.1 Bulk platinum

Physical properties of the face-centred-cubic platinum bulk have been calculated using DFT methods. Figure A1.1 in Appendix A gives a summary of the optimization process for bulk Pt. It was determined that a gamma centred Monkhorst-Pack [90] k-point mesh of 14x14x14 (density: 0.018 $Å^{-1}$) and a 320 eV cut-off energy were sufficient to converge the energies to within ca. 1 meV/atom. Based on the optimized k-point mesh and cut-off energy, a number of single point energy calculations were conducted on a conventional unit cell with different lattice parameters. Fitting the Birch-Murnaghan equation of state [97] to the total energy vs. lattice parameter (cell volume) data resulted in a lattice parameter and bulk modulus of 3.968 Å and 248 GPa, respectively. Both are in reasonable agreement with previous theoretical [71,98] and experimental [99,100] studies.

2.3.2 Pt(111) and Pt(100) slab model

Detailed optimization of Pt(111)-*p*(2x2) and Pt(100)-*p*(2x2) was carried out (see ref [87]) which preceded the present study. The optimization results are summarized in Appendix A2. The Pt(111)-*p*(2x2) slab was modelled using 6 atomic layers with the top 3 allowed to relax in all geometry optimization calculations. All adsorbates were introduced atop the relaxed side of the slab. The bottom 3 layers were fixed in the bulk optimized Pt structure with Pt-Pt bond distance of 2.806 Å. The vacuum gap between periodic slabs was maintained at 12 Å. Use of wider vacuum gaps had a less than 1.0 meV effect on calculated adsorption energies. Finally, for k-point sampling a 5x5x1 mesh was used—ensuring a minimum k-point density of 0.041 $Å^{-1}$, corresponding to 10x10x1, 5x5x1, 4x4x1 and 3x3x1 k-point grids for he *p*(1x1), *p*(2x2), *p*(3x3) and *p*(4x4) supercell, respectively. The Pt(100)-*p*(2x2) slab supercell was based on similar parameters with k-point grids of 9x9x1 and 5x5x1 and 4x4x1 for the *p*(1x1), *p*(2x2) and *p*(3x3) supercells, respectively. The latter slab also consists of 6 layers with the top three relaxed. Both Pt(111) and Pt(100) slabs were oriented such that the surface plane lies on the xy plane and the dipole correction along the z-axis was applied in all energy calculations. The unit cells used in specific calculations in this thesis will be stated in the relevant sections.

The convergence of the calculated energies as a function of the slab thickness showed the following behaviour, as demonstrated in Appendix A2:

- The adsorption energy of O on Pt(111) and Pt(100) surfaces continued to fluctuate (±40 meV variance) even up to very thick slab. Similar fluctuations have also been reported in the literature [101].
- The total energy of the clean slabs, fixed and partially relaxed, fluctuated with a periodic amplitude of ca. 50 meV/atom between 4 and 12 layers. Slabs with O adsorbed had slightly lower amplitudes, as a result within this thickness range large fluctuations in the adsorption energy of O were seen [87].
- An increase in the k-point sampling density along the xy plane lowered the fluctuation amplitude of clean slabs; however, at a great computational cost.

Considering the above, 6 layered slabs were used acknowledging that similar calculations based on differently sized slabs/models may correspond within ±40 meV to calculations in the present study. The *p*(3x3) and *p*(4x4) supercell slabs were based on the same optimized parameters as *p*(2x2) however with appropriately adjusted k-point grids. A cut-off energy of 400 eV was found to give sufficiently converged adsorption energies of oxygen on Pt surfaces. Increasing the cut-off energy further changed

the oxygen adsorption energy by less than 10 meV. Figure 2.2 shows the optimized Pt(111)-*p*(3x3) and Pt(100)-*p*(3x3) surface models and the various adsorption sites present.

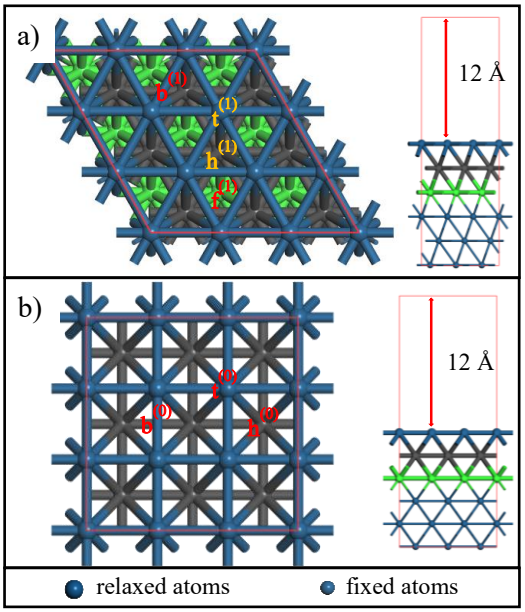

Figure 2.2: Surface models, a) Pt(111)-p(3x3) showing all 4 high symmetry sites, viz. $f^{(1)}$, $h^{(1)}$, $t^{(1)}$ and $b^{(1)}$ representing fcc, hcp, top and bridge sites, respectively, b) Pt(100)-p(3x3) showing 4 high symmetry sites, viz. $b^{(0)}$, $t^{(0)}$ and $h^{(0)}$ representing bridge, top and 4-fold-hollow sites, respectively. Pt atoms are represented as spheres, small (larger) for fixed (relaxed) atoms during geometry optimization and NEB calculations.

2.3.3 Pt[n(111) x n(100)] edge model

The intersection edge between Pt{111} and Pt{100} facets can be modelled using a NP model (cuboctahedron or truncated octahedron) or a NW model. Unlike NP models, NW models isolate the edge effect from corner effects. The simplest and probably most stable NW model for fcc metals is the hexagonal NW. An ideal hexagonal Pt NW grown along the [101] direction exposes 4x Pt{111} facets, 2x{100} facets and two types of edge boundaries, viz. (111)x(100) and (111)x(111). From this NW model it is possible to imagine further reductions giving the desired (111)x(100) edge region formed at the intersection of a Pt{111} and Pt{100} facet. Figure 2.3 gives this illustration using a plane hexagon to show various cuts leading to square, triangular and rhombic geometries. It is clear from this figure that the reduced geometries correspond to at least 50% reduction in atoms needed to model an edge bounded by terraces/facets of a given width. It is also clear that the only reduction useful in the present study is the rhombic shaped cut. The latter has an appropriate intersection angle between Pt{111} and Pt{100} facets, unlike the square and triangular cuts (see Figure 2.3).

The adsorption energy of O* and OH* over edge and terrace sites was used to assess the convergence of calculated energies as a function of NW diameter. Symmetric hexagonal NW models with two atoms along the axial direction (along the y-axis) and minimum vacuum gap of 12 Å between surfaces

belonging to any two neighbouring periodic images were probed with O* and OH* on edge-bridge, central terrace fcc-Pt{111} and bridge-Pt{100} sites. A k-point grid of 1x5x1, based on the converged k-point sampling for slab models, was used. All Pt atoms and adsorbates were allowed to fully relax during geometry optimization calculations. Figure 2.4 presents an illustration of the differently sized NWs and the corresponding convergence results. The adsorption energy of O* and OH* on edge-bridge sites converges more rapidly with NW size than for adsorption on central terrace sites. It is clear that after 6*wt* the adsorption energy of both O and OH only changes by a small amount.

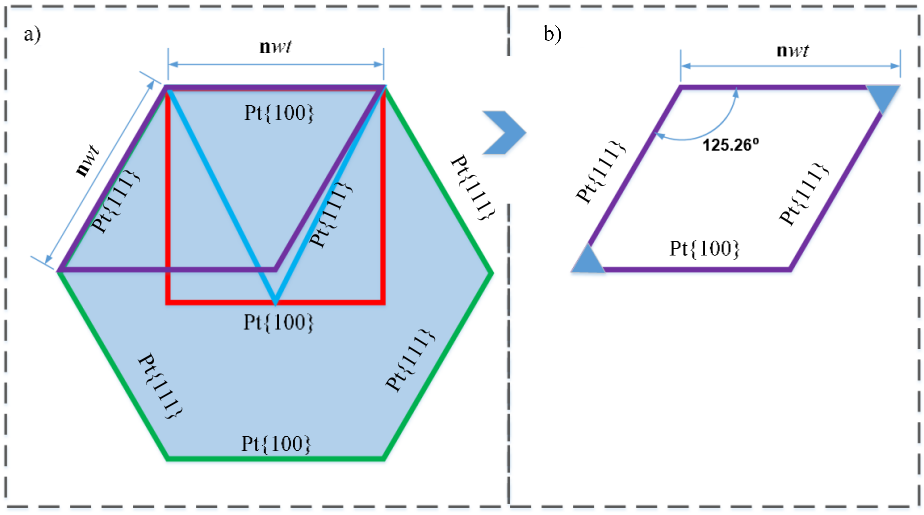

Figure 2.3: (a) Possible reductions of a hexagonal NW in cross-section, (b) Rhombic NW model with *n* atomic rows along each facet; (adapted from [87]).

Rhombic NW models were introduced (see [87]) and were later used to investigate the inter-facet mobility of atomic O under different coverage conditions [95]. Here, these NW models are also considered given their ability to significantly reduce the number of atoms required to model a (111)x(100) edge. Figure 2.5 shows the rhombic NW model used in this study, including the identified near-edge and edge adsorption sites. Figure 2.6 compares the adsorption energy of O* on various sites on hexagonal and rhombic NW models. This comparison shows a deviation of ca. 0.07 eV between adsorption of O* on different NW shapes. Shown in Figure 2.4b are the different adsorption energies of O* on $b^{(e)}$ sites of different models, i.e. NP and NWs. The difference in adsorption energy of O* on these different models is again within 0.07 eV. This variation needs to be acknowledged and considered when comparing across different surface models. Additional optimisation tests were conducted to further ascertain the model variance (see Appendix A3 and [87]).

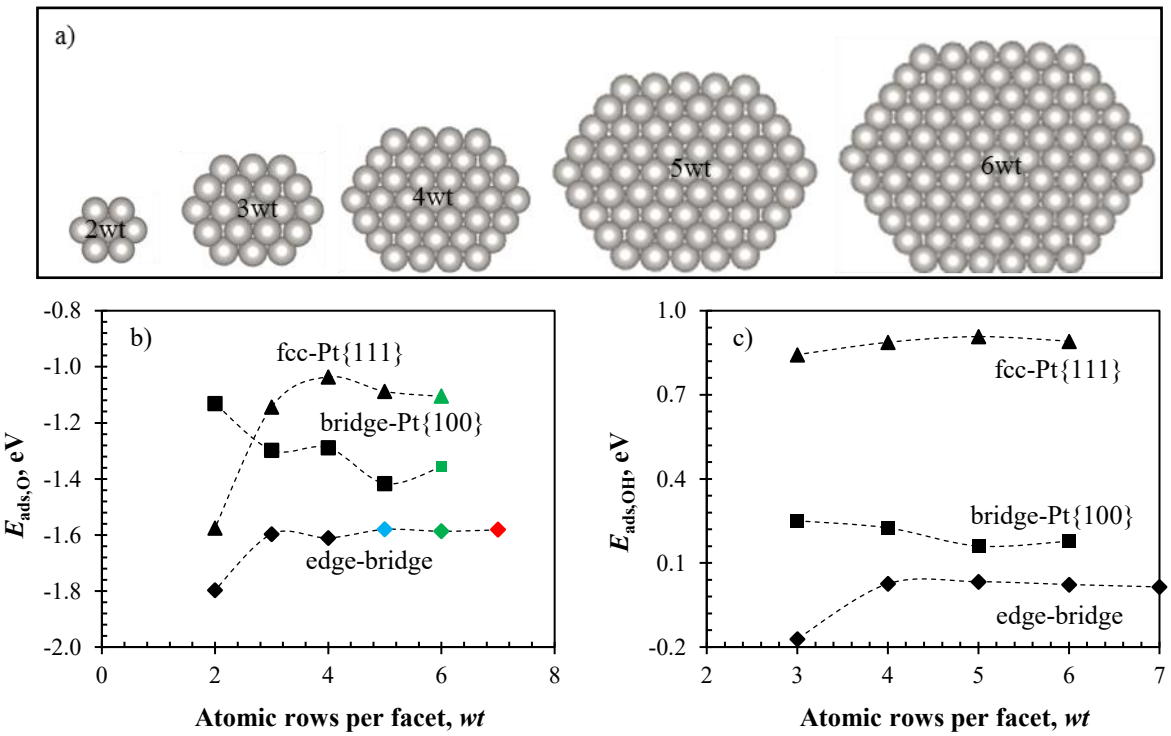

Figure 2.4: (a) axial projection of hexagonal NWs of various sizes, *n*wt refers to the number of atoms along each facet, (b) and (c) adsorption energy of O (ref. ½O_2) and OH (ref. H_2O-½H_2), respectively; over edge-bridge (♦), Pt{111} facet (▲) and Pt{100} facet (■) sites; green and red markers correspond to adsorption on a 147 and 309 atom cuboctahedral NP whilst blue corresponds to adsorption on a rhombic NW model.

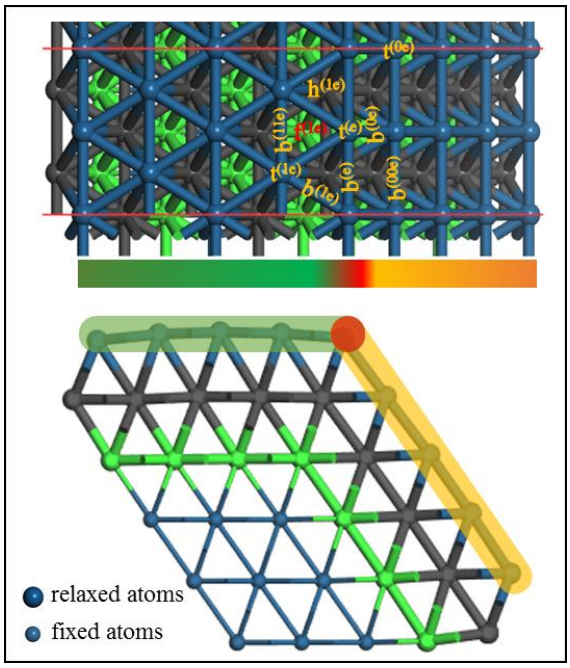

Figure 2.5: Rhombic NW model (Pt[5(111)x5(100)]) with edge sites defined as $b^{(e)}$ and $t^{(e)}$ for edge-bridge and edge-top sites, respectively. Near-edge sites are defined with a superscript (1e) and (0e) for those sites on the {111} and {100} facet, respectively. Pt atoms are represented as spheres, small (larger) for fixed (relaxed) atoms during geometry optimization and NEB calculations.

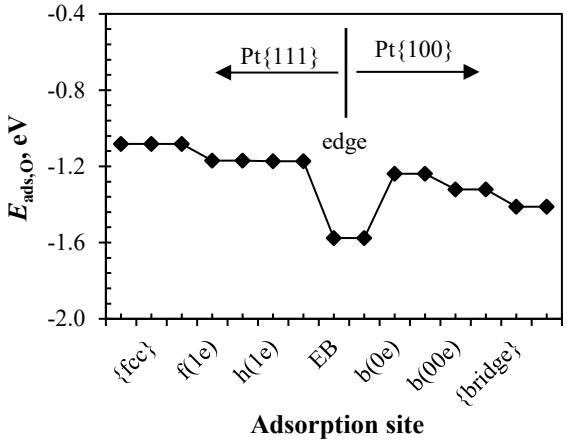

Figure 2.6: Calculated adsorption PES of O over a rhombic NW model; {fcc} and {bridge} adsorption sites correspond to central terrace sites on Pt{111} and Pt{100}, respecively.

2.4 Microkinetic modelling

2.4.1 General introduction

Microkinetic models (MKM) are instrumental in the study of chemical reaction phenomena at fluid-catalyst interfaces. These models give insight into both the surface state, i.e. coverage, and reaction productivity per catalyst sites, i.e. turnover frequency (TOF). Several MKM have been developed and applied in the study of reaction kinetics at the catalyst surface [102–106]. In principle, these models describe the time evolution of a chemical system and can be derived from the Markovian master equation, which itself can be derived from first principles [104,106,107].

$$\frac{dP_\sigma}{dt} = \sum_\beta \left[k_{\sigma\beta}P_\beta - k_{\beta\sigma}P_\sigma\right] \qquad 2.24$$

The Markovian master equation describes the transition of a system from a β microscopic configuration (state) to a σ state; P_σ is the probability of finding a system in a σ configuration and the $\sigma \Rightarrow \beta$ transition probability per unit time is given by $k_{\beta\sigma}$. One of the basic principles here is that the temporal evolution of the system to a new state depends only on the current state.

The simplest and probably most common of these models is the single site approximation (SA) [105]. The basis assumption in single site approximation models is that reaction intermediates are uniformly distributed on the catalyst surface [105,108] and consequently, the probability of finding an ij adsorbate pair is given by,

$$P_{ij} \equiv \theta_i\theta_j \qquad 2.25$$

where the coverage of i, i.e. θ_i, is defined as the number of sites occupied by i adsorbates divided by the total number of surface sites (occupied and unoccupied). Uniform distribution of adsorbates is however only realised in the absence of interactions between adsorbates, which might favour ordering, and if surface mobility of adsorbates is sufficiently fast compared to the system TOF [108]. Moreover, since the SA model also assume independent sites, the adsorption energy of each adsorbate is constant in coverage,

$$E_{ads,i}^{SA}(\Theta) = E_{ads,i}(\Theta \to 0) \qquad 2.26$$

where $E_{ads,i}(\Theta \to 0)$ is the adsorption energy of i at a low coverage limit. The most obvious limitation of this model is that it ignores lateral interactions and consequently gives a poor description of surface topology—leading to an underestimation of the TOF especially when modelling systems with strong repulsive lateral interactions and in the low temperature regions [105].

The next simplest and also common model is based on the mean-field theory, the so-called Bragg-Williams Approximation (BWA) [105,106,109]. This model considers a single site surrounded by a mean-field due to a cloud of adsorbates on the surface. By construction, this model also assumes a uniform distribution of adsorbates on the surface, ignoring correlation effects [105,106,109,110]. Within the BWA model the adsorption energy of any adsorbate i is linearly dependent on the surface coverage function of other adsorbates and is described by,

$$E_{ads,i}^{BWA}(\Theta) = E_{ads,i}(\Theta \to 0) + \sum_{s,j} \varepsilon_{ij}\theta_j \qquad 2.27$$

where ε_{ij} is the interaction energy between an ij pair of adsorbates and the double summation term is over all adsorbate pairs over each considered s pair of sites. For example, any site in a square lattice has 4 nearest-neighbour (NN) and 4 next-nearest-neighbour (NNN) sites—when treating lateral interactions up to the NNN interaction. Hence the double summation in 2.27 will go over all 8 sites [105]. Since at moderate coverage, adsorbates may reorder on the surface to minimise/maximise repulsive/attractive interactions, the lack of correlational effect in BWA models results in underestimation and overestimation of attractive and repulsive lateral interactions, respectively [105].

The quasi-chemical approximation (QCA), naturally accounts for correlational effects—and is considered an improvement to the BWA [102,105,106]. Correlational effects are incorporated since the model explicitly treats an isolated cluster of adsorbates surrounded by a cloud of adsorbates. The occupation of these explicitly treated sites is such that the overall repulsive/attractive interactions are minimized/maximized. According to the QCA, the adsorption energy of i varies with the conditional probability that an adsorbate i has a j neighbour in a given pair of sites, $P(ij|i)$, [102,105,111]:

$$E_{ads,i}^{QCA}(\Theta) = E_{ads,i}(\Theta \to 0) + k_B T \sum_{s} ln\left[\sum_{j} P(ij|i) \exp\left(\frac{\varepsilon_{ij}}{k_B T}\right)\right] \qquad 2.28$$

with k_B and T being the Boltzmann constant and temperature, respectively. The inner sum in the second term accounts for correlation energy between different adsorbates occupying a pair of sites and the outer sum runs over all explicitly considered pairs of sites with a central site in the clusters—giving the overall correlation energy. The conditional probability is calculated from the probability of finding pair of sites occupied by i and j adsorbates, together with the application of Bayes' theorem as, [112]

$$P(ij|i) = \frac{P(j|ij)P_{ij}}{P_i}, \qquad P_i \neq 0 \qquad 2.29$$

$P(i|ij)$[‡] equals unity whilst the probability of finding an adsorbate i on the surface, P_i, is equal to the coverage of adsorbate i, i.e. $P_i = \theta_i$. The probability of finding a pair of adsorbates is determined from the grand-canonical distribution function for a pair of sites which can either be occupied by any of the adsorbates or be vacant. From a simple derivation, the relationship between different adsorbate pairs is given by,[103,105]

$$\frac{P_{ii}P_{jj}}{P_{ij}^2} = \exp\left(\frac{2\varepsilon_{ij} - \varepsilon_{ii} - \varepsilon_{jj}}{k_B T}\right) \tag{2.30}$$

with the following condition (balance) equations,

$$\sum_{ij} P_{ij} = 1 \tag{2.31}$$

and

$$\sum_{j} P_{ij} = \theta_i \tag{2.32}$$

A solution to equations 2.30 – 2.32 can only be calculated numerically for any system with more than one adsorbate—this is computed iteratively using the following equations, where the superscript (m) denotes a value at the m^{th} iteration step [103,105].

$$P_{ij}^{(m+1)} = \sqrt{P_{ii}^{(m)} P_{jj}^{(m)} \exp\left(-\frac{2\varepsilon_{ij} - \varepsilon_{ii} - \varepsilon_{jj}}{k_B T}\right)} \tag{2.33}$$

$$P_{ii}^{(m+2)} = \frac{P_{ii}^{(m)} \theta_i}{P_{ii}^{(m)} + \sum_{j \neq i} P_{ij}^{(m+1)}} \tag{2.34}$$

Each ij element in the converged matrix solution to the above equations representing the probability of finding an ij pair of adsorbates at a given condition. Various other models which explicitly treat larger clusters, e.g. Kikuchi-approximations, have been shown to be in better agreement with kinetic Monte Carlo (kMC) simulations, but at a moderate cost in computational efficiency [106].

Dynamic/kinetic Monte Carlo (DMC/kMC) methods represents the most accurate description of chemical processes on catalyst surfaces [104–106]. In principle, these methods solve the Markovian master equation (2.24) by Monte Carlo approach [104]. As applied in heterogeneous catalysis,

[‡] $P(i|ij)$ is the probability of finding an i occupied site given a pair of sites occupied by i and j

DMC/kMC methods consider a 2D array of sites with special properties such as occupancy, type and number of neighbours. This so-called lattice-gas model maps the coarse-grained position of reaction intermediates—effectively eliminating vibrational transitions which would be more frequent than the reaction/diffusion processes of interest in microkinetic modelling.

Given a lattice-gas (LG) with a specified occupancy state, i.e. $\boldsymbol{\sigma} = \{\sigma_1, \sigma_2, \dots, \sigma_M\}$, the total energy can be calculated adopting a cluster expansion approach [106],

$$E(\boldsymbol{\sigma}) = E_0 + \sum_{i=1}^{M} E_i \sigma_i + \frac{1}{2!} \sum_{i=1}^{M} \sum_{\substack{j=1 \\ j \neq i}}^{M} \varepsilon_{ij} \sigma_i \sigma_j + \cdots \qquad 2.35$$

where E_0 and E_i are the energies of a clean LG surface and LG surface with one i adsorbate. The second term sums over all M sites of the LG surface with σ_i being the occupancy value which equals 1 when a site is occupied by adsorbate i and zero for any other index. The third term describes the pairwise interaction and runs over all M sites. Three-, four- and *N*-body interactions can also be included, however they would require a triple, quadruple and *N*-tuple summation terms, respectively, which are computational expensive [113]. Equation 2.35 together with the Brønsted-Evans-Polanyi (BEP) principle, which relates the activation energy to the reaction energy, can describe both the coverage dependent reaction and activation energies, given a transition in the LG surface [106,113]. With this information DMC/kMC models then solve equation 2.24 using various numerical algorithms over large time scales. The most common of these are First Reaction Method (FRM), Random Selection Method (RSM) and Variable Step Size Method (VSSM) [104,107,113].

2.4.2 Mean-field microkinetic models

In this study, mean-field microkinetic model refers to both the SA and BWA models. As stated already, both SA and BWA models are similar in that they assume uniformly/randomly distributed adsorbates leading to the approximation of the probability of finding any pair of adsorbates as described in 2.25. Therefore, microkinetic models based on SA and BWA assumptions are represented by the steady state solution to the species balance equation,

$$\left(\frac{d\theta_i}{dt} = \sum\nolimits_j \nu_{ij} r_j(\theta_1, \dots, \theta_N) \right)_{i=1,\dots N} \qquad 2.36$$

with:

θ_i – surface coverage of species i (fraction of surface sites occupied by species i)

ν_{ij} – stoichiometric coefficient of species i in reaction j, chosen as negative for reactants

N – total number of surface species

r_j – kinetic rate of elementary reaction step j

The kinetic reaction rate of each elementary step (r_j) can be calculated based on the mass action equation,

$$r_{net} = k_f \theta_A \theta_B - k_r \theta_C \theta_* \tag{2.37}$$

for a typical bimolecular reaction, $A^* + B^* \leftrightarrow C^* + *$, where the asterisk (*) indicates that a given intermediates is adsorbed on a surface (adsorbate-site couple). In equation 2.37, k_f and k_r are the forward and reverse kinetic rate constants, respectively. For surface reaction, the kinetic rate constants can be calculated from the Transition State Theory as follows,

$$k_f = \frac{k_B T}{h} \frac{q^{\ddagger}_{vib,TS}}{q_{vib,IS}} \exp\left(-\frac{E_{a,f}(\Theta)}{k_B T}\right) \tag{2.38}$$

where $q_{vib,IS}$ and $q^{\ddagger}_{vib,TS}$ are the vibrational partition functions of the initial and transition states, respectively; h is the Planck constant. Only real vibrational modes are used to evaluate $q^{\ddagger}_{vib,TS}$. The vibrational partition functions include zero-point energy correction. Lastly, $E_{a,f}(\Theta)$ is the coverage dependent activation energy for the forward reaction—for the SA model this is independent of coverage. The rate constant for the reverse reaction is also calculated using equation 2.38, however, with a different activation energy and initial state partition function—the forward and reverse activation energies are related to the reaction energy ($\Delta_{\text{rxn}}E(\Theta)$) as follows.

$$\Delta_{\text{rxn}}E(\Theta) = E_{a,f}(\Theta) - E_{a,r}(\Theta) \tag{2.39}$$

Adsorption and desorption reactions present a slightly different challenge and their rate constants are calculated from collision theory. Given a typical non-dissociative adsorption of A over a catalyst surface, the net adsorption rate can be calculated as follows,

$$r_{ads,A} = k_{ads,A} p_A \theta_* - k_{des,A} \theta_A \tag{2.40}$$

where θ_* is the fraction of vacant sites on which A can adsorb and p_A is the partial pressure of adsorbate A—this is valid for gas phase A impingement on a solid surface. The adsorption rate constant $k_{ads,A}$ is given by equation 2.41 as follows,

$$k_{ads,A} = \frac{A_{site} S_0}{\sqrt{2\pi m_A k_B T}} \frac{Q^{\ddagger}_{TS}}{Q_{A_{gas}}} \exp\left(-\frac{E_{a,f}(\Theta)}{k_B T}\right) \tag{2.41}$$

with:

$Q_i = q_{trans,i} q_{rot,i} q_{vib,i}$

A_{site} – area of a single catalytic site, [m^2]

m_A – mass of an adsorbate A, [kg]

S_0 – initial sticking probability

The last two parts in equation 2.41 disappear if A adsorption does not have an activation barrier. To ensure thermodynamic consistency, the kinetic rate constant for the reverse (desorption) reaction is calculated as a ratio of the forward rate constant and the equilibrium constant (K_A) as shown below.

$$k_{des,A} = \frac{k_{ads,A}}{K_A} = \frac{k_{ads,A}}{Q_A / Q_{A_{gas}} \exp\left(-\frac{\Delta_{\mathrm{rxn}} E(\Theta)}{k_B T}\right)} \qquad 2.42$$

Q_A and $Q_{A_{gas}}$ is the total non-configurational partition functions of adsorbed and gas phase A, respectively. For the adsorbed state, only the vibrational contributions are considered. $\Delta_{\mathrm{rxn}} E(\Theta)$ is equivalent to the adsorption energy.

For dissociative adsorption of AB, equations 2.40 – 2.42 can be modified as follows,

$$r_{ads,AB} = k_{ads,AB} p_{AB} \theta_*^2 - k_{des,AB} \theta_A \theta_B \qquad 2.40^*$$

$$k_{ads,AB} = \frac{A_{site} S_0}{\sqrt{2\pi m_{AB} k_B T}} \frac{Q_{TS}^{\ddagger}}{Q_{AB_{gas}}} \exp\left(-\frac{E_{a,f}(\Theta)}{k_B T}\right) \qquad 2.41^*$$

$$k_{des,A-B} = \frac{k_{ads,AB}}{K_{AB}} = \frac{k_{ads,AB}}{Q_A Q_B / Q_{AB_{gas}} \exp\left(-\frac{\Delta_{rxn} E(\Theta))}{k_B T}\right)} \qquad 2.42^*$$

The reaction and activation energies and vibrational modes, necessary to evaluate kinetic rate constants for each elementary reaction, can be calculated from DFT data. The coverage dependent reaction and activation energies are given by,

$$\Delta_{\mathrm{rxn}} E_i(\Theta) = \sum \nu_{ij} E_{ads,i}(\Theta) \qquad 2.43$$

and,

$$E_{af,i}(\Theta) = \max\left(0, \Delta_{rxn} E(\Theta), E_{af,i}(\Theta \to 0) + \alpha_i [\Delta_{rxn} E(\Theta) - \Delta_{rxn} E(\Theta \to 0)]\right) \qquad 2.44$$

where α_i is the proximity factor describing the relative position of the transition state to the initial and final states (such that $0 \leq \alpha_i \leq 1$) [114]. Equation 2.44 is based on the BEP principle and the proximity factor can be calculated as,

$$\alpha_i = \frac{E_{af,i}}{E_{af,i} + E_{ar,i}} \qquad 2.45$$

where the activation energies are calculated at a fixed coverage and α_i is assumed to be coverage independent. Equation 2.45 is consistent with Hammond's [115] postulate and has also been applied in previous studies [116,117].

In this study equation 2.36 was solved using numerical integration to obtain steady state properties at various temperatures. A more detailed description of how this model was constructed and solved in a Python programming language is given later and in Appendix D. The solution to QCA models is based on equation 2.36 as well; however, instead of assuming uniform adsorbate distribution the kinetic rate equations are based on calculated probabilities of finding adsorbate-adsorbate pairs.

2.4.3 Calculating lateral interactions

In real systems, co-adsorption of reaction intermediates may result in a net decrease or increase of the total system energy, depending on the number, type, position and sometimes orientation of co-adsorbed particles on a catalyst surface, relative to the total energy of independent particles occupying the same state as the interacting system [105,106,117]. Intuitively, for the ORR reaction, stabilisation effects due to the formation of hydrogen bond networks in systems involving certain configurations of O_2*, O*, OH* and H_2O* are anticipated [118,119]. Due to changes in surface deformation energy with increasing coverage, certain configurations may also result in stabilisation—despite the lack of H-bond networks or favourable dipole-dipole interactions [117]. The converse is also true, an increase in total energy can arise due to repulsive interactions between closely co-adsorbed intermediates, e.g. O* – O *, O_2* – O* [95].

Whilst a more complete representation of these *N*-body interactions may be written in a cluster expansion form (cf. equation 2.35) with *N* going up to the total number of particles on the surface, the associated computational cost is quite prohibitive. Firstly, much larger unit cells would be required to calculate the total energies of the *N*-body clusters isolated from their periodic images and then once they are incorporated, further computational costs are anticipated due to the complexity of the function describing the total energy. If kMC simulations are used, this leads to further computational penalties as more cluster searches need to be conducted and standard optimization tricks become limited as a

single change in lattice state affects the kinetic rate constants of events occurring far from the enabled event (i.e. occurred event) [113].

This study is therefore limited to pair cluster interactions, i.e. $N = 2$, applied in all kinetic models, i.e. SA, BWA, QCA and kMC. There are two key definitions which underpin how lateral interactions are incorporated in mean-field models presented in this study. The first is a site definition—here a full monolayer (1.00 ML) coverage corresponds to one adsorbate per surface Pt atom. Therefore, each site encloses exactly one Pt atom (see Figure 2.7) and within each site there are multiple high symmetry states, e.g. $f^{(1)}$, $h^{(1)}$, $t^{(1)}$ and $b^{(1)}$ on Pt(111) surface. Only one state can be occupied per site. In kMC simulations performed here, the simultaneous occupation of multiple adsorption states by multiple adsorbates per Pt atom (site definition in Figure 2.7) is possible, however it is accompanied by an appropriate energy correction based on pair interactions given in Appendix B.

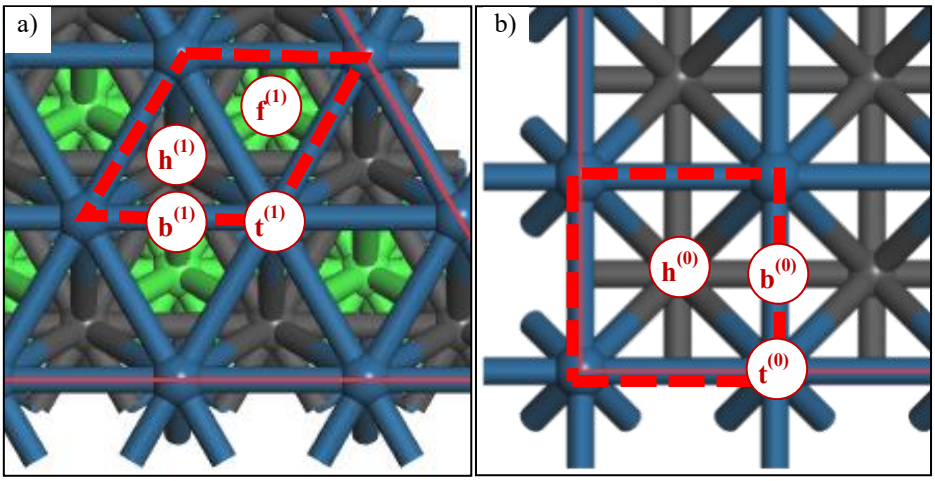

Figure 2.7: Illustration of high-symmetry adsorption states on (a) Pt(111) and (b) Pt(100) surface—dashed red lines mark a single surface site.

Chapter 3 will show that the key adsorption states are $b^{(1)}$ and $b^{(0)}$ for O_2*, $f^{(1)}$ and $b^{(0)}$ for O*, $t^{(1)}$ and $b^{(0)}$ for OH*/H*, $b^{(1)}$ for OOH* and $t^{(1)}$ and $t^{(0)}$ for H_2O* on Pt(111) and Pt(100) surfaces. These adsorption states are energetically preferred over others. Therefore, the definition of interaction pairs is based on this information. Figure 2.8 presents the different neighbouring structures for different combinations of adsorption states over the Pt(111) surface. Over the Pt(100) surface only two states are preferred, i.e. $t^{(0)}$ for H_2O* and $b^{(0)}$ for all other intermediates. Therefore, the relevant combinations are $b^{(0)} – b^{(0)}$, $b^{(0)} – t^{(0)}$ and $t^{(0)} – t^{(0)}$ as illustrated in Figure 2.9. Cluster interaction energies have been calculated for each configuration on each surface—the results are presented in Appendix B3 and B4. The interaction energy ($\epsilon_{i,j}$) is defined as the deviation from ideal case of non-interacting particles, and is mathematically expressed as follows,

$$\epsilon_{i,j} = E_{i+j} - \left(E_i^0 + E_j^0\right) + E_{clean\ slab} \qquad 2.46$$

where E_i^0 is the total energy of an independent i species, calculated from DFT over a Pt(111)-p(4x4) or Pt(100)-p(3x3) surface. E_{i+j} is the total energy of species i and j co-adsorbed on a Pt(111)-p(4x4) or Pt(100)-p(3x3) surface. The unnumbered sites in Figures 2.8 and 2.9 have been left out due to the absence of stable minima—in the kMC simulations these are given a large repulsive cluster energy, > 1.2 eV, to enforce their infeasibility[§]. In mean-field models, only the first 6 and 8 neighbours over the Pt(111) and Pt(100) surfaces are respectively considered. Appendix B3 and B4 present calculated interaction energies of various clusters on Pt(111)-p(4x4) and Pt(100)-p(3x3) slab surfaces, respectively. These energies will be incorporated in microkinetic analyses presented in Chapters 4 - 6. On a Pt(111)-p(3x3) supercell, the pair interaction clusters were found to interact complexly with their periodic images. As a result, the p(4x4) supercell was instead used in modelling of pair interactions.

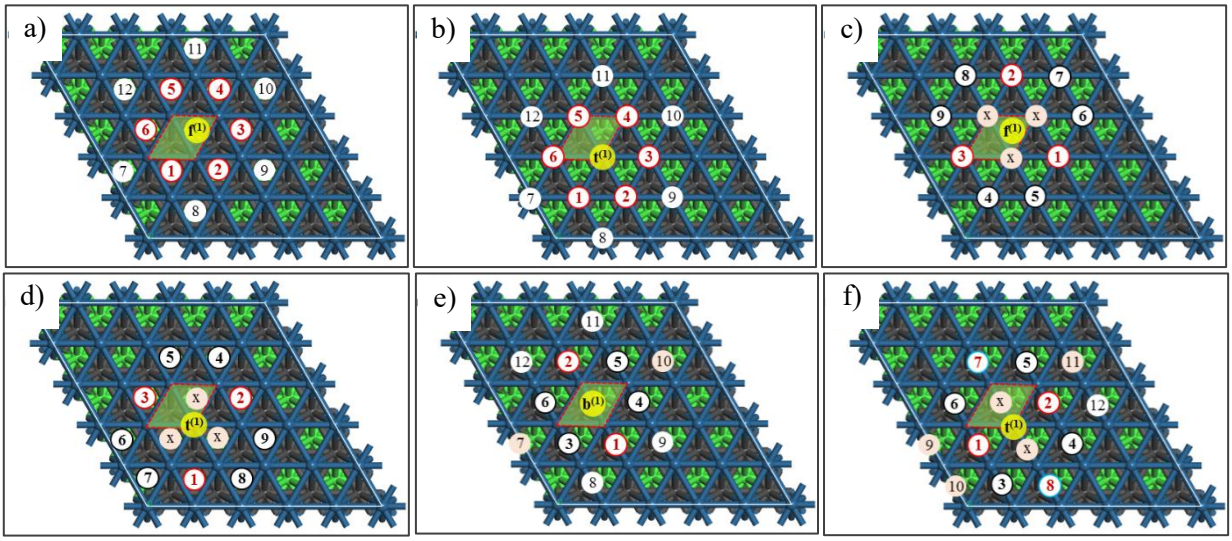

Figure 2.8: Neighbouring sites on Pt(111) surfaces; (a) $f^{(1)}$ - $f^{(1)}$, (b) $t^{(1)}$ - $t^{(1)}$, (c) $f^{(1)}$ - $t^{(1)}$, (d) $t^{(1)}$ - $f^{(1)}$, (e) $b^{(1)}$ - $b^{(1)}$ and (f) $t^{(1)}$ - $b^{(1)}$ neighbouring structures; pairs with 'x' marked sites are not included in the BWA and QCA models. This simplification only affects bridge-top and fcc-top interactions; furthermore, it is valid at moderate to low coverages where such crowding is unlikely.

It is computationally convenient to structure interaction energies between various pairs into shells. Over the Pt(111) surface the first 6 neighbours are considered and incorporated into BWA and QCA microkinetic models. Tables 2.1 and 2.2 present a summary of pairwise interaction energies between a central adsorbate over a Pt(111)-p(4x4) and Pt(100)-p(3x3) surface and its first set of neighbours, respectively. It is assumed that all A-B interactions are energetically equivalent to B-A interactions.

[§] Introducing a large and repulsive interaction energy for pairs which are found to be unstable (see 'x' marked sites in Figures 2.8 and 2.9) allows for the model to reduce if not eliminate the occurrence of these states thereby matching quantum-chemical calculations which predict these to be unstable/unfavourable.

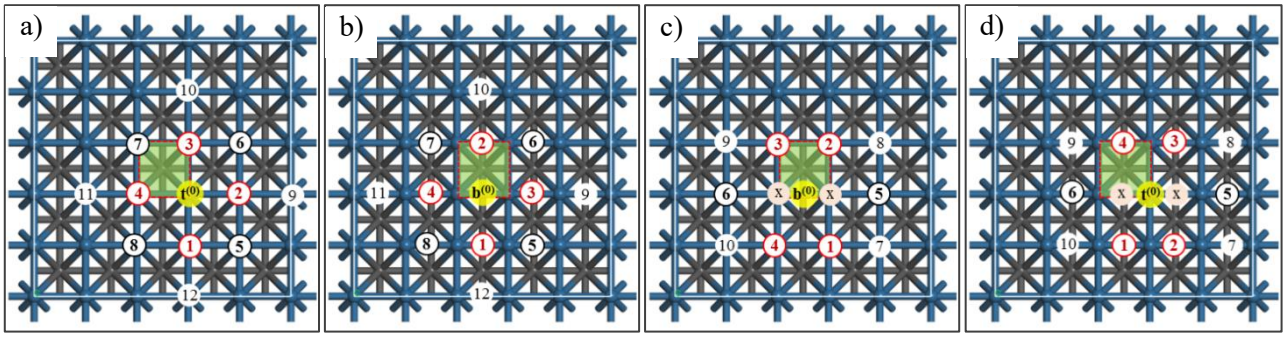

Figure 2.9: Neighbouring sites on Pt(100) surfaces; (a) $t^{(0)}$ - $t^{(0)}$, (b) $b^{(0)}$ - $b^{(0)}$, (c) $b^{(0)}$ - $t^{(0)}$ and (d) $t^{(0)}$ - $b^{(0)}$ neighbouring structures; pairs with 'x' marked sites are not included in the BWA and QCA models. This simplification only affects bridge-top interactions; furthermore, it is valid at moderate to low coverages where such crowding is unlikely.

Lateral interactions on Pt(111) and Pt(100)

The BWA and QCA models make use of pair-interaction energies in order to incorporate coverage effects. Table 2.1 show different pair interactions on Pt(111)-*p*(4x4) surface only for the first 6 neighbours of a central adsorbate as numbered in Figure 2.8. As an example, O*-O* pair interactions of the first 6 neighbours are all equal to 0.257 eV. At θ_O = 1.0 ML, considering only the first 6 neighbour interactions, the BWA and QCA predicted adsorption energy of O* will be -1.289 eV (adsorption energy at low coverage) + 6x 0.257 eV = 0.253 eV. Therefore, θ_O = 1.0 ML is unlikely even at 0 K. The interaction energy between the first 6 H*-H* pairs equals to 0.019 eV; much lower compared to O*-O* interactions. Also considering only the first 6 pair interactions at θ_H = 1.0 ML, the adsorption energy of H* equals to -0.530 eV + 6x 0.019 eV = -0.416 eV. Therefore, a 1.0 ML coverage of the Pt(111) surface with H* adsorbate is quite likely.

Although also based on $t^{(1)}$ – $t^{(1)}$ pairs, OH*-OH* interactions are less trivial. Two of the first 6 neighbours have an interaction energy of -0.221 eV. The attractive interaction is due to hydrogen bonding between the O atom of the central OH* and H atom of neighbouring OH* intermediate. The central OH* adsorbate can also form an additional hydrogen bonding link with a third OH* neighbour. The remaining 3 of the 6 neighbours cannot form hydrogen bonding and these have interaction energies of 0.037 eV. At θ_{OH} = 1.0 ML, the OH* adsorption energy is ca. 0.855 eV + 3x (-0.221 eV) + 3x (0.037 eV) = 0.303 eV. Therefore, high coverage of the Pt(111) with OH* adsorbates is energetically more favourable, i.e. 0.855 eV at 1/16 ML vs. 0.303 eV at 1 ML.

For O_2*-O_2* interactions, the first two neighbours (see Figure 2.8e) were calculated, however consistently converged to different structures. In the BWA and QCA models it was decided to use the same interaction energies for these pairs as one calculated for the 3rd – 6th pair, i.e. 0.110 eV. If any of the microkinetic simulations predict very high O_2* coverages the latter will need to be revised. Using

Figure 2.8 and the data in Appendix B2, the rest of Table 2.1 was populated as outlined for O*-O*, H*-H* and O_2*-O_2*, above.

Table 2.1: Pairwise interaction energies (in eV) between ORR intermediates adsorbed over a Pt(111)-*p*(4x4) slab surface; energies presented here correspond to the pair structures suggested in Figure 2.8.

1st neighbour						
	O_2*	O*	H*	OH*	OOH*	H_2O*
O_2*	0.110	0.096	0.087	0.060	0.054	0.001
O*	-	0.257	0.043	0.013	0.068	-0.042
H*	-	-	0.019	0.015	0.057	0.021
OH*	-	-	-	-0.221	-0.036	-0.048
OOH*	-	-	-	-	0.054	-0.353
H_2O*	-	-	-	-	-	-0.330
2nd and 3rd neighbours						
O_2*	0.110	0.096	0.087	0.060	0.054	0.001
O*	-	0.257	0.043	0.013	0.068	-0.042
H*	-	-	0.019	0.015	0.057	0.021
OH*	-	-	-	-0.221	-0.036	-0.048
OOH*	-	-	-	-	0.054	-0.353
H_2O*	-	-	-	-	-	-0.330
4th, 5th and 6th neighbours						
O_2*	0.110	0.096	0.030	0.004	0.054	0.009
O*	-	0.257	0.034	0.052	0.068	0.033
H*	-	-	0.019	0.015	0.022	0.021
OH*	-	-	-	0.037	0.009	0.003
OOH*	-	-	-	-	0.054	0.031
H_2O*	-	-	-	-	-	0.074

Table 2.2: Pairwise interaction energies (in eV) between ORR intermediates adsorbed over a Pt(100)-*p*(3x3) slab surface; energies presented here correspond to the pair structures suggested in Figure 2.9.

1st and 2nd neighbours					
	O_2*	O*	H*	OH*	H_2O*
O_2*	0.057	0.057	0.024	0.005	-0.210
O*	-	0.055	0.007	-0.217	-0.306
H*	-	-	0.005	0.003	-0.002
OH*	-	-	-	-0.137	-0.175
H_2O*	-	-	-	-	-0.285
3rd and 4th neighbours					
O_2*	0.980	0.520	0.179	0.472	-0.040
O*	-	0.423	0.154	0.328	0.028
H*	-	-	0.013	0.105	-0.016
OH*	-	-	-	0.334	0.049
H_2O*	-	-	-	-	0.049
5th, 6th, 7th and 8th neighbours					
O_2*	0.051	0.058	0.001	0.018	0.000
O*	-	0.082	0.014	0.030	0.000
H*	-	-	-0.001	0.002	0.000
OH*	-	-	-	0.025	0.000
H_2O*	-	-	-	-	0.000

Table 2.2 shows the interaction energies between pairs of ORR intermediates on Pt(100)-*p*(3x3). This table was also populated in the same manner as Table 2.1 above but using data in Appendix B4 and the information given in Figure 2.9. In summary, on Pt(111) only the OH*-OH*, OH*-H_2O*, OOH*-H_2O* and H_2O*-H_2O* nearest-neighbour pairs have appreciable attractive interactions. Other interactions are repulsive with the most repulsive involving closely co-adsorbed O* and O_2* intermediates. On Pt(100) pair interactions with OH* are attractive when hydrogen bonding network is formed and repulsive in the absence of H-bond networks. Stronger repulsions occur when neighbours share a Pt atom. On both surfaces H* - *X**, with *X** being any ORR intermediate including H*, are repulsive but much weaker than other repulsively interacting pairs. Therefore, θ_H = 1.0 ML is possible on both Pt(111) and Pt(100) surfaces.

CHAPTER 3: Mobility of ORR Intermediates over Pt Surfaces

3.1 Introduction

The oxygen reduction reaction (ORR) is structure sensitive [10,20–24,32] and its dominant reaction pathway varies on different type of catalyst surfaces [26–28,30]. DFT studies have shown that Pt(111) surfaces can efficiently facilitate OH hydrogenation to H_2O but not O* hydrogenation to OH*. Pt(100) surfaces can efficiently facilitate O* hydrogenation to OH* but not OH* hydrogenation to H_2O* [26,27]. The ORR mechanism over Pt(111) surface is reported to proceed via a peroxyl mechanism where O_2* dissociation is preceded by the first proton-electron transfer process—the oxygen-oxygen bond then breaks after OOH* formation with a lower activation energy [27,28,30]. Conversely, over Pt(100) facets the activation energy for O_2* dissociation is among the lowest barriers in the ORR mechanism on this surface [26,27]. Consequently, the ORR proceeds via a direct dissociation mechanism with two proton-electron transfer steps for O* → OH* → H_2O*. Considering the differences in reaction pathway it is of interest to understand whether any species exchange occurs between Pt{111} and Pt{100} facets on multifaceted catalyst surfaces. For such diffusion to occur and be relevant in the kinetic modelling of ORR over multifaceted Pt surfaces, intra- and inter-facet diffusion rates of ORR intermediates need to be fast. These are determined by the diffusion barriers of each intermediate between its various adsorption minima on the potential energy surface. Temperature and surface coverage can also influence intra- and inter-facet diffusion rates.

Therefore, two crucial questions arise from the above, (1) how mobile are ORR intermediates on Pt NP surfaces and (2) can ORR intermediates be exchanged between adjacent surfaces. This Chapter presents DFT calculations on the study of interaction and mobility of ORR intermediates over Pt(111) and Pt(100) surfaces. Rhombic Pt NW models are used to study the diffusion energetics of ORR intermediates between Pt{111} and Pt{100} facets in the absence of the effect from corner sites (cf. to NP models).

3.2 Methods and surface models

3.2.1 Quantum Chemical Calculations

Spin-polarized periodic DFT calculations were conducted using the Vienna *ab initio* Simulation Package (VASP) [81,84,120]. All calculations were performed using the Perdew-Burke and Ernzerhof (PBE) generalized gradient approximation (GGA) exchange-correlation functional [62] with the projector augmented wave (PAW) method [85,86]. In all DFT calculations performed here on, the cut-off energy was set to 400 eV. Further computational details were discussed in Chapter 2, Subsection 2.2.2.

3.2.2 Surface models

Figure 3.1 presents three surface models used to study intra- and inter-facet mobility of ORR intermediates over multifaceted Pt surfaces. The Pt{111} and Pt{100} facets, in multifaceted Pt surfaces, were modelled as 6-layered Pt(111)-*p*(4x4)** and Pt(100)-*p*(3x3) slab supercells, respectively. These slab surfaces were cleaved from bulk platinum with an optimised conventional lattice parameter of 3.968 Å. In all calculations the k-point density and vacuum gap between surface atoms belonging to periodic images was kept less than 0.041 $Å^{-1}$ and more than 12 Å, respectively. More details on the number of relaxed/fixed atomic layers, available sites on the different surface models are shown in Figure 3.1.

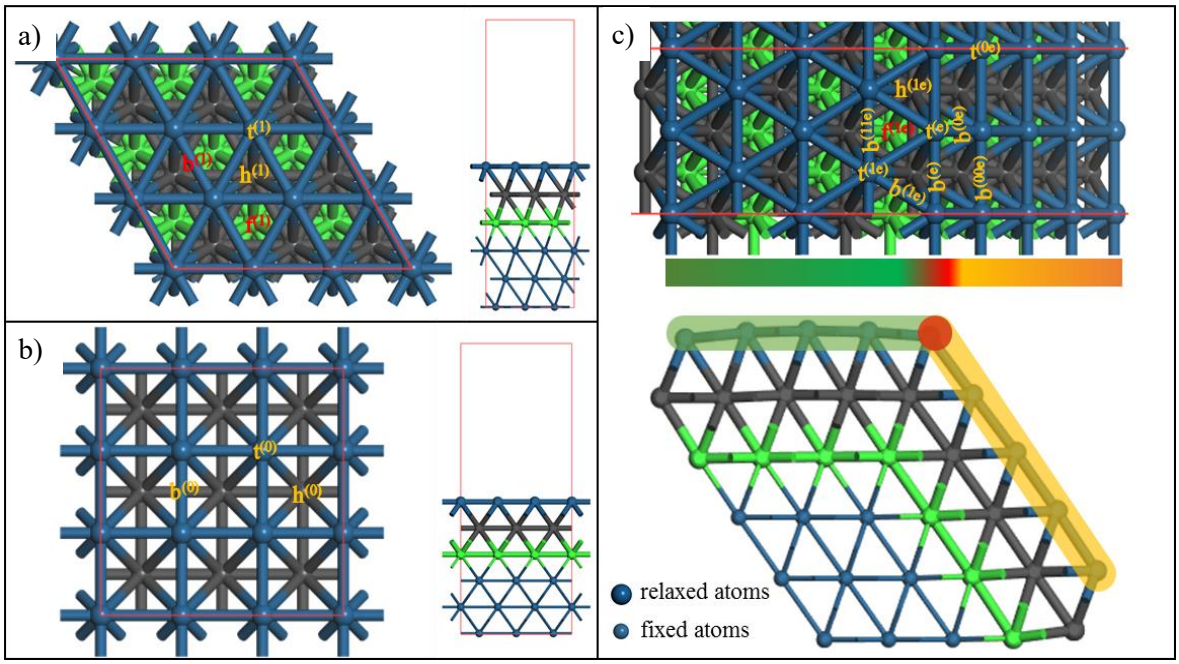

Figure 3.1: Surface models, a) Pt(111)-*p*(3x3) showing all 4 high symmetry sites, b) Pt(100)-*p*(3x3) showing all 3 high symmetry sites and c) the Pt[5(111)x5(100)] NW model showing edge and near-edge sites.

** Shown in Figure 3.1 is the Pt(111)-*p*(3x3) instead of the *p*(4x4) supercell; both surfaces show the same sites and were modelled with similar physical parameters, i.e. thickness and vacuum gap. The *p*(4x4) supercell was mainly considered in order to improve the accuracy of the estimated pair interaction energies.

Inter-facet diffusion is modelled over an infinite rhombic NW model with 6 atomic layers beneath each facet and 5 atomic rows along each terrace, i.e. Pt[5(111)x5(100)] [95]. The Pt[5(111)x5(100)] NW model is periodic along its axial direction, y-axis, and each unit cell consist of two Pt atoms along the y-axis. A gamma centred Monkhorst-Pack k-point mesh of 1x5x1 was used in all NW calculations. A vacuum gap of at least 12 Å was maintained between periodic NW models. The diffusion barriers were calculated from converged and optimized transition states as outlined in Subsection 2.2.2. All metal atoms were fixed during vibrational analyses.

3.3 ORR intermediates over Pt(111) surfaces

The interaction of ORR intermediates, i.e. O_2*, O*, H*, OH, OOH* and H_2O*, with Pt(111) surface sites is probed over four high-symmetry adsorption sites, i.e. $t^{(1)}$ (atop a Pt atom), $b^{(1)}$ (across two Pt atoms over bridge), $f^{(1)}$ (above a face centred cubic, 3-fold site) and $h^{(1)}$ (above a hexagonal close pack, 3-fold site)—superscript (1) refers to the (111) facet/surface. The adsorption of these intermediates on Pt(111) surfaces has been extensively investigated previously [27,30,121]. Figure 3.2 summarises the PES for diffusion of ORR intermediates over the Pt(111)-*p*(4x4) surface; each of these PES diagrams is discussed in the following Subsections.

3.3.1 O_2* adsorption and diffusion

The adsorption of O_2* over Pt(111) surface sites has been reported to occur over $b^{(1)}$, $f^{(1)}$ and $h^{(1)}$ sites with adsorption energies of -0.46 to -0.69 eV/O_2 [27,30,121,122] -0.63 eV/O_2 [122] and -0.45 eV/O_2 [122], respectively. Adsorption on $t^{(1)}$ sites was found to be unstable [87]. These three adsorption sites were probed using initial geometries with an O-O bond axis parallel to the surface and its centre of mass above the adsorption site symmetry point. Table 3.1 presents the adsorption energy of O_2* and O* on a Pt(111) surface and their corresponding geometric properties. The adsorption of O_2* is influenced by surface coverage, at a 1/16 ML coverage O_2* adsorbs more strongly by 0.08 eV compared to at 1/9 ML coverage and has a slightly longer O–O bond length (see Table 3.1). Considering this coverage effect, the calculated adsorption energies are in good agreement with other theoretical calculations [121,122]. At 1/16 ML coverage the O–O bond length is longer whilst Pt–O bond lengths appear shorter compared to adsorption states at 1/9 ML coverage—however the actual differences are quite small (see Table 3.1). The latter may be an indication that due to slightly larger relaxation freedom, the Pt(111)-*p*(4x4) surface is able to pull O_2* slightly closer.

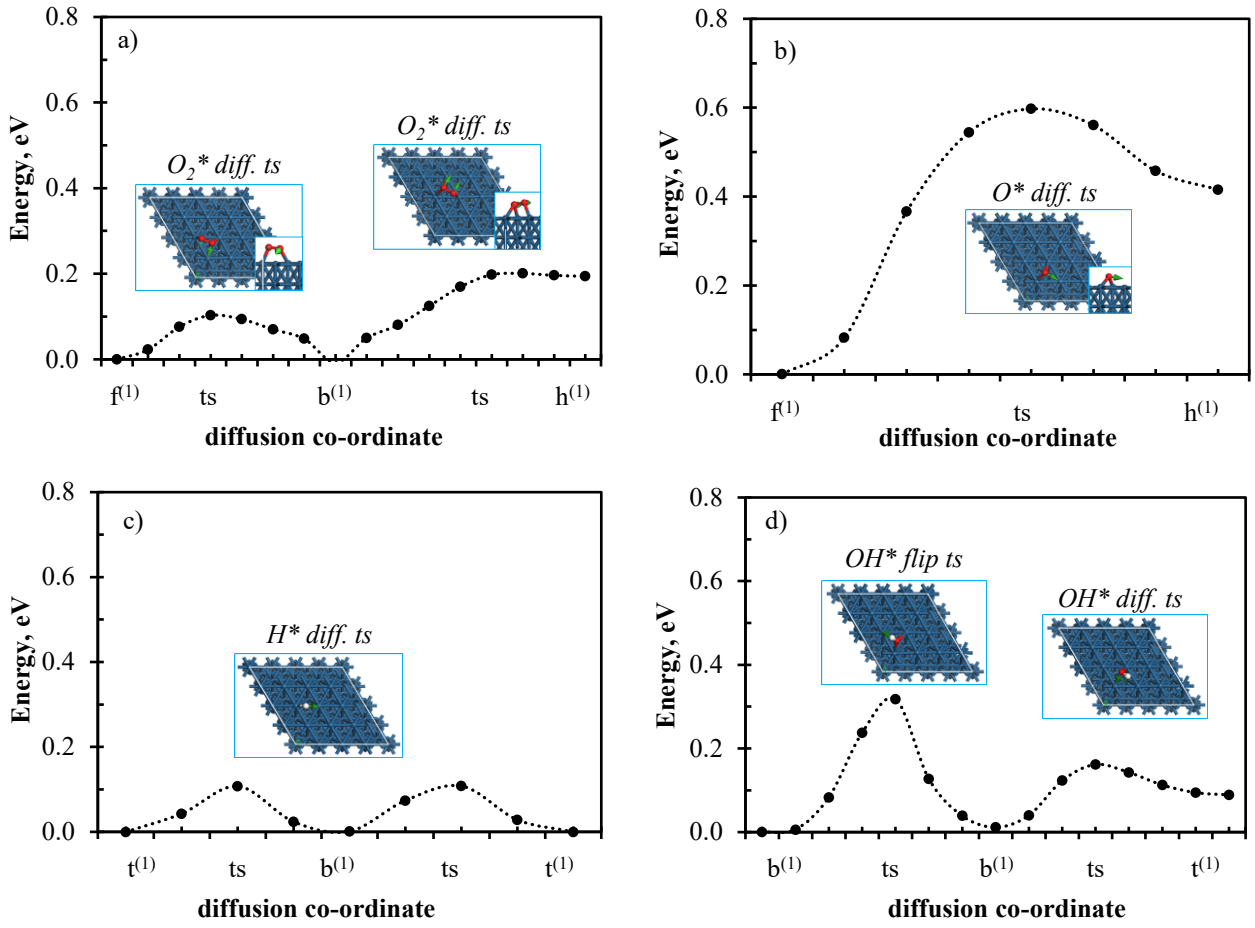

Figure 3.2: Diffusion profiles for (a) O_2*, (b) O*, (c) H* and (d) OH* over Pt(111)-*p*(4x4) surface, plotted to scale and relative to the adsorption energy on the first site; the inserts correspond to the optimized transition states with the vectors indicating the direction of the imaginary vibrational modes.

Table 3.1: Adsorption properties of O_2* and O* over Pt(111)-*p*(4x4) sites [Pt(111)-*p*(3x3)]; adsorption energies relative to H_2/H_2O (see equation 2.23) and values in (brackets) are reported relative to O_2(g).

Site:	**O_2***			**O***	
	$b^{(1)}$	$f^{(1)}$	$h^{(1)}$	$f^{(1)}$	$h^{(1)}$
E_{ads} [eV]	4.338 (-0.794) [4.418]	4.346 (-0.786) [4.495]	4.538 (-0.594) [4.617]	1.277 (-1.289) [1.330]	1.693 (-0.874) [1.731]
$d_{O\text{-}O}$ [Å]	1.364 [1.361]	1.404 [1.396]	1.393 [1.386]		
$d_{Pt\text{-}O}$ [Å]	2x 2.019 [2x 2.028]	2.014, 2x 2.157 [2.022, 2x 2.180]	2.025, 2.215, 2.200 [2.031, 2x 2.224]	2.049 [2.040]	2.048 [2.042]

Since O_2 can collide and impinge on any of the high-symmetry Pt(111) sites, possibly with different sticking probabilities, it is interesting to consider intra-facet diffusion of O_2* between $b^{(1)}$, $f^{(1)}$ and $h^{(1)}$ sites. This information is also crucial in understanding the propensity of O_2* to reorganise on the surface. The calculations show that the transition between $b^{(1)}$ and $f^{(1)}$ states is rather facile with a diffusion barrier of 0.103 eV (see Figure 3.2a). This barrier is only ca. 0.08 eV lower than that reported by Yang, Wang and Yu [122] at 0.25 ML coverage over a p(2x2) supercell surface. A

negligible barrier, < 0.01 eV, was calculated for the O_2* $h^{(1)} \rightarrow b^{(1)}$ diffusion step (see Table B2.1 in Appendix B), also in agreement with literature considering variations in surface coverages [122].

3.3.2 O* adsorption and diffusion

Atomic oxygen adsorbed on a Pt(111) surface has two local minima, i.e. $f^{(1)}$ and $h^{(1)}$ states. Previous calculations have shown that whilst initial geometries with O* above $b^{(1)}$ sites converge to either an $f^{(1)}$ or $h^{(1)}$ state, when O* starts directly above a surface Pt atom, i.e. $t^{(1)}$, the converged structure has an imaginary vibrational mode—indicating that it is not at a PES minimum [87]. Over a Pt(111)-*p*(4x4) surface, $f^{(1)}$ and $h^{(1)}$ O* adsorption states have Pt–O bond lengths of ca. 2.05 Å and adsorption energies of 1.277 eV and 1.693 eV, respectively (see Table 3.1). Over a Pt(111) surface, O* can be formed via O_2* dissociation, OOH* dissociation, OH* dissociation or OH-OH coupling—both $f^{(1)}$ and $h^{(1)}$ adsorption states are likely. NEB calculation were performed to map the intra-facet diffusion pathway, i.e. $f^{(1)} \rightarrow h^{(1)}$, of O* over a Pt(111) surface (see Figure 3.2b). A diffusion barrier of 0.597 eV was calculated based on an optimised transition state. This diffusion barrier compares well with 0.58 eV [93] and 0.47 – 0.52 eV [123] reported in previous studies. A closer look at the transition state reveals why all attempts to probe the $b^{(1)}$ states consistently resulted in either an $f^{(1)}$ or $h^{(1)}$ state. The $b^{(1)}$ sites accommodate the transition states for O* diffusion between $f^{(1)}$ and $h^{(1)}$ states (see insert on Figure 3.2b). Overall, the low energy states of O* on Pt(111) surface are isolated by relatively high energy states limiting the diffusion between $f^{(1)}$ states at low temperatures and coverage. However, O* diffusion from $h^{(1)}$ to $f^{(1)}$ only has a 0.182 eV barrier; as result all O* intermediates formed over $h^{(1)}$ would easily reorganise.

3.3.3 H* adsorption and diffusion

H_2 dissociates to two H* intermediates upon adsorption on Pt surfaces.[27,30,53] Over the Pt(111)-*p*(4x4) surface, H* has a local minimum on all four high-symmetry sites. These adsorption states are nearly isoenergetic with the largest energy difference being 0.055 eV (see Table 3.2). Moreover, adsorption energies at 1/16 ML and 1/9 ML coverages correspond to within 0.02 eV. Figure 3.2c presents the diffusion profile of H* along a path joining two $t^{(1)}$ sites. This profile shows two peaks corresponding to transition states for diffusion between $t^{(1)}$ and $b^{(1)}$ states—a diffusion barrier of 0.108 eV was calculated for this path. Other diffusion pathways, such as $t^{(1)} \rightarrow f^{(1)}$, $t^{(1)} \rightarrow h^{(1)}$, $f^{(1)} \rightarrow b^{(1)} \rightarrow h^{(1)}$, were also investigated (see Table B2.1 in Appendix B). Although energy maxima were found, vibrational analyses showed them to be saddle points, each with two imaginary modes, one in the diffusion coordinate and another in a perpendicular direction. The low diffusion barriers further suggest that the H* PES over Pt(111) surfaces is rather flat and H* intermediates are sufficiently mobile under reaction conditions (see Table B2.1).

Table 3.2: Adsorption properties of H* over Pt(111)-*p*(4x4) sites [Pt(111)-*p*(3x3)].

Site:	**$f^{(1)}$**	**$h^{(1)}$**	**$t^{(1)}$**	**$b^{(1)}$**
E_{ads} [eV]	-0.571 [-0.553]	-0.516 [-0.505]	-0.530 [-0.526]	-0.529 [-0.512]
$d_{Pt\text{-}H}$ [Å]	1.867 [1.868]	1.866 [1.866/1 1.870]	1.555 [1.555]	1.761 [1.760]

3.3.4 OH* adsorption and diffusion

On Pt(111) surfaces OH* adsorbs with two local minima, $t^{(1)}$ and $b^{(1)}$ states. Whilst $t^{(1)}$ states can have three unique in-plane rotations, i.e. with H above $f^{(1)}$, $b^{(1)}$ or $h^{(1)}$ site, their adsorption energy is unaffected by the direction of the O-H bond axis. Adsorption over a $b^{(1)}$ site on the other hand has two microstates, i.e. $b^{(1)a}$ and $b^{(1)b}$ where the O-H bond axis points over an $f^{(1)}$ and $h^{(1)}$ site, respectively (see Figure B1.1 in Appendix B1). The energy difference between these $b^{(1)}$ states is ca. 0.01 eV (see Table 3.3). Whilst a transition state for OH* rotation above a $t^{(1)}$ site could not be located, a transition state for the OH* flip between $b^{(1)}$ states was found and optimized (see first maximum in Figure 3.2d). The transition between $b^{(1)}$ states, i.e. OH* flip, has a barrier of 0.318 eV, which is more than twice the diffusion barrier between $b^{(1)}$ and $t^{(1)}$ states, 0.150 eV (also shown in Figure 3.2d). Given the latter, it stands to reason that the transition between the $b^{(1)}$ states may also occur via diffusion to a $t^{(1)}$ state followed by rotation and then diffusion to a new $b^{(1)}$ state, particularly at low temperatures.

Table 3.3: Adsorption properties of OH* over Pt(111)-*p*(4x4) sites [Pt(111)-*p*(3x3)].

Site:	**$t^{(1)}$**	**$b^{(1)a}$**	**$b^{(1)b}$**
E_{ads} [eV]	0.855 [0.869]	0.766 [0.827]	0.778 [0.836]
$d_{O\text{-}H}$ [Å]	0.980 [0.981]	0.985 [0.985]	0.983 [0.984]
$d_{Pt\text{-}O}$ [Å]	1.980 [1.981]	2x 2.142 [2x 2.149]	2x 2.148 [2x 2.153]

[a]with -H over the $f^{(1)}$ site; [b]with -H over the $h^{(1)}$ sites

3.3.5 H_2O* adsorption and diffusion

A water molecule over Pt(111) surface only adsorbs above $t^{(1)}$ sites with a much longer Pt-O bond distance than any other intermediate discussed thus far. Above $t^{(1)}$ sites of a Pt(111)-*p*(4x4), H_2O* adsorption states have an adsorption energy of -0.252 eV (only ca. 0.03 eV more stable than over a Pt(111)-*p*(3x3) surface). Adsorbed H_2O* has a $\underline{d}_{Pt\text{-}O}$ of 2.331 Å, $d_{O\text{-}H}$ of 0.979 Å and a H-O-H bond angle of 105.4° (cf. 104.5° calculated for a free H_2O molecule in a vacuum). Attempts to calculate the transition state for H_2O* rotation failed, showing almost no variation in H_2O* adsorption energy with rotation about the Pt-O axis. The energy barrier for H_2O* diffusion between two $t^{(1)}$ states was calculated to be 0.167 eV.

3.3.6 OOH* adsorption and diffusion

Geometry optimisation calculations show that OOH* adsorbs above $b^{(1)}$ sites with its O-OH bond axis parallel to the surface plane and the O-H axis pointing above an adjacent $b^{(1)}$ site (see Figure B1.2). The adsorption geometry of OOH* with this state has a $d_{O\text{-}O}$, $d_{O\text{-}H}$ and $d_{Pt\text{-}O}$ of 1.514 Å, 0.990 Å and 2.218/1.991 Å, respectively. The adsorption energy was calculated to be 3.882 eV and 3.936 eV at 1/16 ML and 1/9 ML coverage, respectively. Other adsorption geometries of OOH* were found, however these were much less stable (see Figure B1.2). Given the low OOH* dissociation barrier, ca. 0.05 eV from DFT [27,121], OOH* diffusion between $b^{(1)}$ states was not investigated further.

3.4 ORR intermediates over a Pt(100) surface

The Pt(100) surface has three high symmetry sites; these are, $t^{(0)}$ (atop a Pt atom), $b^{(0)}$ (across two Pt atoms) and $h^{(0)}$ (4-fold-hollow)—as on the Pt(111) surface above, the (0) superscripts indicates that these are sites on a (100) surface/facet. Over this surface, the ORR can be thought to have only five intermediates, namely O_2*, O*, H*, OH* and H_2O* (due to rapid O_2* dissociation, OOH* is unlikely to form [26,27]). In both the present study and previous studies [26,27] geometry optimisation calculations with an initial OOH* above a $b^{(0)}$ site converged to dissociated products, i.e. O* and OH*. The exception to this were mono-dentate states with OOH* attached to either a $b^{(0)}$ or $t^{(0)}$ site via an oxygen-end with the -OH head protruding out of plane (see Figure B1.2b). The latter states are not discussed further as they are unlikely to play a significant role in the ORR process. Figure 3.3 summarises the PES diagrams for the diffusion of ORR intermediates over Pt(100)-*p*(3x3).

3.4.1 O_2*, O* and H* adsorption and diffusion

Although $b^{(0)}$ and $h^{(0)}$ sites are probed for O_2* adsorption, only initial geometries with O_2* above a $b^{(0)}$ site converged to an undissociated state. This behaviour is in agreement with a previous theoretical study which does not report $h^{(0)}$ adsorption states for O_2* [27]. According to Duan and Wang [26], an $h^{(0)}$ adsorption state for O_2* is 0.81 eV higher in energy than a $b^{(0)}$ state, further supporting a position that the $h^{(0)}$ adsorption states are not crucial for ORR analyses in this study. Table 3.4 presents a summary of adsorption properties of O_2*, O*, H*, OH* and H_2O* over Pt(100)-*p*(3x3) surfaces. Compared to adsorption over Pt(111), O_2* adsorbs more strongly over the $b^{(0)}$ site with an adsorption energy of 3.888 eV (see Table 3.4). Attempts to locate the transition state for O_2* diffusion between two $b^{(0)}$ states consistently led to O_2* dissociation—a reasonable behaviour considering that this would potentially share the same reaction coordinate as the facile elementary step of O_2* dissociation [26,27].

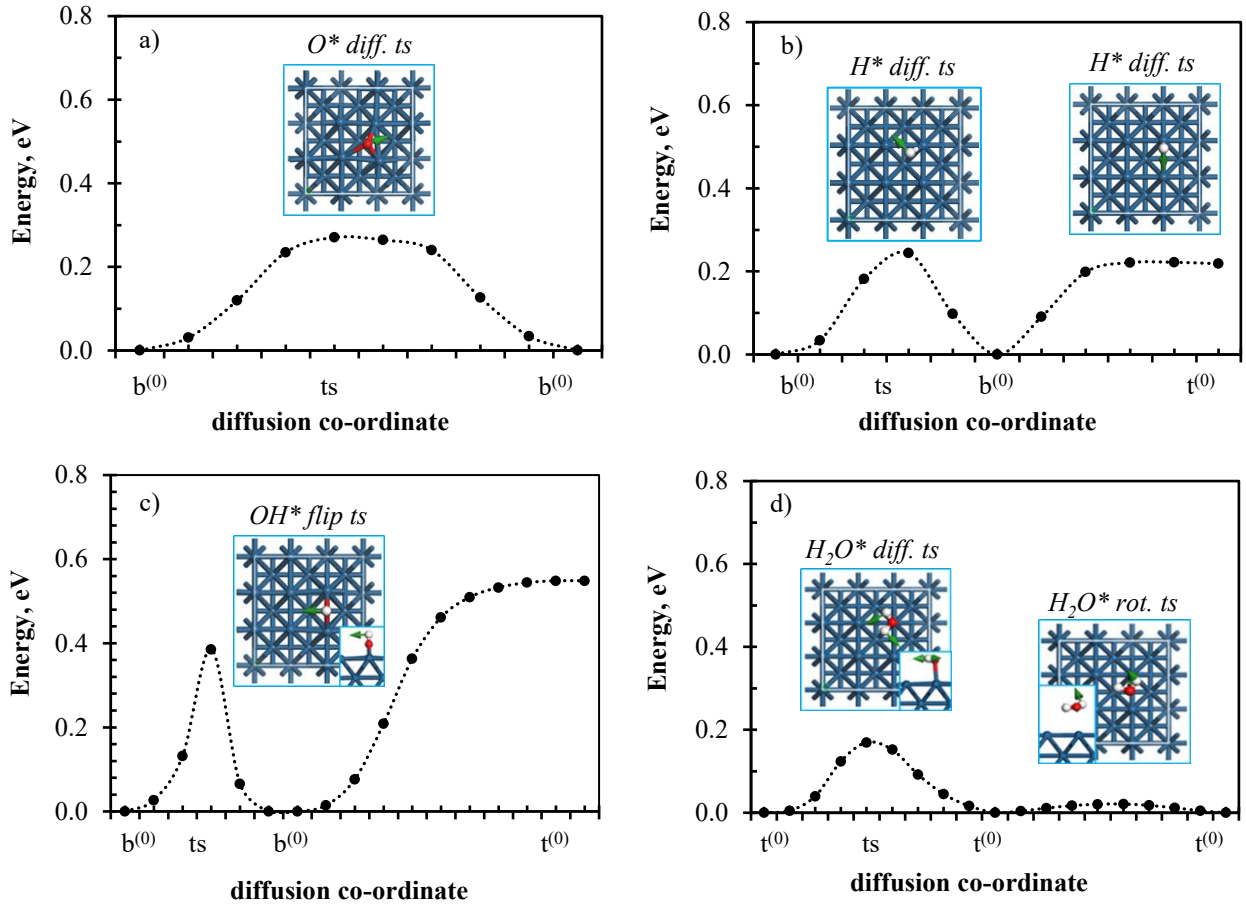

Figure 3.3: Diffusion profiles for (a) O*, (b) H*, (c) OH* and (d) H2O* over Pt(100)-*p*(3x3) surface, plotted to scale and relative to the adsorption energy on the first site; the inserts correspond to the optimized transition states with the vectors indicating the direction of the imaginary vibrational mode.

Table 3.4: Adsorption properties of O_2*, O*, H*, OH* and H_2O* over Pt(100)-*p*(3x3) sites; values in (brackets) are relative to gas phase O_2 and ½O_2, for O_2* and O*, respectively.

Species:	**O_2**	**O**	**H**		**OH**		**H_2O**
Site:	**$b^{(0)}$**	**$b^{(0)}$**	**$b^{(0)}$**	**$t^{(0)}$**	**$b^{(0)}$**	**$t^{(0)}$**	**$t^{(0)}$**
E_{ads} [eV]	3.888 (-1.244)	1.222 (-1.344)	-0.688	-0.470	0.205	0.753	-0.294
$d_{O\text{-}H}$ [Å]					0.983	0.980	0.981
$d_{O\text{-}O}$ [Å]	1.363						
$d_{Pt\text{-}H}$ [Å]			2x 1.752	1.558			
$d_{Pt\text{-}O}$ [Å]	2x 1.980	2x 1.937			2x 2.098	1.963	2.320
$\angle_{H\text{-}O\text{-}H}$ [°]							105.26

Like molecular oxygen, atomic O* preferentially adsorbs above $b^{(0)}$ sites, with an adsorption energy of 1.222 eV. Probing O* adsorption above the $t^{(0)}$ and $h^{(0)}$ sites did not lead to any new local minima which could be confirmed via vibrational analyses. Therefore, only diffusion between adjacent $b^{(0)}$ sites was considered for O* over Pt(100) surfaces. Transition state search calculations show a

relatively flat maximum with a three-fold coordination of O* with Pt atoms at the surface, only possible due to large surface reconstruction (see insert pane in Figures 3.3a). Although this maximum only has real vibrational modes, its smallest mode points along the diffusion pathway and is 21.2 cm^{-1}. The actual transition state for O* diffusion between $b^{(0)}$ states will have a similar energy to the former maximum resulting in an estimated diffusion barrier of ca. 0.271 eV.

Atomic hydrogen has two local minima states, namely $b^{(0)}$ and $t^{(0)}$ as shown in Table 3.4. Adsorption over a $b^{(0)}$ site is 0.218 eV more stable than over a $t^{(0)}$ site. Adsorbed H* can transition between $b^{(0)}$ and $t^{(0)}$ states with a maximum barrier of 0.221 eV (see Figure 3.3b). Despite similar geometries, H* adorbs more strongly over $b^{(0)}$ then over $b^{(1)}$ sites whilst over $t^{(0)}$ its adsorption energy is ca. 0.06 eV weaker than above $t^{(1)}$ sites. A direct transition between adjacent $b^{(0)}$ states has a similar diffusion barrier of 0.244 eV (see Figure 3.3b).

3.4.2 OH* and H_2O* adsorption and diffusion

The last two ORR intermediates to be discussed here are OH*, with $b^{(0)}$ and $t^{(0)}$ adsorption states, and H_2O* which only has $t^{(0)}$ adsorption states. Various rotational states of OH* above a $t^{(0)}$ site seem to be isoenergetic, (a similar behaviour was observed for adsorption on Pt(111) above $t^{(1)}$ sites). The adsorption energy of OH* was calculated to be 0.205 eV and 0.753 eV over $b^{(0)}$ and $t^{(0)}$ sites, respectively (see Table 3.4). Whilst adsorption atop $t^{(0)}$ sites closely resembles OH* adsorption above Pt(111) sites, the $b^{(0)}$ sites are much more strongly binding giving rise to a deeper potential energy minimum between two $t^{(0)}$ states. Figure 3.3c shows profiles for both the off-plane rotation (OH flip) of the $b^{(0)}$ OH* state, with a barrier of 0.386 eV, and the diffusion from $b^{(0)}$ to $t^{(0)}$ states, whose barrier is estimated to be at least equal to the energy difference between the $b^{(0)}$ and $t^{(0)}$ states, i.e. 0.548 eV. The latter estimation was made after failure to locate a transition state, despite all forces perpendicular to the diffusion path having been converged to within 0.02 eV/Å in numerous NEB calculations. It can be argued that the $t^{(0)}$ adsorption state is actually a shallow minimum and the transition state for OH* diffusion away for a $t^{(0)}$ site is energetically very close to the $t^{(0)}$ minimum.

H_2O* adsorbs above $t^{(0)}$ sites with an adsorption energy of -0.294 eV at 1/16 ML coverage (cf. -0.222 eV over Pt(111)-*p*(3x3)). Bond lengths and angles of H_2O* atop a $t^{(0)}$ and $t^{(1)}$ sites are reasonably similar (see Table 3.4). Despite the latter, H_2O* atop a $t^{(0)}$ site has a maximum when rotated about its Pt-O axis, unlike on Pt(111) atop a $t^{(1)}$ site. This is likely due to the open nature of a Pt(100) surface compared to the densely packed Pt(111) surface. Figure 3.3d shows a diffusion and rotational profile for H_2O* above a Pt(100)-*p*(3x3) surface. From this it can be seen that rotation is more facile than diffusion with respective barriers of 0.021 eV and 0.170 eV.

3.5 ORR intermediates over Pt NW edge sites

It has already been shown that the mobility of most ORR intermediates is characterised by relatively flat PESs over both Pt(111) and Pt(100) extended surfaces. This mainly correlates with small differences in their energy minima. The two exceptions are for O* and OH* diffusion over Pt(111) and Pt(100), respectively. On multifaceted Pt NWs/NPs ORR intermediates can also diffuse between two adjacent facets. Previous studies implicitly assumed that this inter-facet species exchange, i.e. over-edge diffusion, of ORR intermediates is limited by the highly reactive edge sites and as such does not significantly influence the overall ORR activity [15,25,29,37]. However, detailed analyses of PESs for diffusion near edge sites have not been thoroughly investigated for all key species. Only the diffusion of O* has been extensively investigated over Pt(211) and step-doubled Pt(211) surfaces [93,124], 55 and 147 atom cuboctahedral nanoparticles [125] and rhombic Pt nanowires [95]. The DFT calculated diffusion barriers are in the range 0.4 – 1.1 eV for edge → {111} facet and ca. 0.6 eV for edge → {100} facet [95,124,125]. The application of stepped-surface to represent NP edges is limited by influences of the step-height [93,124].

The PES diagram for diffusion of ORR intermediates from the near-edge Pt{111} facet sites toward near-edge Pt{100} facet sites via edge sites are presented in Figure 3.4. The rest of this Chapter discusses the adsorption and diffusion properties of O_2*, O*, H*, OH* and H_2O* over rhombic Pt NW surfaces. This information is crucial for the development of more detailed microkinetic models to study realistic-multifaceted catalyst surfaces.

3.5.1 O_2* adsorption and diffusion over Pt NW edge

Over Pt(111) and Pt(100) surfaces, O_2* preferentially adsorbs above bridge sites with adsorption energies of 4.338 eV and 3.888 eV, respectively. Diffusion of O_2* over Pt(111) surface has a very low barrier whilst over Pt(100) O_2* dissociation is preferred over diffusion. Over Pt NW (near-) edge region different adsorption states of O_2* have been calculated. Figure 3.5 and Table 3.5 present an illustration of various O_2* adsorption states near-edge sites and the corresponding adsorption properties, respectively. Briefly, at edge region O_2* has the lowest energy states on $b^{(e)}$ sites, 3.511 eV. Furthermore, O_2* adsorbs more strongly over near-edge $b^{(1e)}$, $f^{(1e)}$ and $h^{(1e)}$ sites on the Pt{111} facet compared to extended Pt(111)-*p*(3x3) surface. On the other hand, O_2* adsorption over near-edge sites on the Pt{100} facet is slightly weaker than adsorption over extended Pt(100)-*p*(3x3) surface. The latter is possibly due to coverage effects (see Table 3.5). Geometrically, the O-O bond length seems to be slightly longer for near-edge adsorption states compared to extended surface states. Adsorption sites located at edge, near-edge {111} and near-edge {100} terraces are herein denoted with superscripts (e), (1e)/(11e) and (0e)/(00e), respectively (see Figure 3.1).

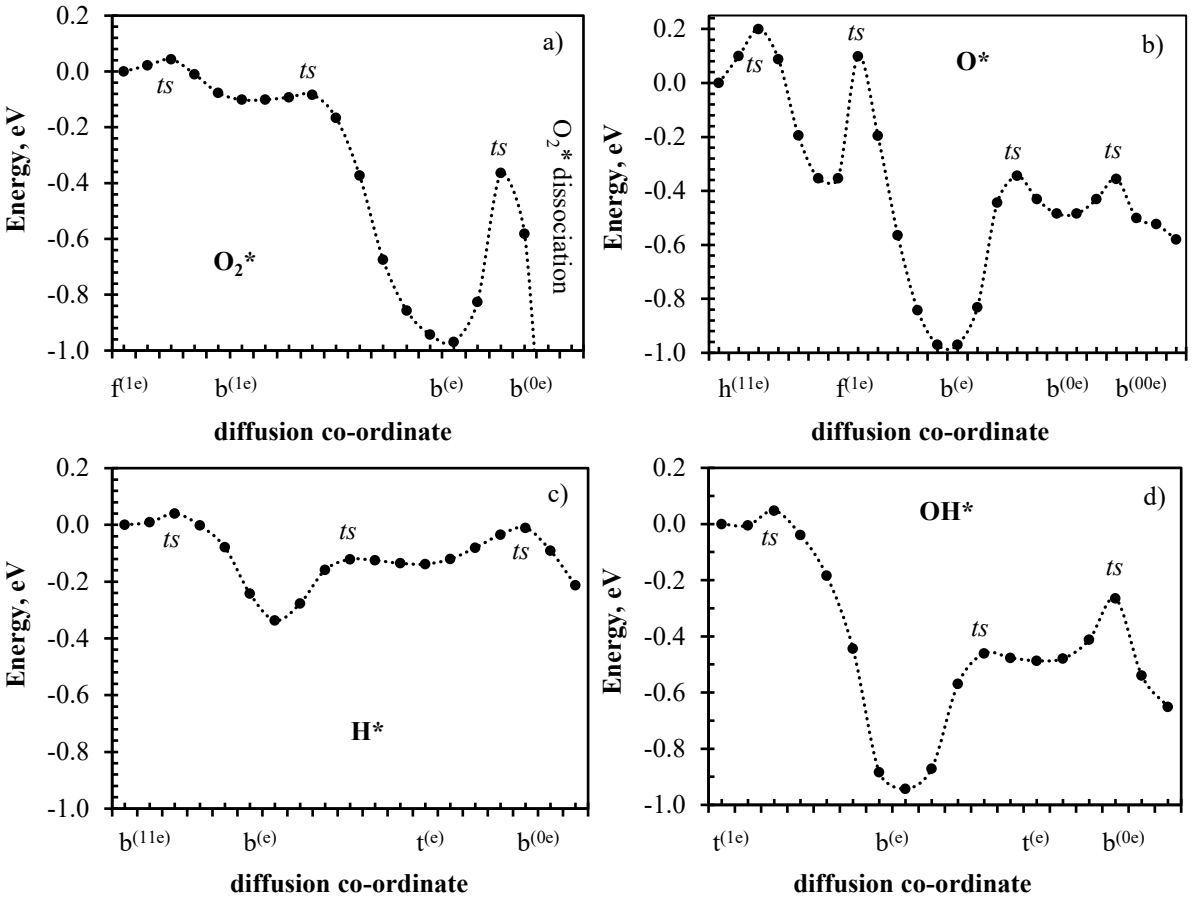

Figure 3.4: Diffusion profiles for (a) O_2*, (b) O*, (c) H* and (d) OH* over Pt NW edge and near-edge sites, plotted to scale and relative to the adsorption energy on a Pt{111} facet site; $h^{(11e)}$ in (b) is the second hcp site from the NW edge.

Table 3.5: Adsorption properties of O_2* over edge and near-edge sites of a Pt[5(111)x5(100) NW model; values in (brackets) are relative to O_2(g).

Site:	**$b^{(e)}$**	**$h^{(1e)}$**	**$b^{(1e)}$**	**$b^{(11e)}$**	**$f^{(1e)}$**	**$b^{(0e)}$**	**$b^{(00e)}$**
E_{ads} [eV]	3.511 (-1.621)	4.230 (-0.902)	4.379 (-0.753)	4.517 (-0.616)	4.481 (-0.651)	3.924 (-1.208)	3.956 (-1.176)
$d_{O\text{-}O}$ [Å]	1.385	1.440	1.384	1.378	1.409	1.371	1.375
$d_{Pt\text{-}O}$ [Å]	2x 1.960	2x 2.128, 2.038	1.995, 2.024	2x 2.004	2.019, 2x 2.178	1.973, 1.980	2x 1.976

The diffusion pathway for O_2* from the edge towards terraces sites was investigated. A transition state could be located for diffusion towards the $f^{(1)}$ site. On the other hand, all diffusion pathways probed for O_2* diffusion towards $b^{(0e)}$/$b^{(00e)}$ sites resulted in dissociation of O_2* to two O* atoms co-adsorbed over adjacent $b^{(0e)}$ sites—a similar behaviour was observed for O_2* diffusion over the Pt(100)-*p*(3x3) surface. Figure 3.4a presents a combined profile for O_2* diffusion from a $b^{(e)}$ to $f^{(1e)}$ and dissociation to 2x O* over $b^{(0e)}$ sites. The $b^{(e)}$ → $f^{(1e)}$ O_2* diffusion step has an effective energy

barrier of 1.013 eV. A dissociation barrier of 0.642 eV was calculated for dissociation of O_2* on a $b^{(e)}$ site to 2x O* intermediates over neighbouring $b^{(0e)}$ sites.

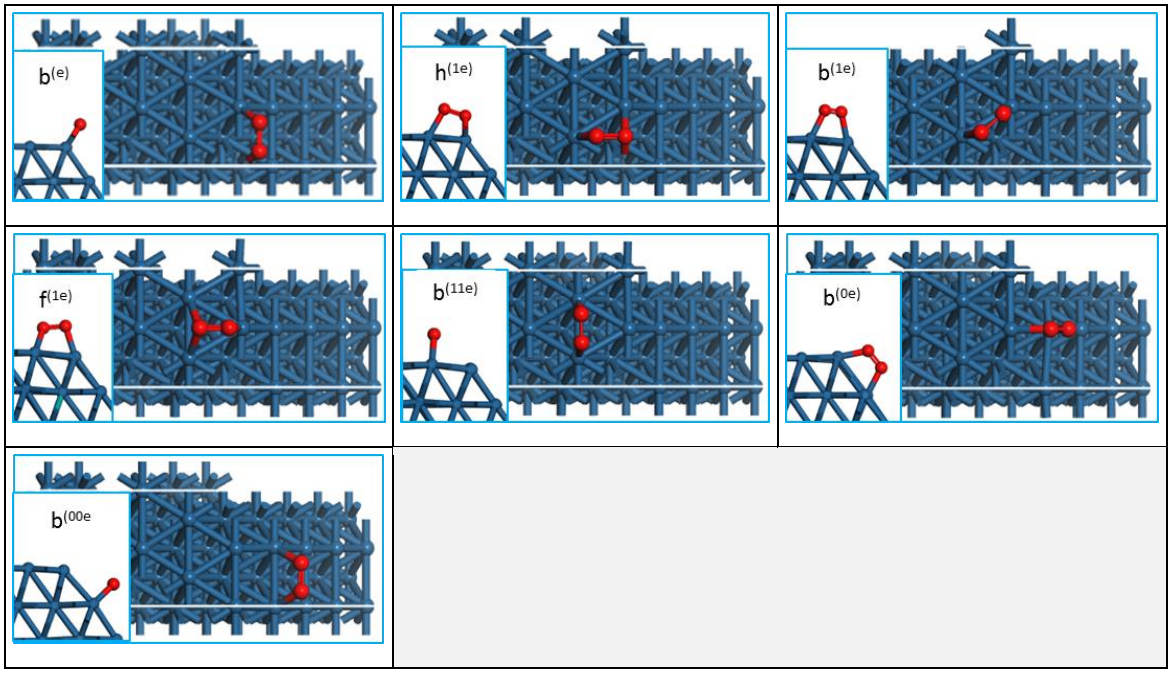

Figure 3.5: Adsorption state of O_2* over edge and near-edge sites of a Pt[5(111)x5(100)] NW model.

3.5.2 O* adsorption and diffusion over Pt NW edge

The diffusion of O* over Pt[5(111)x5(100)] NW edge sites has previously been reported [95]. Figure 3.4b gives a summary of the PES for O* diffusion. Similar to O_2*, the PES for O* inter-facet diffusion has deep energy minima above $b^{(e)}$ sites at the edge. Figure 3.6 and Table 3.6 illustrates the adsorption structures of O* at near-edge sites and their corresponding adsorption properties, respectively. The adsorption geometry, i.e. Pt-O bond length, for O* adsorption above $b^{(e)}$ is similar to adsorption over $b^{(0)}$ sites on Pt(100)-*p*(3x3). An interesting note for O* (even O_2*) adsorption over $b^{(e)}$ sites is that the resultant Pt-O-Pt (Pt-O-O-Pt) plane is oblique to both the {111} and {100} facet plane. Adsorption of O* above $b^{(00e)}$ sites is also oblique to the {100} surface plane, in fact it points slightly towards the edge (see Figure 3.6). The $b^{(e)}$ → $f^{(1e)}$ and $b^{(e)}$ → $b^{(0e)}$ diffusion barriers for O* were calculated to be 1.069 eV and 0.626 eV, respectively, in agreement with previous studies [95,124,125]. Whilst various starting position of O* over $h^{(1e)}$ near-edge NW sites were probed, they all consistently converged to a $b^{(e)}$ adsorbed O* [95].

Table 3.6: Adsorption properties of O* over edge and near-edge sites of a Pt[5(111)x5(100)] NW model. values in (brackets) are relative to ½O_2(g).

Site:	**b$^{(e)}$**	**f$^{(1e)}$**	**b$^{(0e)}$**	**b$^{(00e)}$**
E_{ads} [eV]	0.906 (-1.660)	1.523 (-1.043)	1.393 (-1.173)	1.297 (-1.269)
d_{Pt-O} [Å]	2x 1.936,	2.092, 2x 2.035	1.952, 1.946	2x 1.947

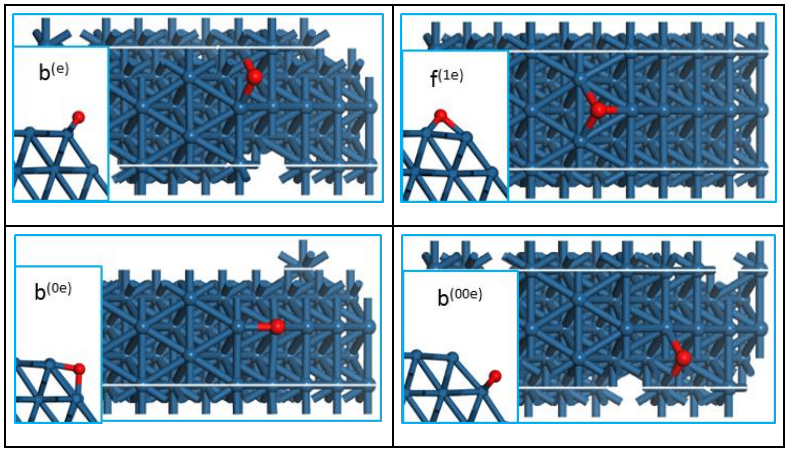

Figure 3.6: Adsorption state of O* over edge and near-edge sites of a Pt[5(111)x5(100)] NW model.

3.5.3 H* adsorption and diffusion over Pt NW edge

Adsorption of H* over edge and near-edge sites has been probed over various sites (see Figure 3.7). H* diffusion over edge was found to have a flatter PES compared to both O_2* and O*—with the lowest adsorption states above b$^{(e)}$ sites (see Table 3.7). Adsorption of H* above near-edge sites on a {111} facet is up to 0.17 eV weaker than equivalent adsorption on Pt(111)-*p*(4x4) slab sites. On the other hand, H* adsorption over near-edge sites on a {100} facet is comparable, i.e. agrees within ca. 0.04 eV, to equivalent adsorption on Pt(100)-*p*(3x3) slab sites. These differences may be due to a number of factors including differences in coverage and local edge influence [95]. Figure 3.4c shows a complete PES for the inter-facet diffusion of H* intermediates. The calculated barriers for H* diffusion from edge sites towards terraces are 0.376 eV and 0.336 eV, for b$^{(e)}$ → b$^{(11e)}$ and b$^{(e)}$ → b$^{(0e)}$ steps, respectively. The latter diffusion step is found to go via a t$^{(e)}$ state which lies above the b$^{(0e)}$ state in energy (see Figure 3.4c). Interestingly, H* adsorbed above a b$^{(e)}$ makes a wider angle with the {111} surface normal and closer to the edge than H* above a t$^{(e)}$.

Table 3.7: Adsorption properties of H* over edge and near-edge sites of a Pt[5(111)x5(100)] NW model.

Site:	**b$^{(e)}$**	**t$^{(e)}$**	**f$^{(1e)}$**	**t$^{(1e)}$**	**b$^{(11e)}$**	**b$^{(0e)}$**	**b$^{(00e)}$**	**t$^{(0e)}$**
E_{ads} [eV]	-0.748	-0.549	-0.400	-0.491	-0.411	-0.624	-0.664	-0.506
d_{Pt-H} [Å]	2x 1.790	1.565	2.013, 2x 1.827	1.553	2x 1.766	1.788, 1.739	2x 1.758	1.561

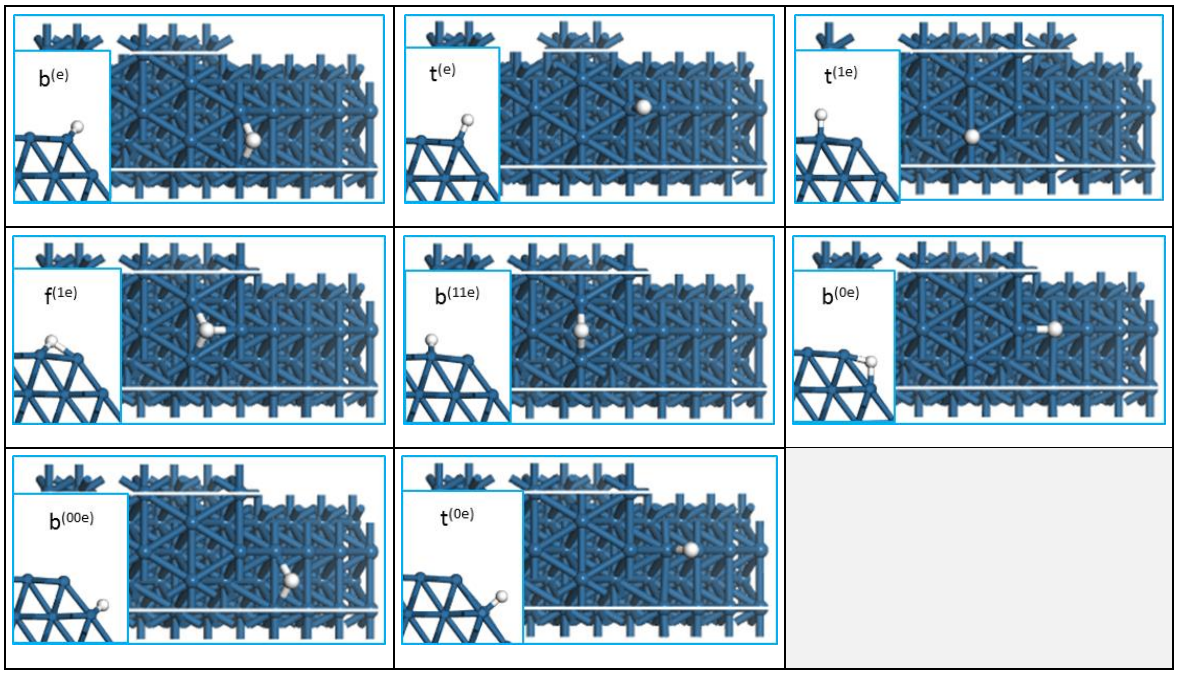

Figure 3.7: Adsorption state of H* over edge and near-edge sites of a Pt[5(111)x5(100)] NW model.

3.5.4 OH* adsorption and diffusion over Pt NW edge

The adsorption of OH* over edge and near-edge sites is rather interesting and unique, compared to that of O_2*, O* and H*. Given that OH* is asymmetric, its orientation might influence its adsorption strength. Figure 3.8 presents the different adsorption minima of OH* at edge and near-edge sites. The geometric and energetic properties of these adsorption states are given in Table 3.8. Briefly, the orientation of the O-H bond for OH* adsorption at edge and near-edge sites can change the adsorption energy by up to 0.04 eV. Similar to O_2* and O*, the adsorption of OH* has the lowest minimum above a $b^{(e)}$ adsorption site (see Figure 3.4d and Table 3.8). The adsorption geometry of OH* at near-edge sites is similar to OH* geometry atop equivalent adsorption sites on extended surfaces (see Tables 3.3, 3.4 and 3.8). Adsorption over $b^{(e)}$ and $t^{(e)}$ sites form an oblique angle with the {111} and {100} surface normal vectors (see Figure 3.8). Geometrically, OH* adsorption over $b^{(e)}$ and $t^{(e)}$ sites is more similar to equivalent adsorption over Pt(100) than Pt(111) surfaces—although OH* binds closer to the surface and stronger at edge sites than over both Pt(111) and Pt(100) sites. This oblique adsorption state may also be responsible for the reported disruption in hydrogen-bond network over stepped Pt surfaces.

Figure 3.4d shows that the highest OH* diffusion barrier corresponds to $b^{(e)} \rightarrow t^{(1e)}$ diffusion; this barrier was calculated to be 0.991 eV and is 0.310 eV higher than the $b^{(e)} \rightarrow b^{(0e)}$ diffusion barrier. As was the case for H* diffusion from $b^{(e)}$ to $b^{(0e)}$, OH* diffusion towards the $b^{(0e)}$ goes via a $t^{(e)}$ state. Although not shown in Figure 3.4, the barrier for OH* rotation, i.e. OH* flip from a $b^{(e)}$ state with H on the {100} facet to a $b^{(e)}$ state with H on the {111} facet, was calculated. This transition

has an energy barrier of 0.309 eV (cf. to 0.318 eV and 0.386 eV for OH* flip over Pt(111) and Pt(100) surfaces, respectively).

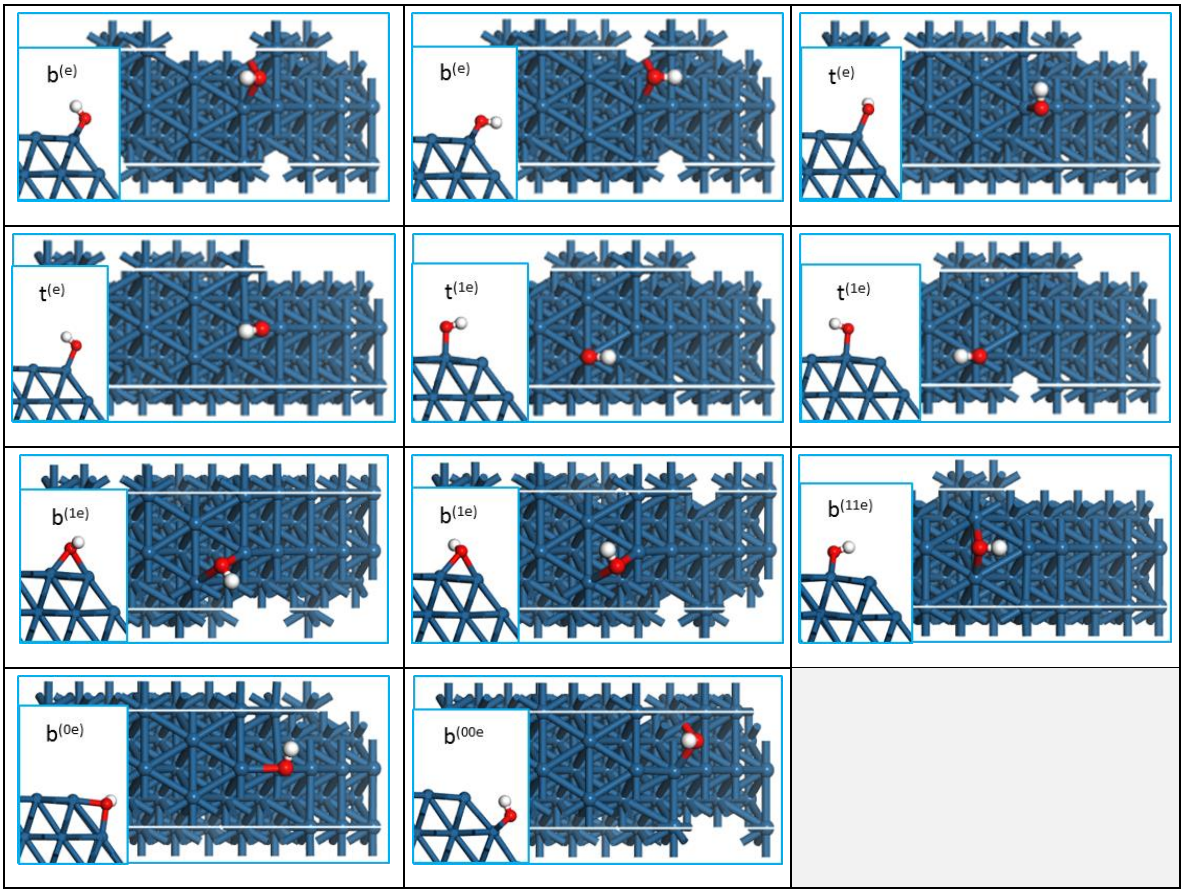

Figure 3.8: Adsorption state of OH* over edge and near-edge sites of a Pt[5(111)x5(100)] NW model.

Table 3.8: Adsorption properties of OH* over edge and near-edge sites of a Pt[5(111)x5(100)] NW model in the same order as structures in Figure 3.8; all values in [brackets] represent adsorption where the O-H bond points to the edge.

Site:	**b$^{(e)}$**	**t$^{(e)}$**	**t$^{(e)}$**	**t$^{(1e)}$**	**b$^{(1e)}$**	**b$^{(11e)}$**	**b$^{(0e)}$**	**b$^{(00e)}$**
E_{ads} [eV]	-0.003 [-0.023]	0.454	0.495	0.941 [0.978]	0.899 [0.941]	[0.950]	0.289	[0.296]
$d_{O\text{-}H}$ [Å]	0.980 [0.980]	0.980	0.980	0.980 [0.980]	0.984 [0.983]	[0.984]	0.982	[0.984]
$d_{Pt\text{-}O}$ [Å]	2x 2.104 [2x 2.098]	1.951	1.958	1.985 [1.988]	2.145, 2.212 [2.160, 2.197]	[2x 2.146]	2.147 2.094	[2x 2.095]

3.5.5 H_2O* adsorption and diffusion over Pt NW edge

The inter-facet diffusion of H_2O* is not particularly interesting given that over both Pt(111) and Pt(100) surfaces it binds less strongly than all other ORR intermediates (see Sections 3.3 and 3.4). Despite this knowledge, some results on the PES for inter-facet diffusion of H_2O* are presented here. For all edge and near-edge H_2O* adsorption states the O-H bond lengths agree within 0.004 Å. Moreover, these compare well with O-H bond lengths of H_2O* over extended surfaces.

On the other hand, Pt-O bond lengths vary by up to 0.182 Å with adsorption on {111} near-edge sites having the longest bond distance (see Table 3.9). It also appears that the orientation of the H_2O* adsorbate above $t^{(e)}$ marginally affects the angle between the Pt-O bond axis and terrace normal vectors (see Figure 3.9).

Despite these geometric differences the adsorption energies of H_2O* above $t^{(e)}$ sites is less affected by rotation (see Table 3.9). At $t^{(e)}$ sites H_2O* adsorbs ca. 0.17 eV and 0.06 eV more strongly than on $t^{(1e)}$ and $t^{(0e)}$, respectively. This results in a relatively shallow PES for inter-facet diffusion of H_2O* much like H* (cf. O_2*, O* and OH*). The calculated diffusion barriers for H_2O* $t^{(e)} \rightarrow t^{(1e)}$ and $t^{(e)} \rightarrow t^{(0e)}$ transitions are 0.260 eV and 0.227 eV, respectively.

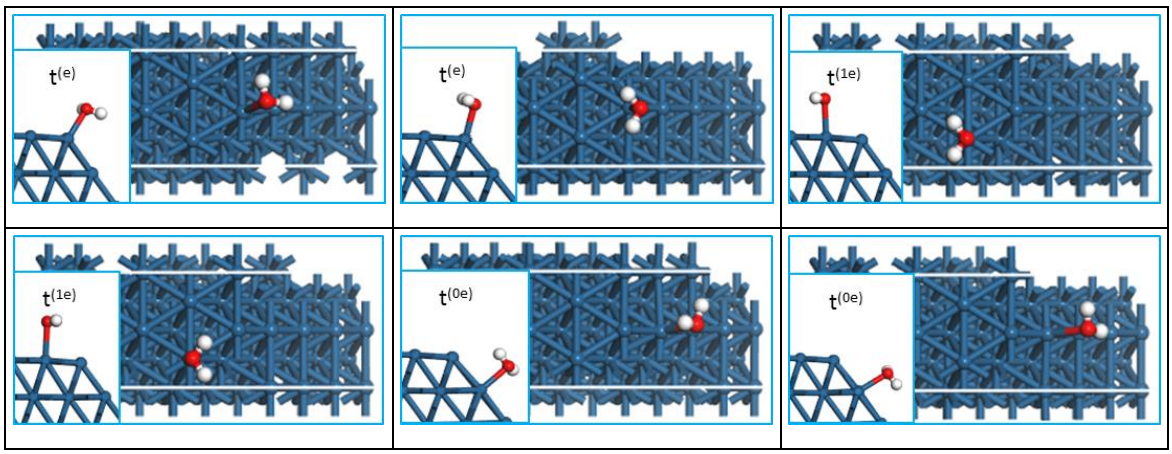

Figure 3.9: Adsorption state of H_2O* over edge and near-edge sites of a Pt[5(111)x5(100)] NW model.

Table 3.9: Adsorption properties of H_2O* over edge and near-edge sites of a Pt[5(111)x5(100)] NW model, in the same order of appearance as structures in Figure 3.9.

Site:	**$t^{(e)}$**	**$t^{(e)}$**	**$t^{(1e)}$**	**$t^{(1e)}$**	**$t^{(0e)}$**	**$t^{(0e)}$**
E_{ads} [eV]	-0.363	-0.360	-0.140	-0.195	-0.299	-0.275
$d_{O\text{-}H}$ [Å]	0.991, 0.979	2x 0.980	2x 0.978	2x 0.980	2x 0981	2x 0.981
$d_{Pt\text{-}O}$ [Å]	2.297	2.294	2.513	2.457	2.351	2.339
$\angle_{H\text{-}O\text{-}H}$ [°]	104.94	105.69	105.10	104.55	104.83	104.96

3.5.6 Coverage effects on adsorption energy

Lateral interactions between edge adsorbed reaction intermediates can influence their stability quite significantly. Already seen, O*-O* pairs on nearest $f^{(1)}$ and $f^{(1)}$ sites share a surface Pt atom and their interaction energy is 0.257 eV (see Appendix B3). On Pt(100) the interaction energy between Pt atom sharing O* pair is 0.423 eV (see Appendix B4). Since co-adsorption on edge site resembles the latter, equally large interactions are possible. The interaction energy between two nearest neighbour O*-O* intermediates on edge sites is 0.455 eV. Between nearest neighbour OH*-OH*

and O_2*-O_2* pairs the repulsive interactions were calculated to be 0.364 eV and 1.060 eV, respectively (see Table 5.1 and Figure 5.2). This suggests that with increasing coverage the adsorption strength of O_2*, O and OH* decreases. It has already been reported how this coverage effect affects the inter-facet diffusion of O* on rhombic NW surfaces [95].

3.6 Discussion

The consequence of fast intra-facet diffusion of reaction intermediates on the catalyst performance is that at low surface coverages the reaction will occur at relatively faster rates compared to slow/immobile reaction intermediates. This is also true in cases where the surface concentration of active intermediates is dominated by spectator species. In the latter cases, the probability of finding the required pairs of intermediates occupying adjacent sites for a given reaction step is greatly lowered, resulting in lower performance. Moreover, depending on the intermediate mobility, adsorption structures and islands may form further influencing both the kinetic rate and reaction pathway.

Investigation of the mobility of ORR intermediates over Pt surfaces has demonstrated quite clearly that most ORR intermediates are quite mobile over terrace sites. Only O* and OH* were found to have substantially higher diffusion barriers, comparable to activation energies of the kinetically most limited reaction steps. Figure 3.10 presents an alternative pathway for moving the position of OH* intermediates given an O*-OH* co-adsorbed pair cluster. This involves a proton (hydrogen) exchange between O* and OH*. Given the relatively high mobility of O* on Pt(100), i.e. diffusion barrier of 0.271 eV, and the attractive lateral interaction between O* and OH*, there is a significant likelihood of O*-OH* clusters. The activation energy for the hydrogen transfer is 0.063 eV whilst the reconfiguration of the new OH* (OH* flip) has a high energy barrier of 0.578 eV because of attractive lateral interactions (cf. 0.386 eV for OH flip, -0.217 eV O*-OH* interactions and compares well with 0.547 eV for OH* diffusion). The diffusion of O* away from the newly formed OH* also has comparable barrier to the latter. Therefore, these alternative pathways will provide a complete mechanism for OH* mobility, however with comparable rate constants. A similar mechanism does not provide an improved pathway for O* mobility on Pt(111).

On Pt NW edge sites both O* and OH* together with O_2* adsorb strongly and their PES is characterized by a deep well at $b^{(e)}$ sties. Due to these deep adsorption minima, the energy barriers for diffusion from $b^{(e)}$ sites towards $f^{(1e)}$/$t^{(1e)}$/$b^{(0e)}$ sites are higher still. This therefore suggests that the implicit assumptions made in many kinetic models investigating ORR activity over model nanoparticles [15,25,29,37,126] are justified in the absence of lateral interactions between co-adsorbed intermediates.

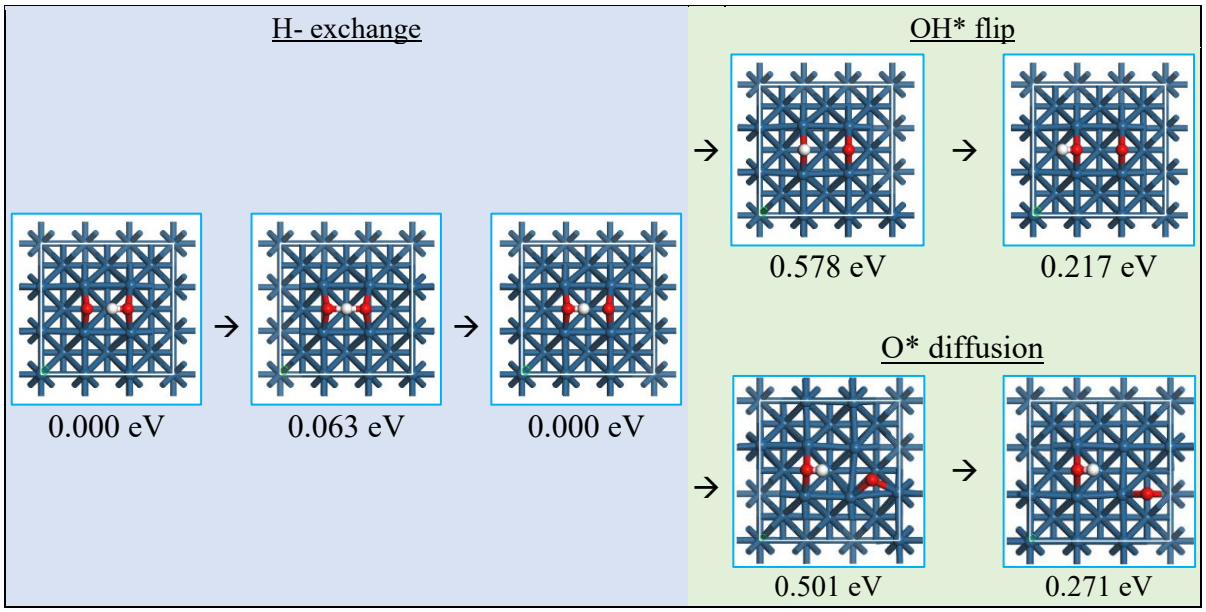

Figure 3.10: Alternative OH* mobility pathway on the Pt(100)-*p*(3x3) surface (energies are normalised to the energy of the first image).

Comparing diffusion barriers over extended surfaces with diffusion barriers from the edge, it is noted that the associated transition states may have closely similar energies—and the source of the observed difference in the diffusion barrier from edge sites towards terrace sites is the high reactivity of the $b^{(e)}$ sites towards adsorbing *OCS**. A rational design approach would then involve poisoning or modification of these sites; the latter is considered in Chapter 6.

Under operating conditions the system might also self-adjust due to lateral interactions at high coverage conditions [95]. In this case, self-poisoning of edge sites by *OCS** intermediates flattens the PES for inter-facet diffusion. Figure 3.11 presents simplified PES diagrams for the diffusion of various ORR intermediates between the Pt{111} and Pt{100} facets via the edge. As indicated above, there is a deep well in these PES diagrams at the edge region (black profile). Considering various cases where adsorption occurs over a pre-covered edge (and at close proximity as illustrated in Figure 3.11e) the deep well in the PES diminishes because of repulsive interactions between co-adsorbed intermediates. A detailed analysis of this coverage effect on inter-facet diffusion of O* was presented in Ref. [95]. There it was shown that at higher edge coverages the diffusion barriers for O* from $b^{(e)}$ towards $f^{(1e)}$ and $b^{(0e)}$ are significantly lowered due to repulsive lateral interaction between co-adsorbed O* atoms. This behaviour is anticipated to also affect the PES of other ORR intermediates (as shown in Figure 3.11)—Chapter 5 will consider inter-facet diffusion of ORR intermediate and how it affects the overall ORR activity over multifaceted Pt NWs.

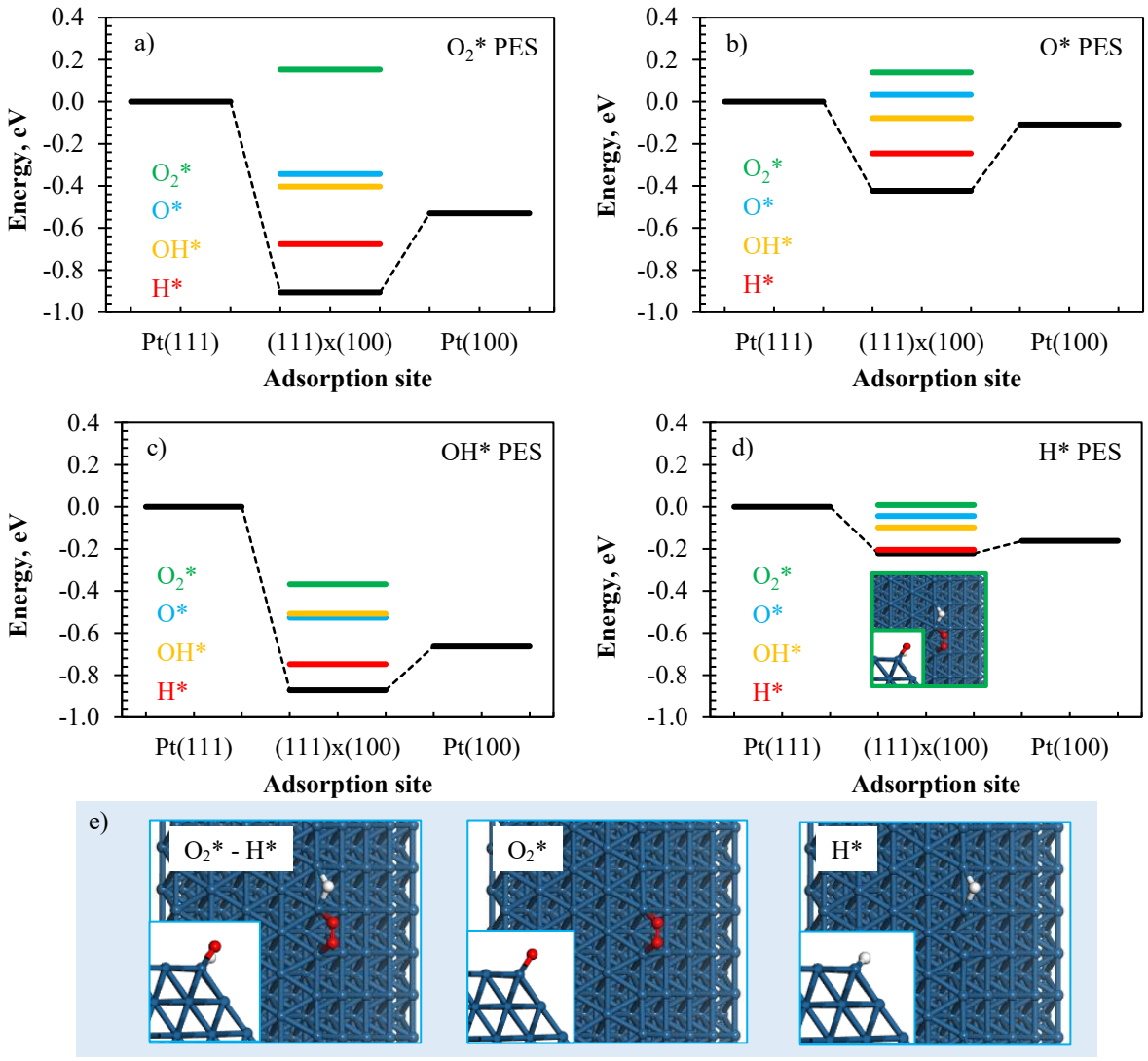

Figure 3.11: Calculated adsorption energies of (a) O_2*, (b) O*, (c) OH* and (d) H* (on the most stable Pt(111)-*p*(3x3), Pt NW edge and Pt(100)-*p*(3x3) sites) relative to the equivalent adsorption energy on the most stable Pt(111)-*p*(3x3) adsorption site. Effect of edge coverage on adsorption energy illustrated by considering adsorption on a precovered surface with O_2* (green), O* (blue), OH* (yellow) and H* (red); (e) (left) adsorption of H* on O_2* precovered edge and (middle/right) O_2*/H* adsorption on clean edge.

In summary, intra-facet diffusion of ORR intermediates should not limit the reaction given that the highest diffusion barriers are appreciably lower than the highest activated reaction steps over Pt(111) and Pt(100) surfaces. Whilst O* and OH* are less mobile on Pt(111) and Pt(100) surfaces, respectively, the fast mobility of H* will ensure the availability of appropriate reactive pairs. Some reaction intermediates can easily diffuse toward the edge from either terrace. Furthermore, the diffusion barriers from edge toward Pt{100} facet is much lower than the barriers toward Pt{111} facet. Lateral interactions may play a significant role in enabling inter-facet diffusion of various ORR intermediates. Overall, at the gas/solid interface migration of H* between Pt{111} and Pt{100} facets is facile and can influence surface coverage if one facet is prone to higher coverages with H* than its adjacent neighbour.

CHAPTER 4:ORR Activity at Pt(111) and Pt(100) Surfaces

4.1 Introduction

Experimental studies have shown that the ORR is a structure sensitive reaction with its kinetic activity increasing in the order Pt(100) < Pt(110) ≈ Pt(111) in a non-adsorbing $HClO_4$ electrolyte [10,23]. The structure sensitivity further extends to high-index surfaces and depends on the terrace length [24,32]. Whilst experimental studies give information regarding the activity of different substrates, the information is generally limited when it comes to detailed mechanistic processes. Microkinetic models may provide this information [7,51,52,109,110,127–131].

Different classes of kinetic models have been proposed in the last decade. Huang and Eikerling [131] recently reviewed these methods—grouping them into (1) Tafel equation-based models, i.e. empirical, and (2) first-principles based microkinetic models [7,51,52,109,110,127–131]. The latter consider, to different degrees, the complex nature of the ORR at an electrolyte/solid interface. Wang *et al.*[127] proposed a double-trap method where instead of assuming a rate determining step *a priori*, a carefully chosen set of elementary reactions was used to develop adsorption isotherms for O* and OH* intermediates and current density as functions of electrode potential. Whilst their model was able to explain previous experimental results, its fitted free energies were subsequently found to be at odds with data obtained from first principles methods [131].

Later studies used a combination of first principles calculated reaction energetics and either dynamic Monte Carlo simulations (DMC) [129], mean-field kinetic models [51,109,110] or coverage independent models [52,53]. These models were able to explain some aspects of experimental observations, albeit with some limitation. Rai's DFT + DMC model [129] was able to accurately predict experimentally measured surface coverages of oxygen containing species (*OCS**) under water-discharge reaction conditions. Jinnouchi *et al.* [51] proposed a mean-field microkinetic model for the ORR over Pt(111). Although also in good agreement with both O* and OH* experimentally determined surface coverage, and measured current density over a wide potential range, 0.6 – 1.0 V (vs. the standard hydrogen electrode, SHE), it is not entirely first principles based—the reference free energies for the O* and OH* reduction reactions are fitted to experimental data.

Hansen *et al.* [52] presented a completely first principles based microkinetic model for the ORR over Pt(111) surface. Their predicted voltage-current density plot agreed well with previous experiments. However, the model does not incorporate coverage effects and as such predicts much higher oxygen containing species coverage in disagreement with experiments [51]. Recently, Eberle and Horstmann [109] presented an extended first principles based microkinetic model for the ORR over a Pt(111) surface. In their model they considered both Langmuir Hinshelwood (LH) and Eley-Rideal (ER) kinetics—more specifically, the following reactions were used to describe ER hydrogenation steps,

$$H^+ + e^- + * \leftrightarrow H* \quad \text{R1}$$

$$O_2* + H^+ + e^- \leftrightarrow OOH* \quad \text{R2}$$

$$O* + H^+ + e^- \leftrightarrow OH* \quad \text{R3}$$

$$OH* + H^+ + e^- \leftrightarrow H_2O* \quad \text{R4}$$

$$OOH* + H^+ + e^- \leftrightarrow HOOH* \quad \text{R5}$$

in addition to the other LH based hydrogenation steps listed in Table 1.1. Using activation barriers of 0.30 eV and a Butler-Volmer equation they incorporated potential-dependency into their microkinetic model. Their results highlight the importance of lateral interactions and furthermore, they find that the ORR proceeds via the ER pathway. Noteworthy is the prediction of high O_2* coverage in the 0.2 – 0.8 V potential region. This contradicts previous models and experiments and may be due to the underestimation of O_2* - O_2* interactions [51]. Most recently, Fantauzzi *et al.* [53] performed microkinetic analysis of the ORR over Pt(111) under dry conditions, i.e. gas/solid interface.

With an intention to investigate the overall ORR activity over multi-faceted Pt surfaces, this study considers a simplified model. In this model the ORR occur at a gas/solid interface, much like the recent model of Fantauzzi *et al.* [53]—except that the present model also incorporates surface coverage effects on the ORR activity. Despite obvious limitations of this model, its predicted results may still be instrumental in future studies concerned with the investigation of inter-facet dependency. This Chapter investigates the ORR activity, i.e. H_2O evolution rate, over both Pt(111) and Pt(100) surfaces. Reaction pathway and dependence of the ORR activity on each elementary reaction—employing Campbell's degree of rate control analysis[132]—are discussed.

4.2 Methods and surface models

4.2.1 Quantum Chemical Calculations

The ORR energetics over Pt(111)-*p*(3x3) and Pt(100)-*p*(3x3) supercell models were calculated from DFT; computational setup details are discussed in Subsections 2.2.2 and 2.3.2. The change in electronic energy upon reaction is calculated as,

$$\Delta_{\mathrm{rxn}} E_i = E_{FS,i} - E_{IS,i} \tag{4.1}$$

where $E_{IS,i}/E_{FS,i}$ is the total energy (without zero-point correction) of the initial/final state in reaction i; these energies are calculated from appropriate *p*(3x3) supercell slabs. For bimolecular reactions the interaction energy is also accounted for. Adsorption/desorption reaction energetics are based on a gas phase reference state. The activation energy for reaction i is calculated as,

$$E_{af,i} = E_{TS,i} - E_{IS,i} \tag{4.2}$$

where $E_{TS,i}$ is the total energy (without zero-point correction) of the transition state. Transition states were located using the climbing image nudged elastic band (CI-NEB) [96] method, optimized and verified via vibrational analyses. Appropriate corrections were made in cases of bimolecular reactions, i.e. $E_{IS,i}$ was corrected for the energy cost to bring reactants to a co-adsorbed state from infinite separation—this ensured thermodynamic consistency (Table E7.1 and E7.2 in Appendix E7, presents a summary of corrected activation energies). Coverage effects on reaction and activation energies were incorporated as discussed in Section 2.4.

4.2.2 Adsorbate interactions

Coverage effects on the ORR activity were considered by modelling pairwise interactions between co-adsorbed intermediates. Tables 2.1 and 2.2 present a summary of the key interaction energies applied in the mean-field microkinetic models. The majority of pair interactions over the Pt(111) surface are repulsive in nature. The highest of these repulsion interactions is due to O_2* - O_2*, O* - O* pairs. Over the same surface, nearest neighbour, OH* - OH*, OH* - H_2O* and H_2O* - H_2O* interactions are quite attractive. These pairs are stabilised via hydrogen bonding. The latter interactions are responsible for the reported preferred honeycomb structure at moderate to high OH* and H_2O* coverage over Pt(111) [8,133–136]. Over Pt(100) surfaces the most stable adsorption states are above bridge sites for all intermediates except for H_2O which adsorbs above top sites. Interactions between nearest neighbour O* - OH* and OH* - OH* pairs are attractive. The latter interactions are responsible for the *p*-geometry of OH* on Pt(100) surfaces, i.e. parallel rows of OH* on bridge sites interacting via hydrogen-bonding [118]. Other attractive interactions are between H_2O* - O_2*, H_2O* - O*, H_2O* - OH* and H_2O* - H_2O* pairs (see Table 2.2). Despite

the strong stabilisation (ca. -0.60 eV) between a nearest neighbour OH*(top) - H_2O* (top) pair, the total energy of the OH*(bridge) - H_2O*(top) nearest neighbour pair is ca. 0.130 eV more stable relative to $2H_2O(g)$ and $½H_2(g)$. Therefore, the adsorption site preference of OH* is unlikely to be influenced by high H_2O* coverages. All these attractive interactions result from hydrogen bonding.

Other pair interactions between ORR intermediates are repulsive over Pt(100) surface. The strongest repulsion exists when bridge adsorbates are adsorbed along a straight line, sharing one surface Pt atom. These interactions (shown in Tables 2.1 and 2.2) are incorporated in the mean-field microkinetic models discussed in Section 2.3 and constructed in Appendix D.

4.2.3 Microkinetic models

Four types of microkinetic models were used differing in the way lateral interactions are treated (see Section 2.3). The SA approximation model is likely to be inapplicable in this case considering the strong repulsive and attractive interactions between ORR intermediates. Whilst species mobility is potentially not limiting, SA is more likely to overestimate surface coverage and consequently underestimate ORR activity at moderate to low temperature conditions [105]. The BWA model will most likely lead to a better description considering the low diffusion barriers of key ORR intermediates. However, at high OH* and H_2O* coverages this model will likely give a poor description of the system as these intermediates are prone to forming ordered structures [8,133–136]. Moreover, the highly repulsive interactions between nearest neighbour oxide species (OH* excluded) will be severely overestimated. The QCA model will likely be able to give a good description of the system in spite of high OH* and H_2O* coverages, provided that diffusion is fast. Whilst over Pt(111) OH* has a very low diffusion barrier over Pt(100) actual OH* diffusion is somewhat slower. Other processes such as proton transfer between a nearest neighbour OH* - O* pair and the low barrier for out of plane rotation (flip) of OH* may compensate for low OH* mobility. Therefore, QCA may still be a good approximation. The kMC model should in principle provide the best description regardless of interaction energies, surface coverage and intermediate mobility in a given system. This performance is however limited by the level of detail considered which may unfortunately come with significant computational costs. The largest limitations in the kMC model are likely to result from the simple interaction clusters considered, here only pairwise interactions are considered.

Other simplifications relate to adsorption and surface coordination (dentate) of ORR intermediates. Over Pt(111) the monodentate species are O*(fcc and hcp), H*(top), O_2*(bridge); OH*(top) is bidentate as it takes up a top and bridge sites; H_2O*(top) and OOH*(bridge) are tridentate with bridge-top-bridge adsorption structures. Over Pt(100) O_2*(bridge), O*(bridge) and H*(bridge) are

monodentate; OH*(bridge) is bidentate with a bridge-hollow structure and H_2O*(top) is tridentate with a bridge-top-bridge structure. The exact structures, angles and distances, are not important at all as the chemistry is contained in the specified cluster energies. It is worth noting that the kMC model has been constructed such that the relative orientation of asymmetric adsorbates is accounted for.

4.2.4 Microkinetic simulations

Assumptions

Various assumptions have been made in order to solve the different microkinetic models. To simplify the comparison now and in later Chapters, the sticking coefficient/probability was assumed to be 1.0 over all surfaces and independent of coverage and temperatures. Moreover, adsorption processes were assumed to be barrierless. Both Pt(111) and Pt(100) surfaces were assumed to be pristine and without any reconstruction. The area of each reaction sites on Pt(111) and Pt(100) was assumed to be 6.82 $Å^2$ and 7.87 $Å^2$, respectively. Since a gas/solid interface is considered, solvation effects were not included.

Simulations approach

The steady state solutions to the balance equation in 2.36 were obtained by solving coupled ODEs using the SciPy ode package in Python 3.7, specifically the LSODA ODE solver [137] which automatically switches between the implicit Adams method and the stiff backward differential formula (BDF) method [138]. Given the long list of reaction steps and intermediates, especially in Chapters 5 and 6, integration seemed to be the most practical approach. The integration time was adjusted to achieve steady state coverage and rates of individual species and reaction steps, respectively. Furthermore, the absolute and relative tolerances were set to 10^{-14} and 10^{-13}, respectively. Recently, this approach was shown to accurately describe the temperature programmed desorption profile of CO from Fe(100) [117].

Simulation conditions

The base simulations considered a gas composition of 33 kPa O_2, 67 kPa H_2 and 0 kPa H_2O. These partial pressures were kept constant during integration. For the sensitivity analyses, i.e. effect of total pressure, gas composition and humidity, only the parameter being tested was changed whilst keeping other setting the same. For mean-field microkinetic models, steady state rates and coverages were simulated at different temperatures, from 300 K to 900 K with 20 K steps.

kMC simulations were only conducted at 400 K, 600 K and 800 K over periodic Pt(111) and Pt(100) surface consisting of a 20x20 lattice, containing 400 sites. All kMC simulations were

performed using the Zacros code [139–141] and random number generator seeding constants of 135 and 246. Given that the system consists of vary fast (surface diffusion) and very slow (hydrogenation reactions) reactions, stiffness scaling was enabled on all reaction steps with a scaling factor 3.0 [139]. The latter setting accelerates the simulation by enabling rare events. For all diffusion steps the diffusion barriers were obtained from Chapter 3; the BEP constants of 0.5 were assumed for diffusion steps. The pre-factors were calculated at 300 K and kept constant in all simulations. These simulations also included surface diffusion of different adsorbates.

Analyses

There are three key analyses discussed herein, (1) the ORR activity, (2) ORR pathway and (3) key elementary reaction steps, at various temperatures. The ORR activity is obtained directly from the steady state solution to the microkinetic model (in kMC simulations this is an average value) and is equivalent to the evolution rate of H_2O* from the catalyst surface. The reaction pathway analysis is based on the number of turns of each reaction in the mechanism relative to the turnover frequency of H_2O* desorption, i.e. r_i/r_{H_2O}. Any reaction whose ratio with r_{H_2O} is near zero cannot be considered significant under modelled conditions. The sign indicates the direction of the reaction, negative for reverse reactions.

The degree of rate control analyses gives further information, instead of showing which pathway toward H_2O* is dominant (or what different steps contribute) it indicates which steps are critical from a design perspective. Improving a rate limiting step with minimal influence on the other reaction steps should lead to improved performance. Campbell's [132] degree of rate control is given by,

$$X_{rc,i} = \left(\frac{\partial \ln\left(r_{H_2O}\right)}{\partial \ln(k_i)}\right)_{k_{j\neq i},K_j} \tag{4.3}$$

and describes the effect of changing the activation energy of reaction step i on the reaction of interest. It should be noted that this does not change the thermodynamics of the system—it only lowers the energy of the transition states, thus changing the forward and reverse rate constants to the same extant. In the present study, the gradient (4.3) was approximated from three points generated from $0.99k_i$, k_i and $1.01k_i$ simulations; a denser sampling did not change the predicted rate control behaviour.

Polarization curve simulations

Despite the main assumption of a gas/solid interface, polarization curves were generated. The computational hydrogen electrode (CHE) model [7,52,142] was applied to investigate the effect of

potential on the ORR rate, specifically on the adsorption equilibria of H*. This was applied on the H_2 adsorption reaction where the change in electrode potential shifts reference for adsorbed H*. Polarization curves were modelled at 358 K and 1 bar total pressure (33 kPa O_2 and 67 kPa H_2).

4.3 ORR energetics over extended Pt surfaces

4.3.1 Reaction over Pt(111)-*p*(3x3) surface

At a gas/Pt(111) interface, the $4e^-$ transfer ORR mechanism involves three adsorption-desorption reactions, i.e. $O_2 + * \leftrightarrow O_2*$, $H_2 + 2* \leftrightarrow 2H*$ and $H_2O + * \leftrightarrow H_2O$ with * being a vacant site on Pt(111). The O_2 and H_2O adsorption-desorption reactions are similar in that they adsorb molecularly over one vacant site—contrary to the latter, H_2 dissociates upon adsorption taking up two vacant sites. The adsorption energies for these molecules have already been reported in Chapter 3 and are -0.714 eV/O_2, -1.052 eV/H_2 and -0.222 eV/H_2O (see Table 3.3).

The adsorbed intermediates undergo various transformation steps ultimately resulting in H_2O* which then desorb to complete the catalytic cycle. Table 4.1 presents, for different reaction process over Pt(111), the initial, transition and final state structures and energy changes. In the case of O_2*, two transformation processes are possible. Direct dissociation which has an activation energy of 0.407 eV and an activated bond length of 2.007 Å (cf. 1.396 Å of the ground state). Alternatively, the hydrogenation step can precede dissociation—this has an activation energy of 0.416 eV and an activated bond length of 1.492 Å which can be compared to the ground state O-H bond length of OOH*. This second reaction is influenced by H* coverage as well—meaning at high H* coverage (low availability of vacant sites) O_2* hydrogenation can dominate the direct dissociation pathway. OOH* can dissociate with a low activation energy of 0.036 eV leading to O* and OH* intermediates. The activated 'O – O' bond in OOH* dissociation is 0.328 Å shorter than that of O_2* dissociation.

The resulting O* and OH* intermediates can undergo hydrogenation to become OH* and H_2O*, respectively. The activation energies for these reactions were calculated to be 0.969 eV and 0.175 eV, respectively. It should be noted that so far the O* hydrogenation appears to have the highest activation energy as reported previously [27,28,30]. The OH*-OH* disproportionation (coupling) reaction can also occur. A much lower activation energy was calculated for this reaction—this is of course partly due to the stabilised initial, transition and final state as a result of hydrogen bonding (see Table 4.1). The reverse of this reaction, i.e. O* hydrolysis, offers an alternative pathway for O* removal as OH*. The formation and desorption of H_2O_2* has not been considered given the low OOH* dissociation barrier. The calculated reaction and activation energies are in reasonable agreement with previous DFT studies [27,28,30]. Calculations in

Chapter 3 have looked at the mobility of the various intermediates. On Pt(111) most ORR intermediates are sufficiently mobile, the only exception is O*. Considering calculated barriers for the different reaction processes, it is clear that diffusion will be orders of magnitude faster than the slowest reactions. As a result, mean-field microkinetic models, especially the QCA model should give a reasonable approximation of the ORR activity. Model input parameters and coverage corrected reaction energetics are presented in Table E7.1 in Appendix E2.

4.3.2 Reaction over Pt(100)-*p*(3x3) surface

The O-O bond cleavage highlights the major difference between the ORR over Pt(100) and Pt(111) surfaces. Over Pt(100), O_2* dissociation is more facile than over Pt(111) and a barrier of 0.143 eV was calculated—consequently, the OOH* intermediate is quite unstable (see Chapter 3) [26]. Li *et al.* [27] calculated an activation barrier of 0.53 eV for O_2* hydrogenation on this surface and the dissociation of OOH* was barrierless.

Clearly, O_2* will rather dissociate forming two O* intermediates which can undergo multiple hydrogenation steps. Table 4.2 presents reaction energetics of the ORR over Pt(100)-*p*(3x3). The first hydrogenation step was calculated to occur with an activation energy of 0.532 eV (0.437 eV lower that the equivalent step on a Pt(111) surface). However, the second hydrogenation steps, i.e. OH* + H* → H_2O* + *, has an overall activation energy of 0.886 eV. To find the transition state the process had to be broken down into two steps. The first step was H* diffusion from a bridge state to an atop state (activation energy of 0.215 eV) and then the second involved OH* hydrogenation by an atop adsorbed H* intermediate (activation energy of 0.687 eV)—combining these processes give an overall activation barrier of 0.886 eV (0.199 eV[††] + 0.687 eV). A transition state for direct hydrogenation of H* and OH* on $b^{(0)}$ could not be located (see Table 4.2).

The OH*-OH* coupling reaction provides an alternative pathway for OH* removal as H_2O*. The calculated activation energy for this reaction was 0.383 eV (cf. to 0.040 over a Pt(111) surface). As was argued for the Pt(111) case, the low activation energy calculated for this reaction is only possible because of stabilisation of the transition state by hydrogen bonding. Over the Pt(111) surface the hydrogen bonding stabilises the O-bridge transition state whilst on Pt(100) the OH* near a top site is stabilised by hydrogen bonding with the second OH* involved in the OH*-OH* coupling reaction (see Tables 4.1 and 4.2). Comparing to previous DFT calculations in the literature, the calculated energetics over the Pt(100) surface in this study are also in good agreement [26,27]. Over the Pt(100) surface diffusion of all ORR intermediates have barriers lower than the

[††] Energy difference between bridge adsorbed H* and atop adsorbed H*

highest activated reaction step—the highest diffusion barrier is for OH*. The calculated ORR energetics data over both Pt(111) and Pt(100) can now be used to perform microkinetic analyses at a gas/solid interface. A summary of model input parameters and coverage corrected reaction energetics on Pt(100) is presented in Table E7.2 in Appendix E.

Table 4.1: Oxygen reduction reaction over Pt(111)-*p*(3x3) surface, initial, transition and final state structure, distance between bond forming atoms($d_{X\text{-}Y}$, Å) and state energy relative to initial state (E^0, eV).

REACTION	Initial state	Transition state	Final state
$O_2^{b(1)}$ → $O^{f(1)} + O^{f(1)}$	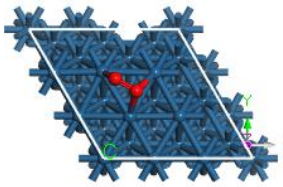 $E^0 = 0.0$ | $d_{O\text{-}O} = 1.396$	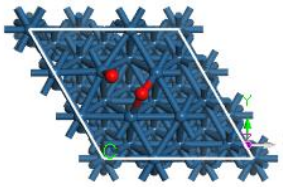 $E^0 = 0.407$ | $d_{O\text{-}O} = 2.007$	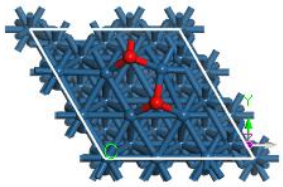 $E^0 = -1.200$ | $d_{O\text{-}O} = 2.998$
$O^{f(1)} + H^{t(1)}$ → $OH^{b(1)}$	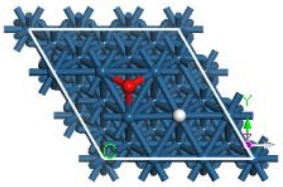 $E^0 = 0.0$ | $d_{O\text{-}H} = 3.331$	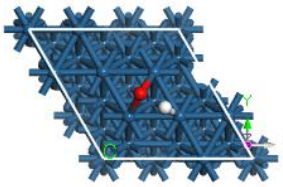 $E^0 = 0.969$ | $d_{O\text{-}H} = 1.594$	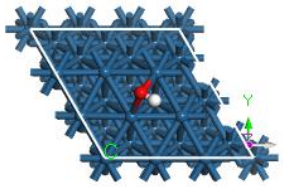 $E^0 = -0.038$ | $d_{O\text{-}H} = 0.984$
$OH^{t(1)} + H^{t(1)}$ → $H_2O^{t(1)}$	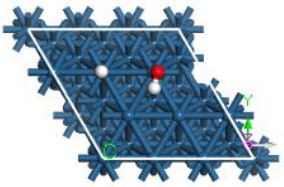 $E^0 = 0.0$ | $d_{O\text{-}H} = 3.175$	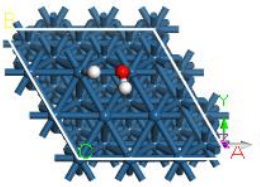 $E^0 = 0.175$ | $d_{O\text{-}H} = 1.688$	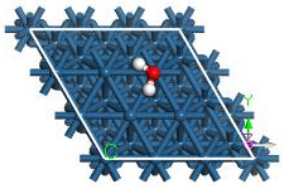 $E^0 = -0.603$ | $d_{O\text{-}H} = 0.980$
$OH^{b(1)} + OH^{t(1)}$ → $H_2O^{t(1)} + O^{f(1)}$	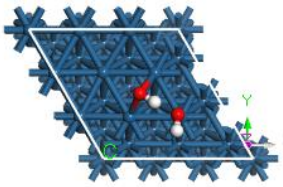 $E^0 = 0.0$ | $d_{O\text{-}H} = 1.496$	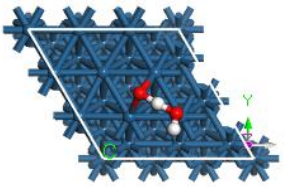 $E^0 = 0.040$ | $d_{O\text{-}H} = 1.195$	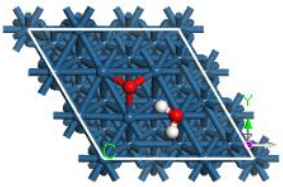 $E^0 = -0.268$ | $d_{O\text{-}H} = 0.980$
$O_2^{b(1)} + H^{t(1)}$ → $OOH^{b(1)}$	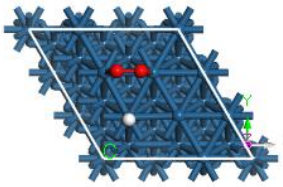 $E^0 = 0.0$ | $d_{O\text{-}H} = 2.861$	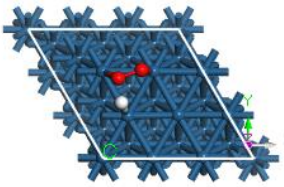 $E^0 = 0.416$ | $d_{O\text{-}H} = 1.492$	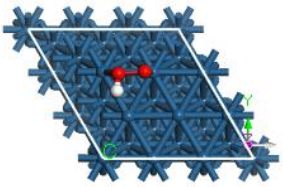 $E^0 = -0.077$ | $d_{O\text{-}H} = 0.991$
$OOH^{b(1)}$ → $OH^{t(1)} + O^{f(1)}$	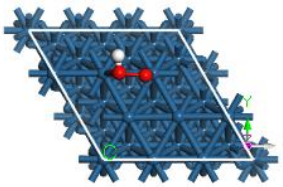 $E^0 = 0.0$ | $d_{O\text{-}O} = 1.481$	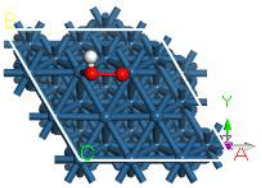 $E^0 = 0.036$ | $d_{O\text{-}O} = 1.679$	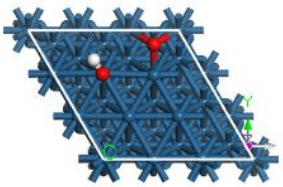 $E^0 = -1.667$ | $d_{O\text{-}O} = 3.383$

Table 4.2: Oxygen reduction reaction over Pt(100)-*p*(3x3) surface, initial, transition and final state structure, distance between bond forming atoms ($d_{X\text{-}Y}$, Å) and state energy relative to initial state (E^0, eV).

REACTION	Initial state	Transition state	Final state
$O_2^{b(0)}$ → $O^{b(0)} + O^{b(0)}$	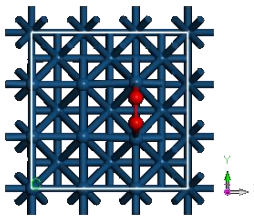 $E^0 = 0.0$ | $d_{O\text{-}O} = 1.363$	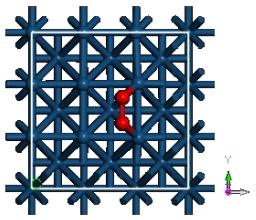 $E^0 = 0.143$ | $d_{O\text{-}O} = 1.385$	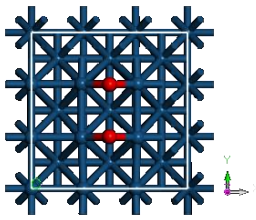 $E^0 = -1.388$ | $d_{O\text{-}O} = 2.814$
$O^{b(0)} + H^{b(0)}$ → $OH^{b(0)}$	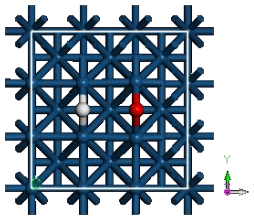 $E^0 = 0.0$ | $d_{O\text{-}H} = 2.917$	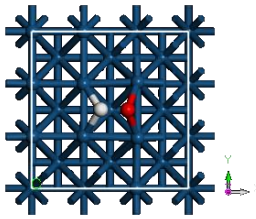 $E^0 = 0.532$ | $d_{O\text{-}H} = 1.509$	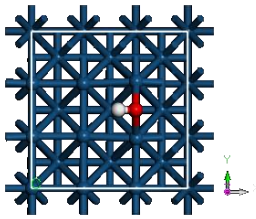 $E^0 = -0.335$ | $d_{O\text{-}H} = 0.983$
$OH^{b(0)} + H^{b(0)}$ → $OH^{b(0)} + H^{t(0)}$	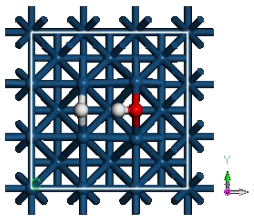 $E^0 = 0.0$ | $d_{O\text{-}H} = 2.964$	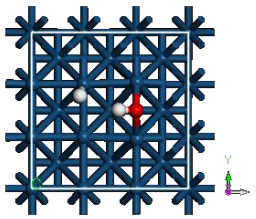 $E^0 = 0.215$ | $d_{O\text{-}H} = 3.117$	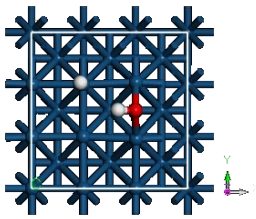 $E^0 = 0.199$ | $d_{O\text{-}H} = 3.312$
$OH^{b(0)} + H^{t(0)}$ → $H_2O^{t(0)}$	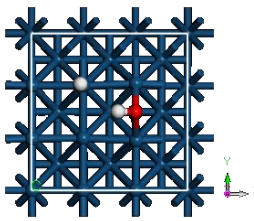 $E^0 = 0.0$ | $d_{O\text{-}H} = 3.312$	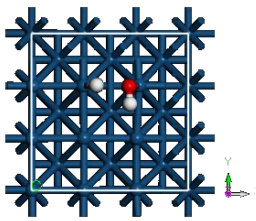 $E^0 = 0.687$ | $d_{O\text{-}H} = 1.858$	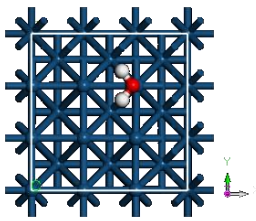 $E^0 = 0.003$ | $d_{O\text{-}H} = 0.979$
$OH^{b(0)} + OH^{b(0)}$ → $H_2O^{t(0)} + O^{b(0)}$	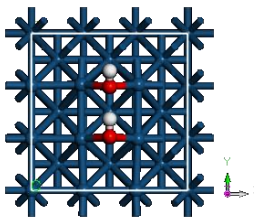 $E^0 = 0.0$ | $d_{O\text{-}H} = 1.762$	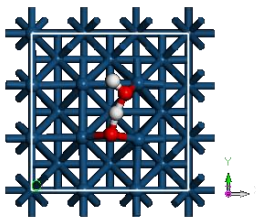 $E^0 = 0.383$ | $d_{O\text{-}H} = 1.205$	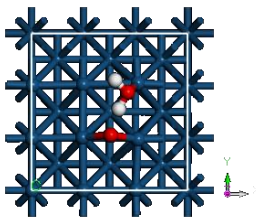 $E^0 = 0.348$ | $d_{O\text{-}H} = 1.030$

4.4 ORR activity over extended Pt(111) surfaces

The experimental ORR rate on Pt(111) in 0.1 M $HClO_4$ is 0.59 mA.cm^{-2} (equivalent to 1.26 s^{-1} per site assuming a site area of 6.82 Å^2) at an electrode potential of 0.9 V vs. SHE and 300 K [23]. This rate increases with decreasing electrode potential until it reaches a diffusion limited current density. Microkinetic models of the ORR on Pt(111) in an aqueous electrolyte have been proposed in several studies [109,110,143]. These models predict ORR activities in the range of 2.13 x10^{-4} to 4.26 s^{-1} per site at 0.9 V vs. SHE and 300 K. In addition to this wide variation in predicted ORR activities, these models also predict significantly different surface coverage profiles. These large variations may be due to differences in considered reaction mechanisms, reaction energetics and the way lateral interactions were treated. Despite the latter, these models provide useful insights into the ORR process [109,110,143]. Qi and Li [110] highlighted the effect of lateral interactions on the ORR activity volcano diagram. On the other hand, Hansen *et al.* [143] demonstrated the good agreement between the kinetic and thermodynamic ORR activity volcano diagrams. Finally, Eberle and Horstmann [109] demonstrated the importance of both lateral interactions and ER reaction steps in microkinetic models of the ORR. In the absence of lateral interactions, the ORR rate was ca. 8 orders of magnitude lower than the rate predicted by a mean-field approximation microkinetic model. Moreover, ER reaction rates were more than 10 orders of magnitude larger than LH reaction rates [109].

Fantauzzi *et al.* [53] developed a microkinetic model of the ORR on Pt(111) under gaseous conditions. Since their model does not explicitly treat lateral interactions between reaction intermediates, they predicted very high oxygen coverages (θ_O > 9.0 ML) at T < 600 K and consequently low ORR rates. Their predicted ORR rates increased monotonically with increasing temperature. Furthermore, they reported that at T < 900 K the ORR rate is controlled by O* hydrogenation to OH* whilst at T > 900 K the O_2* dissociation reaction is rate-controlling.

4.4.1 Steady state ORR activity

The steady state ORR rates, i.e. H_2O evolution rates, have been modelled using the SA (without lateral interactions), BWA, QCA and kMC microkinetic models, at different temperatures under gaseous conditions. Figure 4.1 presents the steady state H_2O evolution rates over a wide temperature range and Figure 4.2 gives the corresponding surface coverage functions. All three models (SA, BWA and QCA) predict ORR rates which increase with temperature and reach maximum before decreasing at high temperatures. There is a large difference in the position of the ORR rate maximum predicted by the coverage independent SA model compared to predictions by the coverage dependent BWA and QCA models. The latter models are in better agreement with each other. Below 540 K, the BWA and QCA

predicted ORR rates are higher than SA predicted rates and above 540 K the SA predicted rates are higher. Furthermore, kMC predicted ORR activity is higher than all other predictions at 400 K, 600 K and 800 K (see Figure 4.1).

According to the coverage independent SA microkinetic model, the ORR activity at low temperatures (< 400 K) is several orders of magnitude lower than the prediction by other models and also the expected kinetic rate from experiments (>> 1.26 s^{-1} at 300 K [23]). These low ORR rates were also predicted in studies by Eberle and Horstmann [109] and Fantauzzi *et al.* [53] which excluded lateral interactions. Surface coverage profiles in Figure 4.2 are very useful and can be used to rationalise the large discrepancy between experiments and coverage independent microkinetic models (SA). Figure 4.2 shows that for the SA model (solid lines) the Pt(111) surface is fully covered with O* at temperatures below 400 K. With increasing temperature, the H* coverage increases monotonically up to 600 K, reaching a maximum value of 0.64 ML before decreasing monotonically with increasing temperature. The fraction of empty sites increases monotonically between 500 K and 900 K whilst the O* coverage decreases monotonically in the same range.

The low ORR rates at T < 400 K can be attributed to the competitive adsorption of oxygen and hydrogen. High O* coverages limit H_2 adsorption and as a result lead to very low H* coverages which consequently lead to lower ORR rates. The latter explains why at these low temperatures O* hydrogenation was found to be a rate-controlling step by Fantauzzi *et al.* [53]. Experiments [10], empirical ORR kinetic models [51] and first principles based DMC microkinetic models [129] (with coverage effects) report lower surface coverages of Pt(111) with adsorbed O*. This discrepancy in surface coverage is a direct consequence of excluding lateral interactions. In Subsection 2.4.3 it was argued that a full O* monolayer on Pt(111) is unlikely to form due to strongly repulsive O*-O* lateral interactions (see Appendix B3). The full O* coverage at low temperature predicted by the coverage independent microkinetic models are a further indication that lateral interactions are important. Moreover, a simple adjustment of the adsorption energy of gas molecules is inadequate. Fantauzzi *et al.* [53] who considered a gas/Pt(111) interface and only accounted for lateral interactions by adjusting the adsorption energies of H_2, O_2 and H_2O to match temperature programmed desorption measurements, ignoring the interactions between other intermediates and their influence on activation energies, predicted very high coverages of the Pt(111) surface with O* and low ORR rates at $T \leq 600$ K.

At a high temperature region, the O* coverage predicted by the SA model decreases significantly becoming dominated by H* around 540 K and by both H* and vacant sites (*) above 600 K (see

Figure 4.2). Concomitantly with this change in surface coverage is the rise in ORR activity, reaching a maximum around 740 K. This result is consistent with the behaviour reported by Fantauzzi *et al.*[53], albeit a shift in their profiles toward higher temperatures. This shift may be a result of multiple factors including variations in pre-exponential factors and reaction energetics. Nonetheless, the trends seem rather similar.

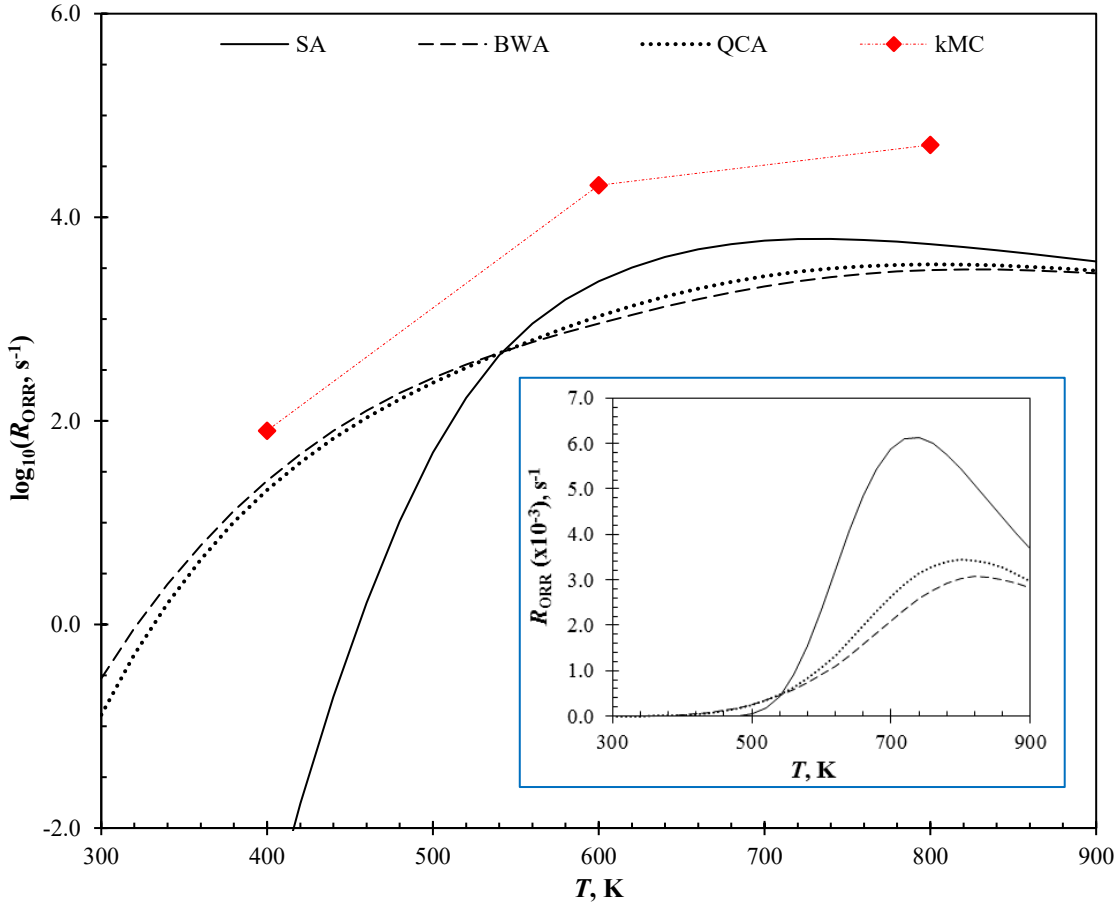

Figure 4.1: Evolution rates (R_{ORR}) of H_2O from Pt(111) considering a gas/surface interface (with a stoichiometric gas composition ($H_2/O_2 = 2$) and a total pressure of 1 bar) predicted by SA (—), BWA (− − −), QCA (·····) and kMC (diamond markers) microkinetic models at various temperatures; the insert shows the ORR rate as a function of temperature in a linear scale to highligh the position of the rate maxima and differences in ORR rate at high temperatures.

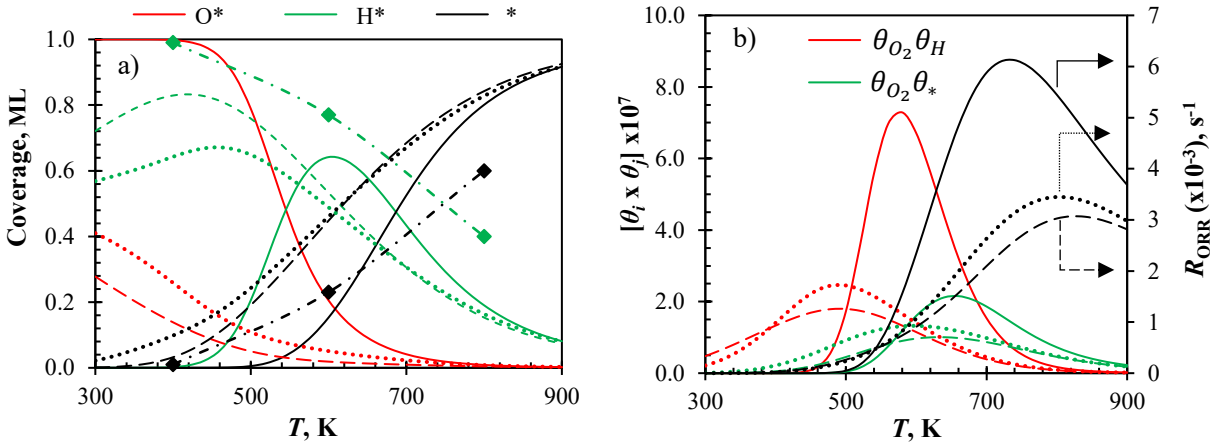

Figure 4.2: (a) Surface coverage of major species and (b) concentration factor in rate expressions of important reaction steps, under steady state conditions during ORR over Pt(111) considering a gas/surface interface (with a stoichiometric gas composition ($H_2/O_2 = 2$) and a total pressure of 1 bar); predicted by SA (—), BWA (− − −) and QCA (·····) microkinetic models at various temperatures. kMC predicted coverages shown with green and black diamond markers for H* and *, respectively.

The BWA, QCA and kMC models account for lateral interaction between reaction intermediates. As a result, their predicted kinetic rates and surface coverages are a step closer toward experimental measurements at moderate to low temperatures. In this study, both BWA and QCA models predict a surface coverage dominated by H* intermediates at moderate to low temperatures (see Figure 4.2a). This qualitatively agrees with experimental studies which have reported that at low electrode potentials Pt surfaces are covered with H* intermediates whilst the O* + OH* layer only forms at high electrode potentials [20]. Figure 4.1a-b shows that the QCA and BWA models are in good agreement. This of course in not surprising given that H* intermediates which are weakly interacting (see Table 2.1) dominate the surface. At high temperatures all three models are anticipated to converge to each other—under these conditions the total surface coverage is low, and adsorbates are energetic enough to be highly mobile. It is clear from Figure 4.1 and 4.2 that this is indeed the case, both in terms of ORR activity and surface coverage. The observed maximum in the ORR rate seems to be caused by the rapidly decreasing surface fraction of key reaction intermediates. Figure 4.2b present the $\theta_{O_2}\theta_H$ and $\theta_{O_2}\theta_*$ products as a function of temperatures. Both $\theta_{O_2}\theta_H$ and $\theta_{O_2}\theta_*$ profiles increase with temperature and pass through a maximum before decreasing monotonically at high temperatures. Since the individual rates are functions of surface coverage and rate constant, the increasing rate constants with temperature may be dominated by decreasing surface coverages (concentration) at high temperatures.

The kMC simulations were conducted at 400 K, 600 K and 800 K (and 67 kPa H_2 and 33 kPa O_2) on a 20x20 Pt(111) lattice with 400 sites. Various adsorption/desorption and surface reactions were considered together with intra-facet diffusion of all reaction intermediates (except for OOH*). The

ORR rate was then simply calculated as the total number of H_2O molecules formed per sites divided by the simulation time. Figure H1.1 in Appendix H presents the ORR rate as a function of time at 400 K, 600 K and 800 K. The rate convergence/equilibration is faster at high temperatures. The steady state ORR rates are also presented in Figure 4.1 (red diamond markers) where they are clearly higher than ORR rates predicted by all other microkinetic models. At the three investigated temperatures, the surface is predominately covered with H* adsorbates whose coverage slowly decreases with temperature (see Figure 4.2a). Further analyses show (1) the ORR proceeds via a peroxyl pathway at all three temperatures and (2) at 400 K, 600 K and 800 K more than 50% of OOH* dissociation leads to O* on weakly adsorbing hcp sites and consequently result in a lower O* removal barrier as OH* via hydrogenation. The combination of the latter may explain why kMC predicts higher ORR rates. In summary, kMC simulations predict high H* coverages leading to limited room for O_2* dissociation (favouring hydrogenation instead) and because OOH* dissociation leads to both fcc and hcp O* intermediates, the O* removal rate is overall improved.

4.4.2 ORR pathway analysis

The ORR can proceed via different pathways over the Pt(111) surface. The first node concerns the O-O bond cleavage; in the considered mechanism this can proceed via either O_2* + * → 2O* or OOH* + * → OH* + O*. The reaction energetics are not sufficient to determine conclusively which of these two pathways will be followed. The reason for the latter is that kinetic rates are not only functions of the activation energy, but also pre-exponential factor and surface coverage. The second node is around the removal of O* which can either follow a direct path (O* + H* → OH* + *) or a hydrolysis pathway (O* + H_2O* → 2OH*). Although the former has a very high activation energy, the latter may be kinetically limited by low surface coverage with H_2O* adsorbates.

Figure 4.3a describes the reaction pathway as the contribution each elementary step makes toward forming a single H_2O molecule and Figure 4.3b shows the degree of rate control as a function of temperature. In Figure 4.3a the ratio of the direct O_2* dissociation to the ORR rate is zero at low temperatures and increases monotonically to 0.5 at high temperature. On the other hand, the ratio of O_2 hydrogenation is 0.5 at low temperatures and decreases monotonically to zero at high temperatures. The ORR pathway over the Pt(111) surface seems to be independent of the way lateral interactions are incorporated (see Figure 4.3). At T < 440 K, the ORR exclusively follows a peroxyl pathway, i.e. O_2* → OOH* → OH* → H_2O*. Above 700 K the dissociative pathway is followed. A mixed pathway is followed between 440 K and 700 K. Over the whole range, O* hydrolysis plays no role in the ORR process over Pt(111).

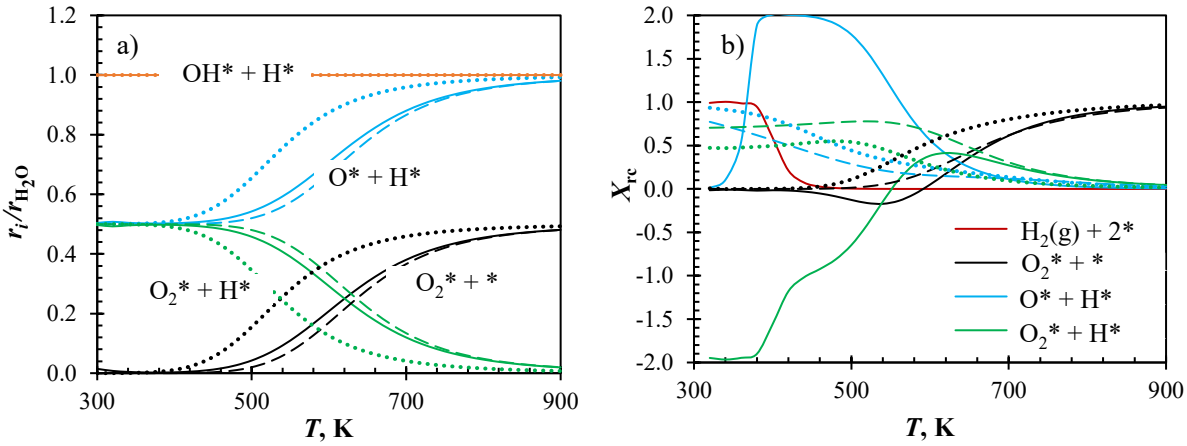

Figure 4.3: (a) ORR reaction pathway over Pt(111) and (b) Campbell's [132] degree of rate control plot for steady state ORR over Pt(111) surface considering a gas/surface interface (with a stoichiometric gas composition ($H_2/O_2 = 2$) and a total pressure of 1 bar); predicted by SA (—), BWA (− − −) and QCA (·····) microkinetic models at various temperatures.

In terms of rate controlling reaction steps, Figure 4.3b shows some interesting trends. At high temperatures the system is controlled by the O_2* dissociation. The latter is true for all three microkinetic models, i.e. SA, BWA and QCA. At low temperatures, the SA model shows that H_2 adsorption is rate limiting as the surface is fully covered with O* in this range. Slightly above this point (> 380 K) the rate controlling step is O* hydrogenation. This is in good agreement with similar analyses by Fantauzzi *et al.* [53]. Also based on the SA model, O_2* hydrogenation is rate inhibiting below 540 K since it competes with O* hydrogenation for available H* intermediates. The BWA and QCA models predict an O* hydrogenation – O_2* hydrogenation controlling behaviour between 300 K and 660 K; O_2* hydrogenation is more controlling between 460 K and 660 K. On the other hand, kMC simulations at 400 K, 600 K and 800 K predicted a peroxyl ORR pathway. The largest contribution of direct O_2* dissociation pathway was still only 5% at 800 K. Given the very high H* coverages on Pt(111) predicted by the kMC model, it is unsurprising why the peroxyl pathway is preferred over the dissociative pathway. Due to high computational costs it was not practical to perform the degree of rate control analysis using kMC.

4.4.3 Sensitivity to total pressure, composition and humidity

The effect of total pressure, gas humidity and excess H_2 on the ORR kinetics was also investigated (see Figure 4.4a-b). Using a total pressure of 10 bar results in a significant increase in ORR rate at high temperatures for all models. At a low temperature region, both BWA and QCA see an improvement in the ORR rate whilst the SA model actually shows lower rates compared to 1 bar simulations. Both the improvement at high temperatures and worsening at low temperatures, in the case of the SA model, can be explained by increased oxygen coverage at high pressure. The ORR rate increases at high

temperature since the increase in kinetic rate constants is further complemented by a relatively high O* coverage.

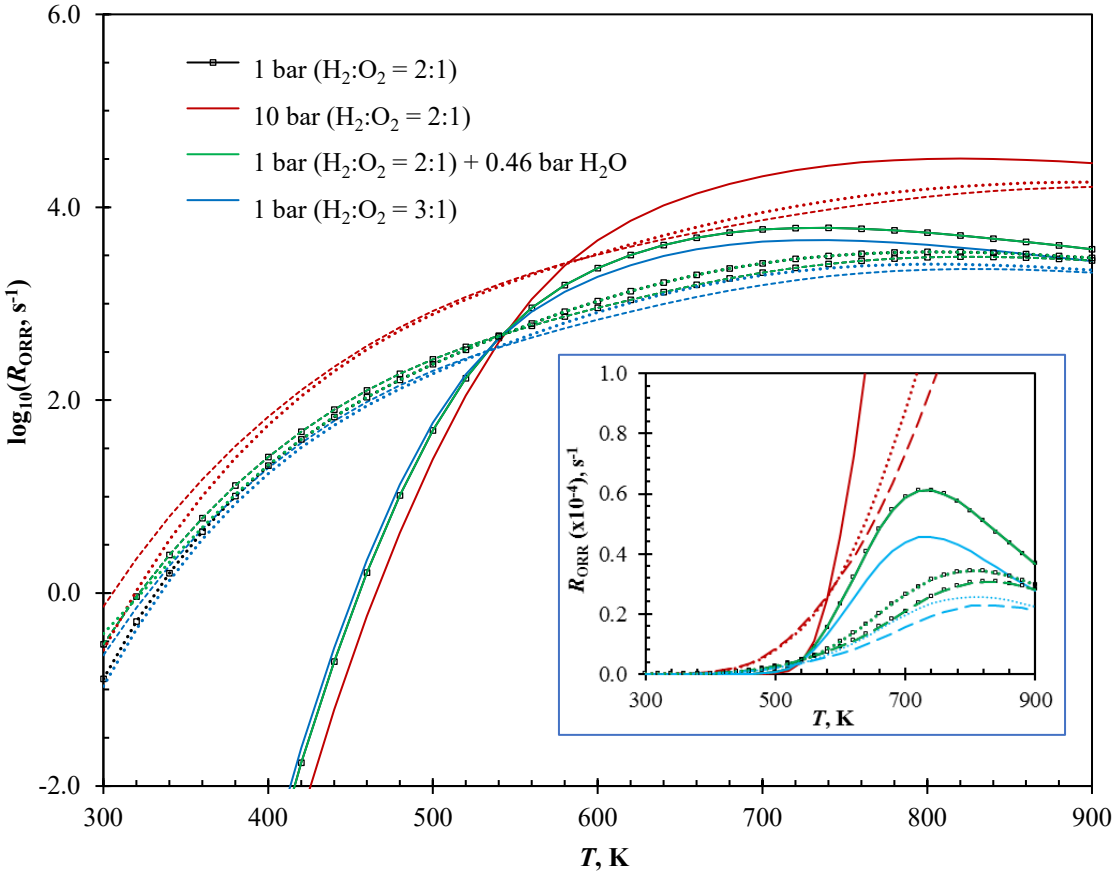

Figure 4.4: Effects of pressure, humidity and feed stoichiometry on evolution rates (R_{ORR}) of H_2O from Pt(111) surface considering a gas/surface interface predicted by SA (—), BWA (− − −) and QCA (·····) microkinetic models at various temperatures. the insert presents the same data however in a linear scale.

Water can influence the ORR rate at low temperatures provided its presence increases surface coverage of Pt(111) with H_2O* adsorbates—consequently leading to increased O* hydrolysis rates—offering an alternative pathway to the rate controlling O* hydrogenation step. Under simulated moist conditions, i.e. H_2O(g) partial pressure of 0.46 bar (ca. 80% relative humidity at 358 K) and a total pressure of 1.46 bar, the ORR rate is the same as under dry conditions at a total pressure of 1 bar (see Figure 4.3). As mentioned earlier, the role of the O* hydrolysis reaction in the mechanism, especially at low temperature conditions where O* hydrogenation is partially rate controlling, is dependent on the H_2O* coverage which unfortunately remains extremely low even under moist conditions (see Figure F1.1 in Appendix F).

The other effect investigated was that of excess H_2 (or limited O_2 reactant). Keeping a total pressure of 1 bar, ORR rates were modelled under conditions where the H_2:O_2 ratio was 3:1 (cf. stoichiometric

ratio of 2:1). This resulted in much lower ORR rates compared to rates at stoichiometric composition and 1 bar pressure (see Figure 4.3). Increasing the total pressure to 1.33 bar keeping the 3:1 gas composition also resulted in lower ORR rates compared to base case (stoichiometric gas composition at 1 bar). The latter was done to ensure a constant chemical potential of H_2 under both stoichiometric and nonstoichiometric composition. The decrease in ORR rates is due to the slight increase in the H* coverage at the expense of O* coverage—consequently lowering the reaction rates of the rate-limiting steps, O* hydrogenation and O_2* dissociation.

4.5 ORR activity over extended Pt(100) surface

The experimentally measured ORR rate on Pt(100) in 0.1 M $HClO_4$ at 0.9 V vs. SHE and 300 K is 0.92 s^{-1} per site (assuming a site area of 7.87 $Å^2$) [23]. This rate increases with decreasing electrode potential. Microkinetic studies of the ORR over Pt(100) surfaces are scarce. The ORR activity on this surface has been estimated based on reactivity toward O* and OH* intermediates [29]. Furthermore, Qi and Li [110] presented a simple mean-field microkinetic model describing the ORR at an electrolyte/Pt(100) and electrolyte/Pt(111) interface, with hydrogenation steps involving a solvated proton. At low electrode potentials, their model predicted ORR rates of 10^4 - 10^5 $mA.cm^{-2}$ (equivalent to 2.46 x10^4 s^{-1} and 2.46 x10^5 s^{-1} per site assuming a site area of 7.87 $Å^2$). At electrode potentials below 0.4 V vs. SHE, the Pt(100) surface was mostly empty and the combined O* and OH* coverage was less than 0.3 ML. The ORR rate decreased with increasing electrode potential in a similar manner to the decrease on Pt(111) [110] and experimental observations [23]. Unlike on Pt(111), on Pt(100) the dominant surface intermediate was predicted to be O_2* with a 0.5 ML coverage between 0.4 V and 1.0 V vs. SHE [110]. This high O_2* coverage is due to underestimation of lateral interactions, especially interactions between O_2* intermediates. Furthermore, experimental studies reporting such high O_2* coverages could not be found.

4.5.1 Steady state ORR activity

The steady state ORR rates have been modelled using the SA (without lateral interactions), BWA, QCA and kMC microkinetic models, at temperatures between 300 K and 900 K. Figure 4.5 presents steady state H_2O* evolution rates whilst Figure 4.6a gives the corresponding surface coverage functions. The coverage independent ORR rates increase monotonically with temperature up to 700 K where a sharp jump is observed. Beyond 700 K, the ORR rates increase and pass through a maximum at 840 K before decreasing monotonically (see Figure 4.5). Furthermore, the coverage independent model predicts very high O* coverages, ca. 1.0 ML, on Pt(100) at T < 700 K and a sharp decrease in O* coverage at 700 K. Beyond 700 K, the O* and OH* coverages decrease monotonically from ca.

0.2 ML at 700 K (see Figure 4.6a). According to the SA model, the ORR rates at T < 700 K are several orders of magnitude lower on Pt(100) compared to Pt(111), under the same conditions. These extremely low rates are a result of a nearly 1.0 ML coverage of Pt(100) with O* adsorbates and an extremely low fraction of H* adsorbates on Pt(100) at T < 700 K. The sharp increase in the ORR rate at 700 K can also be explained by the sharp decrease in O* adsorbates and increase in the fraction of H* and OH* adsorbates on Pt(100).

Above 700 K the ORR activity increases, overshooting even that predicted by the BWA and QCA models. This happens concurrently with the decrease in the O* coverage and increase in other surface species including H*, OH* and vacant sites (*).

The BWA and QCA models address the problem of coverage effects by correcting the adsorption energy of each reaction intermediate accordingly depending on its neighbours. Simulation results show that BWA and QCA models predict higher ORR rates even at low temperatures, unlike the SA model (see Figure 4.5). The ORR rate vs. temperature profile predicted by the BWA model has two rate maxima, at 480 K (2.33 $x10^5$ s^{-1} per site) and above 900 K. Similarly, the QCA model also predicts two rate maxima, however, at 580 K (3.40 $x10^6$ s^{-1} per site) and at 860 K (1.59 $x10^7$ s^{-1} per site). Both BWA and QCA models predict higher ORR rates at 300 K than the SA model. Moreover, the BWA and QCA predicted ORR rates below 400 K are much more similar to each other than to the SA predicted rates.

There are two key behaviours observed from the BWA and QCA simulations. The first concerns their good agreement at low temperatures and the second relates to the observed transition at 500 K and 620 K for the BWA and QCA model, respectively. Both phenomena can be explained using surface coverage. Figure 4.6a illustrates that at low temperatures the surface coverage of H*, O* and OH* predicted by the BWA and QCA models are quite similar, explaining the observed similarities in ORR rates in this temperature range. The decrease in the O* and O_2* coverage with increasing temperature occurs concomitantly with an increase in H* coverage (see Figure 4.6b). In the BWA model, the O* and O_2* coverages decrease sharply immediately after the first maximum in the rate profile. The latter is also true in the QCA model; however, the decrease is less sharp and occurs immediately after the first maximum in the ORR rate profile. Figure 4.6b presents the $\theta_{O_2}\theta_*$ and $\theta_O\theta_H$, profiles predicted by the BWA and QCA models. The sudden decrease in $\theta_{O_2}\theta_*$ and $\theta_O\theta_H$, product at 480 K (BWA) and 580 K (QCA) correlates well with the first maximum of the ORR rate. The high surface coverage with O* and O_2* predicted by the QCA model leads to high ORR rates compared to BWA rates (see Figure 4.6b).

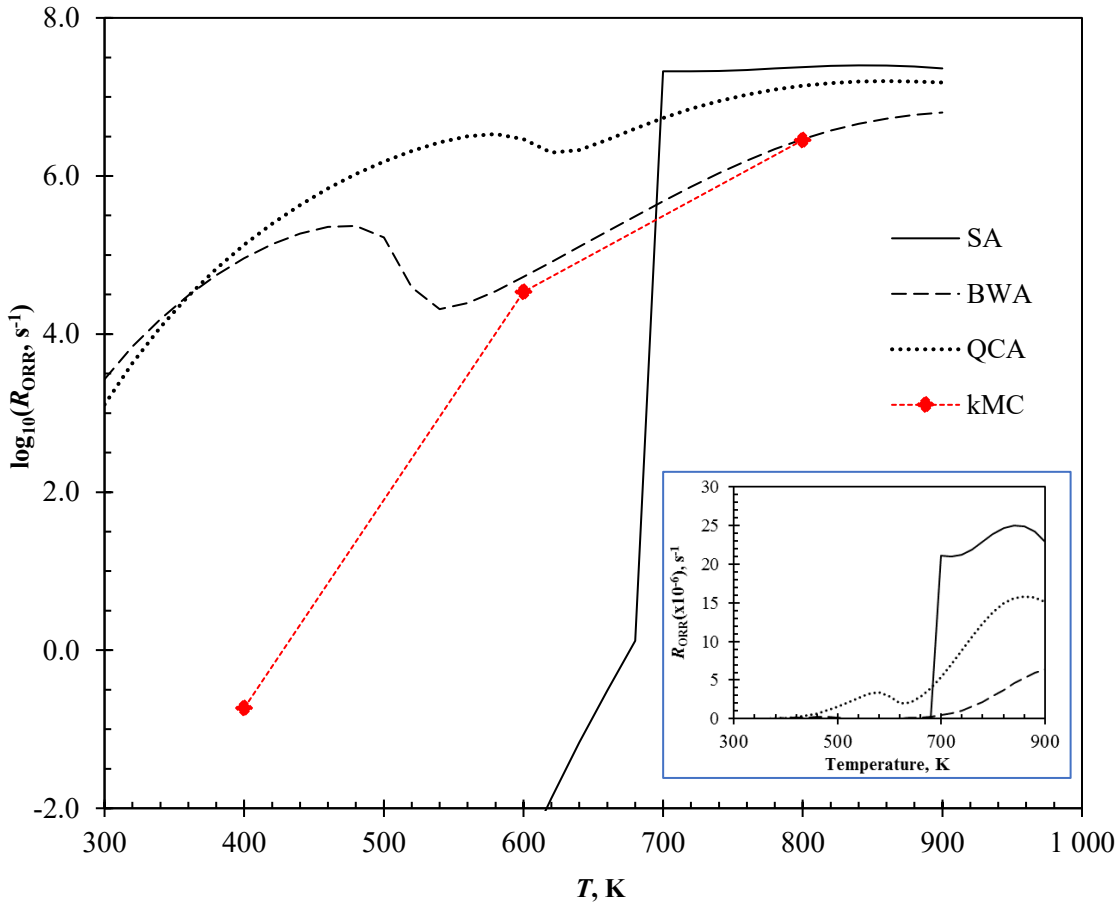

Figure 4.5: Evolution rates (R_{ORR}) of H_2O from Pt(100) considering a gas/surface interface (with a stoichiometric gas composition ($H_2/O_2 = 2$) and a total pressure of 1 bar) predicted by the SA (—), BWA (– – –), QCA (·····) and kMC (diamond markers) microkinetic models at various temperatures; the insert shows the ORR rate as a function of temperature in a linear scale to highligh the position of the rate maxima and differences in ORR rate at high temperatures.

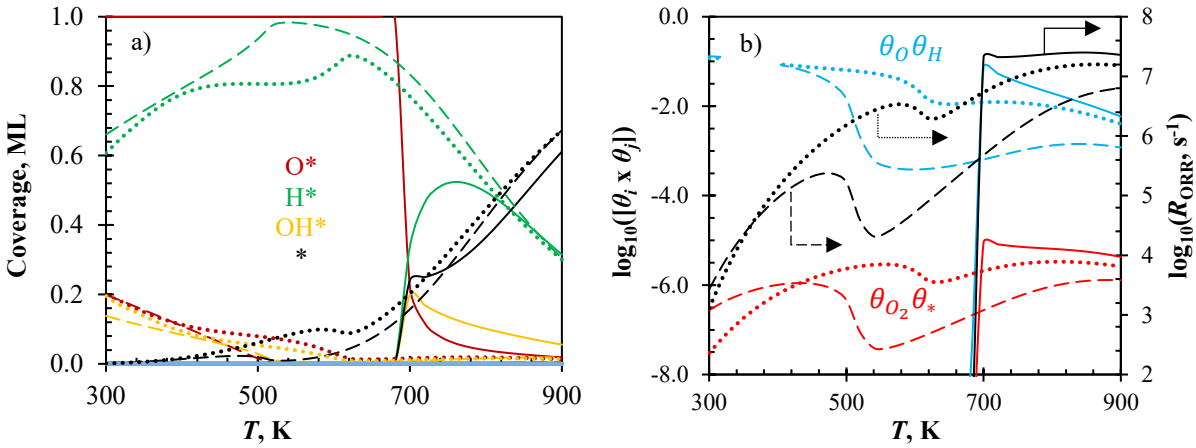

Figure 4.6: (a) Surface coverage of major species and (b) concentraction factor in rate expressions of important reaction steps, under steady state conditions during ORR over Pt(100) surface considering a gas/surface interface (with a stoichiometric gas composition ($H_2/O_2 = 2$) and a total pressure of 1 bar); predicted by SA (—), BWA (– – –) and QCA (·····) microkinetic models at various temperatures.

The BWA model predicts lower O_2* and O* coverages owing to its inherent overestimation of repulsive lateral interactions [105]. Based on a sensitivity analysis, this behaviour was identified to be caused by surface poisoning by H* adsorbates. Figure F1 in Appendix F presents ORR rate and surface coverage profiles at different adsorption energies of H_2 on Pt(100). At high adsorption energies, the surface concentration of H* increases to near 1.0 ML leading to fewer vacant sites and consequently decreasing O_2* dissociation rates.

The kMC simulations were conducted at 400 K, 600 K and 800 K (and 67 kPa H_2 and 33 kPa O_2) on a 20x20 Pt(100) lattice with 400 sites. Various adsorption/desorption and surface reactions were considered together with intra-facet diffusion of all reaction intermediates. The ORR rate was then calculated as the total number of H_2O molecules formed per sites divided by the simulation time. Figure H1.2 in Appendix H presents the ORR rate as a function of time at 400 K, 600 K and 800 K. The steady state ORR rates are also shown in Figure 4.5 (red diamond markers) where they can be seen to be in good agreement with the BWA model prediction at 600 K and 800 K whilst several orders of magnitude lower at 400 K. There are 1.92, 1.46 and 1.04 H* adsorbates per site on Pt(100) at 400 K, 600 K and 800 K, respectively. This is equivalent to 0.95, 0.73 and 0.52 H* adsorbates per Pt(100) bridge states (each site on Pt(100) has two bridge states, see Figure 2.7b), at 400 K, 600 K and 800 K, respectively. The extremely high coverage with H* on Pt(100) at 400 K limits the number of available sites for O_2 adsorption and dissociation resulting in extremely low ORR rates. At high temperatures, i.e. 600 K and 800 K, kMC predicted ORR rates are in good agreement with BWA and lower than the QCA and SA predicted ORR rates. Both QCA and SA models have appreciable O* and OH* coverages whilst the BWA and kMC models have much lower *OCS** coverages. Moreover, because of these low coverages the assumptions of random distribution in the BWA matches the reality modelled in the kMC simulations.

4.5.2 ORR pathway analysis

The pathway analysis can give a good insight to the observed ORR rates. Figure 4.7a presents the ORR pathway over Pt(100) whilst Figure 4.7b presents the degree of rate control profiles. The key profiles in Figure 4.7a are the O* hydrogenation (blue), OH* hydrogenation (orange) and O* hydrolysis (red). For the latter, the SA and QCA predicted ratios are 2.0 , 0.0 and -1.0 (negative simply means the reaction proceeds backward) at T < 700 K, respectively. At T > 700 K, the O* hydrogenation and O* hydrolysis ratios decrease slightly whilst the OH* hydrogenation ratio increases proportionately. On the other hand, the BWA model only agrees well with both SA and QCA models at T < 500 K. Above 500 K, the O* hydrogenation and O* hydrolysis ratios decrease whilst the OH* hydrogenation

increases proportionately. Interestingly, the ratios calculated from kMC simulations at 400 K, 600 K and 800 K, also correlate better with the BWA model results than with the other two models.

Therefore, the analysis in Figure 4.7a suggests that the reaction pathway is independent from the model assumptions at T < 500 K. Despite the large difference in ORR rate predicted by the QCA and SA models, they both proceed via the same pathway between 300 K and 900 K. The BWA model is an exception, above 500 K the OH* hydrogenation reaction plays a substantial role, almost halves the number of O* hydrogenation and OH*-OH* coupling (reverse hydrolysis of O*) reaction events needed for a single H_2O* desorption event. At higher temperatures the model predictions should converge to one another as was the case on Pt(111). Because of low OH* coverage in BWA and kMC simulations above 500 K, the OH*-OH* coupling reaction rate is lower. In kMC simulations only 50% of H_2O* is formed via the latter reaction and this occurs in the order, O_2 adsorption → O_2* dissociation → 2x O* hydrogenation → OH*-OH* coupling → O* hydrogenation → 1x OH* hydrogenation, and forms two H_2O* molecules. OH* hydrogenation occurs because an OH* neighbour is unavailable under these conditions as the surface is nearly saturated with H* adsorbates.

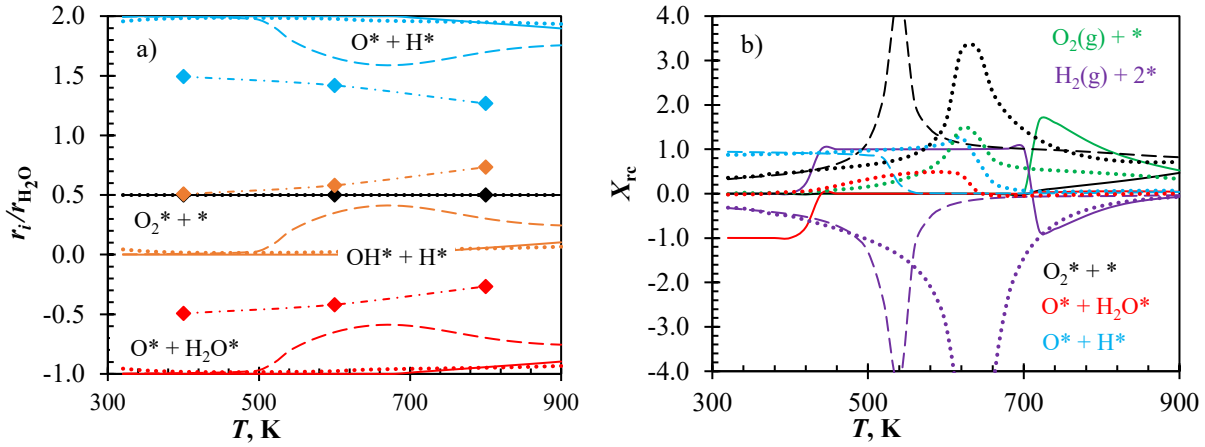

Figure 4.7: (a) ORR reaction pathway over Pt(100) and (b) Campbell's [132] degree of rate control plot for steady state ORR over Pt(100) surface considering a gas/surface interface (with a stoichiometric gas composition ($H_2/O_2 = 2$) and a total pressure of 1 bar); predicted by SA (—), BWA (− − −), QCA (·····) and kMC (diamond markers) microkinetic models at various temperatures.

Despite similar reaction pathways, the ORR over Pt(100) is controlled by different reactions depending on modelling assumptions. For the SA model between 400 K and 700 K the rate is limited by H_2 adsorption which is anticipated given that in this range the surface is fully covered with O* adsorbates (see Figure 4.6a). Below 400 K the ORR rates from the SA model are extremely low, and the predicted degree of rate control may not be reliable due to potential numerical errors. Above 700 K, the SA model predicts that the ORR rate is limited first by O_2 adsorption (up to ca. 800 K) and then by O_2*

dissociation (beyond 900 K). Therefore, within this model at high temperatures the rate is limited by the availability of oxygen intermediates and H_2 adsorption inhibits the rate as it competes with O_2 adsorption.

The BWA model predicts O* hydrogenation as a rate controlling step at low temperatures. This is potentially a consequence of the reaction pathway. The current pathway requires 2x O* hydrogenation events for a single H_2O* desorption event because it proceeds via OH*-OH* coupling; as a result, a higher strain/load is added on the O* step which in this case also happens to have the highest barrier (given that the ORR does not follow a direct OH* hydrogenation pathway). Above 500 K the system becomes strongly limited by O_2* dissociation and inhibited by H_2 adsorption. This also coincides with the transition observed in the ORR rate profiles (see Figure 4.5 and 4.6b). The nearly two orders of magnitude decrease in $\theta_{O_2}\theta_*$, between 500 K and 560 K, explains the corresponding decrease in the ORR rate, since O_2* dissociation is the rate-limiting step in this temperature range. The QCA model predicts similar rate-limiting steps as the BWA model, however with shifted profiles to higher temperatures (see Figure 4.7b). Interestingly, the two reaction rate maxima predicted by the BWA and QCA models (see Figure 4.5) coincide well with the change in the rate-determining step.

4.5.3 Sensitivity to total pressure, gas composition, and moisture

The effects of total pressure, water partial pressure and excess H_2 on the ORR rate were investigated. Figure 4.8 presents the ORR rates predicted under different simulation conditions aimed at studying model sensitivity. Increasing the total pressure from 1 bar to 10 bar results in increased surface coverage predicted by all three models. As a result, compared to the 1 bar, at 10 bar the ORR rates were lower/unchanged and higher at a low and high temperature range, respectively (see Figure 4.8). The high temperature ORR rate maximum is expected to shift up in temperature at high pressure conditions. Introduction of water vapour, i.e. 0.46 bar, had no effect on the ORR rate predicted by all three models (see Figure 4.6). The latter is not surprising since over Pt(100) the ORR is mostly limited by the availability of O*, i.e. O_2* dissociation. Increasing H_2O* coverage only serves the O* hydrolysis step, however due to high OH* coverages and lower activation energy the reverse reaction dominates. To simulate excess H_2, a nonstoichiometric 3:1 H_2(g):O_2(g) ratio and constant total pressure of 1 bar was used. Across all three models, a nonstoichiometric gas composition at 1 bar leads to lower ORR rates (see Figure 4.6). Changing gas composition at constant H_2 partial pressure was also tested and resulted in a similar behaviour to the 3:1 H_2(g):O_2(g) at 1 bar.

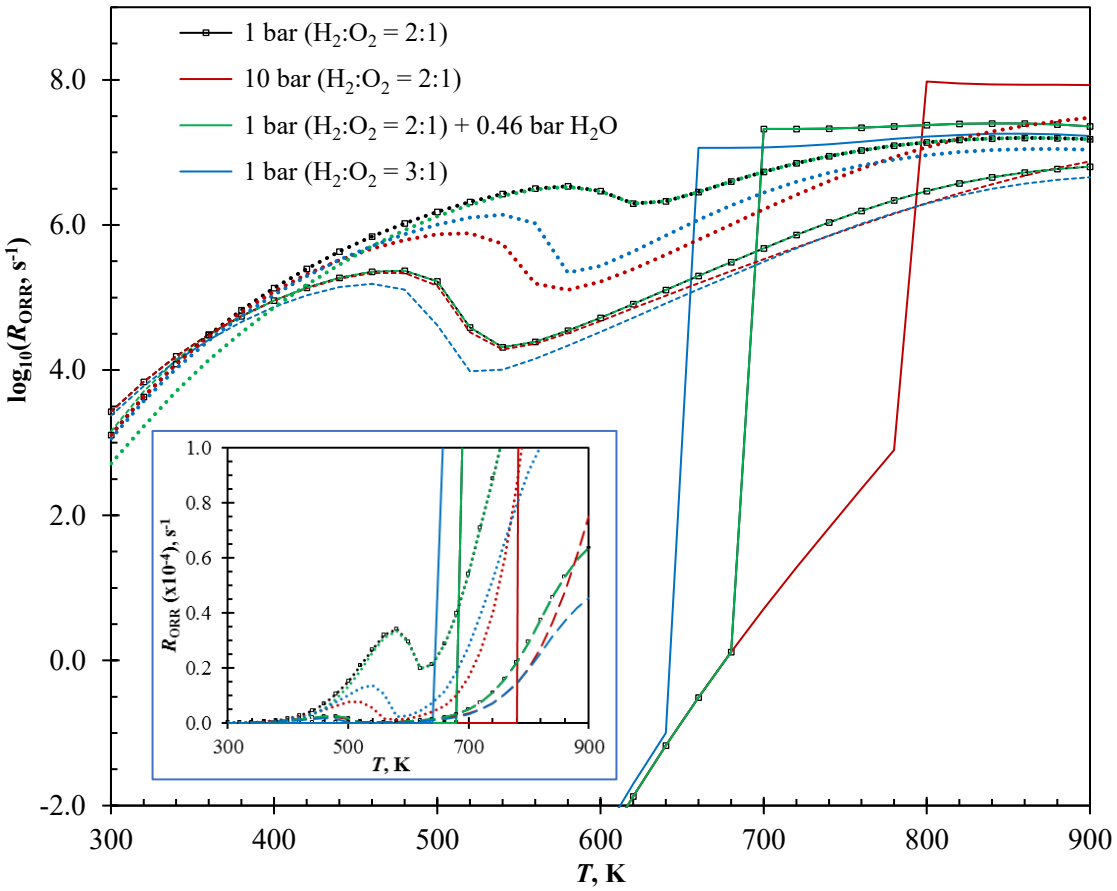

Figure 4.8: Effects of pressure, humidity and feed stoichiometry on evolution rates (R_{ORR}) of H_2O from Pt(100) surface considering a gas/surface interface predicted by SA (—), BWA (− − −) and QCA (·····) microkinetic models at various temperatures. the insert presents the same data however in a linear scale.

4.6 Polarization curves for ORR over Pt(111)/Pt(100) surfaces

The chemical hydrogen electrode (CHE) model can be used to calculate potential dependent adsorption free energy for all H_2 adsorption steps as follows [7],

$$G_{Ads,H_2} = 2G_{H*} - G_{H_2(g)} - 2G_* + e(U_C^0 - U_c) + \mathrm{pH}ln(10) \qquad 4.4$$

where G_i is the Gibbs free energy of species i (adsorbed/free gas). The other parameters are $U_c(U_c^0)$, pH and e which are electrode potential (reference), negative log of proton concentration and elementary charge, respectively. Polarization curves (electrode potential vs. current density plots) were generated based on equation 4.4. This merely shifts the adsorption strength of H* by adjusting the reference ($H^+ + e^-$) state according to equation 4.4 at different electrode potentials. Steady state ORR rates were calculated, from which the current density was modelled as,

$$j_k(U_c) = R_{H_2O}(U_c) \cdot n \cdot F \qquad 4.5$$

for a given steady state H_2O evolution rate, $R_{H_2O}(U_c)$ in mol.cm^{-2}.s^{-1}. n = 2 and F = 96485 A.s.mol^{-1} are number of electrons transferred and Faraday constant, respectively. The polarization curves are constructed at 358 K, 0.33 bar O_2 and 0.67 bar H_2 over extended Pt(111) and Pt(100) surfaces with a site area of 6.82 Å^2 and 7.87 Å^2, respectively. The SA model was shown to predict very low ORR rates at low temperatures. Therefore, only BWA and QCA model predicted polarization curves are presented here.

Experimental measurements of the ORR activity over Pt(111) and Pt(100) single crystalline electrodes under RDE conditions show current densities of 0.59 mA.cm^{-2} and 0.49 mA.cm^{-2} at 0.9 V (vs. reversible hydrogen electrode, RHE) in a 0.1 M $HClO_4$ electrolyte, respectively [23]. Figure 4.9 presents polarization curves in the current density range of 0 – 0.5 mA.cm^{-2}. The BWA predicted overpotentials, at a current density of 0.5 mA.cm^{-2}, are 0.87 V and 0.48 V over Pt(111) and Pt(100) surfaces, respectively. The QCA model predicts even higher overpotentials at this current density for both surfaces (Figure 4.9a, c). Clearly, predictions based on both microkinetic models for both Pt(111) and Pt(100) surfaces deviate from experimental measurements (0.59 mA.cm^{-2} and 0.49 mA.cm^{-2} at 0.9 V vs. SHE [23]). Various factors may be responsible for the deviation between these models and experiments. These factors include, solvation effects, dispersion effects and Eley-Rideal reaction steps. The latter were shown to significantly improve the correspondence between experimental ORR rates and rates predicted by a mean-field microkinetic model [109].

The Pt(111) surface is predominantly covered with H* at low potentials, < 0.1 V, and at high potentials O* is most predominant with the rest of the surface vacant (Figure 4.6b). The OH* coverage in the whole range is << 0.001 ML (Figure 4.6b). Over the Pt(100) surface, a substantial surface fraction of OH* adsorbates is present over the whole potential range (Figure 4.6d). Both in terms of ORR activity and surface coverage, the present models are not in agreement with experimental measurements. This deviation is expected given that the models consider a gas/solid environment (compared to electrolyte/solid in experiments) and the potential treatment in equation 4.4 may not be adequate—much closer predictions would expected if ER reaction steps are also considered [52,109].

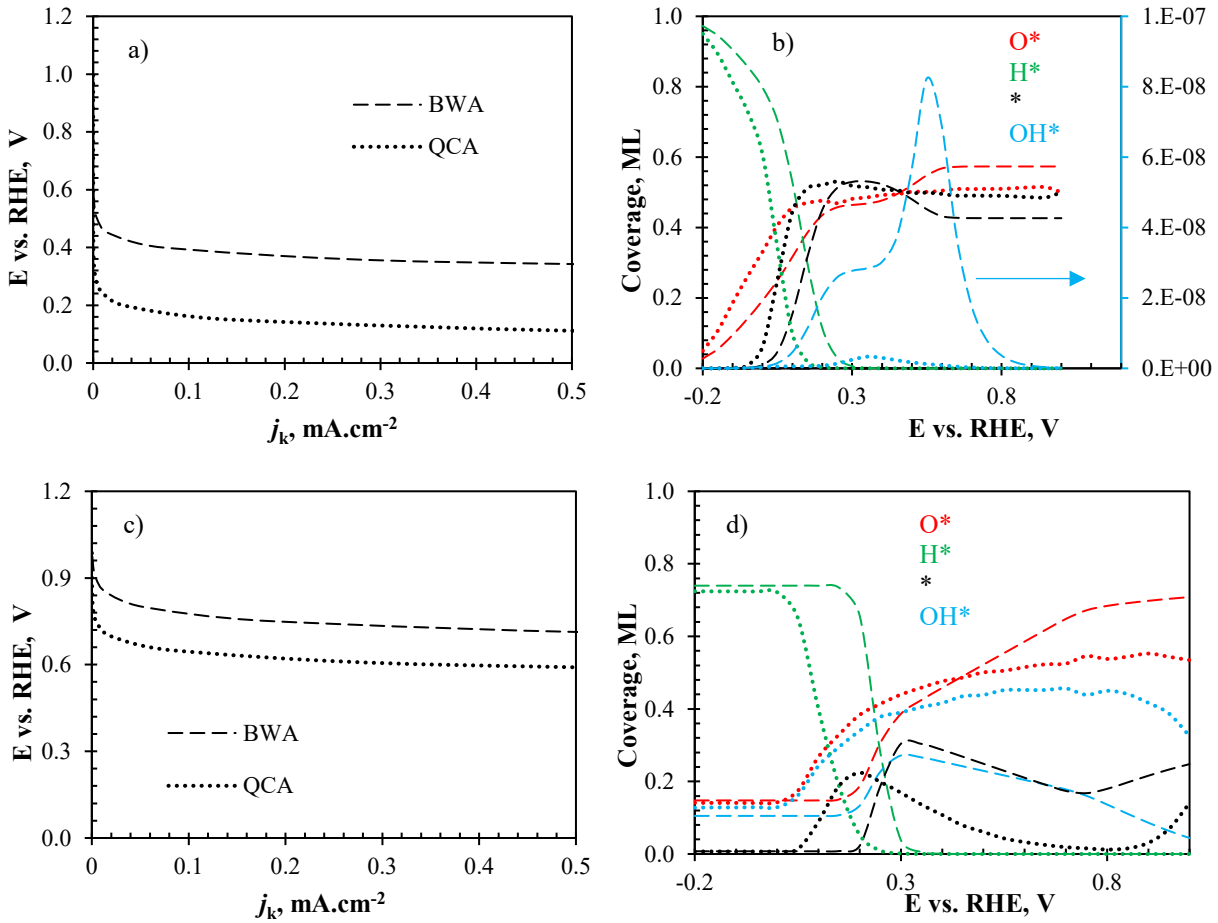

Figure 4.9: Polarization curves for ORR over (a) Pt(111) and (c) Pt(100) surfaces and the coverage at different potentials over (b) Pt(111) and Pt(100) surfaces.

4.7 Conclusions

Various DFT calculations have been conducted to obtain both reaction energetics and lateral interaction parameters for the ORR over Pt(111) and Pt(100) surfaces. Calculated reaction energetics were consistent with previous literature. Considering a gas/solid interface, ORR rates over both Pt(111)—which have been previously described by Fantauzzi *et al.* [53] however, without explicit consideration of coverage effects—and Pt(100) surfaces were modelled using different microkinetic models, i.e. SA, BWA, QCA and kMC. The majority of available microkinetic studies in the literature only consider Pt(111) surfaces.

Interesting information regarding the effects of coverage, temperature, pressure and the presence of water in the bulk phase has been reported. The rates increased with temperature as expected and there was a change in the rate determining step with increasing temperature—the reaction pathway changes with temperature for the Pt(111) surface and for the Pt(100) surface a change was only predicted by the BWA model. On Pt(111) surfaces the ORR follows a peroxyl pathway at low temperatures and a dissociative pathway at high temperatures. On the other hand, the ORR pathway on Pt(100) follows a

dissociative pathway with OH* removal occurring via the OH*-OH* coupling reaction instead of direct OH* hydrogenation. The Pt(100) surface is predicted to have higher ORR activities compared to the Pt(111) surface—this may be caused by an inhibitive barrier for O* hydrogenation on Pt(111) and a trace coverage of H_2O* on this surface—the latter limits the alternative O* hydrolysis pathway. The OH*-OH* coupling pathway over the Pt(100) surface is responsible for H_2O* formation. As a result, facile mobility of OH* on Pt(100) is required; based on the predicted ORR pathway on Pt(100), the activation energy of the rate determining step at low temperature is only 0.016 eV lower than the diffusion barrier of OH* on this surface. Therefore, the predicted ORR rates on this surface are not significantly affected by slow OH* mobility at low temperatures. The peculiar behaviour in the ORR rate vs. temperature profile on Pt(100) was explained based on the surface coverage and degree of rate control profiles. Moreover, this behaviour was seen to be quite sensitive to the adsorption strength of H* on Pt(100) and coverage of Pt(100) with H* intermediiates.

According to kMC simulations the Pt(111) and Pt(100) surfaces are predominately covered with H* adsorbates even at high temperatures. This high coverage explains the predicted high ORR rates on Pt(111) surfaces at 400 K, 600 K and 800 K, as well as the good agreement between kMC and BWA ORR rates on Pt(100) surfaces at 600 K and 800 K. At 400 K all Pt(100) bridge sites are occupied by H* intermediates leading to extremely low ORR rates compared to BWA and QCA models.

Chapter 5 will consider possible cooperation between adjacent Pt{111} and Pt{100} facets—this is possible to study with the present system although the predicted activity order seems to contradict experimental observations under electrochemical conditions. This simple case is still instrumental, in a sense that it will also provide useful information regarding the effective exchange rates of ORR intermediates between adjacent surfaces—something still lacking in available ORR models.

In conclusion, the Pt(100) surface is more ORR active than Pt(111) under gaseous conditions. The ORR over the Pt(100) surface proceeds via an OH*-OH* coupling pathway and OH* removal does not limit the ORR activity at temperatures below 900 K. The ORR rate limiting processes are the same on both Pt(111) and Pt(100) surfaces and they are also temperature dependent, i.e. O* removal (O* hydrogenation) at low temperatures and O_2* dissociation at high temperatures.

CHAPTER 5:ORR Activity over Multifaceted Pt NW Surfaces

5.1 Introduction

The ORR activity is structure sensitive—over single-crystal Pt facets it increases in the order Pt(100) < Pt(110) ≈ Pt(111) under a 0.1 M $HClO_4$ electrolyte [10,20,23]. Furthermore, on high-index planes composed of *n* atomic rows along {111} terraces with periodic single atom steps of either (111) or (100) type, the ORR activity increases with decreasing *n*, for $n > 2$ [24]. High-index Pt surfaces with *n* atomic rows along {100} terraces and atomic steps of type (111) or (110) possess terrace size independent ORR activities [24]. The improvement in the ORR activity as a function of terrace size is argued to be due to the weakening in the adsorption strength of reaction intermediates compared to extended Pt(111) surfaces [32,144].

Komanicky *et al.* [35] prepared nano-faceted single crystalline Pt surfaces with alternating Pt{111} and Pt{100} terraces. The ORR activity measured from these nano-faceted surfaces was found to be higher than a simple linear combination of activities from constituent Pt(111) and Pt(100) surfaces [34]. This was also true over shape selected cuboctahedral NP arrays [36]. Based on these results, it was then postulated that a cooperative behaviour must exist between adjacent terraces (see Figure 5.1). Oxygen is thought to adsorb on a {100} terrace before diffusing to a {111} terrace where its reduction is more facile [36]. No theoretical study has investigated and corroborated this postulation yet.

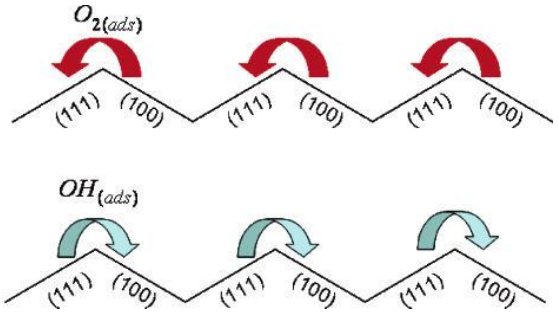

Figure 5.1: Schematic illustration of cooperative mechanism of ORR on (111)-(100) nanofaceted Pt surfaces, as proposed by Komanicky *et al.* [34,36].

Recently, a proposal was made regarding the role of the step in high-index surfaces on the ORR activity—according to the study, O_2* at edge-bridge sites dissociates forming two O* intermediates—

due to lateral interactions one O* atom diffuses to the step bottom where it is weakly bound and hence provides a much more facile pathway for O* removal as OH* [145]. The mobility of O* over Pt edge sites has been investigated using DFT calculations. Whilst high diffusion barriers are reported at low coverages [124,125,146], it was shown that lateral interactions do flatten the PES enabling faster diffusion [146]. O_2*, O* and OH* were found to have high energy barriers for diffusion away from edge sites. When coverage effects are considered, this might change; since repulsive lateral interactions can weaken the stability O* and O_2* at edge sites resulting in the flattening of the diffusion PES (see Figure 3.11).

Despite multiple indications of cooperative behaviour in multi-faceted Pt surfaces [24,32,34,36,147], existing models which aim to predict the overall ORR activity over multi-faceted Pt NPs all assume independent facets [15,16,25,29,37]—calculating the overall ORR activity as a linear combination of ORR activities of extended terraces and isolated step-edge sites. This Chapter ambitiously sets to investigate the overall ORR activity from multi-faceted Pt surfaces at the gas/solid interface without any *a priori* assumptions related to cooperative behaviour of adjacent facets.

5.2 Methods and Surface Models

5.2.1 Quantum Chemical Calculations

The Pt{111} and Pt{100} terraces of a multi-faceted Pt surface are modelled as Pt(111)-*p*(3x3) and Pt(100)-*p*(3x3) slab surfaces, respectively. Reaction energetics data over these surfaces have been generated in Chapter 4; and Chapter 3 discussed the reactivity and mobility of ORR intermediates on these model surfaces. The third surface type in the considered multi-faceted Pt surface model are edge sites formed at the intersection of two facets, Pt{111} and Pt{100}. The latter edge sites are of type (111)x(100) and are present in cuboctahedral and truncated octahedral NP models as well as in hexagonal NW model. This study considered a rhombic Pt[5(111)x5(100)] NW model to represent this surface type, i.e. (111)x(100) edge; the adsorption and mobility of ORR intermediates over this surface was investigated in Chapter 3—this Chapter will consider the obtained energetics there. The ORR can also occur at the interface between two surface types, e.g. hydrogenation of O* on edge sites by H* on terrace sites.

In this Chapter the dissociative ORR mechanism involving edge – Pt{111} and edge – Pt{100} sites is discussed. The energetics are calculated using DFT with a Pt[5(111)x5(100)] NW model from Chapter 2. The computational setup used is covered in Subsection 2.2.2 as well as in Section 3.2. The data on ORR intermediate mobility and ORR reaction energetics on terrace and at terrace-edge boundary is used to generate ORR microkinetic models.

To ensure that the overall thermodynamics are consistent, near-edge and NW terrace site adsorption properties toward all ORR intermediates were equated to extended *p*(3x3) surfaces; such that, for Pt{*hkl*} → edge diffusion of intermediate i, the barrier is calculated as:

$$E_{act,i}[Pt\{hkl\} \rightarrow edge] = E_{act,i}[edge \rightarrow Pt\{hkl\}] - \left(E_{ads-Pt(hkl),i} - E_{ads-edge,i}\right) \qquad 5.1$$

where $E_{ads-Pt(hkl),i}$ is taken to be the adsorption energy of species i over the most stable adsorption site on a Pt(*hkl*)-*p*(3x3) slab surface. $E_{ads-edge,i}$ is the adsorption energy of species i over the most stable edge sites on a Pt[5(111)x5(100)] NW model. The near-edge reaction energetics were also corrected accordingly. This guarantees direct comparison between extended Pt(*hkl*) and Pt{*hkl*} performance.

5.2.2 Adsorbate Interactions

The OOH* intermediate was not considered over edge and near-edge sites because of its very low dissociation barriers on terrace sites—therefore, lateral interaction models only considered O_2*, O*, H*, OH* and H_2O*. Moreover, a crude assumption was made—edge bound intermediates were only considered to interact with edge bound intermediates and near-edge species interact exclusively with other terrace species on the relevant terrace. The implication of the latter is an underestimation of O_X*(terrace)-$O_{X'}$*(edge) interaction. Whilst this cannot be thoroughly justified, the extra relaxation room available for edge adsorbed intermediates, i.e. terrace species only have 180° of space vs. ca. 240° room over the edge, suggests that repulsive interactions will be minimised for terrace-edge vs. terrace-terrace clusters. Moreover, edge-edge interactions are likely to be more significant—consequently incorporating them should give a closer estimation of the real system compared to no interactions at all.

Figure 5.2 shows the interaction cluster between adsorbates which bind on edge-bridge sites, in this case O* is shown interacting with H* intermediates. Figure 5.2 further displays the number of neighbours in the 1st and 2nd shells and corresponding interaction energies—terrace-edge interactions are omitted. DFT calculations were used to generate interaction energies for these cluster (see Table 5.1). To minimize self-interaction between periodic images, a Pt NW model with 4 Pt atoms along the axial direction of each periodic image was used (see Figure 5.2). It is not difficult to imagine that the difference between model sizes used to generate reaction energetics vs. interaction energies have little impact—the largest effect on the activation barriers would be equivalent to 2nd shell interactions at most (see Table 5.1). The 2nd shell interactions were halved since a centrally adsorbed species interacts with both the co-adsorbed species and its periodic image (see Figure 5.2)—the halving

deals with double counting. Since terrace-edge interactions are excluded, the probability of finding an (i-edge)(j-terrace) pair was estimated as $P_{ij} = \theta_{i,edge}\theta_{j,terrace}$ and was applied in the QCA model.

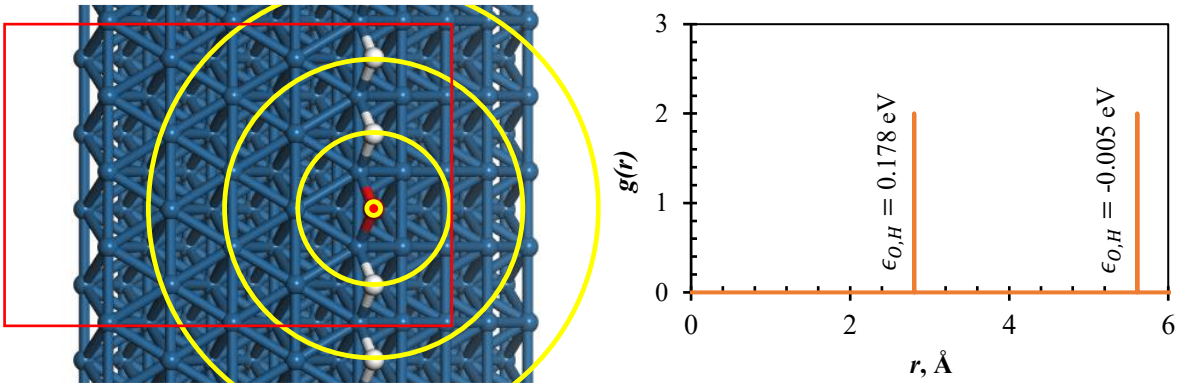

Figure 5.2: Edge-edge interaction pairs on a Pt NW model. Also shown along side this figure is a radial pair-distribution function for an edge - edge interaction between O*-H* pairs.

The co-adsorption geometry and energy of ORR intermediate on edge-bridge sites compares well with equivalent co-adsorption on the Pt(100)-p(3x3). The most repulsive lateral interactions are between O_2*-O_2*, O_2*-O*, O_2*-OH* and O*-O* (see Tables 2.2 and 5.1). Lateral interactions between H*-H* are weakly repulsive and comparable with interactions on Pt(111) and Pt(100) surfaces (see Tables 2.1, 2.2 and 5.1). Therefore, the edge sites will likely be predominantly covered with H* adsorbates when lateral interactions are incorporated, similar to the Pt(111) and Pt(100) surfaces. Figure 3.11 presents an illustration of how lateral interactions between edge adsorbates influence the adsorption strength.

Table 5.1: First and second energy interaction shells for ORR intermediates over Pt NW edge.

1st shell	O_2*	O*	H*	OH*	H_2O*
O_2*	1.060	0.563	0.230	0.503	-0.028
O*	-	0.455	0.178	0.345	0.006
H*	-	-	0.017	0.124	-0.006
OH*	-	-	-	0.364	0.073
H_2O*	-	-	-	-	-0.203
2nd shell	O_2*	O*	H*	OH*	H_2O*
O_2*	0.066	0.054	0.062	0.054	0.000
O*	-	0.040	-0.005	-0.006	0.000
H*	-	-	0.015	0.000	0.000
OH*	-	-	-	0.043	0.000
H_2O*	-	-	-	-	0.084

5.2.3 Microkinetic models for multi-faceted surface

The description of microkinetic processes over a multi-faceted surface within kMC is rather straightforward. This is possible due to spatial resolution of where events occur and which events can

occur where [107,148–150]. On the other hand, microkinetic analyses over multi-faceted surfaces using SA, BWA and QCA models are not as trivial. For Fischer-Tropsch synthesis, van Helden *et al.* [151] constructed a mean-field microkinetic model over a multi-faceted Co NP model. They coupled the balance ODEs together with a site constraint to normalising surface coverages.

$$\sum_{s}\sum_{i}\theta_{i,s} = 1 \qquad 5.2$$

This constraint may however lead to underestimation of rates of bimolecular reactions. As it is, 5.2 will lead to a coverage of species i on surface type A of $\theta_{i,A} = \theta^{*}_{i,A}\chi_{A}$, where χ_{A} is the number of active sites on surface type A relative to the total number of active sites on a model NP and $\theta^{*}_{i,A}$ is the reference coverage at the centre of surface type A. Given a sufficiently wide surface type A, the bimolecular reaction will be described as $r = k\theta^{*}_{x,A}\theta^{*}_{y,A}$ with the overall rate given by $r\chi_{A}$; the latter deviates by a factor of χ_{A} from a system based on constraint 5.2, $r = k\theta^{*}_{x,A}\theta^{*}_{y,A}\chi^{2}_{A}$. This study considers the following site balance constraints,

$$\sum_{j}\theta_{j,Pt\{111\}} = 1, \quad \sum_{j}\theta_{j,Pt\{100\}} = 1, \quad \sum_{j}\theta_{j,edge} = 1 \qquad 5.3$$

and solves the system of couple ODEs as illustrated in Figure 5.3—with different surface types connected via diffusion and reactions at boundary interface. To avoid potential problems with surface type coupling, the whole process is modulated by adjusting the processes at the boundary interface by a χ_{edge}. Therefore, it is assumed that the difference in the number of Pt{111} and Pt{100} surface sites is minimal—since the latter is at most within the same order of magnitude, this assumption is quite reasonable. A > 2 order of magnitude separation between TOF over the two surfaces should be well represented. The modulation, i.e. χ_{edge}, will be adjusted between three values, 1.0, 0.34 and 0.004.

5.2.4 Microkinetic Simulations

Assumptions

The key assumptions in the present Chapter are as follows.

- The sticking probability is unity over all surface types
- X*(terrace) – Y*(edge) lateral interactions equal to zero
- Distribution of Pt{111} and Pt{100} terrace equal
- BEP factors (equation 2.44) for all diffusion and edge boundary reactions equal to 0.5

- OH*-OH* interactions at the edge sites are only repulsive as only bridge adsorption states are considered. This limits the formation of hydrogen-bond networks between OH* adsorbates. However, the H_2O* interaction energies could favour such hydrogen-bond networks. Given the high exothermicity of OH* adsorption over $b^{(e)}$ sites compared to $t^{(e)}$, unless all edge-top sites are covered with OH* adsorbates forming a continuous hydrogen-bonded chain (network), the $b^{(e)}$ states are more stable.
- Intra-facet mobility of ORR intermediates is assumed to be sufficiently fast.

These assumptions are not anticipated to significantly influence the overall conclusions herein.

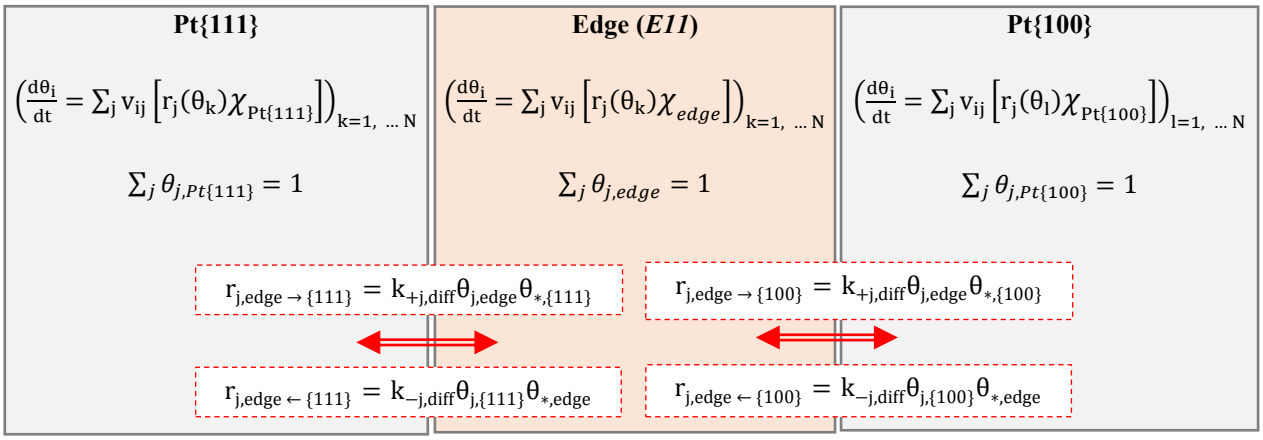

Figure 5.3: Overall set of ODEs involved in a multifaceted surface model.

Simulation approach

The steady state solution to the balance equations in Figure 5.3 was obtained by solving coupled ODEs using the SciPy ODE package in Python 3.7, specifically the LSODA ODE solver [137] which automatically switches between the implicit Adams method and the stiff backward differential formula (BDF) method [138]. Given the long list of reaction steps and intermediates, integration seemed to be the most practical approach as opposed to solving a system of nonlinear equations. The integration time was adjusted to achieve steady state coverage and rates of individual species and reaction steps, respectively. Furthermore, the absolute and relative tolerances were set to 10^{-14} and 10^{-13}, respectively. The latter settings were necessary to get converged solutions, especially from the BWA and QCA simulations.

Simulation conditions

Similar to Chapter 4, a stoichiometric gas composition (0.33 bar O_2 and 0.67 bar H_2 no water) at 1 bar total pressure is considered. Partial pressures are kept constant during integration and the steady state

solution (surface coverages) is used to compute steady state kinetic rates. A temperature range of 300 K to 900 K was considered for SA, BWA and QCA simulations.

Analyses

This Chapter considers three types of analyses, viz. ORR activity, ORR pathway and degree of rate control (DRC), similar to considerations in Chapter 4. The activity comparison is done by comparing intrinsic kinetic rate from each facet to the ones predicted in Chapter 4 for the same surface type under the same simulation conditions. The DRC analysis considered either H_2O* desorption from Pt{111} or Pt{100} as a key reaction step. This makes sense considering the difference in ORR rates of the Pt(111) and Pt(100) surfaces. Looking at a combined effect would mask interesting features of the less active surface type. Overall control will however be based on relative distribution of the site types and their respective activities. It should be noted that a linear combination of rates from Pt{111} and Pt{100} facets in coupled multi-faceted systems is different to current reported studies. The intrinsic ORR rates predicted from coupled multi-faceted surfaces already incorporate inter-facet dependency.

5.3 ORR energetics over Pt NW edge sites

In addition to facilitating inter-facet exchange of ORR intermediates, edge sites can be directly involved in the ORR catalysis. It has already been noted that O_2* diffusion from $b^{(e)}$ sites towards $b^{(0e)}$/$b^{(00e)}$ sites results in a dissociated state of two O* atoms each adsorbed over a $b^{(0e)}$ site (Chapter 3)—the oxygen-oxygen bond dissociation is an important step in the ORR mechanism—its dissociation barrier over the edge towards the {100} facet was calculated to be 0.642 eV. This section presents calculated ORR energetics over edge and near-edge sites. These energies are calculated using DFT and the same Pt NW model, as in Chapter 3, with two Pt atoms along the NW axis in the periodic unit cell.

5.3.1 O_2* dissociation

Four unique O_2* dissociation paths over edge sites were investigated, viz. $O_2^{b(e)} \rightarrow 2O^{b(e)}$, $O_2^{b(e)} \rightarrow 2O^{b(0e)}$, $O_2^{b(e)} \rightarrow O^{b(e)} + O^{b(0e)}$ and $O_2^{b(e)} \rightarrow O^{b(e)} + O^{f(1e)}$. Table 5.3 illustrates the different dissociation processes (Figure E8.1 presents corresponding PES diagrams) and the associated reaction energetics are summarized in Table 5.2 (for all ORR processes at edge region). Transition states for $O_2^{b(e)} \rightarrow 2O^{b(0e)}$ and $O_2^{b(e)} \rightarrow O^{b(e)} + O^{f(1e)}$ were located, optimised and verified (based on vibrational analyses). Whilst a maximum was located for the $O_2^{b(e)} \rightarrow 2O^{b(e)}$ step, its vibrational analysis produced two imaginary modes. The latter is not surprising given that the located transition state consists of two O* atoms each over a $t^{(e)}$ site. The largest of the two imaginary modes is parallel to the reaction coordinate whilst the other points in a perpendicular direction (similar to the transition state for O* diffusion

between $b^{(e)}$ and $b^{(0e)}$ sites). A transition state could not be located for the $O_2^{b(e)} \rightarrow O^{b(e)} + O^{b(0e)}$ step; given the low diffusion barrier for $O^{b(0e)} \rightarrow O^{b(e)}$ (see Figure 3.4b), the final state of the latter O_2* dissociation step can be obtained from the $O_2^{b(e)} \rightarrow 2O^{b(0e)}$ step followed by O* diffusion to a vacant $b^{(e)}$ site. The lowest dissociation barrier for O_2* over edge sites was calculated to be 0.642 eV for the $O_2^{b(e)} \rightarrow 2O^{b(0e)}$ step (cf. 0.407 eV and 0.143 eV over Pt(111) and Pt(100) slabs, respectively). Other barriers were much higher, up to 1.2 eV for $O_2^{b(e)} \rightarrow 2O^{b(e)}$ (see Table 5.2). Several studies have investigated O_2 dissociation over edge sites of Pt(211) [152], Pt(321) kinked surface [153], *n*(111)x(111) high-index surfaces where *n* = 2, 3 and 4 [145], and model NPs [94,154]. The calculated activation energies vary significantly depending on the dissociation process and local environment to the edge. Over Pt(211) and Pt(321) the reported dissociation barriers are between 0.5 and 1.0 eV [152,153], over *n*(111)x(111) barriers vary between 0.09 eV and 0.16 eV [145] and over small NP models 0.38 eV and 0.69 eV [94,154]. The present study finds dissociation barriers consistent with Pt(211) surface and NP models surface despite the obvious differences in edge site environment.

Table 5.2: Calculated reaction ($\boldsymbol{\Delta_{rxn}E}$) and activation ($\boldsymbol{E_a}$) energies for ORR steps over edge and near-edge sites of a Pt[5(111)x5(100)] NW model; all energy values are reported in eV.

A) O_2 dissociation			**B) O hydrogenation**		
Reaction	$\Delta_{rxn}E$	E_a	**Reaction**	$\Delta_{rxn}E$	E_a
$O_2^{b(e)} \rightarrow 2O^{b(e)}$	-0.720	1.189	$O^{b(00e)} + H^{b(e)} \rightarrow OH^{b(00e)}$	-0.278	0.567
$O_2^{b(e)} \rightarrow 2O^{b(0e)}$	-0.868	0.642	$O^{b(e)} + H^{b(00e)} \rightarrow OH^{b(e)}$	-0.269	0.819
$O_2^{b(e)} \rightarrow O^{b(e)} + O^{f(1e)}$	-0.852	1.123	$O^{b(e)} + H^{t(1e)} \rightarrow OH^{b(e)}$	-0.465	0.604
			$O^{f(1e)} + H^{b(e)} \rightarrow OH^{b(1e)}$	0.108	1.135
C) OH hydrogenation			**D) OH coupling**		
Reaction	$\Delta_{rxn}E$	E_a	**Reaction**	$\Delta_{rxn}E$	E_a
$OH^{t(e)} + H^{t(0e)} \rightarrow H_2O^{t(e)}$	-0.355	0.916	$OH^{b(e)} + OH^{b(00e)} \rightarrow H_2O^{t(e)} + O^{b(00e)}$	0.463	0.486
$OH^{t(0e)} + H^{t(e)} \rightarrow H_2O^{t(0e)}$	-0.501	0.280	$OH^{b(e)} + OH^{b(00e)} \rightarrow H_2O^{t(0e)} + O^{b(e)}$	0.236	0.349
$OH^{b(e)} + H^{t(1e)} \rightarrow H_2O^{t(e)}$	0.132	0.886	$OH^{b(e)} + OH^{t(1e)} \rightarrow OH^{t(e)} + OH^{b(1e)}$	0.280	0.433
$OH^{t(1e)} + H^{b(e)} \rightarrow H_2O^{t(1e)}$	-0.358	0.565	$OH^{t(e)} + OH^{b(1e)} \rightarrow H_2O^{t(e)} + O^{f(1e)}$	-0.073	0.109
			$OH^{b(e)} + OH^{t(1e)} \rightarrow H_2O^{t(1e)} + O^{b(e)}$	-0.097	0.041
E) H transfer between edge/near-edge O/OH					
Reaction	$\Delta_{rxn}E$	E_a	**Reaction**	$\Delta_{rxn}E$	E_a
$OH^{b(1e)} + O^{b(e)} \rightarrow O^{f(1e)} + OH^{b(e)}$	-0.184	0.438	$OH^{b(e)} + O^{b(00e)} \rightarrow O^{b(e)} + OH^{b(00e)}$	-0.118	0.087

Table 5.3: Illustration of O_2 dissociation over edge and near-edge sites of a Pt[5(111)x5(100)] NW model.

	Rxn.	IS	TS	FS
(a)	$O_2^{b(e)} \rightarrow 2O^{b(e)}$	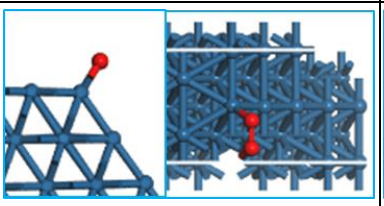	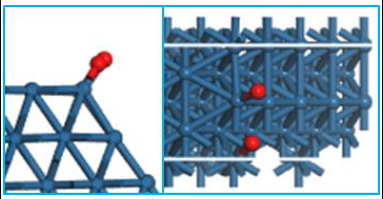	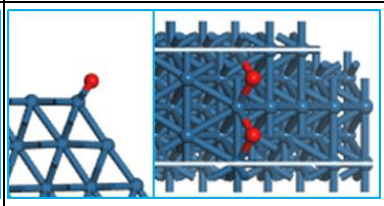
(b)	$O_2^{b(e)} \rightarrow 2O^{b(0e)}$	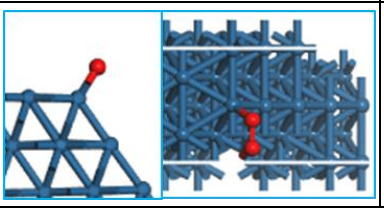	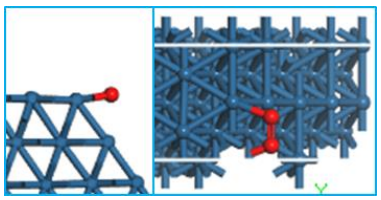	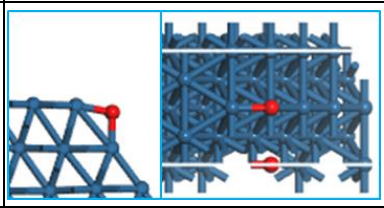
(c)	$O_2^{b(e)} \rightarrow O^{b(e)} + O^{f(1e)}$	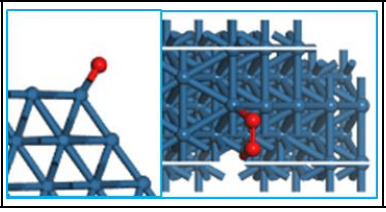	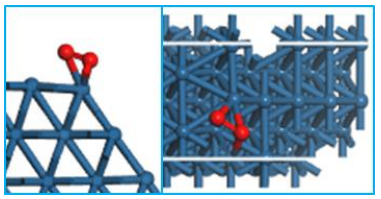	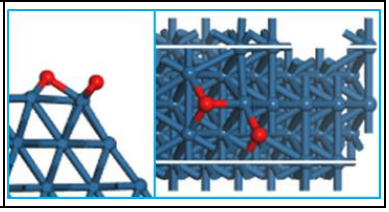

5.3.2 O* hydrogenation

Atomic oxygen adsorbed over edge and near-edge sites can be hydrogenated by neighbouring H* adsorbates forming either edge or near-edge OH* intermediates. Four O* hydrogenation reaction steps at edge and near-edge sites were probed. O* on edge sites can be hydrogenated by H* adsorbed on either $t^{(1e)}/b^{(1e)}/f^{(1e)}$ site on the Pt{111} facet or $b^{(00e)}/t^{(0e)}$ site on the Pt{100} facet. On near-edge sites, O* on $f^{(1e)}$ or $b^{(00e)}$ can be hydrogenated by H* on $b^{(e)}/t^{(e)}$ sites; resulting in a vacant edge site with the OH* occupying a near-edge terrace site, i.e. $b^{(1e)}$ or $b^{(00e)}$. Figure E8.2 and Table 5.4 presents PES and illustrations of these reaction steps, respectively. O* hydrogenation barriers, at edge and near-edge sites, range from 0.567 eV to 1.135 eV. Compared to O* hydrogenation over a Pt(111) slab surface, the (near-)edge barrier (forming OH on $b^{(e)}$ from O* on $b^{(e)}$ plus H* on $t^{(1e)}$) is 0.365 eV lower. On the other hand, O* hydrogenation over edge sites in reactions involving H* from $b^{(00e)}$ sites has a barrier of 0.819 eV (cf. to 0.538 eV over Pt(100) slab surfaces)—moreover, for O* hydrogenation at near edge sites, i.e. O* over $b^{(00e)}$ plus H* over $b^{(e)}$, the reaction barrier is 0.567 eV comparable to the same reaction over extended Pt(100) surface (see Table 5.2 and Table 4.3 Chapter 4). Considering that O* adsorption on $b^{(e)}$ sites is ca. 0.3 eV stronger than over extended Pt(100) $b^{(0)}$ sites, it becomes clear that O* hydrogenation at edge sites is equivalent to the same process over Pt(100) surface and the difference is only due to strong adsorption of O* on $b^{(e)}$ sites.

Table 5.4: Illustration of O hydrogenation over edge and near-edge sites of a Pt[5(111)x5(100)] NW model.

	Rxn.	IS	TS	FS
(a)	$O^{b(00e)} + H^{b(e)} \rightarrow OH^{b(00e)}$	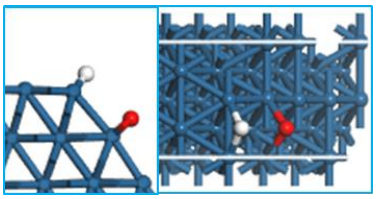	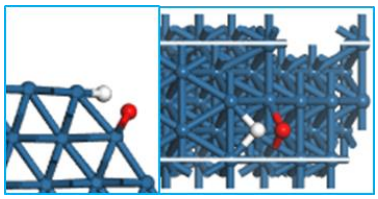	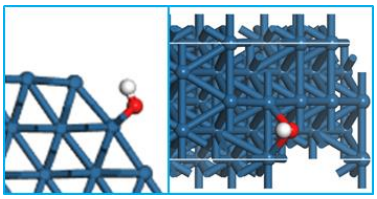
(b)	$O^{b(e)} + H^{t(1e)} \rightarrow OH^{b(e)}$	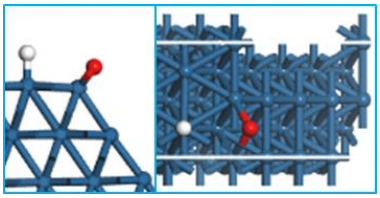	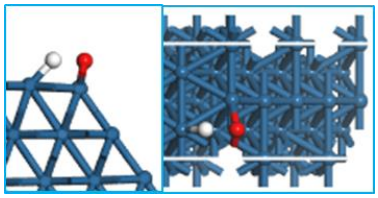	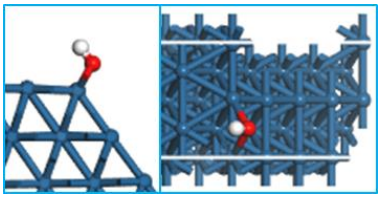
(c)	$O^{b(e)} + H^{b(00e)} \rightarrow OH^{b(e)}$	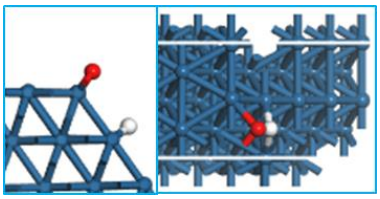	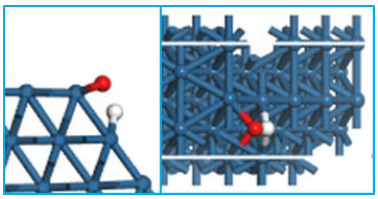	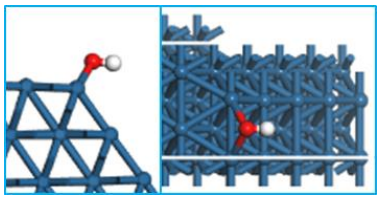
(d)	$O^{f(1e)} + H^{b(e)} \rightarrow OH^{b(1e)}$	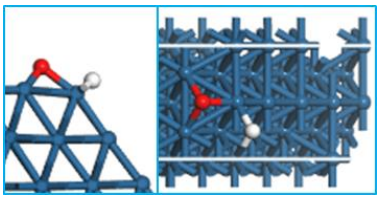	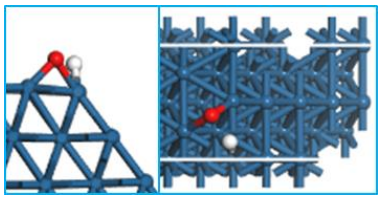	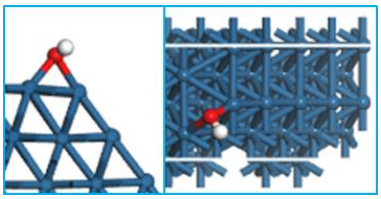

5.3.3 OH* hydrogenation

Over a Pt(111) surface, OH* hydrogenation follows the path $OH^{t(1)} + H^{t(1)} \rightarrow H_2O^{t(1)}$ with an activation energy of 0.176 eV. Over a Pt(100) surface the activation energy for OH* hydrogenation is much higher at 0.886 eV, for the $OH^{b(0)} + H^{b(0)} \rightarrow H_2O^{t(0)}$ path. Hydrogenation of OH at edge and near-edge sites on the Pt{111} facet side was probed for the following steps, $OH^{b(e)} + H^{t(1e)} \rightarrow H_2O^{t(e)}$ and $OH^{t(1e)} + H^{b(e)} \rightarrow H_2O^{t(1e)}$ (see Table 5.5)—the corresponding activation energies were 0.886 eV and 0.565 eV, respectively (see Table 5.2). OH* hydrogenation steps involving edge and Pt{100} bound intermediates proceed via $OH^{t(e)} + H^{t(0e)} \rightarrow H_2O^{t(e)}$ or $OH^{t(0e)} + H^{t(e)} \rightarrow H_2O^{t(0e)}$ with respective activation energies of 0.91 eV and 0.280 eV (see Figure E8.3 and Table 5.2). For initial states with OH*/H* on bridge sites reasonable transition states could not be located—this is not surprising since adsorbates undergo both internal-rotation and diffuse at the same time. For the latter two OH* hydrogenation steps, the overall activation energies will be higher since the initial state will be OH* over $b^{(e)}$ sites not $t^{(e)}/t^{(0e)}$ sites (this can be calculated using data from Chapter 3 and Table 5.2, see reactions 13 and 14 in Table E7.3).

Table 5.5: OH hydrogenation over edge and near-edge sites of a Pt[5(111)x5(100) NW model.

	Rxn.	IS	TS	FS
(a)	$OH^{b(e)} + H^{t(1e)} \rightarrow H_2O^{t(e)}$	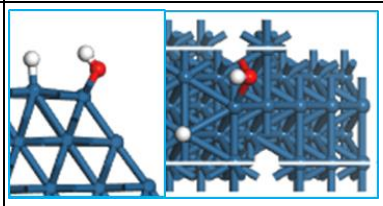	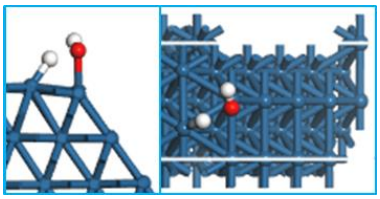	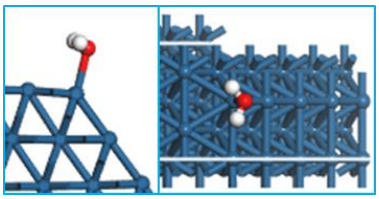
(b)	$OH^{t(1e)} + H^{b(e)} \rightarrow H_2O^{t(1e)}$	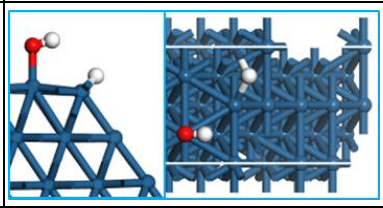	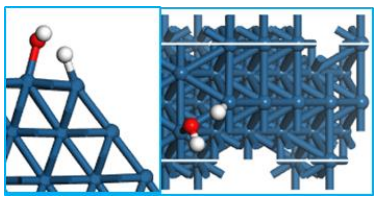	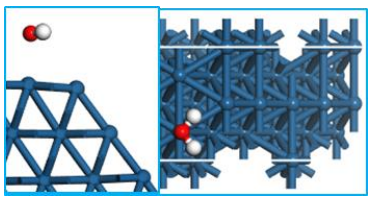
(c)	$OH^{t(e)} + H^{t(0e)} \rightarrow H_2O^{t(e)}$	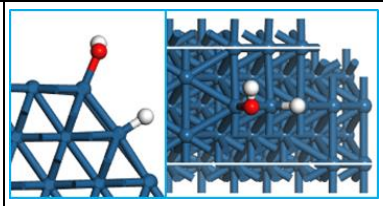	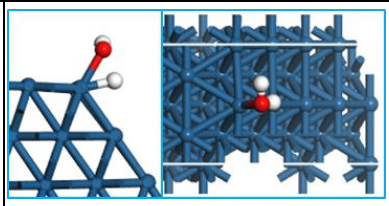	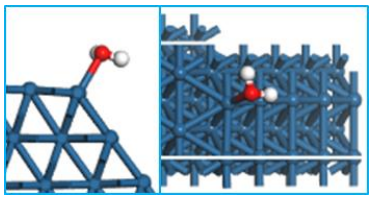
(d)	$OH^{t(0e)} + H^{t(e)} \rightarrow H_2O^{t(0e)}$	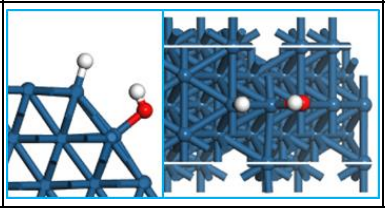	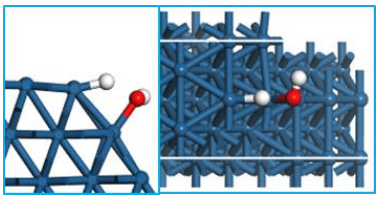	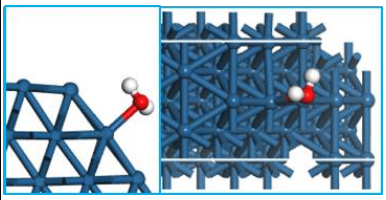

5.3.4 OH* coupling

As was observed for the case of ORR over extended surfaces, over the edge, two co-adsorbed OH* intermediates can couple to form H_2O* and O* intermediates occupying edge and near-edge sites. These reaction steps provided a less activated pathway for OH* or O* reduction over Pt(100) and Pt(111) surfaces, respectively. The present analysis investigates coupling reactions resulting in H_2O* over $t^{(e)}$, $t^{(1e)}$ and $t^{(0e)}$ sites (see Table 5.6). Compared to other edge and near-edge ORR steps, OH*-OH* coupling reactions have much lower activation energies (see Figure E8.4 and Table 5.2). Energetically, these OH*-OH* coupling reaction steps are comparable to equivalent reactions over extended surfaces (see Tables 4.1 and 4.2 in Chapter 4 and Table 5.2).

5.3.5 H—transfer over edge

Noting that OH*-OH* coupling over both Pt(111) and Pt(100) surfaces is a relatively facile reaction pathway for O* and OH* removal, respectively (see in Chapter 4 Table 4.1 and 4.2)—an additional reaction steps involving H- transferred between O* and OH* adsorbed on edge and near-edge sites is considered. These reaction steps provide alternative pathways for oxide hydrogenation and may also be at play in intra-facet pathways, especially under surface diffusion limit. The two key reaction steps

considered are (a) $OH^{b(1e)} + O^{b(e)} \rightarrow O^{f(1e)} + OH^{b(e)}$ and (b) $OH^{b(e)} + O^{b(00e)} \rightarrow O^{b(e)} + OH^{b(00e)}$ (see Table 5.2 and Table 5.7). As expected, these reaction steps have rather low activation energies—especially the H- transfer between edge and Pt{100} sites. This also suggests that over Pt(100) surface H- transfer between OH* and O* will likely be fast in an OH* - O* co-adsorbed cluster, the proton will be shared between the two O atoms in a superposition manner. Figure 3.10 shows that on Pt(100) the exchange of H between a co-adsorbed cluster of OH* and O* also has a very low energy barrier of 0.063 eV.

Table 5.6: Illustration of OH coupling over edge and near-edge sites of a Pt[5(111)x5(100) NW model.

D	Rxn.	IS	TS	FS
(a)	$OH^{b(e)} + OH^{b(00e)} \rightarrow H_2O^{t(e)} + O^{b(00e)}$	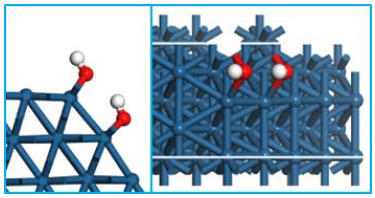	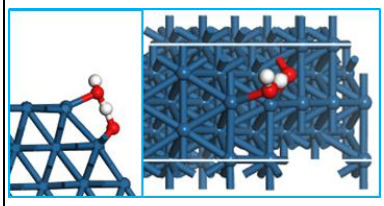	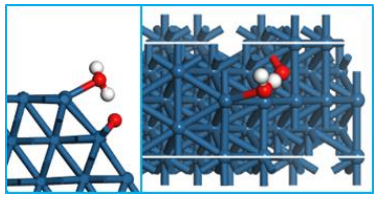
(b)	$OH^{b(e)} + OH^{b(00e)} \rightarrow H_2O^{t(0e)} + O^{b(e)}$	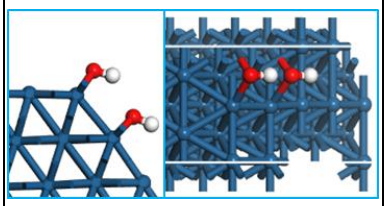	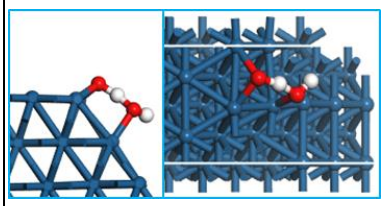	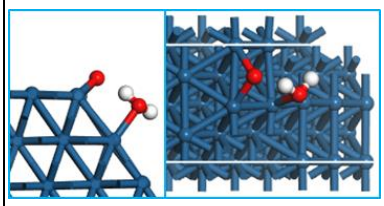
(c)	$OH^{b(e)} + OH^{t(1e)} \rightarrow OH^{b(1e)} + OH^{t(e)}$	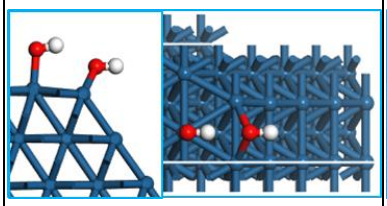	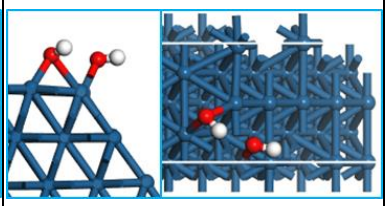	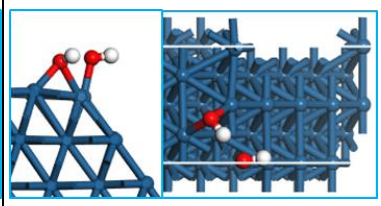
(d)	$OH^{b(e)} + OH^{b(1e)} \rightarrow H_2O^{t(e)} + O^{f(1e)}$	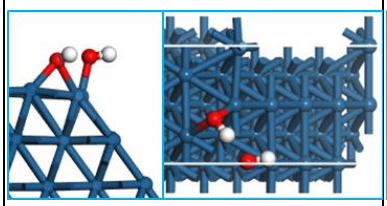	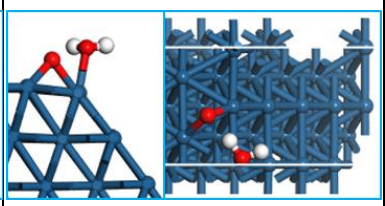	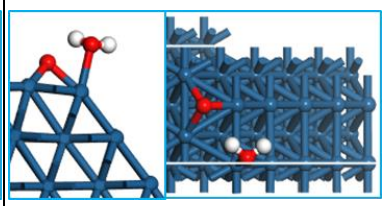
(e)	$OH^{b(e)} + OH^{t(1e)} \rightarrow H_2O^{t(1e)} + O^{b(e)}$	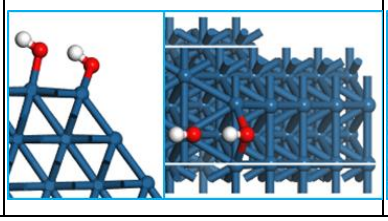	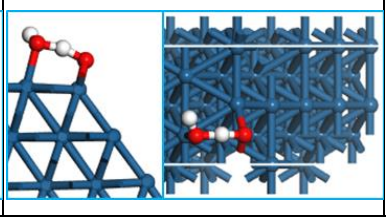	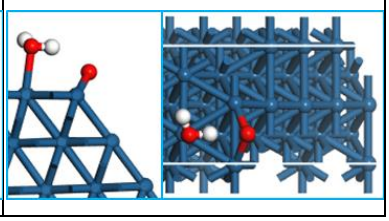

Table 5.7: Illustration of H transfer over edge sites of a Pt[5(111)x5(100)] NW model.

	Rxn.	IS	TS	FS
(a)	$O^{b(e)} + OH^{b(1e)} \rightarrow OH^{b(e)} + O^{b(e)}$	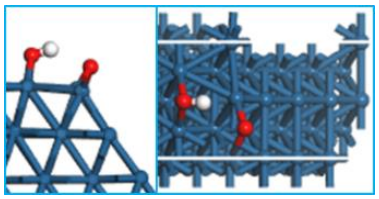	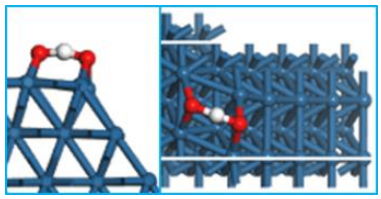	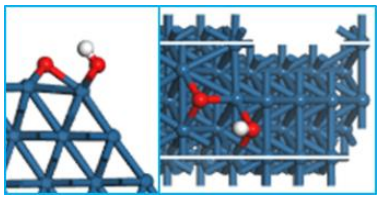
(b)	$HO^{b(e)} + O^{b(00e)} \rightarrow O^{b(e)} + OH^{b(00e)}$	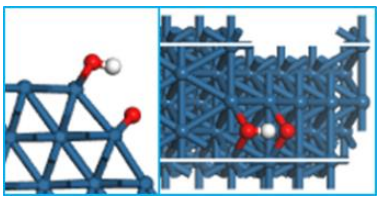	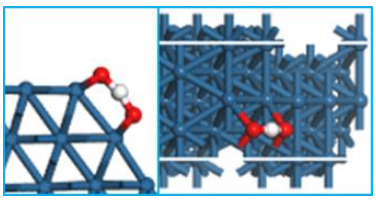	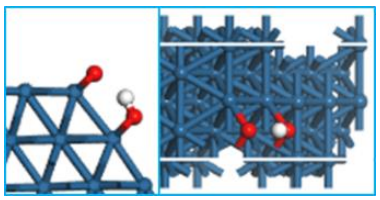

5.4 ORR activity over multifaceted Pt surface

The ORR activity over multifaceted Pt surfaces, consisting alternating Pt{111} and Pt{100} facets, was investigated using different microkinetic models, viz. SA, BWA and QCA. The aim was to investigate the role and effect of inter-facet coupling on the ORR activity and mechanism compared to respective isolated/extended surfaces. Whilst a simplified model consisting of an equal number of Pt{111} and Pt{100} sites was used, the ratio of edge sites to terrace sites was varied, taking three values, 1.00, 0.34 and 0.04. These correspond to three multifaceted Pt surface models, namely $\chi_{edge}(1.00)$, $\chi_{edge}(0.34)$ and $\chi_{edge}(0.04)$; the latter models modulate the coupling of the Pt{111} and Pt{100} facets, giving insight into what happens when fewer edge sites are available to facilitate inter-facet exchange of reaction intermediates. The $\chi_{edge}(1.00)$, $\chi_{edge}(0.34)$ and $\chi_{edge}(0.04)$ models roughly correspond to 4 – 6 nm, ca. 10 nm and > 10 nm cuboctahedral NPs, respectively (see Figure 2.1a). Hexagonal NW models are better approximated by the $\chi_{edge}(0.04)$ model (see Figure 2.1c).

The available data considers the inter-facet exchange of O_2*, O*, H*, OH* and H_2O*, as well as the interfacial ORR steps between edge and terrace sites; O_2* hydrogenation and OOH* dissociation reactions are excluded at this interface. The system energetics were determined in Chapters 3 and 4, and Subsection 5.3. The coverage corrected reaction energetics are summarized in Table E7.3 in Appendix E and the raw model inputs given in Appendix E4. In the next subsections, the intrinsic ORR activity from Pt{111} and Pt{100} terraces is compared with Pt(111) and Pt(100) ORR activities, respectively.

5.4.1 ORR activity over multifaceted surfaces: $\chi_{edge}(1.00)$ model

The $\chi_{edge}(1.00)$ model corresponds to a multifaceted surface with a 1:1:1 distribution of Pt{111}, edge and Pt{100} surface sites, respectively. Within the SA, BWA and QCA models, the surface types are also assumed to be sufficiently large. Figure 5.4 presents a summary of intrinsic ORR rates (H_2O* desorption) from individual surface types (a) and the corresponding surface coverage of major species (b) as predicted by the SA model. The BWA and QCA model predictions under the same conditions are presented in Figures 5.6 and 5.8, respectively.

Coverage independent ORR over a $\chi_{edge}(1.00)$ surface, SA model

The ORR rate from Pt{100} facets is higher than that predicted over extended slab surfaces, i.e. Pt(100), over the whole temperature range studied (see Figure 5.4a). Moreover, this rate is higher than the rate from the Pt{111} facet despite the rate of H_2O* desorption from Pt(111) being higher than Pt(100) rates at a low temperature range. Based on the data presented in Figure 5.4, the intrinsic ORR rates increase in the order Pt(100) << Pt{111} ≈ Pt(111) ≈ edge << Pt{100} at a low temperature range, while at high temperatures the rates increase in the order Pt(111) << Pt{111} < edge << Pt(100) < Pt{100}. Overall, it is clear from this data that the intrinsic ORR rates over multifaceted surfaces are much higher than equivalent slab surfaces.

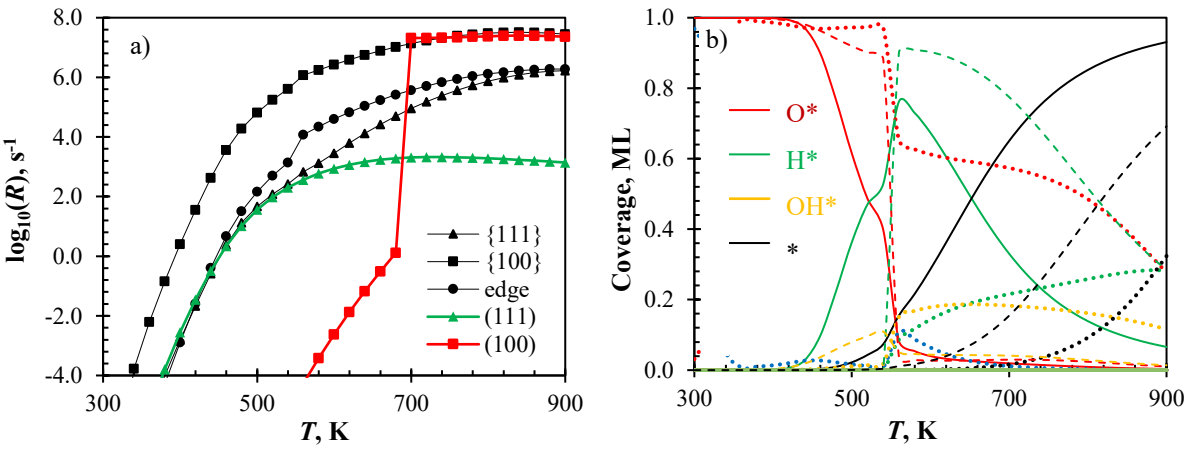

Figure 5.4: SA model predicted ORR activities over a $\chi_{edge}(1.00)$ multifaceted surface model, (a) H_2O evolution rates and (b) surface coverage over {111} facet (—), {100} facet (− − −) and edge sites (·····).

The coverage profiles also give useful insight into what happens when a {111} facet is connected to a Pt{100} facet (see Figure 5.4b). This also explains the observed activity trends shown above. An interesting behaviour observed over Pt(100) was the sharp decrease in the O* coverage from ca. 1 ML to 0.2 ML around 700 K, this was concomitant with a sharp increase in ORR rate (see Figure 4.5 and 4.6); over multifaceted surfaces, this drop in O* coverage shifts to 560 K (see Figure 5.4b).

Unsurprisingly, the surface coverage profiles over the different facets and edge are strongly coupled (shown in Figure 5.4b). Moreover, despite the sharp decrease in O* over Pt{100} sites at ca. 560 K, the intrinsic rate over Pt{100} does not show a similar behaviour, i.e. ignition point, as seen on Pt(100). Due to inter-facet cooperation, the Pt{100} facet is no longer severely poisoned by O* at low temperatures (cf. Pt(100) surface) as a result of inter-facet reactions and intermediate exchange (see Figure 5.4b).

The dominant adsorbates on edge sites at high temperatures are O*, H* and OH*; in contrast, over the Pt{111} and Pt{100} facets H* is the only dominant adsorbate. Further analysis of the reaction pathway shows the nature of this facet inter-dependency (see Figure 5.5). Figure 5.5 presents the reaction pathway analyses for ORR from Pt{111} facet (a) and Pt{100} facet—obtained from dividing all steady state rates by the H_2O evolution rate from Pt{111} and Pt{100} facets, respectively (the sign indicates direction of the reaction as written on each figure, positive = forward). At low temperatures, i.e. T < 560 K, the ORR on Pt{111} follows a peroxyl pathway forming OH* via OOH* dissociation with the resulting O* being hydrogenated via proton exchange between edge OH* and terrace O* (see Figure 5.5a). The resulting OH* intermediates participate in OH*-OH* coupling reactions at the near edge region (involving edge OH* species) at T < 420 K. At 420 K < T < 560 K, a combination of OH* hydrogenation and OH*-OH* coupling at the near-edge region is responsible H_2O* formation. Direct O_2* dissociation at T < 560 K contributes less than 23% in the ORR. At much higher temperatures, OH* coupling at near-edge sites results in the H_2O* formation over the {111} facet—this H_2O* makes up the majority of H_2O desorbing from Pt{111} (see Figure 5.5a). Above 500 K the OH* diffuses from the edge sites toward the {111} facet where it participates in the OH*-OH* coupling reaction forming H_2O* on a Pt{111} facet and O* on an edge site (see Figure 5.5a). In essence, the high ORR rate calculated above 500 K (compared to ORR from Pt(111) surface) is due to facile OH* diffusion and OH*-OH* coupling at near-edge sites (see Figure 5.5a).

Over the Pt{100} facet, the ORR pathway follows O_2* dissociation → H-transfer from OH* on edge to O* on Pt{100} facet site (results in OH* over a Pt{100} facet) → 52% (OH*-OH* coupling over Pt{100} facet) and 48% (OH*-OH* coupling near edge) at T < 540 K. Above 540 K, the ORR follows the path O_2* dissociation → O* hydrogenation → OH*-OH* coupling near edge (see Figure 5.5b). The majority of OH* on the edge is formed from the hydrogenation of O* on edge by H* on Pt{111} facet especially at T < 560 K (see Figure 5.5b). Over both Pt{111} and Pt{100} the ORR pathway is clearly influenced by contributions from the edge sites and not bound by the same bottlenecks as the isolated surfaces (Chapter 4). In particular, O* over Pt{111} and Pt{100} are strongly coupled and

their surface coverage decrease onset at a similar temperature, 460 K; also similar to Pt(111) under similar modelling conditions.

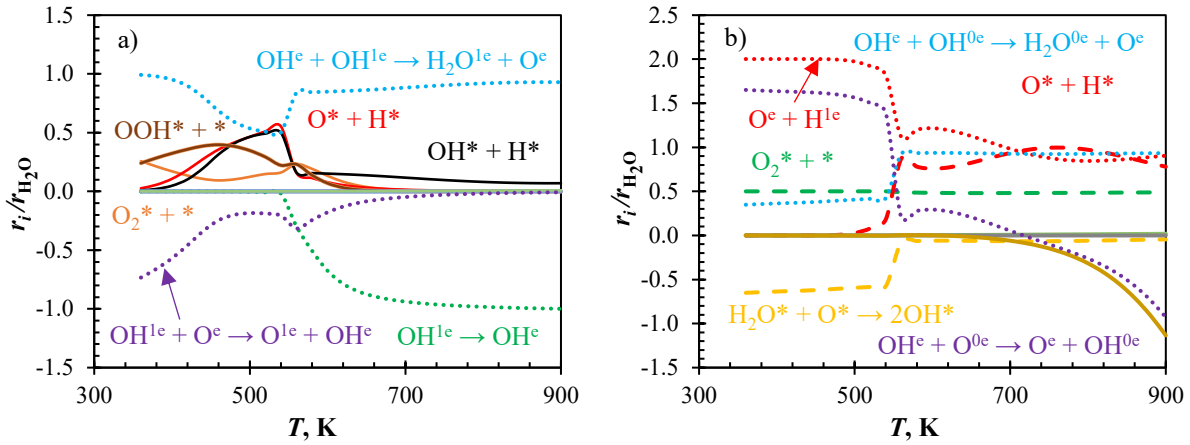

Figure 5.5: SA model predicted ORR pathway over a $\chi_{edge}(1.00)$ multifaceted surface model, (a) Pt{111} and (b) Pt{100}; processes on Pt{111} facet (—), Pt{100} facet (– – –) and involving edge species (·····). Negative values indicate that the reverse reaction contributes to the H_2O evolution rate.

Coverage dependent ORR over a $\chi_{edge}(1.00)$ surface, BWA and QCA

Intrinsic ORR activity, surface coverage, reaction pathway and rate limiting steps were also investigated using BWA and QCA models over a multifaceted surface model. Figures 5.6 and 5.7 present the modelled ORR activities over a χ_{edge} (1.00) surface model and corresponding pathway analysis based on the BWA model, respectively. Similar results from the QCA model are presented in Figures 5.8 and 5.9. As a general note, ORR rates over Pt{111} and Pt{100} are higher than on equivalent slab surfaces above 500 K. Below 500 K the ORR from Pt{111} approximates the rate over Pt(111) whilst over Pt{100} the rate is significantly lower than the rate from Pt(100) (see Figures 5.6 and 5.8). At high temperatures the ORR rate increases in the order Pt(111) << Pt{111} < edge << Pt(100) < Pt{100} whilst at low temperatures, ~ 400 K, the order is Pt(111) ≈ Pt{111} ≈ edge < Pt{100} << Pt(100) for both BWA and QCA models (see Figure 5.6 and 5.8).

The dominant surfaces species is H* on all three surface regions, i.e. {111}, {100} and edge. It also appears that due to the connectivity, the H* coverage over Pt{100} facet is ~ 1 ML at T < 600 K. As a result, the O* and OH* coverages which were at least 0.1 ML over Pt(100) are now ~ 3 orders of magnitude lower. This decrease in O* and OH* coverage and increase in H* over Pt{100} can explain the predicted decrease in ORR rates on Pt{100} compared to Pt(100) rates (see Figure 5.6 and 5.8). This is due to the diffusion of H* from Pt{111} toward Pt{100} at low temperatures (see Figure G4.3b in Appendix G). Figure G4.3a shows that at T < 460 K the adsorption of H_2 on Pt{100} is nearly zero and instead H* diffuses from the Pt{111} facet based on the BWA model. The QCA model also

predicts a slightly similar behaviour (see Figure G4.4). Above 500 K, H_2 adsorbs on Pt{100} facets and then H* adsorbates diffuse toward the Pt{111} facet where some H_2 evolution occurs in addition to H_2O desorption.

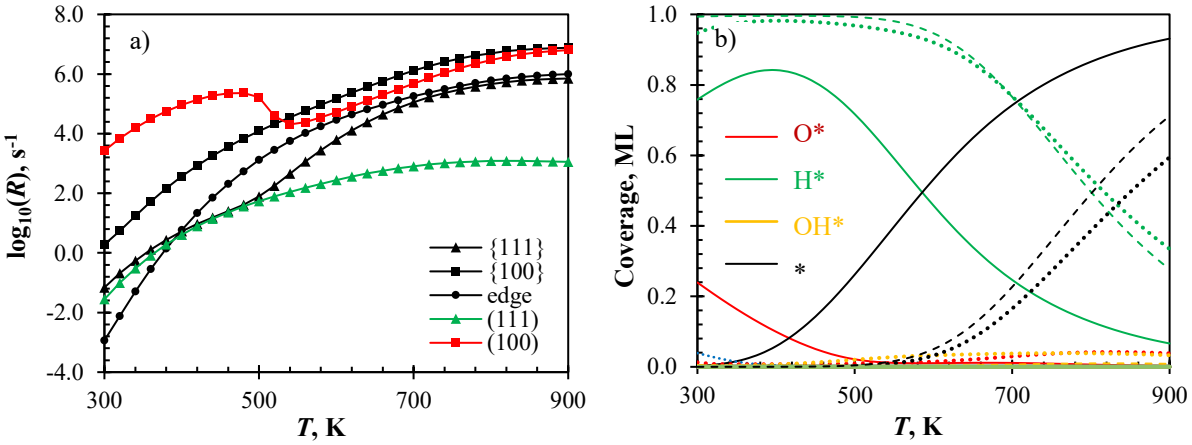

Figure 5.6: BWA model predicted ORR activities over a $\chi_{edge}(\mathbf{1.00})$ multifaceted surface model, (a) H_2O evolution rates and (b) surface coverage over Pt{111} facet (—), Pt{100} facet (− − −) and edge sites (·····).

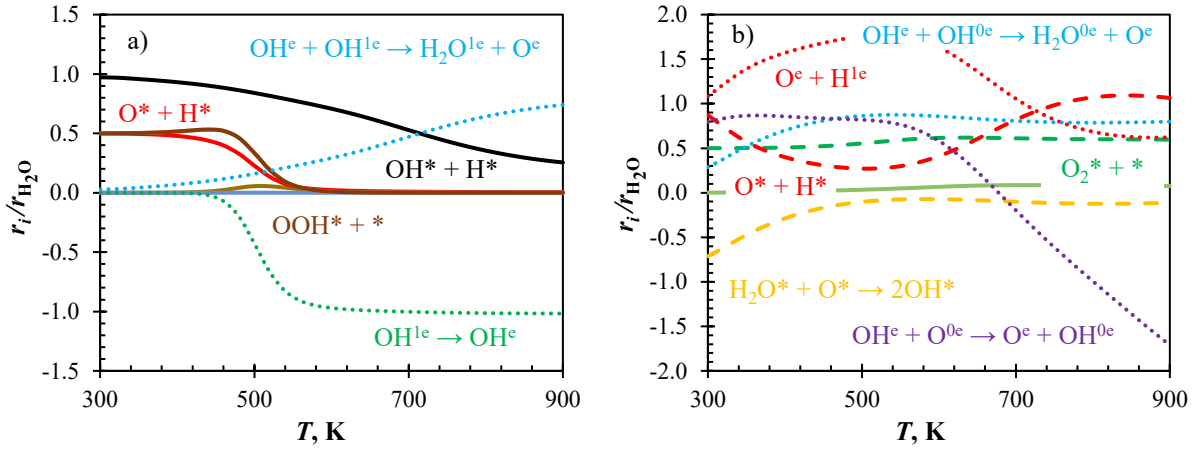

Figure 5.7: BWA model predicted ORR pathway over a $\chi_{edge}(\mathbf{1.00})$ multifaceted surface model, (a) Pt{111} and (b) Pt{100}; processes on Pt{111} facet (—), Pt{100} facet (− − −) and involving edge species (·····). Negative values indicate that the reverse reaction contributes to the H_2O evolution rate.

Figures 5.7 and 5.9 present the reaction pathway analysis for the ORR, over Pt{111} (a) and Pt{100} (b) facets, as predicted by the BWA and QCA model, respectively. Over Pt{100} facets the ORR follows a unique pathway distinctly different from that on a Pt(100) surface (see Figures 5.7b and 5.9b). Instead of O_2* dissociation → O* hydrogenation → OH*-OH* coupling, over Pt{100} the pathway is more complex. At T < 580 K, the ORR proceeds via O_2* dissociation → O* hydrogenation and H-transfer from edge OH* to O* on Pt{100} → OH*-OH* coupling near edge and over Pt{100} (see Figure 5.7b and 5.9b). At high temperatures O* hydrogenation at Pt{100} dominates the near edge H-transfer as a source of OH* intermediates. The QCA model predicts a more significant role of

OH*-OH* coupling over Pt{100}, ~50%, in the entire temperature range (see Figure 5.9b). Both BWA and QCA models highlight the role of the edge in both generating edge OH* intermediates which are involved in the ORR process over both Pt{111} and Pt{100} facets and facilitating OH*/H* exchange.

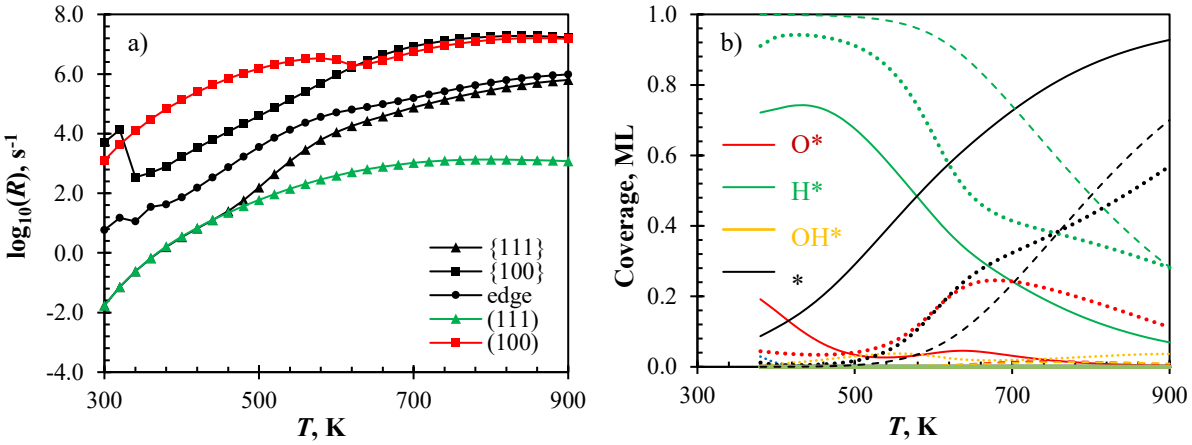

Figure 5.8: QCA model predicted ORR activities over a $\chi_{edge}(\mathbf{1.00})$ multifaceted surface model, (a) H_2O evolution rates and (b) surface coverage over Pt{111} facet (—), Pt{100} facet (− − −) and edge sites (·····).

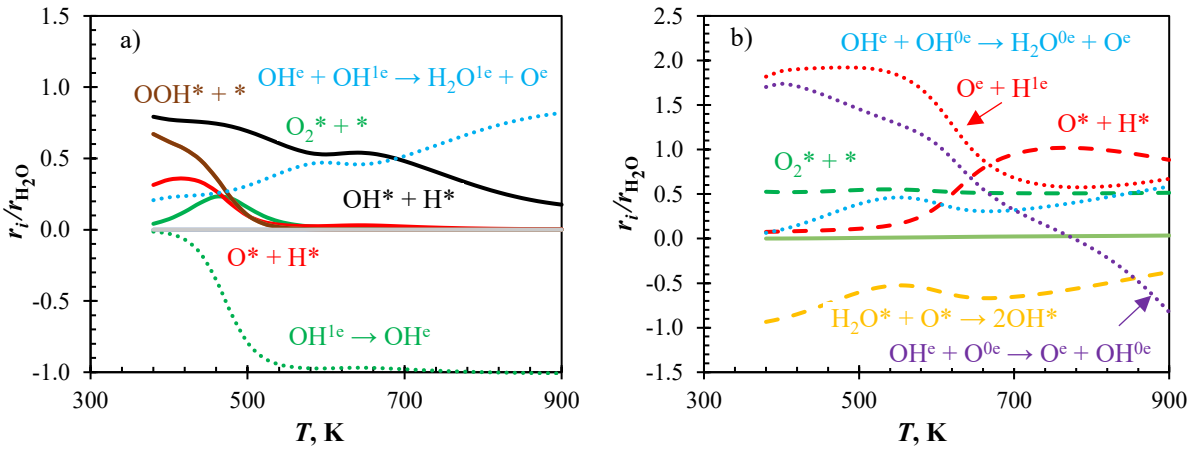

Figure 5.9: QCA model predicted ORR pathway over a $\chi_{edge}(\mathbf{1.00})$ multifaceted surface model, (a) Pt{111} and (b) Pt{100}; processes on Pt{111} facet (—), Pt{100} facet (− − −) and involving edge species (·····). Negative values indicate that the reverse reaction contributes to the H_2O evolution rate.

Over the Pt{111} facet, the pathway predicted by both BWA and QCA has minor differences in fractional contribution of each key step—but the same steps are involved (see Figure 5.7a and 5.9a). At T > 500 K OH* diffuses from edge toward the Pt{111} facet. H_2O* is then formed either via OH* hydrogenation and OH*-OH* coupling involving an edge OH* intermediate—OH* hydrogenation is dominant up to ~700 K (see Figure 5.7a and 5.9a). The ORR pathways over Pt(111) and Pt{111} are similar at low temperatures in that O_2* hydrogenation (OOH* dissociation) dominates direct O_2* dissociation (see Figure 5.7a, 5.9a and 4.3a).

Additional simulations were also conducted to exclusively investigate the effect of inter-facet species exchange in the absence of edge and near-edge reactions (see Figures F2.1 and F2.2 in Appendix F). Based on the BWA model, there is no difference between ORR rates predicted with and without the inclusion of edge and near-edge ORR reaction steps. However, there are differences in the ORR pathway followed—without edge and near-edge reactions the pathway over Pt{111} follows a peroxyl mechanism at T < 500 K and at T > 500 K H_2O* is form exclusively from the hydrogenation of OH* diffusing from Pt{100} to Pt{111} facet via an edge. Over the Pt{100} facet the ORR follows the dissociative pathway with OH* hydrogenation being dominated by OH*-OH* coupling. The ORR from edge sites in these cases is orders of magnitude lower as expected. The latter is expected since H_2O* desorption from edge sites in this case only occurs because of H_2O* diffusion from terrace sites. Given the low H_2O* coverage on terrace sites, the diffusion rates of H_2O* towards edge sites is slow.

Degree of rate control analyses

Degree of rate control analyses were conducted assuming a BWA model—looking at the influence of each reaction step on the rate of H_2O* desorption from Pt{111} and Pt{100} facets (see Figures 5.10). On a Pt{111} facet, the ORR rate is controlled by various rates. At low temperatures, i.e. T < 500 K, O_2* and O* hydrogenation reactions are partially rate limiting. This is actually in reasonable agreement with the prediction over Pt(111), although over Pt(111) O_2* hydrogenation remains controlling up to ca. 700 K under the BWA model assumptions. At T > 500 K, a more interesting behaviour can be observed (see Figure 5.10a). Here OH* transfer from the edge to Pt{111} limits the ORR on Pt{111}—this is also seen from effect of O_2* dissociation over a Pt{100} facet. Because of its higher diffusion barrier, OH*(edge) → OH*(Pt{111}) diffusion is rate limiting and OH*(Pt{100}) → OH*(edge) is not. The ORR over Pt{100} is solely limited by O_2* dissociation (see Figure 5.10b). Over Pt(100), O* hydrogenation limits the ORR at low temperatures, however due to H-transfer between edge OH* and {100} O* the demand on the O* hydrogenation step is reduced. Since the ORR rate from Pt{100} is at least 2 orders of magnitude higher than from Pt{111} and edge, the rate controlling steps for ORR from Pt{100} are the same as that for the overall ORR. The high coverage of the Pt{100} facet with H* adsorbates as a result of H* transfer from Pt{111} toward Pt{100} leads to low O_2* dissociation rates because of fewer empty sites. The latter explains the deviation between the degree of rate control predicted on Pt(100) surfaces and that predicted on Pt{100} facets. Moreover, O_2* dissociation as a rate limiting step on Pt{100} explains why the omitting edge-terrace reaction steps does not change the ORR rates (see Figures F2.1 and F2.2).

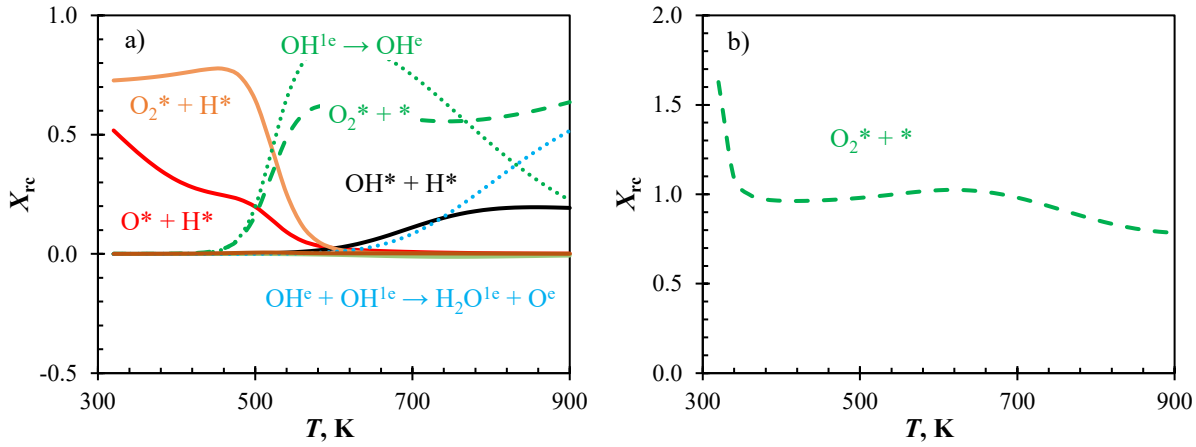

Figure 5.10: BWA modelled degree of rate control analysis over a $\chi_{edge}(\mathbf{1.00})$ multifaceted Pt surface model (a) H_2O^* desorption from Pt{111} and (b) Pt{100}facets as key reactions; showing {111} facet (—), {100} facet (– – –) and over edge (·····) processes with significant effect on the ORR rates.

5.4.2 ORR activity over multifaceted surfaces: $\chi_{edge}(0.34)/(0.04)$ models

Over a $\chi_{edge}(1.00)$ multifaceted surface model, the intrinsic ORR activity from Pt{111} and Pt{100} facets was generally higher than the activity over Pt(111) and Pt(100) surfaces—this was argued to be caused by the participation of the edge in the facet reaction, e.g. H-transfer between edge bound OH* and terrace O* offers another pathway for O* removal as OH*, and inter-facet exchange of OH* adsorbates at higher temperatures. As a result of edge participation in the ORR, a natural question is what happens when there are fewer edge sites than terrace sites. The $\chi_{edge}(0.34)$ multi-faceted surface model considers a case where there are 3x as many {111}/{100} terrace sites as edge sites based on a {111}:edge:{100} ratio of 1:0.34:1. This is equivalent to scaling all reactions involving edge sites by a factor of 0.34 thereby adjusting the contribution of edge sites by considering their ratio to terrace sites. Given the similarities between ORR activity over a $\chi_{edge}(0.34)$ and $\chi_{edge}(0.04)$, only BWA model results are discussed. The QCA and SA model results are given in Appendix F2.2.

Figure 5.11 presents ORR rates and surface coverage over $\chi_{edge}(0.34)$ and $\chi_{edge}(0.04)$ model surfaces based on BWA assumptions. Despite this adjustment in edge diffusion/reaction rates, the observed intrinsic ORR rates from Pt{111} and Pt{100} facets are still higher than over extended Pt(111) and P(100) surfaces at T > 540 K, respectively (see Figure 5.11a,c). The ORR rate from Pt{100} is higher than over all other surfaces considered in the whole temperature range (see Figure 5.11a,c). Moreover, at low temperatures the ORR rate profile from the Pt{111} facet approximates the rate from Pt(111)—this behaviour intensifies with a further decrease in edge rates, i.e. $\chi_{edge}(0.34)$ model to $\chi_{edge}(0.04)$ model. The latter is also true for the coverage profiles (see

Figures 5.11b,d). All this is expected given that slow diffusion and reaction rates at the edge affect the key steps in the ORR pathway over these multifaceted surfaces.

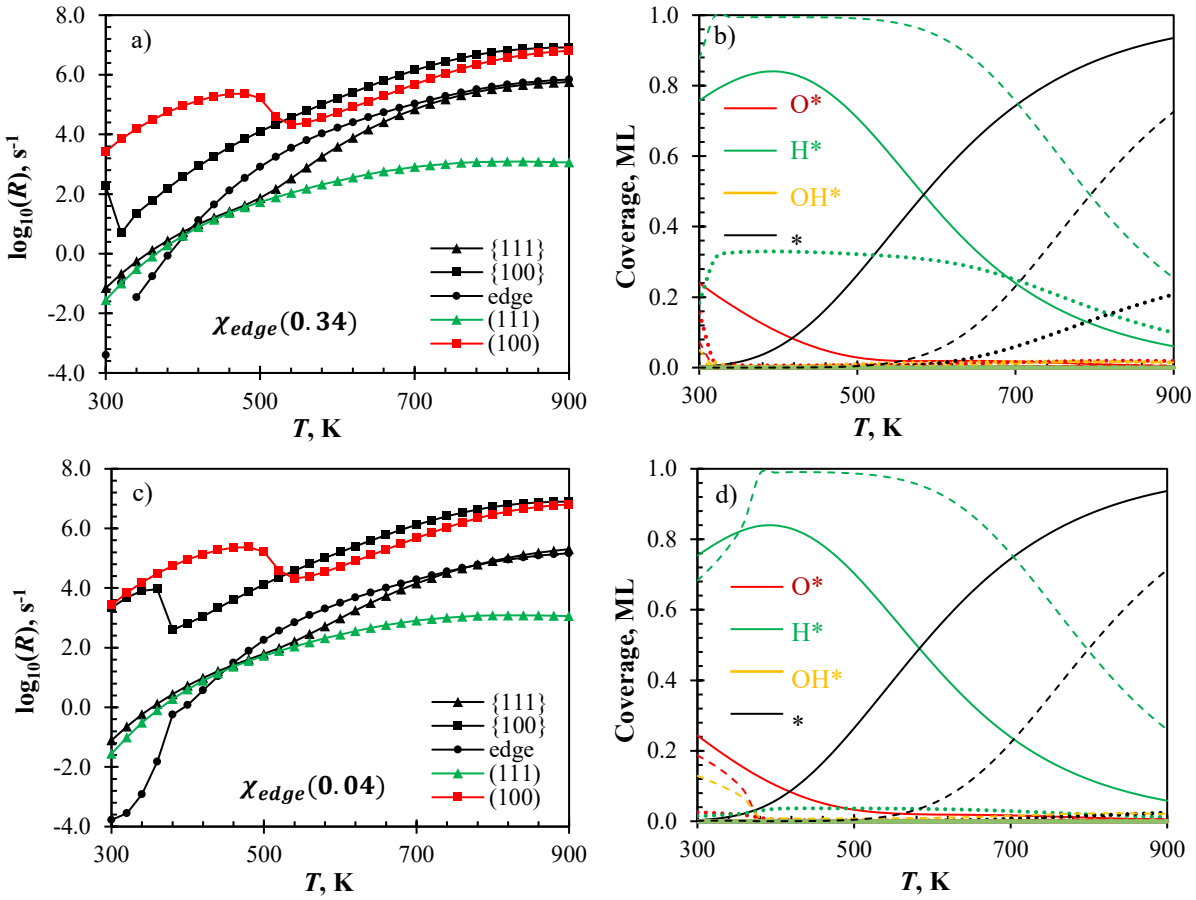

Figure 5.11: BWA model predicted ORR activities over a (a,b) $\chi_{edge}(0.34)$, and (c,d) $\chi_{edge}(0.04)$ multifaceted surface models, (a,c) H_2O evolution rates and (b,d) surface coverage over Pt{111} facet (—), Pt{100} facet (− − −) and edge sites (·····).

The reaction pathway analyses results are presented in Figure 5.12 for the ORR over $\chi_{edge}(0.34)$ and $\chi_{edge}(0.04)$ model surfaces. The Pt{111} and Pt{100} facets respond differently to a decrease in the ratio of edge sites to terrace sites (see Figure 5.12). Here, the ORR pathway over Pt{111} approximates that over Pt(111) surfaces for temperatures below 500 K. At higher temperatures, the pathway involves OH* intermediates diffusing from the edge sites and near-edge reactions. The contribution of the OH* hydrogenation step also increases with the decreasing fraction of edge sites. Over the Pt{100} facet of a $\chi_{edge}(0.04)$ multifaceted surface model, the ORR pathway closely approximates the pathway over Pt(100). Despite the latter, the ORR rate over Pt{100} is still higher than over the Pt(100) surface above 540 K. The closer agreement between ORR on Pt{100} and Pt(100) at low temperatures on $\chi_{edge}(0.04)$ is due to the slower diffusion flux of H* from Pt{111} toward Pt{100} facets.

Degree of rate control analyses were conducted for ORR from Pt{111} and Pt{100} facets of the $\chi_{edge}(0.34)$ and $\chi_{edge}(0.04)$ multifaceted surface models, these are shown in Figure 5.13. Over the Pt{111} facet the ORR rate controlling steps still include OH* diffusion from edge and O_2* dissociation occurring on the Pt{100} facet, at high temperatures (see Figures 5.13). At lower temperatures the rate is controlled by the same steps as Pt(111) and Pt{111} of a $\chi_{edge}(1.00)$ multifaceted surface model. On the other hand, the ORR from a Pt{100} facet is controlled by O_2* dissociation (see Figures 5.13). The other models also predict similar trends to the BWA model (see Appendix F2).

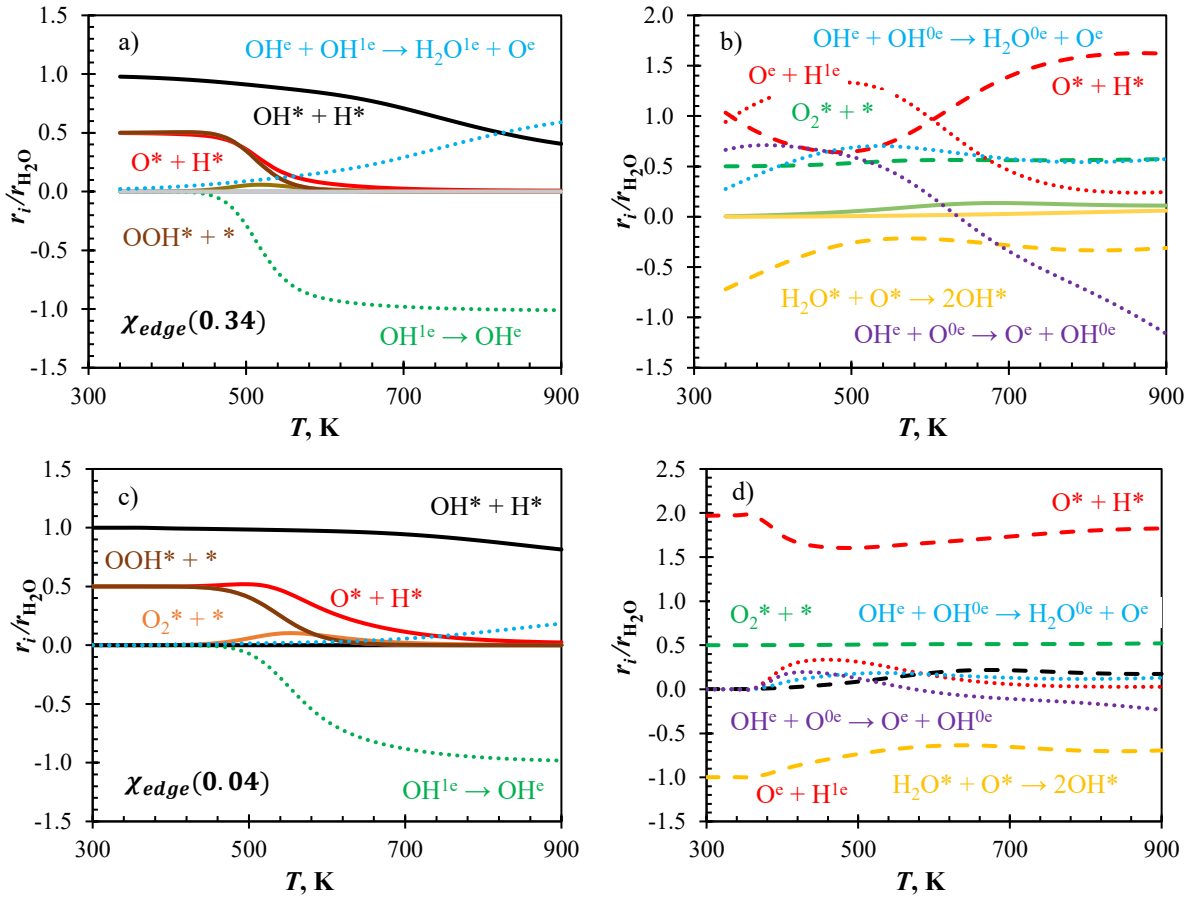

Figure 5.12: BWA model predicted ORR pathway over (a,b) a $\chi_{edge}(0.34)$ and (c,d) a $\chi_{edge}(0.04)$ multifaceted surface models, (a,c) Pt{111} and (b,d) Pt{100}; processes on Pt{111} facet (—), Pt{100} facet (– – –) and involving edge species (·····). Negative values indicate that the reverse reaction contributes to the H_2O* evolution rate.

5.5 Discussion and Conclusions

This Chapter has investigated the ORR process over multifaceted Pt surfaces. The first step involved calculating the ORR energetics at edge and near-edge sites. The energy barriers were strongly influenced by the reactivity of the edge bridge sites toward oxygen containing species. Nevertheless,

these data were incorporated in microkinetic analyses over multifaceted Pt surfaces—also included were the inter-facet diffusion of ORR intermediates. Microkinetic analyses were aimed at investigating the effect of inter-facet connectivity on the intrinsic ORR activity from each facet.

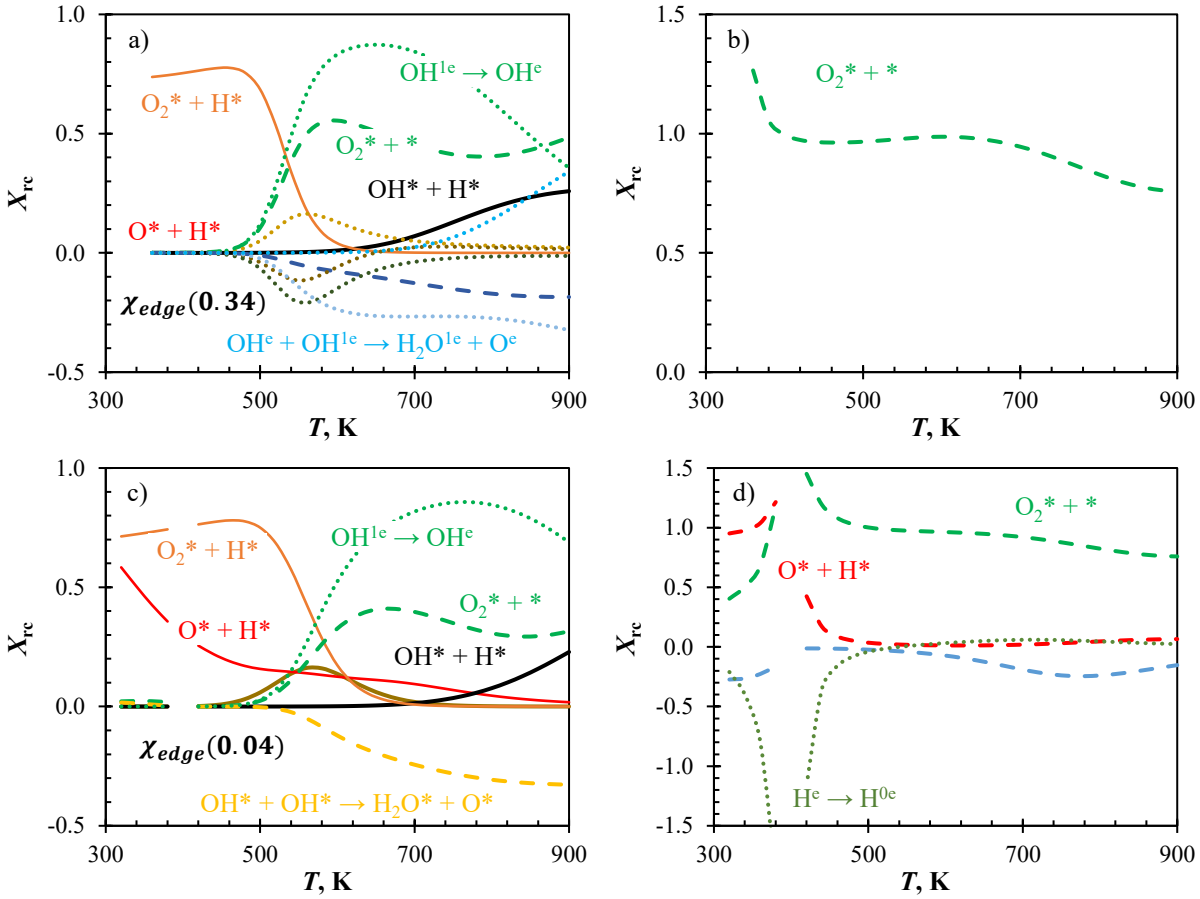

Figure 5.13: BWA modelled degree of rate control analysis over (a,b) a $\chi_{edge}(0.34)$ and (c,d) $\chi_{edge}(0.04)$ multifaceted Pt surface models with H_2O* desorption from (a,c) Pt{111} and (b,d) Pt{100} as key reactions; showing {111} facet (—), {100} facet (– – –) and over edge (·····) processes with significant effect on the ORR rates

Generally, over multifaceted Pt surfaces the intrinsic ORR activity of each facet, i.e. Pt{100} and Pt{111}, is higher than over extended surfaces at moderate to high temperatures. Both inter-facet diffusion and near-edge reactions play a key role on the improved ORR activities. Over Pt{111} facets and above 500 K, the OH* diffusion from a Pt{100} facet, via an edge, becomes the only source of oxygen—no O_2* adsorption occurs on this facet at these conditions. With a decreasing ratio of edge sites to terrace sites, the ORR rate controlling steps and pathway approach the behaviour predicted over extended surface—however, on a Pt{111} facet of a $\chi_{edge}(0.04)$ model, the ORR activity is still influenced by edge and Pt{100} processes at high temperatures. This is responsible for improved ORR activity from this facet at high temperatures. Even when excluding edge and near-edge ORR reaction

steps the intrinsic ORR activity from Pt{111} and Pt{100} facets of multifaceted surface models is still higher than over extended surfaces at T > 540 K. The present results agree, in part, with Komanicky *et al.,* [34,36] regarding a cooperative behaviour of adjacent Pt{111} and Pt{100} facets. However, in the present study OH* diffuses from Pt{100} to Pt{111} contrary to the postulate of Komanicky *et al.,* [34,36] who suggests oxygen diffusion to Pt{111} terraces. This study further suggests that the effect of inter-facet cooperation on the ORR is temperature dependent and model specific.

In summary, present models give a clear indication of how inter-facet exchange of species and reactions at terrace-edge boundaries affect the intrinsic ORR activity—and ultimately the overall ORR activity. A key limitation in the mean-field models is that lateral interactions at surface boundaries are ignored. However, inclusion of these should not significantly change the predicted results because the largest repulsive interactions are already included. The strong contribution of near-edge processes coupled with the low diffusion barrier of OH* over Pt(111) makes the model predictions more probable. Whilst the present results confirm the limitation of literature studies approximating the overall ORR activity as a linear combination of activities from constituent surfaces, this limitation is only significant at very high temperatures, i.e. > 500 K, and would likely not be relevant for low temperature ORR in fuel cells and metal-air batteries. Therefore, to address this, intermediate exchange rates could be manipulated via surface alloying.

CHAPTER 6: Overall ORR Activity over Au and Ag modified Multifaceted Pt Surfaces[‡‡]

6.1 Introduction

Thus far, the ORR over extended and multifaceted Pt surfaces has been discussed based on both density functional theory and mean-field microkinetic modelling. In a bid to investigate the intrinsic ORR activity over each surface, viz. Pt(111), Pt(100), Pt{111} and Pt{100}, it was found that the edge plays a role in enabling inter-facet mixing and participates in H-transfer at near-edge regions. Above 500 K, the ORR activity is controlled by inter-facet diffusion of OH* and O_2* dissociation over a Pt{111} and Pt{100} facet, respectively. This behaviour is particularly interesting since it points towards an opportunity for rational design—where facet boundaries are modified to (selectively) improve species exchange between facets. Over multifaceted Pt surfaces this exchange is only significant above 500 K, well outside the conditions of interest in PEM fuel cell and metal-air battery applications. In Chapter 3 it was argued that at edge sites both O* and OH* adsorb too strongly and consequently result in a deep well in the PES—limiting the inter-facet exchange of these intermediates.

Wei and Liu [126] suggested a NP model where the edges are decorated by Au atoms—this was mainly suggested to improve the stability of Pt NPs at high electrode potentials since Au can suppress oxidation of undercoordinated Pt atoms at edge and corner sites. They found O_2 to adsorb more strongly and dissociate with a lower barrier on Pt{111} facets of Au decorated Pt NPs compared to pure Pt NPs. From this they argued that Au modification will also improve the ORR activity. Other structures involving edge modification were recently discussed by Kodama *et al.* [155] and Liu *et al.* [156]. Kodama *et al.* [155] electrochemically deposited single atomic rows of Au atoms along the step sites of Pt(211), Pt(322) and Pt(755) single-crystal surfaces—the modified stepped surfaces exhibited higher ORR activities compared to equivalent unmodified surfaces. Similar to Wei and Liu [126], Kodama *et al.* [155] argued that the improvement in ORR activity was due to enhanced local ORR activities on Pt{111} terraces. However, Kodama *et al.* [155] argues that the ORR activity increases as a result of further disruption in the H-bond networks or suppression of oxide formation near

[‡‡] Partially published in Ref. [171]

modified edges—this disruption in H-bonding networks has also been reported for unmodified stepped surfaces [32,144]. Liu *et al.* [156] prepared ultrathin Pd_9Au NWs followed by the underpotential deposition of a Cu monolayer and a galvanic displacement of Cu^0_{upd} with Pt^{2+}. The resulting structures were argued to be composed of a Pd core and a Pt shell with Au occupying edge sites. DFT calculations and extended X-ray absorption fine structure (EXAFS) spectroscopy analyses were used to substantiate this claim. The measured ORR activity from this structure was higher than that measured over ultrathin PtPd NWs [157].

Based on results presented in Chapters 3 – 5, it is clear that modification of multifaceted Pt surfaces may lead to improved ORR activities via formation of new boundary sites or improved inter-facet exchange of reaction intermediates. Oxygen containing species (*OCS**) adsorb weakly over Au and Ag compared to Pt surfaces [29]. Therefore, modifying the Pt NW edges with Au or Ag may result in a flattened PES for inter-facet exchange of OCS*. Although surface energies of Au and Ag are lower than Pt [13], surface segregation of these modifiers does not guarantee preferential occupation of edge/corner sites. Based on the Wulff construction theorem [12] and differences in surface energies between the modifiers and Pt, equilibrium NWs/NPs should have Au and Ag at the surface. Strain effects, as a result of lattice size mismatch [99], should also provide an additional driving force for surface segregation of Au and Ag at low concentrations [158], unless the Pt-Au or Pt-Ag mixing enthalpy is higher.

Given this information, surface deposition of Au/Ag on Pt NW/NP surfaces followed by thermal annealing may provide a way to synthesise edge-decorated Pt NWs/NPs. Provided galvanic replacement of a Cu monolayer on Pt NWs/NPs with a mixed solution of Pt^{2+} and *M* (*M* = Au^+ and Ag^+) leads to a stoichiometric PtM monolayer [159], thermal or electrochemical annealing may be used to drive further segregation leading to migration of M atoms towards edge/corner sites. Empirical force field methods have been used quite extensively to study segregation behaviour of mixed metallic systems [160–166]. In particular, surface segregation of Au has been reported in PtAu NPs [163,167]. However, these studies considered relatively high Au contents.

This Chapter investigates the diffusion properties of ORR intermediates over Pt NWs with Au and Ag decorated edges, i.e. Au/Pt and Ag/Pt. First the selection of a modifier is justified in Section 6.3 and in Section 6.4 the energetics are discussed. Sections 6.5 and 6.6 discuss the microkinetic modelling of the ORR activity and pathway over Au/Pt and Ag/Pt multifaceted surfaces, respectively.

6.2 Methods and surface models

6.2.1 Surface model

Additional DFT calculations were performed on edge modified Pt NW models, i.e. where an entire edge atomic row of Pt atoms is replaced with Au/Ag atoms (see Figure 6.1). The DFT parameters were kept at the values given in Chapter 2. Various surface sites, between the Pt{111} and Pt{100} facets, were probed with O_2*, O*, H*, OH* and H_2O* to find the potential energy surface for inter-facet diffusion. Data obtained was then used in microkinetic modelling.

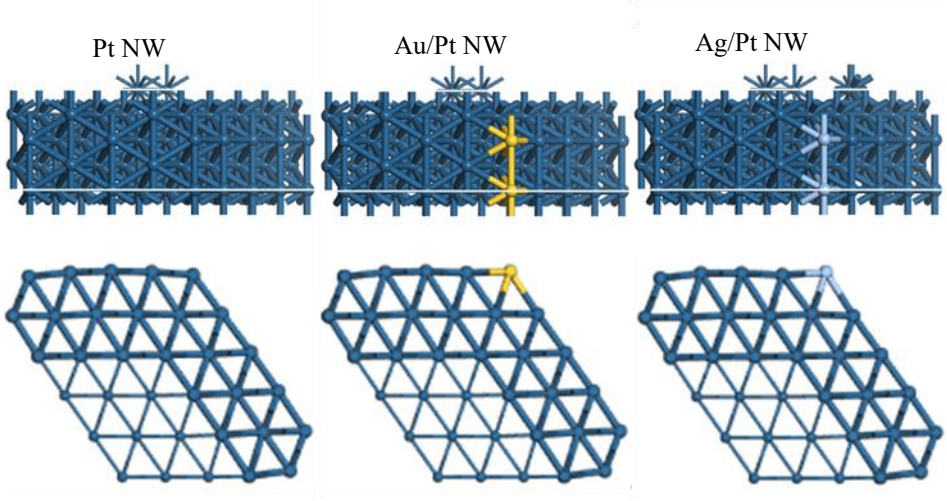

Figure 6.1: Surface models for unmodified, Au and Ag modified Pt NWs.

6.2.2 Molecular dynamics simulations

Classical molecular dynamics (MD) simulations were conducted using DL_POLY Classic [168], to investigate the thermal and segregation properties of Au and Ag modified Pt NWs (see Figure 6.2). Simulations were conducted using canonical ensemble (NVT) sampling with an Evans thermostat [169] and the Velocity Verlet algorithm to integrate equations of motion. A time step of 2 fs was used with a total simulation time of 4 ns to ensure sufficient time for equilibration of the segregation behaviour. Interatomic interactions between two atoms were described based on Sutton-Chen potential [170] and the total energy of a system of atoms was calculated as,

$$U_{total} = \sum_i \epsilon \left[\frac{1}{2} \sum_{j \neq i} \left(\frac{a}{r_{ij}} \right)^n - c\sqrt{\rho_i} \right], \text{ with } \rho_i = \sum_{j \neq i} \left(\frac{a}{r_{ij}} \right)^m \quad 6.1$$

where ϵ, is the interaction energy parameter whilst r_{ij}, and a are the distance between atoms i and j and lattice parameter, respectively. m and n are integer parameters chosen such that $m > n$. A complete set of these parameters can be found in Ref. [171]. Homonuclear interaction energy parameters (ϵ) were obtained from Kimura *et al.* [172]—for heteronuclear interactions mixing rules

were applied [171]. MD simulations were conducted at temperatures ranging from 300 K to well above the melting point which was identified using the Steinhardt bond order analyses [173]. The main purpose of these thermal annealing simulations was to ascertain if the pristine edge decorated NWs (shown in Figure 6.2) were stable.

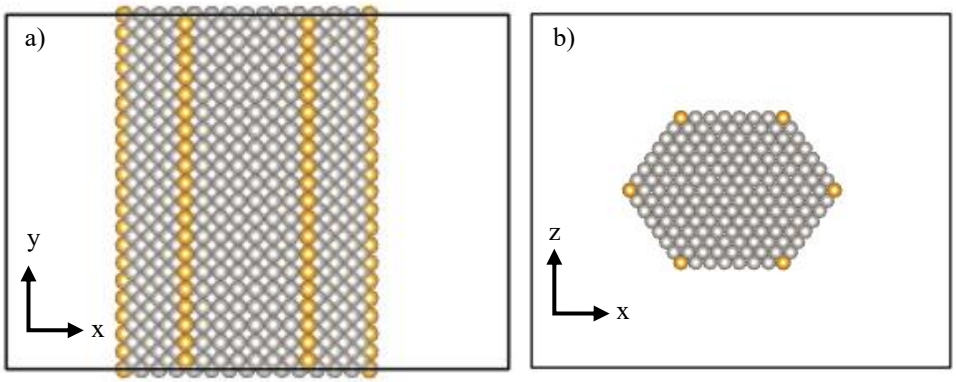

Figure 6.2: Illustration of a an edge-modified hexagonal Pt NW model with 8 atomic rows along each terrace.

6.2.3 Microkinetic simulations

The simulation assumptions, approach, conditions and data analyses performed in this Chapter are based on Chapter 5. Therefore, direct comparison is possible between predicted results. The intrinsic ORR activities of Au/Pt{111}, Au/Pt{100}, Ag/Pt{111} and Ag/Pt{100} facets are discussed and compared to ORR activities of Pt(111)/{111} and Pt(100)/{100} extended/terrace sites of unmodified Pt surfaces. As was the case in Chapter 5 three multifaceted surface models are considered, these are $\chi_{edge,M}(1.00)$, $\chi_{edge,M}(0.34)$ and $\chi_{edge,M}(0.04$) multifaceted models with M = Au and Ag

6.3 Selection of edge modifier

Selection of candidate edge modifiers requires consideration of (i) reactivity toward *OCS**, (ii) electrochemical stability, i.e. standard reduction potential, and (iii) surface/cohesive energy relative to Pt. Elements around Pt on the periodic table were compared to Pt in terms of requirements (i) to (iii) (see Table 6.1). Elements with a lower cohesive/surface energy than Pt will likely prefer to segregate to the surface as desired in this study. Moreover, elements with a more positive reduction potential will be more suitable for application under ORR conditions. Cohesive energy data was obtained from Ref. [100] and the standard reduction potentials from Ref. [174]. The reactivity towards *OCS** was calculated based on DFT using hexagonal NW models whose edges were replaced with *M* (*M* = Ru, Rh, Pd, Ag, Os, Ir and Au)—the data is reported in Table 6.1. From this information it was found that only Pd, Ag and Au satisfied the three requirements—Rh has a marginally lower cohesive energy than Pt, however is highly reactive towards both O* and OH* (see Table 6.1). The next crucial question is

how to prepare Pt NWs/NPs with modified edges. A mixed-metal monolayer on Pd was prepared by Zhang *et al.* [159] using a galvanic replacement method in a two component solution. It was further argued that the monolayer composition corresponded well with the solution composition [159].

Table 6.1: Thermodynamic properties of near-Pt elements, suitable (green)/unsutiable (red) as edge modifiers.

	Ru	Rh	Pd	Ag
E^0 [V], vs. SHE	0.46	0.60	0.95	0.80
$E_{cohesive}$ [kJ/mol]	650	554	376	284
$E_{ads,\ O}$ [eV/O]	-3.33	-2.39	-1.00	0.35
$E_{ads,\ OH}$ [eV/OH]	-3.67	-3.04	-2.34	-1.97

	Os	Ir	Pt	Au
E^0 [V], vs. SHE		1.15	1.18	1.50
$E_{cohesive}$ [kJ/mol]	788	670	564	364
$E_{ads,\ O}$ [eV/O]	-3.97	-2.82	-1.58	-0.12
$E_{ads,\ OH}$ [eV/OH]	-4.16	-3.22	-2.54	-1.79

Following the method of Zhang *et al.* [159] upon the replacement of Cu^0_{upd} with a Pt:Au, Pt:Ag and Pt:Pd mixed monolayer, thermal annealing can be used to effect surface segregation. Classical molecular dynamics simulations have been performed to investigate the segregation behaviour of modified Pt NWs [171]. In this study, thermal annealing of an edge decorated Pt NW (see Figure 6.2) was simulated to ascertain whether edge Au and Ag would remain at edge sites, or segregate toward surface or subsurface sites. Despite a poor prediction of the bulk melting temperature of Pt by Sutton-Chen potential methods, DFT calculated segregation energies verified that the predicted segregation behaviour for the PtAu and PtAg systems was at least reliable [171].

Figure 6.3 presents the molecular dynamic simulation results detailing the trace trajectories of Au/Ag atoms between 2 and 4 ns of the simulations at different temperatures. It is clear that Au and Ag atoms remain on the surface layer even at near-melting point temperatures. However, these atoms do not appear to be preferentially stable at edge sites. In fact, there is substantial Au/Ag enrichment on Pt{100} facets (see Figure 6.3) [171]. Energy minimisation simulations show that the low energy structures of Pt_9Au and Pt_9Ag NW systems[§§] have Au atoms on the surface and Ag atoms mostly on the surface with a few atoms in the 2nd and 4th subsurface layers, respectively [171]. The key conclusion from this is that both Au and Ag atoms populate the surface layer—therefore, these were chosen as

[§§] The total energy of hexagonal nanowire models with randomly distributed Au/Ag and Pt atoms was optimized/minimised by successive atomic swaps in order to obtain the most stable atomic configuration for a given system [171].

candidate edge modifiers. According to MD simulations, Pd atoms in PtPd systems diffuse toward the core [171]. Therefore, the Pd modification was not considered further for now.

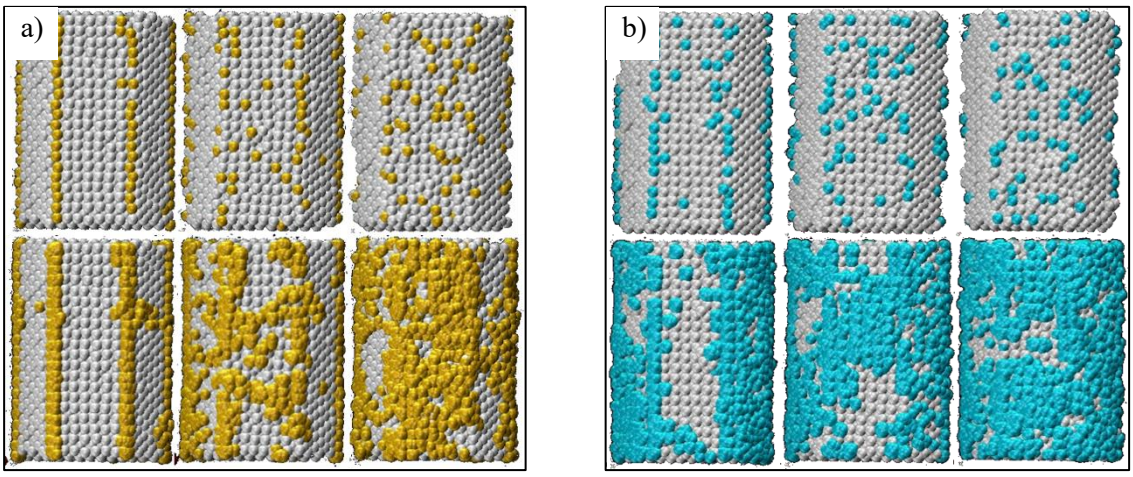

Figure 6.3: (a) Final structure (top) and merged structures (trajectories) between 2 ns and 4 ns at 0.008 ns time steps (bottom) from an Au/Pt NW simulation. Left to right: 800 K, 900 K and 1000 K (b) Final structure (top) and merged structures (trajectories) between 2 ns and 4 ns at 0.008 ns time steps (bottom) from an Ag/Pt NW simulation. Left to right: 800 K, 900 K and 1000 K [171].

6.4 ORR intermediates on Au/Pt and Ag/Pt NW surfaces

The adsorption of various ORR intermediates, i.e. O_2*, O*, H*, OH* and H_2O*, over edge and terrace sites of Au/Pt and Ag/Pt NW models was investigated. The DFT-calculated adsorption energies at 0 K without zero-point energy corrections are presented in Figure 6.4 for each reaction intermediate.

6.4.1 H* adsorption

The adsorption energy of H* is -0.526 eV and -0.688 eV over Pt(111) and Pt(100) surfaces, respectively—over $b^{(e)}$ and $t^{(e)}$ sites H* adsorbs with an energy of -0.748 eV and -0.549 eV, respectively. Modification of Pt NW edges with Au or Ag does not seem to significantly influence the adsorption energy of H* over terrace sites—adsorption over Au/Ag modified edge sites is however weaker than over unmodified Pt NW edges (see Figure 6.4a). Moreover, over Ag modified edges H* adsorption is endothermic, 0.220 eV on $t^{(e)}$ sites and 0.218 eV on $b^{(e)}$ sites, whilst over Au modified $b^{(e)}$ sites the adsorption energy is -0.157 eV (i.e. 0.590 eV weaker than over pure Pt NW edges) and is 0.117 eV on $t^{(e)}$ sites.

6.4.2 O_2* adsorption

Molecular oxygen adsorbs with an energy of 4.418 eV and 3.888 eV (relative to gaseous H_2 and H_2O) over Pt(111) and Pt(100) bridge sites, respectively. Over equivalent terrace sites of an unmodified Pt NW the adsorption energy of O_2* is within 0.1 eV of that calculated over extended surfaces (see Figure 6.4b). Over terrace bridge sites of Au/Pt and Ag/Pt NW models, the adsorption energy of O_2*

increases by up to 0.3 eV relative to adsorption on pure Pt NW surfaces (see Figure 6.4b). The latter corresponds well with previous reports over an Au decorated Pt NP [126].

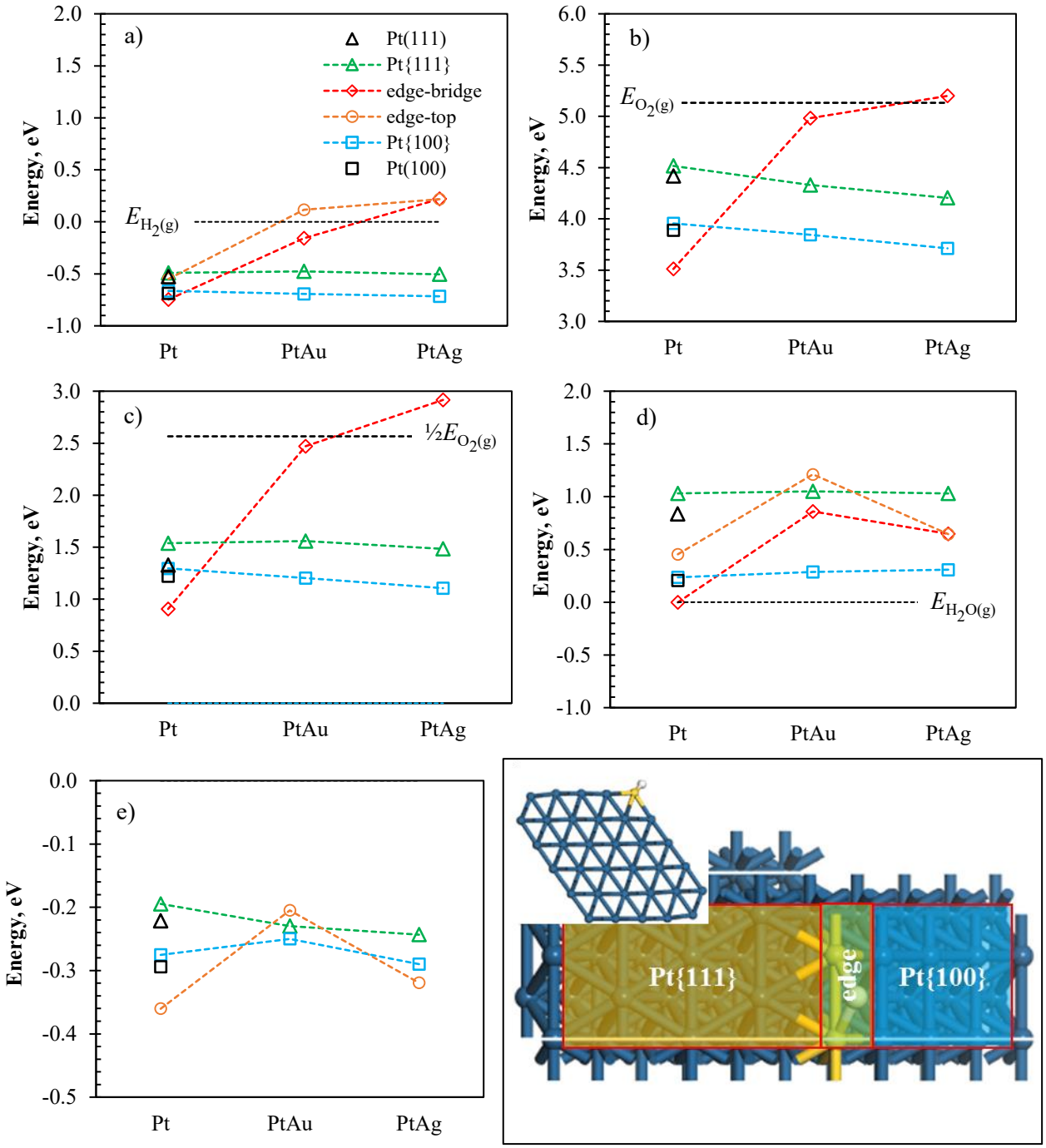

Figure 6.4: Adsorption energy of (a) H*, (b) O_2*, (c) O*, (d) OH* and (e) H_2O* relative to H_2 and H_2O in the gas phase—without zero point correction and at 0 K, on modified and unmodified Pt surfaces.

This stabilisation may be due the coupled electronic and geometric factors—modified NWs have less surface curvature and undercoordinated Au/Ag atom draws less electrons from near edge surface atoms than undercoordinated Pt atoms. Whilst O_2* adsorption on Pt NW edge sites has an energy of 3.511 eV, over Au/Pt and Ag/Pt NW edge sites the adsorption energy is 4.981 eV and 5.199 eV—considering

that the energy of O_2 in the gas phase relative to H_2 and H_2O is 5.132 eV, over Ag/Pt NW edge sites O_2* adsorption is endothermic (see Figure 6.4b).

6.4.3 O* adsorption

The adsorption of O* over Pt(111) fcc sites and Pt(100) bridge sites is quite similar [95]. The adsorption strength of O* over Pt{111} and Pt{100} terraces is ca. 0.1 eV and 0.2 eV weaker than equivalent adsorption on extended surfaces, respectively. Edge modification does not affect the adsorption energy over terrace sites by more than 0.2 eV (see Figure 6.4c). Similar to the adsorption of O_2* over edge sites, over Pt edge sites O* adsorbs significantly more strongly than over Pt{111} terraces and modification with Au lowers the adsorption significantly whilst Ag modification result in endothermic adsorption of O* (see Figure 6.3c). Whilst intuitively both O_2* and O* should adsorb more strongly on Ag modified edge than on Au [7,29], this was not the case. This reversed stability was not caused by coverage effects (see Table G1.1 in Appendix G), but it may be due to geometric and electronic effects.

6.4.4 OH* and H_2O* adsorption

Adsorption of OH* over terrace and edge sites was also investigated (see Figure 6.4d). The adsorption energy over Pt{111} and Pt{100} surfaces corresponded well with adsorption over Pt(111) and Pt(100)—the difference in adsorption energy between Pt{111} and Pt{100} sites is ca. 0.8 eV. Interestingly, unlike both O_2* and O*, the adsorption energy of OH* over Au and Ag modified edge sites lies between adsorption energies over M/Pt{111} and M/Pt{100} facets (see Figure 6.4d). This interesting result suggests that whilst Au/Pt and Ag/Pt NWs will facilitate OH* exchange, the diffusion of O_2* and O* from Pt{111} and Pt{100} terrace sites towards the edge might be limited because of their weak adsorption on modified edge sites. Similar to OH*, edge modification does not limit H_2O* exchange between M/Pt{111} and M/Pt{100} facet sites (see Figure 6.4e).

6.4.5 Diffusion energetics over Au/Pt and Ag/Pt surfaces

Whilst adsorption energies give a lot of important information regarding the thermodynamics of the system, knowledge of the diffusion barriers is critical in understanding and modelling the rates of inter-facet species exchange. These have been calculated for H*, O*, OH* and H_2O* (see Appendix G1)—O_2* diffusion barrier were not calculated due to its weak adsorption energy over modified edges. Instead O_2* diffusion from edge sites toward terrace sites was treated as a barrierless process. Table 6.2 presents the calculated diffusion barriers of H*, O*, OH* and H_2O* over Au/Pt and Ag/Pt NW surfaces.

Reactions at edge and near-edge sites are not considered since H*, O* and O_2* coverages over modified edge sites ought to be low. The adsorption strength of these intermediates at modified edge sites is less than -0.16 eV relative to a gas phase reference state. Therefore, the microkinetic model data presented herein is only influenced by inter-facet diffusion.

Table 6.2: Diffusion barrier for inter-facet exchange of ORR intermediates over modified Pt NW edge sites; energies corrected for the difference in the adsopriton energy on extended surfaces vs. NW terraces (near-edge).

		(111) --> edge		edge --> (100)	
		E_a [eV]	$\Delta_{rxn}E$ [eV]	E_a [eV]	$\Delta_{rxn}E$ [eV]
O_2*	Pt	0.029	-0.906	-	0.376
	PtAu	0.564	0.564	0.000	-1.094
	PtAg	0.782	0.782	0.000	-1.312
O*	Pt	0.646	-0.423	0.626	0.316
	PtAu	1.335	1.142	0.118	-1.250
	PtAg	1.620	1.587	0.007	-1.694
H*	Pt	0.195	-0.194	0.336	0.059
	PtAu	0.547	0.396	0.179	-0.531
	PtAg	0.823	0.774	0.055	-0.909
OH*	Pt	0.119	-0.892	0.681	0.228
	PtAu	0.498	-0.029	0.250	-0.635
	PtAg	0.156	-0.243	0.182	-0.420
H_2O*	Pt	0.121	-0.139	0.224	0.066
	PtAu	0.017	0.017	0.000	-0.089
	PtAg	0.000	-0.091	0.018	0.018

6.5 ORR activity over multifaceted Au/Pt surface

Based on calculated adsorption energies and diffusion barriers, modification of Pt NW edges with Au should lead to hindered inter-facet exchange of O_2* and O* and improved OH* exchange (see Table 6.2). The ORR rates over multifaceted Au/Pt NW surfaces were simulated using the SA, BWA and QCA microkinetic models. Three multifaceted surface models are considered, i.e. $\chi_{edge}(1.00)$, $\chi_{edge}(0.34)$ and $\chi_{edge}(0.04)$. Corrected energetics used in the following microkinetic simulations are given in Table E7.4.

6.5.1 Steady state ORR rates

The ORR rates from all three multifaceted surface models are presented alongside corresponding surface coverages in Figure 6.5 (BWA model) and Appendix G2 (QCA model). From the BWA simulated results, it is clear that the effect of inter-facet exchange of ORR intermediate species on the reaction rates decreases with relative density of edge sits, i.e. χ_{edge}. In $\chi_{edge}(1.00)$ and $\chi_{edge}(0.34)$

surface models, the ORR rate from Pt{111} terraces are higher than those from Pt(111) surface in the whole temperature range (see Figure 6.5). In the $\chi_{edge}(0.04)$ model, the effects are much smaller, especially at low temperatures. From Au/Pt{100} terraces the ORR rate are higher than from Pt(100) above 520 K—this effect is much smaller over the $\chi_{edge}(0.04)$ model due to limited inter-facet cooperation. The coverage of the Pt{100} and the Au/Pt{100} facets with H* adsorbates is higher, near 1 ML, compared to the extended Pt(100) surface at low temperatures. This explains their lower ORR rates compared to the Pt(100) surface (see Figures 6.5, 5.6 and 5.11). Decreasing the ratio of edge to terrace sites leads to improved correspondence between the {100} facets and the Pt(100) surface. On the other hand, the higher ORR rates predicted by the QCA model on Au/Pt{100} also corresponds well with lower terrace coverage with H* adsorbates (Figure G2.1 in Appendix G). All simulations show that edge sites in Au/Pt surfaces are mostly vacant with the largest coverage being OH* (10^{-4} - 10^{-6} ML). Interesting to note, over Au modified surfaces the ORR rates from Au/Pt{100} facet are higher than the rates from Pt(100) and Pt{100} at T > 520 K.

6.5.2 Reaction pathway analysis

With regards to reaction pathway, Figure 6.6 presents the pathway analysis generated from BWA model results—interesting trends are observed. Over Au/Pt{111} surface the ORR follows the peroxyl mechanism (O_2* + H* > OOH* > OH* + O*) at low temperatures and at high temperatures OH* diffuses from the Pt{100} facet toward the Pt{111} facet where it is hydrogenated to H_2O*. The change in reaction pathway occurs below 420 K over the $\chi_{edge}(1.00)$ model and at ca. 460 K over the $\chi_{edge}(0.34)$ model—over the $\chi_{edge}(0.34)$ at low temperature, up to 30 % of desorbing water from Au/Pt{111} diffuses from the Au/Pt{100} facet (see Figure 6.6a and 6.6c). Over the $\chi_{edge}(0.04)$ model the change in reaction pathway is rather interesting; below 460 K the pathway is dominated by the peroxyl mechanism. Between 460 K and 700 K a combination of peroxyl, O_2* dissociation and OH* flow from Au/Pt{100} facet contribute to the ORR from Au/Pt{111} surface—the relative contributions change with temperature and the O_2* dissociation reaches a maximum of 20 % at 660 K (see Figure 6.6e). The reduced contribution of OH* flow from Au/Pt{100} facet to the Au/Pt{111} ORR rates is due to reduced edge site density and hence OH* flux; however, OH* flux from Au/Pt{100} → Au/Pt{111} onset at a lower temperature than over unmodified Pt surfaces.

Over the Au/Pt{100} facet the pathway is rather straightforward, O_2* dissociates forming O* which undergo hydrogenation to OH* intermediates. Water is formed predominantly via the OH*-OH* coupling pathway. The contribution of OH* hydrogenation occurs at T > 520 K and is 18 %, 25 % and

36 % over the $\chi_{edge}(1.00)$, $\chi_{edge}(0.34)$ and $\chi_{edge}(0.04)$ multifaceted surface models, respectively (see Figure 6.6). The latter model approaches the Pt(100) model behaviour (see Chapter 4).

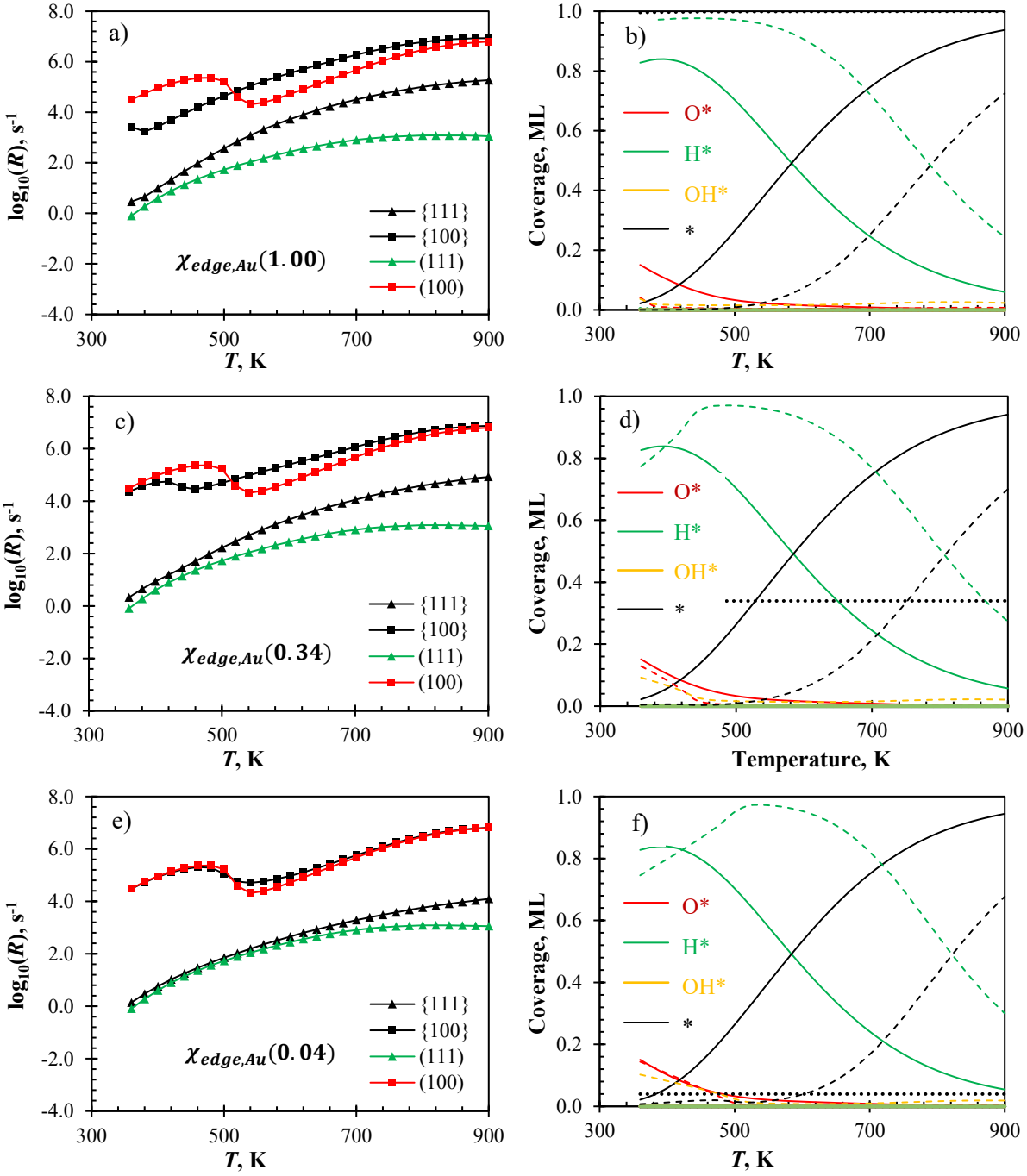

Figure 6.5: BWA model predicted ORR activity over a multifaceted Au/Pt surface, (a, c, e) H_2O evolution rates and (b, d, f) surface coverage over Au/Pt{111} facet (—), Au/Pt{100} facet (– – –) and edge sites (·····), for a $\boldsymbol{\chi_{edge}(1.00)}$ model (a, b), $\boldsymbol{\chi_{edge}(0.34)}$ model (c, d) and $\boldsymbol{\chi_{edge}(0.04)}$ model (e, f).

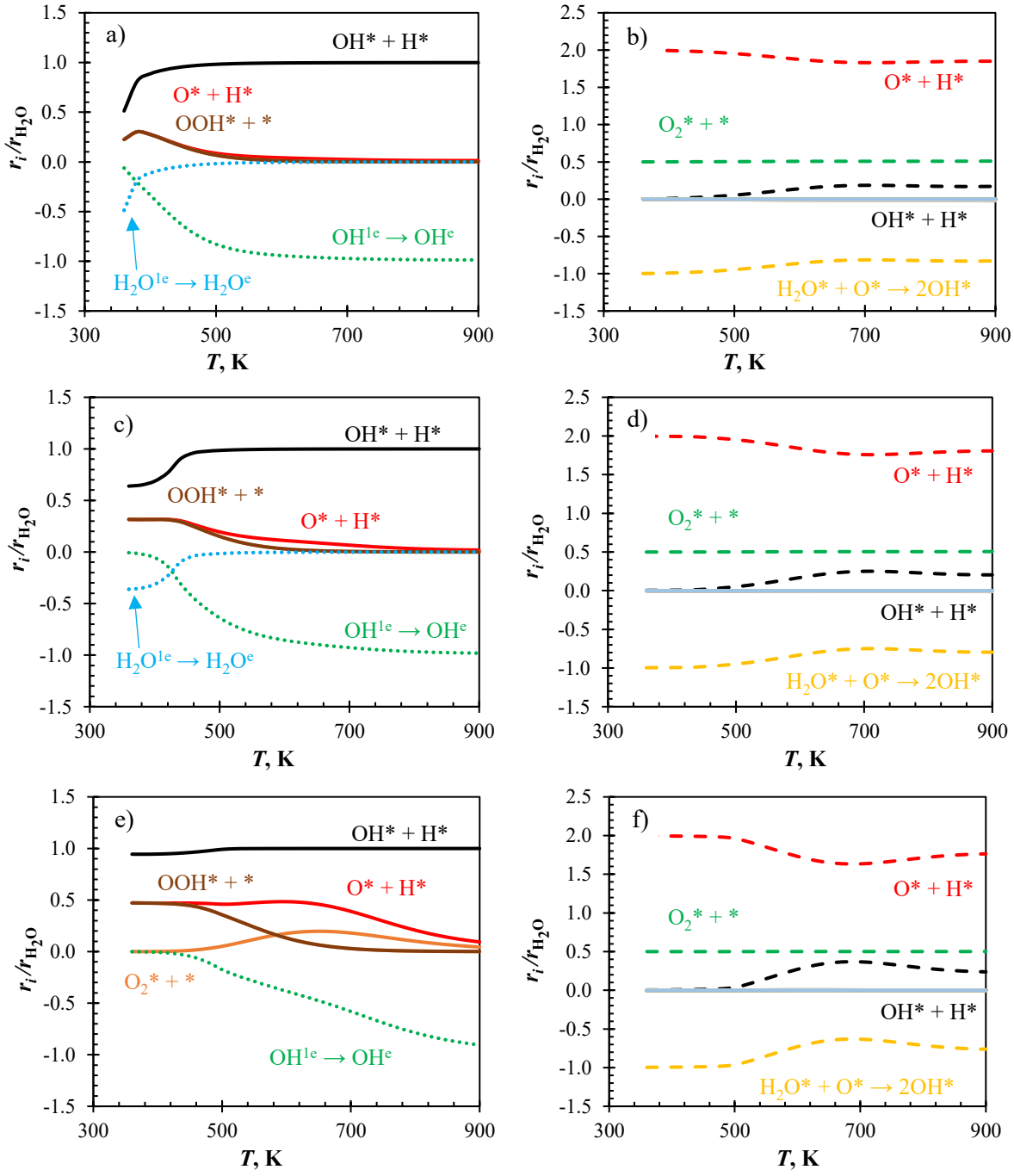

Figure 6.6: BWA model predicted ORR pathway over a multifaceted Au/Pt surface, (a, c, e) over Au/Pt{111} facet and (b, d, f) Au/Pt{100} facet; processes on Au/Pt{111} facet (—), Au/Pt{100} facet (− − −) and involving edge species (·····). Negative values indicate that the reverse reaction contributes to the H_2O evolution rate—(a,b) $\chi_{edge}(\mathbf{1.00})$, (c,d) $\chi_{edge}(\mathbf{0.34})$ and (e,f) $\chi_{edge}(\mathbf{0.04})$ models.

6.5.3 Degree of rate control analysis

Figure 6.7 present the degree of rate control analysis of the ORR activity from Au/Pt{111} and Au/Pt{100} facet of a $\chi_{edge}(0.34)$ multifaceted surface model. Interpretation of this data is not as trivial as in the previous cases, owing to the high degree of coupling between process on different

terrace types. The ORR from Au/Pt{100} facets, of a $\chi_{edge}(0.34)$ multifaceted surface, is controlled by O* hydrogenation below 420 K and O_2* dissociation above 420 K. The diffusion of H* and OH* from Au/Pt{100} towards the Au/Pt{111} facet increases the number of vacant sites consequently increasing O_2 adsorption and dissociation rates. Over Au/Pt{111} facet, the ORR is limited by OH* diffusion from Au/Pt{100} to Au/Pt{111} facet. OH*-OH* coupling over Au/Pt{100} seem to inhibit the ORR over Au/Pt{111} above 480 K. The latter is expected given that the inter-facet exchange of OH* is also dependent on the coverage of Au/Pt{100} with OH* and increasing OH*-OH* coupling rate on the Au/Pt{100} facet lowers the OH* coverage.

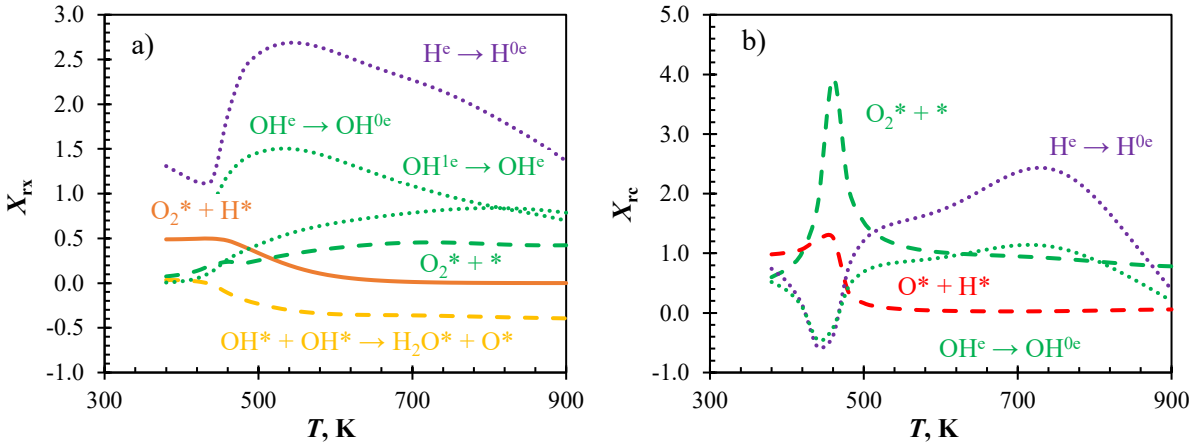

Figure 6.7: BWA predicted degree of rate control analysis over a $\chi_{edge}(0.34)$ multifaceted Au/Pt surface, H_2O desorption from (a) Pt{111} and (b) Pt{100}facet as a key reaction; showing {111} facet (—), {100} facet (– – –) and over edge (·····) processes with significant effect on the ORR rates.

6.6 ORR activity over multifaceted Ag/Pt surface

Over Ag modified Pt NW edge sites, the OH* diffusion barriers are the lowest in all three NW models, i.e. unmodified, Au and Ag modified models (see Table 6.2). These low diffusion barriers may result in further improvements of the activities observed from the Au modified system. As with the Au system, the ORR activity over three multifaceted Ag/Pt models has been investigated. The results from a BWA model are presented here whilst the QCA results are given in Appendix G3. The ORR rates and surface coverages for different multifaceted surface models are presented in Figure 6.8. The reaction pathway plots over the different surface models are shown in Figure 6.9.

6.6.1 Steady state ORR rates

Based on the BWA model, the H_2O evolution rate, over Ag/Pt{111} facets, is higher than over Ag/Pt{100} above 480 K and below 720 K on both $\chi_{edge}(1.00)$ and $\chi_{edge}(0.34)$ multi-faceted surface models. Over the $\chi_{edge}(0.04)$ model the rate is only marginally higher over Ag/Pt{111} than over Ag/Pt{100} between 520 K and 660 K. Over the entire temperature range and on all three multi-faceted

models, the ORR rates from Ag/Pt{111} are significantly higher than rates from Pt(111), Pt{111} and Au/Pt{111} surfaces (see Figures 5.6a, 6.5a,c,e, and 6.8a,c,e). In contrast, the ORR rate from Ag/Pt{100} facets of the $\chi_{edge}(1.00)$ and $\chi_{edge}(0.34)$ were significantly lower above 520 K. This decrease in ORR rates on Ag/Pt{100} was also seen on the Ag/Pt{111} facet, suggesting that the decrease is not caused by the transfer of OH* intermediates to the Ag/Pt{111} facet, rather the corresponding decrease in ORR on Ag/Pt{111} is a result of falling ORR rates on Ag/Pt{100}. Similar to previous observations (ORR on Pt{100}), the increase in H* coverage toward 1.0 ML is concomitant with a sharp decrease in ORR rate. Figure F1.2 shows how the ORR rate on Pt(100) correlates to H* coverage. The trend in surface coverage over Ag/Pt{111} and Ag/Pt{100} compares well with that predicted over Pt(111) and Pt(100) surfaces, respectively—a ca. 20 K downward shift in the coverage trends was predicted over Ag/Pt{111} surface vs. Pt(111) (see Figures 4.2a, 4.6a and 6.8a,c,e). On Ag/Pt{100} the H* coverage was higher than on Pt(100) explaining the larger decrease in the ORR rates compared to rates on the extended Pt(100) surface.

Additionally, over Ag/Pt{111} surfaces there is a partial build up in O* coverage at high temperature, due to the slow OH*-OH* coupling reaction occurring over Ag/Pt{111} facet. The QCA model predicts O* coverage up to 0.4 ML over the $\chi_{edge}(1.00)$ surface model—this decreased with decreasing relative density of edge sites but remained higher than prediction by BWA (see Figure G3.1). The ORR rates predicted by the QCA model are quite interesting. From Ag/Pt{100} the ORR approximates that from Pt(100) however the rate from Ag/Pt{111} is more than 100x faster than over Pt(111) even at the lowest edge site density considered, i.e. $\chi_{edge}(0.04)$, over the whole temperature range (see Figure G3.1). The maximum coverage of the Ag/Pt{100} facet with H* adsorbate was less than 0.9 ML in the whole temperature range.

6.6.2 Reaction pathway analysis

The ORR pathway over this surface was also investigated and Figure 6.9 presents the predicted results based on the BWA model over the three multifaceted surface models. Over Ag/Pt{111}, the ORR pathway is completely different to that previously observed over Au/Pt{111}, Pt{111} and Pt(111) surfaces. Over the whole temperature range, the ORR proceeds via OH* diffusion (from {100} → {111}) and OH* hydrogenation to H_2O*. The latter is true for all multifaceted models studied. On the other hand, the ORR over Ag/Pt{100} facet follows the OH*-OH* coupling pathway below 480 K after which contributions from direct OH* hydrogenation increases to > 50 % (see Figures 6.9b, d and e). This is caused by low OH* coverages and high H* coverages, the former limits the OH*-OH* coupling rate which depends on the square of the low coverage values.

Therefore, the overall ORR pathway over Ag modified multifaceted surfaces presents the highest inter-facet cooperation even at low temperatures. This cooperation is even evident in the predicted degree of rate control behaviour over Ag/Pt{111} and Ag/Pt{100} (see Figure 6.10). The latter facets are controlled by the same reaction steps above 500 K. Below this temperature OH* transfer to Ag/Pt{111} and O* hydrogenation over Pt{100} limit the ORR rate over Ag/Pt{111} and Ag/Pt{100} facets, respectively. Analyses of the QCA generated data suggest a similar reaction pathway from Ag/Pt{111}, however from the Ag/Pt{100} facet, OH* hydrogenation plays no role in the H_2O* formation over the whole temperature range studied. This is because the QCA predicted surface coverage with OH* is higher and the coverage with H* does not approach 1.0 ML as is the case in BWA results. Therefore, resulting in higher OH*-OH* coupling rates than direct OH* hydrogenation rates on the {100} facet.

6.7 Summary and Discussion

The ORR activity on modified multi-faceted Pt surfaces has been investigated. Compared to the reaction activity and pathway on extended surfaces and unmodified multi-faceted surfaces, edge modification can lead to improved ORR activity, particularly on {111} type facets. Figure 6.11a presents the comparison of ORR rates predicted by the BWA model on various surfaces at different temperatures.

The ORR rate from Pt(111) surface increases monotonically with temperature between 300 K and 900 K and remains the lowest compared to other surfaces. On this surface the ORR proceeds via a peroxyl pathway up to ca. 500 K from which it follows a dissociative pathway. It is limited by O* hydrogenation at low temperatures and O_2* dissociation at high temperatures. On multi-faceted Pt surfaces the ORR rate from the Pt{111} facet (equivalence of the Pt(111) surface) is almost equal to that rate on Pt(111), but only up to 500 K, thereafter the rate on Pt{111} increases exponentially and becomes several orders of magnitude higher. With regards to the pathway followed by the ORR on this surface, at low temperature the ORR pathway is similar to the pathway on Pt(111) whilst at high temperatures, i.e. $T > 500$ K, the ORR neither follows a peroxyl nor dissociative pathway. Instead, the OH* adsorbates diffuse from the Pt{100} facet toward the Pt{111} facet where they are easily hydrogenated to H_2O*. This behaviour explains the very high ORR rates on this facet at $T > 500$ K. Furthermore, the rate limiting step at $T < 500$ K is the same as on Pt(111) whilst at $T > 500$ K, the ORR is limited mostly by the inter-facet exchange of OH* and the dissociation of O_2* on the adjacent Pt{100} facet.

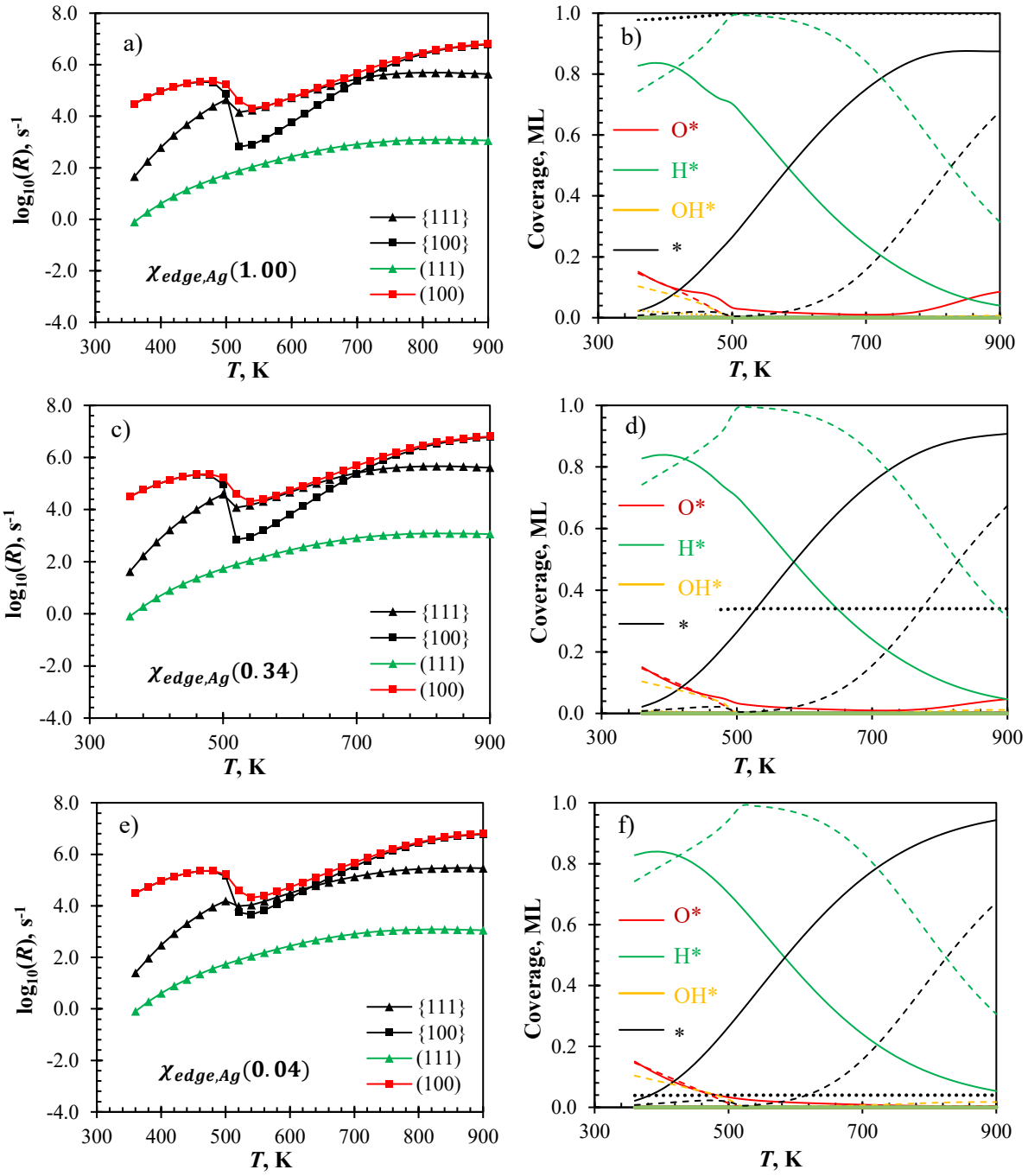

Figure 6.8: BWA model predicted ORR activity over a multifaceted Ag/Pt surface, (a, c, e) H_2O evolution rates and (b, d, f) surface coverage over Ag/Pt{111} facet (—), Ag/Pt{100} facet (– – –) and edge sites (·····), for a $\boldsymbol{\chi_{edge}(1.00)}$ model (a, b), $\boldsymbol{\chi_{edge}(0.34)}$ model (c, d) and $\boldsymbol{\chi_{edge}(0.04)}$ model (e, f).

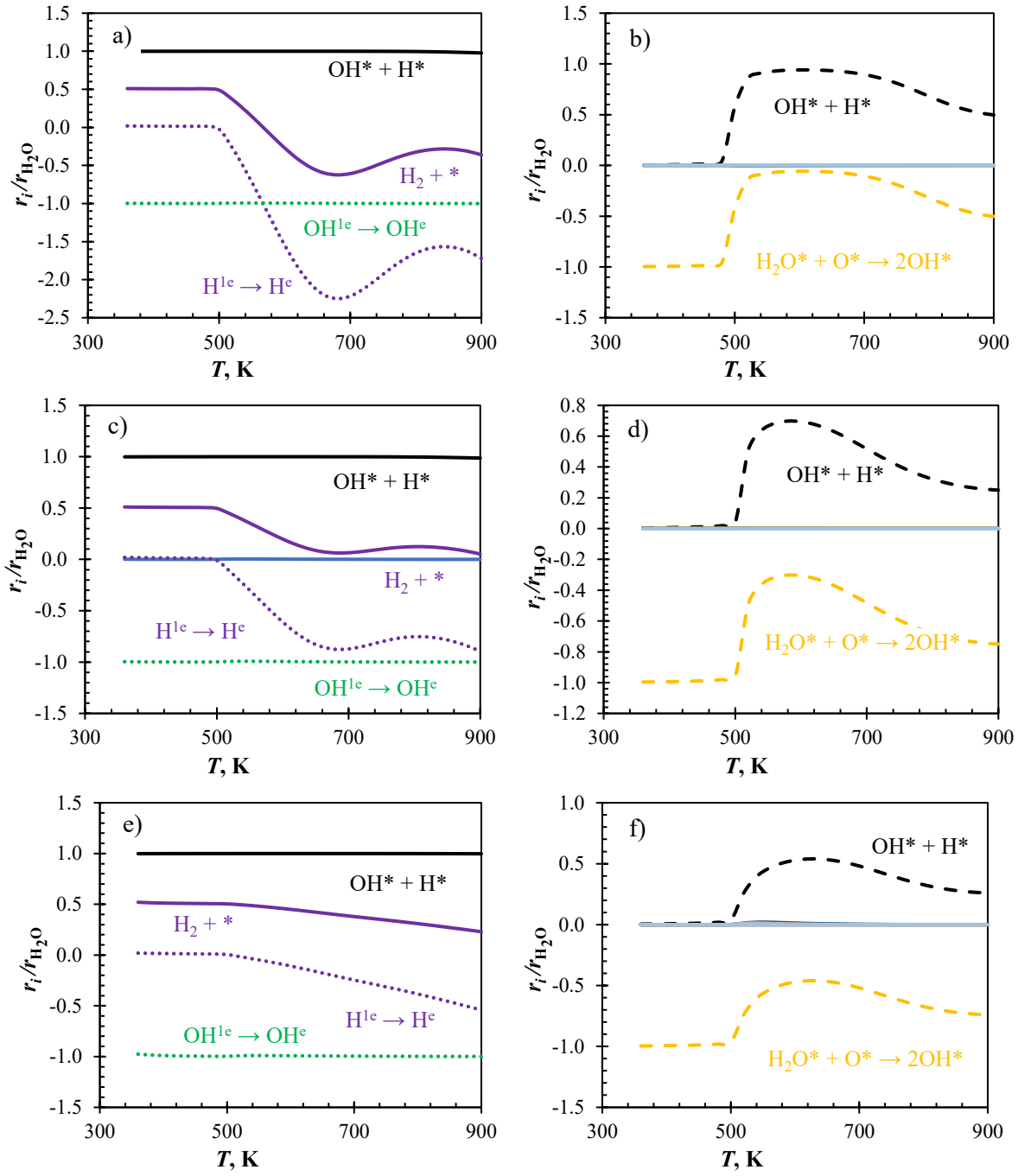

Figure 6.9: BWA model predicted ORR pathway over a multifaceted Ag/Pt surface , (a, c, e) over Ag/Pt{111} facet and (b, d, f) Ag/Pt{100} facet; processes on Ag/Pt{111} facet (—), Ag/Pt{100} facet (− − −) and involving edge species (·····). Negative values indicate that the reverse reaction contributes to the H_2O evolution rate—(a,b) $\boldsymbol{\chi_{edge}(1.00)}$, (c,d) $\boldsymbol{\chi_{edge}(0.34)}$ and (e,f) $\boldsymbol{\chi_{edge}(0.04)}$ models.

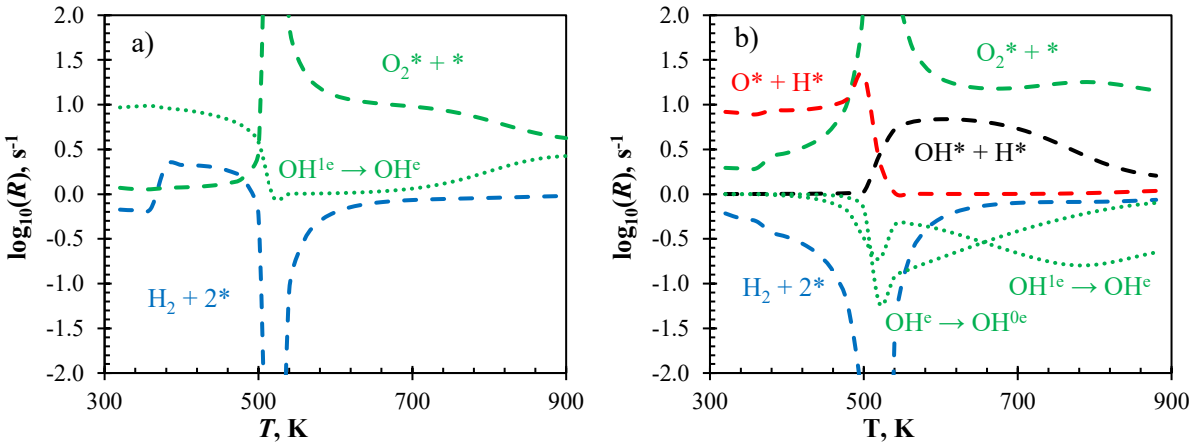

Figure 6.10: BWA predicted degree of rate control analysis over a $\chi_{edge}(0.34)$ multifaceted Ag/Pt surface, H_2O desorption from (a) Pt{111} and (b) Pt{100}facet as a key reaction; showing {111} facet (—), {100} facet (– – –) and over edge (·····) processes with significant effect on the ORR rates.

Modification of edge sites with Au and Ag further improves the ORR rates on {111} type surfaces. On both Au/Pt{111} and Ag/Pt{111} facets, the ORR rates are higher than on Pt(111) surface. The ORR pathway on these facets is similar, and it involves the diffusion of OH* adsorbates from adjacent {100} type facets toward the respective {111} facets where they undergo hydrogenation to H_2O*. On Ag/Pt{111} facets the ORR has higher rates than on other equivalent {111} type surfaces and also proceeds purely via the OH* exchange pathway even at temperatures as low as 360 K. The inter-facet exchange rates of OH* adsorbates on both Au and Ag modified systems are higher than on unmodified Pt surfaces. According to the BWA model, on Ag/Pt{111} facet, between 520 K and 700 K, the ORR rates are higher than on the coupled Ag/Pt{100} facet. The latter is not caused by fast OH* diffusion rates from Ag/Pt{100} toward Ag/Pt{111} but the associated depletion of OH* adsorbates on Ag/Pt{100} as a result of surface poisoning by H* adsorbates. The ORR on Au/Pt{111} and Ag/Pt{111} facets is limited by the inter-facet exchange of OH* adsorbates and O_2* dissociation occurring on the coupled {100} facets (see Figures 6.7 and 6.10).

The comparison of ORR rate profiles on the {100} type surfaces is less trivial. This is because of the peculiar behaviour of the ORR rate on these surfaces. On the Pt(100) surface the ORR rate increases from ca. 10^3 s^{-1} at 300 K passing through a maximum at 480 K and then decreasing sharply thereafter before increasing again after 540 K (see Figure 6.11). The degree of rate control analysis was able to show that on this surface the ORR is controlled by two reactions; O* hydrogenation up to ca. 540 K and then O_2* dissociation thereafter. This change is due to the extinction of vacant sites as the coverage with H* adsorbates increases towards a full monolayer. The sharply decreasing fraction of vacant sites and O_2* adsorbates leads to slower O_2* dissociation rates which ultimately lead to the extinction of

O* and OH* intermediates and a change in the ORR rate limiting step before a complete transition after 540 K. An extinction-ignition-extinction behaviour can explain the predicted bimaximal ORR rate profile.

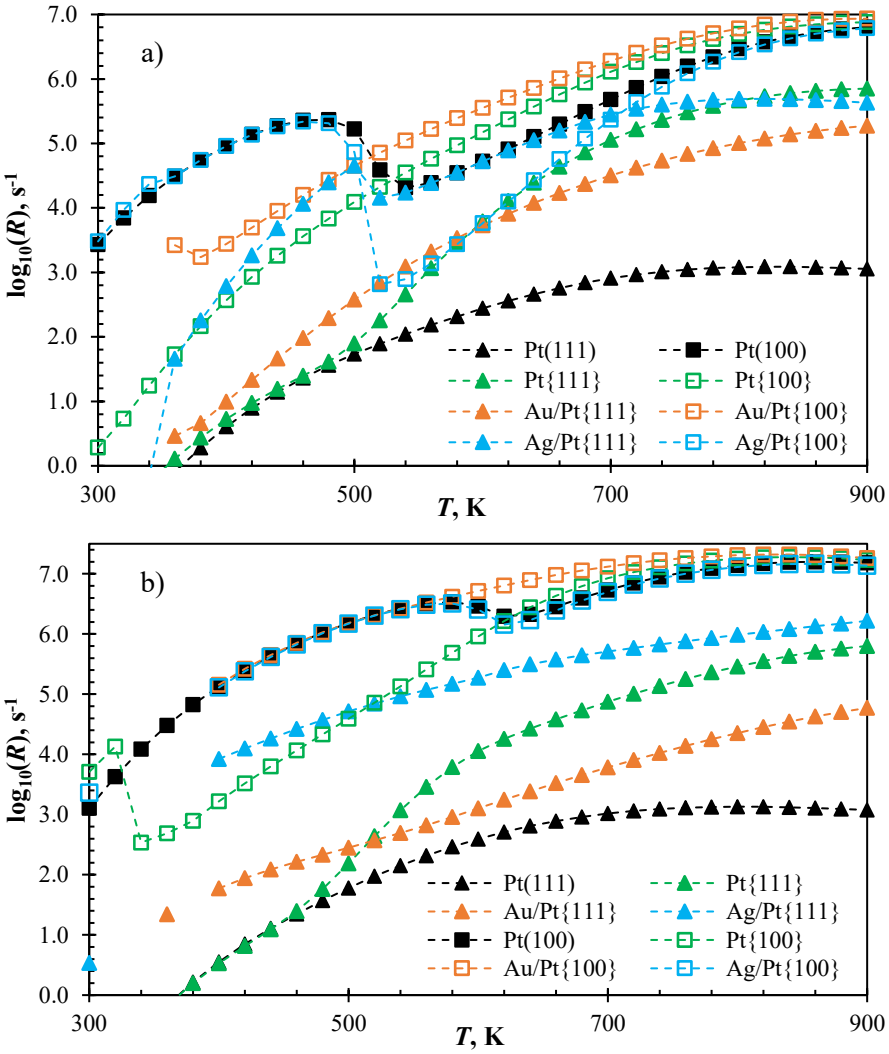

Figure 6.11: (a) BWA and (b) QCA predicted ORR rates over various χ_{edge} (1.00) multi-faceted surfaces under dry gas compositions (H_2:O_2 = 2:1) and 1 bar.

On Pt{100} the ORR rate does not have the same bimaximal feature as the ORR on Pt(100). Instead, the ORR rate on this facet starts lower than the rate on Pt(100) at low temperatures and then increase monotonically exceeding the rate on Pt(100) at 540 K and then plateaus near 900 K. On this facet the ORR pathway is similar to that on Pt(100) if near-edge reactions are omitted. Including the latter reactions leads to the participation of near-edge OH*-OH* coupling reactions in the ORR pathway however it does not change the net ORR rate (see Figures F2.1, F2.2, 5.9 and 5.12). Due to inter-facet connectivity, at low temperatures, H* adsorbates diffuse from Pt{111} toward Pt{100} and as a result the surface coverage with H* increases to near a monolayer (see Figure in G4.1 and Figure 5.8).

Because of this high H* coverage, the ORR rate becomes limited by O_2* dissociation at temperatures as low as 300 K (cf. 540 K on Pt(100) surfaces).

Au and Ag modification improves the OH* diffusion rates from {100} facets toward {111} facets and lowers the temperature at which this diffusion starts to occur. On Au/Pt{100} the ORR rate profile is similar to that on Pt{100}. On the other hand, the ORR rate profile on Ag/Pt{100} resembles that on Pt(100) except between 520 K and 700 K where the {100} facet is less active than the {111} facet. The latter is due to a higher barrier for H* diffusion from Ag/Pt{111} toward Ag/Pt{100} facet compared to other multifaceted surfaces. Figure G4.3 shows that at low temperatures the inter-facet diffusion of H* on Ag/Pt surfaces is nearly zero whilst on Au/Pt and Pt multi-faceted surfaces H* diffuses from {111} towards {100} at low temperatures and {100} toward {111} at higher temperatures.

6.8 Conclusions

Inter-facet exchange of ORR intermediates has been investigated over multifaceted Pt surfaces—in these simulations it was observed that exchange of OH* between Pt{111} and Pt{100} facets had a significant effect on the ORR activity and pathway. At high temperatures the ORR rates from Pt{111} facets were higher, and the mechanisms involved the diffusion of OH* from Pt{100} → edge → Pt{111} facet. Pt NWs with Ag and Au edges were considered to study their effect on the inter-facet mobility of reaction intermediates. First, MD simulations showed Au and Ag atoms are good candidate elements for surface modification of Pt NWs. These atoms remain on the surface under thermal annealing. However, since neither Au nor Ag prefer the edge sites over terrace sites other treatment conditions are needed to prepare model Pt structures with Au and Ag modified edges.

DFT calculations show that on these modified surfaces the transport of reaction intermediates differs greatly from unmodified systems. The OH* diffusion barriers between the {111} and {100} facets of Au and Ag modified are lowered significantly compared to pure multi-faceted Pt. On the other hand, the diffusion of O_2* and O* from either facet to the next is prohibited because of weak adsorption of these molecule on Au/Ag edge sites. Interestingly, the diffusion barriers of H* from {100} toward {111} facets were higher for Ag modified surfaces than on any other surface studied here.

Microkinetic simulations show very interesting results. Despite some differences in actual rate magnitudes, both QCA and BWA models predict very high ORR rates on {111} facets of modified Pt surfaces compared to Pt(111). These high rates are predicted even at low temperatures unlike on Pt{111} where improved rates are only seen at high temperatures.

CHAPTER 7:General Conclusions and Outlook

The primary objective of this study was to develop an understanding of the nature and extent of inter-facet cooperation between adjacent Pt{111} and Pt{100} facets and how this influences the ORR activity and mechanism over multi-faceted Pt surfaces. Using a combination of DFT calculations and microkinetic simulations, an entirely first principles based mechanistic insight into this phenomenon was established. Furthermore, various options were explored to positively influence inter-facet cooperation.

The important considerations for this phenomenon are the (1) ORR activity and mobility of its intermediates on terrace surfaces, (2) diffusion energetics associated with inter-facet mobility of ORR intermediates and (3) energetics associated with reaction steps involving near-edge and edge intermediates. The energetics associated with these processes were generated from DFT. Microkinetic simulations were than performed to ascertain, in particular, the role of inter-facet mobility of reaction intermediates on the ORR activity and pathway.

Based on DFT calculations, over Pt(111) and Pt(100) surfaces, it can be concluded that most ORR intermediates are highly mobile. With the exception of O* on Pt(111) and OH* on Pt(100), the diffusion barriers of all ORR intermediates are lower than 0.3 eV. The diffusion of O* on Pt(111) involves a transition between an fcc site and an hcp site via a bridge site and has an energy barrier of 0.597 eV. The large difference in the stability of O* on these adsorption sites is responsible for this high diffusion barrier. On Pt(100), the OH* diffusion barrier is 0.548 eV, also high because of the difference in the adsorption energy of OH* on bridge and top sites.

Microkinetic analyses of the ORR process were conducted assuming a gas/solid interface with a stoichiometric gas composition, H_2:O_2 = 2:1. Coverage effects on the adsorption and reaction energies were incorporated based on cluster expansion within the Bragg-Williams Approximation (BWA) and a Quasi-Chemical Approximation (QCA) methods. From microkinetic simulations, it was shown that lateral interactions are extremely important, especially at low temperatures. Excluding the effects of lateral interactions in microkinetic simulations results in very low ORR activities, especially at low

temperatures, in contradiction with experiments. These low rates are due to the site-blocking effect of O* which is predicted to have very high coverages at low temperatures.

The ORR rates predicted by the BWA and QCA models are in closer agreement with experiments than predicted rates in the absence of lateral interactions. Both BWA and QCA predict high ORR activities on Pt(100) compared to Pt(111). At low temperatures, the ORR on both Pt(111) and Pt(100) surfaces is limited by O* hydrogenation. The high activity on Pt(100) compared to Pt(111) can then be explained based on the low activation energy for O* hydrogenation on Pt(100) compared to Pt(111), i.e. 0.532 eV vs. 0.969 eV. At high temperatures the high ORR activity on Pt(100) compared to Pt(111) can also be explained by the fact that on both surfaces O_2* dissociation is rate-limiting and on Pt(100) O_2* dissociation is more facile.

The ORR pathway on Pt(111) is temperature dependent and less affected by the method by which lateral interactions are incorporated. The peroxyl and dissociative pathways are followed at low and high temperature regions, respectively. On Pt(100), the ORR pathway is less sensitive to temperature. Furthermore, it follows a dissociative pathway with OH*-OH disproportionation reaction responsible for H_2O* formation, unlike on Pt(111) where H_2O* is formed via OH* hydrogenation. The BWA model and kinetic Monte Carlo model predict a mixed OH*-OH* disproportionation – OH* hydrogenation process.

It was postulated that the diffusion of O* from Pt{111} facet toward the Pt{100} and OH* in the opposite direction, could provide an alternative ORR pathway on multi-faceted Pt surfaces. Depending on the difficulty of this inter-facet exchange, the ORR activity can be higher than on isolated surfaces. DFT calculations show that O* diffusion from a Pt{111} facet toward a Pt{100} facet has a highest diffusion barrier of 0.646 eV, for the O*(Pt{111} facet, $f^{(1e)}$) → O*(edge) step, i.e. inter-facet mobility limit. On the other hand, OH* diffusion from a Pt{100} to a Pt{111} facet has a highest diffusion barrier of 0.991 eV, for the OH*(edge) → OH*(Pt{111} facet) step, i.e. inter-facet mobility limit. Lateral interactions at edge sites can lower this barrier by destabilising the adsorption at edge sites.

Over multi-faceted surfaces the ORR proceeds via a unique pathway way which is temperature dependent. Moreover, the ORR rate-limiting reaction steps on Pt{100} and Pt{111} facets differ from Pt(100) and Pt(111) surfaces, respectively. On the ORR activity, fast H* mobility leads to a facile flow toward Pt{100} facets at low temperatures and toward Pt{111} facets at high temperatures. The former leads to low coverage of Pt{100} facets with O* and OH* adsorbates compared to equivalent coverages on Pt(100) surfaces—consequently lowering the ORR activity. At the same time, the high coverage of Pt{100} facets with H* decreases the fraction of empty sites for O_2* dissociation. This is

why on Pt{100} the ORR rate is controlled by O_2* dissociation. The flow of H* away from Pt{100} facets at high temperatures leads to improved O_2* dissociation rates and consequently higher ORR rates compared to Pt(100).

On the other hand, at low temperatures the ORR activity, pathway and rate-controlling steps are the same on Pt{111} facets as on Pt(111) surfaces. Above 500 K (and slightly lower for QCA models), the ORR rate on Pt{111} facets becomes significantly higher than on Pt(111) surfaces. This is due OH* diffusion from edge sites toward Pt{111} facets. Consequently, the ORR follows a unique pathway in which O_2* adsorption, dissociation and O* hydrogenation have insignificant contributions in the formation of H_2O* on Pt{111}. The ORR activity on Pt{111} facets is then limited by O_2* dissociation occurring on adjacent Pt{100} facets and the diffusion of OH* adsorbates toward Pt{111} facets from Pt{100} facets.

These results suggest a new catalyst design approach, where the exchange of OH* adsorbates between Pt{100} and Pt{111} facets can be manipulated to influence the ORR activity and pathway. Here, modification of Pt NW edges with Au and Ag was considered. The Au and Ag modified edge sites interact weakly with OH* adsorbates and their interaction with O_2* and O* adsorbates is nearly endothermic. DFT calculations show that on Au modified Pt NWs the highest diffusion barrier for OH* (Au/Pt{100} → Au/Pt{111} flow) is 0.885 eV (cf. 0.991 eV unmodified Pt NWs) and on Ag modified Pt NWs the highest diffusion barrier for OH* is 0.603 eV (Au/Pt{100} → Au/Pt{111} flow). The highest inter-facet diffusion barriers of O* (Pt{111} → Pt{100} flow) were calculated to be 1.335 eV and 1.620 eV on Au and Ag modified Pt NWs, respectively. These results are evidence that surface modification does not only enable improved diffusion properties but also selectivity.

Microkinetic simulations based on the above data were conducted to determine the effect of edge modification on the ORR activity. The overall conclusions from these simulations is that edge modification improves the OH* exchange rate over a wider temperatures range. Modification with Ag leads to the highest improvement of the ORR rate on {111} facets whilst modification with Au was found to improve the ORR rates on {100} facets more.

In conclusion, this study has found that inter-facet cooperation improves the ORR rate on individual facets of multi-faceted surfaces by enabling reaction intermediate exchange. The OH* diffusion toward {111} facets leads to higher rates there and eliminates the need for O_2* adsorption, hydrogenation and dissociation and perhaps more importantly the need for O* hydrogenation which was found to be rate limiting on isolated Pt(111) surfaces. Furthermore, this study demonstrates that by using surface modification inter-facet diffusion properties of reaction intermediates can be improved selectively.

Whilst this study considers dry conditions, it shows the potential role of inter-facet cooperation in reaction kinetics. It is suggested that future studies consider existing developments in modelling ORR under electrochemical conditions in order to make more direct comparison to experimental studies. Edge modification has the ability to selectively enable inter-facet exchange of some reaction intermediates whilst inhibiting others. Therefore, it should be explored in rational catalyst design. It is further believed that other reaction systems may also benefit from such rational approaches. This study has provided a detailed approach towards a holistic understanding of the ORR process on multi-faceted surfaces. Important observations with deep consequences in practical systems have been highlighted.

References

[1] O. Edenhofer, R. Pichs-Madruga, Y. Sokona, E. Farahani, S. Kadner, K. Seyboth, A. Adler, I. Baum, S. Brunner, P. Eickemeier, B. Kriemann, J. Savolainen, S. Schlömer, C. von Stechow, T. Zwickel, J.C. Minx, eds., Climate Change 2014 Mitigation of Climate Change, Cambridge University Press, Cambridge, 2014.

[2] IEA, The Future of Hydrogen: Seizing Today's Opportunities, Osaka, 2019.

[3] X.Z. Yuan, H. Wang, PEM Fuel Cell Electrocatal. Catal. Layers Fundam. Appl. (2008) 1–87.

[4] A.A. Gewirth, M.S. Thorum, Inorg. Chem. 49 (2010) 3557–3566.

[5] H.A. Gasteiger, S.S. Kocha, B. Sompalli, F.T. Wagner, Appl. Catal. B Environ. 56 (2005) 9–35.

[6] H.A. Gasteiger, D.R. Baker, R.N. Carter, W. Gu, Y. Liu, F.T. Wagner, P.T. Yu, in: D. Stolten (Ed.), Hydrog. Energy, WILEY-VCH Verlag GmbH & Co. KGaA, Weinheim, 2010, pp. 3–16.

[7] J.K. Nørskov, J. Rossmeisl, A. Logadottir, L. Lindqvist, J.R. Kitchin, T. Bligaard, H. Jonsson, J. Phys. Chem. B 108 (2004) 17886–17892.

[8] Z.W. Seh, J. Kibsgaard, C.F. Dickens, I. Chorkendorff, J.K. Nørskov, T.F. Jaramillo, Science (80-.). 355 (2017) eaad4998.

[9] F. Barbir, in: F. Barbir (Ed.), PEM Fuel Cells, Elsevier, Burlington, 2005, pp. 17–32.

[10] N. Markovic, J. Electrochem. Soc. 144 (1997) 1591.

[11] C. Liu, S. Riffat, X. Wang, S. Sui, Y. Su, X. Zhou, J. Mater. Chem. A 5 (2016) 1808–1825.

[12] G.D. Barmparis, Z. Lodziana, N. Lopez, I.N. Remediakis, Beilstein J. Nanotechnol. 6 (2015) 361–368.

[13] L. Vitos, A. V. Ruban, H.L. Skriver, J. Kollár, Surf. Sci. 411 (1998) 186–202.

[14] Y. Xia, Y. Xiong, B. Lim, S.E. Skrabalak, Angew. Chemie Int. Ed. 48 (2009) 60–103.

[15] V. Tripković, I. Cerri, T. Bligaard, J. Rossmeisl, Catal. Letters 144 (2014) 380–388.

[16] K. Kinoshita, J. Electrochem. Soc. 137 (1990) 845.

[17] F.J. Perez-Alonso, D.N. McCarthy, A. Nierhoff, P. Hernandez-Fernandez, C. Strebel, I.E.L. Stephens, J.H. Nielsen, I. Chorkendorff, Angew. Chemie - Int. Ed. 51 (2012) 4641–4643.

[18] L. Su, W. Jia, C. Li, Y. Lei, ChemSusChem 7 (2014) 361–378.

[19] J. Kibsgaard, Y. Gorlin, Z. Chen, T.F. Jaramillo, J. Am. Chem. Soc. 134 (2012) 7758–7765.

[20] N.M. Marković, T.J. Schmidt, V. Stamenković, P.N. Ross, Fuel Cells 1 (2001) 105–116.

[21] N.M. Markovic, H.A. Gasteiger, P.N. Ross, J. Phys. Chem. 99 (1995) 3411–3415.

[22] V.R. Stamenkovic, B. Fowler, B.S. Mun, G. Wang, P.N. Ross, C.A. Lucas, N.M. Markovic, Science (80-.). 315 (2007) 493–497.

[23] S. Kondo, M. Nakamura, N. Maki, N. Hoshi, J. Phys. Chem. C 113 (2009) 12625–12628.

[24] N. Hoshi, M. Nakamura, A. Hitotsuyanagi, Electrochim. Acta 112 (2013) 899–904.

[25] M. Nesselberger, S. Ashton, J.C. Meier, I. Katsounaros, K.J.J. Mayrhofer, M. Arenz, J. Am. Chem. Soc. 133 (2011) 17428–33.

[26] Z. Duan, G. Wang, J. Phys. Chem. C 117 (2013) 6284–6292.

[27] K. Li, Y. Li, Y. Wang, F. He, M. Jiao, H. Tang, Z. Wu, J. Mater. Chem. A 3 (2015) 11444–11452.

[28] Z. Duan, G. Wang, Phys. Chem. Chem. Phys. 13 (2011) 20178–20187.

[29] J. Greeley, J. Rossmeisl, A. Hellmann, J.K. Norskov, Zeitschrift Für Phys. Chemie 221 (2007) 1209–1220.

[30] D.C. Ford, A.U. Nilekar, Y. Xu, M. Mavrikakis, Surf. Sci. 604 (2010) 1565–1575.

[31] V.R. Stamenkovic, B.S. Mun, M. Arenz, K.J.J. Mayrhofer, C.A. Lucas, G. Wang, P.N. Ross, N.M. Markovic, Nat. Mater. 6 (2007) 241–247.

[32] A.S. Bandarenka, H.A. Hansen, J. Rossmeisl, I.E.L. Stephens, Phys. Chem. Chem. Phys. 16 (2014) 13625–13629.

[33] Y. Takesue, M. Nakamura, N. Hoshi, Phys. Chem. Chem. Phys. 16 (2014) 13774–13779.

[34] V. Komanicky, A. Menzel, H. You, J. Phys. Chem. B 109 (2005) 23550–23557.

[35] V. Komanicky, A. Menzel, K.C. Chang, H. You, J. Phys. Chem. B 109 (2005) 23543–23549.

[36] V. Komanicky, H. Iddir, K.-C. Chang, A. Menzel, G. Karapetrov, D. Hennessy, P. Zapol, H. You, J. Am. Chem. Soc. 131 (2009) 5732–5733.

[37] G.A. Tritsaris, J. Greeley, J. Rossmeisl, J.K. Nørskov, Catal. Letters 141 (2011) 909–913.

[38] A. Mahata, A.S. Nair, B. Pathak, Catal. Sci. Technol. 9 (2019) 4835–4863.

[39] Y. Nie, L. Li, Z. Wei, Chem. Soc. Rev. 44 (2015) 2168–2201.

[40] H. Lv, D. Li, D. Strmcnik, A.P. Paulikas, N.M. Markovic, V.R. Stamenkovic, Nano Energy 29 (2016) 149–165.

[41] D. Li, N.M. Markovic, Y. Kang, H. Lv, V.R. Stamenkovic, Annu. Rev. Chem. Biomol. Eng. 7 (2016) 509–532.

[42] M. Shao, Q. Chang, J.-P. Dodelet, R. Chenitz, Chem. Rev. 116 (2016) 3594–3657.

[43] C. Zhang, X. Shen, Y. Pan, Z. Peng, Front. Energy 11 (2017) 268–285.

[44] T. Asset, R. Chattot, M. Fontana, B. Mercier-Guyon, N. Job, L. Dubau, F. Maillard, ChemPhysChem 19 (2018) 1552–1567.

[45] R. Jiang, S. on Tung, Z. Tang, L. Li, L. Ding, X. Xi, Y. Liu, L. Zhang, J. Zhang, Energy Storage Mater. 12 (2018) 260–276.

[46] V. Stamenković, T.J. Schmidt, P.N. Ross, N.M. Marković, J. Phys. Chem. B 106 (2002) 11970–11979.

[47] U.A. Paulus, A. Wokaun, G.G. Scherer, T.J. Schmidt, V. Stamenkovic, V. Radmilovic, N.M. Markovic, P.N. Ross, J. Phys. Chem. B 106 (2002) 4181–4191.

[48] V. Stamenković, T.J. Schmidt, P.N. Ross, N.M. Marković, J. Electroanal. Chem. 554–555 (2003) 191–199.

[49] M. Escudero-Escribano, P. Malacrida, M.H. Hansen, U.G. Vej-Hansen, A. Velazquez-Palenzuela, V. Tripkovic, J. Schiotz, J. Rossmeisl, I.E.L. Stephens, I. Chorkendorff, Science (80-.). 352 (2016) 73–76.

[50] J.F. Huang, P.K. Tseng, Chem. Sci. 9 (2018) 6134–6142.

[51] R. Jinnouchi, K. Kodama, T. Hatanaka, Y. Morimoto, Phys. Chem. Chem. Phys. 13 (2011) 21070–21083.

[52] H.A. Hansen, V. Viswanathan, J.K. Nørskov, J. Phys. Chem. C 118 (2014) 6706−6718.

[53] D. Fantauzzi, T. Zhu, J.E. Mueller, I.A.W. Filot, E.J.M. Hensen, T. Jacob, Catal. Letters 145 (2015) 451–457.

[54] R.G. Parr, Y. Weitao, Density-Functional Theory of Atoms and Molecules, Oxford University Press, New York, 1994.

[55] E.G. Lewars, Computational Chemistry: Introduction to the Theory and Applications of Molecular and Quantum Mechanics, 2nd ed., Springer Netherlands, Dordrecht, 2011.

[56] M. Springborg, in: M. Springborg (Ed.), Density-Functional Methods Chem. Mater. Sci., John Wiley & Sons, Chichester, 1997, pp. 1–16.

[57] W. Kohn, A.D. Becke, R.G. Parr, J. Phys. Chem. 100 (1996) 12974–12980.

[58] P. Hohenberg, W. Kohn, Phys. Rev. 136 (1964) B864–B871.

[59] W. Kohn, L.J. Sham, Phys. Rev. 140 (1965) A1133–A1138.

[60] J.P. Perdew, A. Ruzsinszky, J. Tao, V.N. Staroverov, G.E. Scuseria, G.I. Csonka, J. Chem. Phys. 123 (2005).

[61] P. Taylor, O. Heinonen, A Quantum Approach to Condensed Matter Physics, Cambridge University Press, Cambridge, 2003.

[62] J.P. Perdew, K. Burke, M. Ernzerhof, Phys. Rev. Lett. 77 (1996) 3865–3868.

[63] J.P. Perdew, Y. Wang, Phys. Rev. B 45 (1992) 13244–13249.

[64] B. Hammer, L.B. Hansen, J.K. Nørskov, Phys. Rev. B - Condens. Matter Mater. Phys. 59 (1999) 7413–7421.

[65] A.D. Becke, J. Chem. Phys. 98 (1993) 5648–5652.

[66] C. Adamo, V. Barone, J. Chem. Phys. 110 (1999) 6158–6170.

[67] J.P. Perdew, S. Kurth, A. Zupan, P. Blaha, Phys. Rev. Lett. 82 (1999) 2544–2547.

[68] J. Tao, J.P. Perdew, V.N. Staroverov, G.E. Scuseria, Phys. Rev. Lett. 91 (2003) 3–6.

[69] R. Armiento, A.E. Mattsson, Phys. Rev. B 72 (2005) 085108.

[70] A. Stroppa, G. Kresse, New J. Phys. 10 (2008) 063020.

[71] A.E. Mattsson, R. Armiento, J. Paier, G. Kresse, J.M. Wills, T.R. Mattsson, J. Chem. Phys. 128 (2008) 084714.

[72] K. Berland, V.R. Cooper, K. Lee, E. Schröder, T. Thonhauser, P. Hyldgaard, B.I. Lundqvist, Reports Prog. Phys. 78 (2015) 066501.

[73] P.L. Cilliers, Phase diagram for the co-adsorption of O and OH on Pt(100) and Pt(111) as determined by DFT, MSc. dissertation, University of Cape Town, 2015. Available: http://hdl.handle.net/11427/27897.

[74] S. Grimme, J. Comput. Chem. 27 (2006) 1787–1799.

[75] S. Grimme, J. Antony, S. Ehrlich, H. Krieg, J. Chem. Phys. 132 (2010) 154104.

[76] A. Tkatchenko, M. Scheffler, Phys. Rev. Lett. 102 (2009) 6–9.

[77] H. Rydberg, B.I. Lundqvist, D.C. Langreth, M. Dion, Phys. Rev. B - Condens. Matter Mater. Phys. 62 (2000) 6997–7006.

[78] M. Dion, H. Rydberg, E. Schröder, D.C. Langreth, B.I. Lundqvist, Phys. Rev. Lett. 92 (2004) 22–25.

[79] J. Klimeš, D.R. Bowler, A. Michaelides, J. Phys. Condens. Matter 22 (2010) 022201.

[80] K. Lee, É.D. Murray, L. Kong, B.I. Lundqvist, D.C. Langreth, Phys. Rev. B 82 (2010) 081101.

[81] G. Kresse, J. Hafner, Phys. Rev. B 47 (1993) 558.

[82] G. Kresse, J. Hafner, J. Phys. Condens. Matter 6 (1994) 8245–8257.

[83] G. Kresse, J. Furthmüller, Comput. Mater. Sci. 6 (1996) 15–50.

[84] G. Kresse, J. Furthmüller, Phys. Rev. B 54 (1996) 11169–11186.

[85] P.E. Blöchl, Phys. Rev. B 50 (1994) 17953–17979.

[86] G. Kresse, D. Joubert, Phys. Rev. B 59 (1999) 1758–1775.

[87] T. Gambu, A DFT Study of the Interaction of Ox with Pt Nanorod Edge Sites: A Model for the ORR Activity on Pt Nanoparticle Edges, MSc. dissertation, University of Cape Town, 2015. Available: http://hdl.handle.net/11427/20054.

[88] M. Payne, M. Teter, D. Allan, T. Arias, J. Joannopoulos, Rev. Mod. Phys. 64 (1992) 1045–1097.

[89] H. Ibach, H. Lüth, Solid-State Physics: An Introduction to Principles of Materials Science, 4th ed., Springer Berlin Heidelberg, Berlin, Heidelberg, 2009.

[90] H.J. Monkhorst, J.D. Pack, Phys. Rev. B 13 (1976) 5188–5192.

[91] D.J. Chadi, M.L. Cohen, Phys. Rev. B 8 (1973) 5747–5753.

[92] M. Methfessel, A.T. Paxton, Phys. Rev. B 40 (1989) 3616–3621.

[93] T. Ogawa, A. Kuwabara, C.A.J. Fisher, H. Moriwake, T. Miwa, J. Phys. Chem. C 117 (2013) 9772–9778.

[94] P.C. Jennings, H.A. Aleksandrov, K.M. Neyman, R.L. Johnston, Phys. Chem. Chem. Phys. 16 (2014) 26539–26545.

[95] T.G. Gambu, M.A. Petersen, E. van Steen, Catal. Today 312 (2018) 126–131.

[96] G. Henkelman, B.P. Uberuaga, H. Jónsson, J. Chem. Phys. 113 (2000) 9901–9904.

[97] F. Birch, Phys. Rev. 71 (1947) 809–824.

[98] H. Yang, S. Kumar, S. Zou, J. Electroanal. Chem. 688 (2013) 180–188.

[99] W.P. Davey, Phys. Rev. 25 (1925) 753–761.

[100] C. Kittel, Introduction to Solid State Physics, 8th ed., John Wiley & Sons, Hoboken, 2005.

[101] D.J. Liu, J.W. Evans, ChemPhysChem 11 (2010) 2174–2181.

[102] V.P. Zhdanov, Surf. Sci. 111 (1981) 63–79.

[103] V.P. Zhdanov, Elementary Physicochemical Processes on Solid Surfaces, Springer US, Boston, MA, 1991.

[104] A.P.J. Jansen, An Introduction to Kinetic Monte Carlo Simulations of Surface Reactions, Springer Berlin Heidelberg, Berlin, Heidelberg, 2012.

[105] A. Hellman, K. Honkala, J. Chem. Phys. 127 (2007) 194704.

[106] M. Pineda, M. Stamatakis, J. Chem. Phys. 147 (2017) 024105.

[107] L. Kunz, F.M. Kuhn, O. Deutschmann, J. Chem. Phys. 143 (2015) 044108.

[108] K. Reuter, in: Model. Simul. Heterog. Catal. React., Wiley-VCH Verlag GmbH & Co. KGaA, Weinheim, Germany, 2011, pp. 71–111.

[109] D. Eberle, B. Horstmann, Electrochim. Acta 137 (2014) 714–720.

[110] L. Qi, J. Li, J. Catal. 295 (2012) 59–69.

[111] V.P. Zhdanov, J. Chem. Phys. 114 (2001) 4746–4748.

[112] A. Papoulis, Probability, Random Variables, and Stochastic Processes, McGraw-Hill, New York, 1965.

[113] F. Hess, J. Comput. Chem. 40 (2019) 2664–2676.

[114] L.C. Grabow, A.A. Gokhale, S.T. Evans, J.A. Dumesic, M. Mavrikakis, J. Phys. Chem. C 112 (2008) 4608–4617.

[115] G.S. Hammond, J. Am. Chem. Soc. 77 (1955) 334–338.

[116] E.D. Hermes, A.N. Janes, J.R. Schmidt, ACS Catal. 8 (2018) 272–282.

[117] T. Gambu, R. Abrahams, E. van Steen, Catalysts 9 (2019) 310.

[118] D. Vasić, I. Pašti, N. Gavrilov, S. Mentus, Russ. J. Phys. Chem. A 87 (2013) 2214–2218.

[119] R. Jinnouchi, K. Kodama, Y. Morimoto, J. Electroanal. Chem. 716 (2014) 31–44.

[120] G. Kresse, J. Hafner, J. Phys. Condens. Matter 6 (1994) 8245–8257.

[121] Z. Duan, G. Wang, Phys. Chem. Chem. Phys. 13 (2011) 20178.

[122] Z. Yang, J. Wang, X. Yu, Phys. Lett. Sect. A Gen. At. Solid State Phys. 374 (2010) 4713–4717.

[123] D.C. Ford, Y. Xu, M. Mavrikakis, Surf. Sci. 587 (2005) 159–174.

[124] T. Ogawa, A. Kuwabara, C.A.J. Fisher, H. Moriwake, J. Phys. Chem. C 118 (2014) 23675–23681.

[125] G. Peng, M. Mavrikakis, Nano Lett. 15 (2015) 629–634.

[126] G.-F. Wei, Z.-P. Liu, Phys. Chem. Chem. Phys. 15 (2013) 18555–18561.

[127] J.X. Wang, J. Zhang, R.R. Adzic, J. Phys. Chem. A 111 (2007) 12702–12710.

[128] J. Rossmeisl, G.S. Karlberg, T. Jaramillo, J.K. Nørskov, Faraday Discuss. 140 (2009) 337–346.

[129] V. Rai, M. Aryanpour, H. Pitsch, J. Phys. Chem. C 112 (2008) 9760–9768.

[130] M. Markiewicz, C. Zalitis, A. Kucernak, Electrochim. Acta 179 (2015) 126–136.

[131] J. Huang, M. Eikerling, Curr. Opin. Electrochem. 13 (2019) 157–165.

[132] C.T. Campbell, J. Catal. 204 (2001) 520–524.

[133] A. Michaelides, P. Hu, J. Chem. Phys. 114 (2001) 513.

[134] H. Ogasawara, B. Brena, D. Nordlund, M. Nyberg, A. Pelmenschikov, L.G.M. Pettersson, A. Nilsson, Phys. Rev. Lett. 89 (2002) 276102.

[135] T. Schiros, L.-Å. Näslund, K. Andersson, J. Gyllenpalm, G.S. Karlberg, M. Odelius, H. Ogasawara, L.G.M. Pettersson, A. Nilsson, J. Phys. Chem. C 111 (2007) 15003–15012.

[136] R. Jinnouchi, A. Nagoya, K. Kodama, Y. Morimoto, J. Phys. Chem. C 119 (2015) 16743–16753.

[137] A.C. Hindmarsh, in: R.S. Stepleman, M. Carver, R. Peskin, W.F. Ames, R. Vichnevetsky (Eds.), Sci. Comput. IMACS Trans. Sci. Comput., Amsterdam, 1983, pp. 55–64.

[138] L. Petzold, SIAM J. Sci. Stat. Comput. 4 (1983) 136–148.

[139] M. Stamatakis, *Zacros*: Advanced Lattice-KMC Simulation Made Easy. 2013. Available: http://tinyurl.com/zacroskmc.

[140] M. Stamatakis, D.G. Vlachos, J. Chem. Phys. 134 (2011) 214115.

[141] J. Nielsen, M. D'Avezac, J. Hetherington, M. Stamatakis, J. Chem. Phys. 139 (2013) 224706.

[142] Y. Li, M.J. Janik, Curr. Opin. Electrochem. 14 (2019) 124–132.

[143] H.A. Hansen, V. Viswanathan, J.K. NØrskov, J. Phys. Chem. C 118 (2014) 6706–6718.

[144] R. Jinnouchi, K. Kodama, A. Nagoya, Y. Morimoto, Electrochim. Acta 230 (2017) 470–478.

[145] J. Yue, Z. Du, M. Shao, J. Phys. Chem. Lett. 6 (2015) 3346–3351.

[146] T.G. Gambu, M.A. Petersen, E. van Steen, Catal. Today 312 (2018) 126–131.

[147] A. Kuzume, E. Herrero, J.M. Feliu, J. Electroanal. Chem. 599 (2007) 333–343.

[148] V.P. Zhdanov, B. Kasemo, J. Catal. 170 (1997) 377–389.

[149] N. Nikbin, N. Austin, D.G. Vlachos, M. Stamatakis, G. Mpourmpakis, Catal. Sci. Technol. 5 (2015) 134–141.

[150] M. Jørgensen, H. Grönbeck, ACS Catal. 7 (2017) 5054–5061.

[151] P. van Helden, J.-A. van den Berg, M.A. Petersen, W.J. van Rensburg, I.M. Ciobîcă, J. van de Loosdrecht, Faraday Discuss. 197 (2017) 117–151.

[152] Z. Šljivančanin, B. Hammer, Surf. Sci. 515 (2002) 235–244.

[153] J.M. Bray, W.F. Schneider, Langmuir 27 (2011) 8177–8186.

[154] P.C. Jennings, H.A. Aleksandrov, K.M. Neyman, R.L. Johnston, Nanoscale 6 (2014) 1153–1165.

[155] K. Kodama, R. Jinnouchi, N. Takahashi, H. Murata, Y. Morimoto, J. Am. Chem. Soc. 138 (2016) 4194–4200.

[156] H. Liu, W. An, Y. Li, A.I. Frenkel, K. Sasaki, C. Koenigsmann, D. Su, R.M. Anderson, R.M. Crooks, R.R. Adzic, P. Liu, S.S. Wong, J. Am. Chem. Soc. 137 (2015) 12597–12609.

[157] C. Koenigsmann, E. Sutter, R.R. Adzic, S.S. Wong, J. Phys. Chem. C 116 (2012) 15297–15306.

[158] W.M.H. Sachtler, R.A. van Santen, Appl. Surf. Sci. 3 (1979) 121–144.

[159] J. Zhang, M.B. Vukmirovic, K. Sasaki, A.U. Nilekar, M. Mavrikakis, R.R. Adzic, J. Am. Chem. Soc. 127 (2005) 12480–12481.

[160] S.K.R.S. Subramanian, B.R. Venkat, J. Babu, Phys. Rev. B 72 (2005) 195405.

[161] S.K.R.S. Sankaranarayanan, V.R. Bhethanabotla, B. Joseph, Phys. Rev. B 71 (2005) 195415.

[162] S.Ö. Kart, A. Erbay, H. K, T. Cagin, M. Tomak, Manuf. Eng. 31 (2008) 11–13.

[163] Z. Yang, X. Yang, Z. Xu, J. Phys. Chem. C 112 (2008) 4937–4947.

[164] Z. Qiao, H. Feng, J. Zhou, Phase Transitions 87 (2014) 59–70.

[165] H. Yaghoubi, J. Mol. Liq. 230 (2017) 305–314.

[166] C. Van der Walt, J.J. Terblans, H.C. Swart, AIP Adv. 7 (2017) 055102.

[167] L. Deng, W. Hu, H. Deng, S. Xiao, J. Phys. Chem. C 114 (2010) 11026–11032.

[168] W. Smith, T.R. Foreste, I.T. Todorov, The DL_POLY Classic User Manual, 2011.

[169] D.J. Evans, O.P. Morriss, Comput. Phys. Reports 1 (1984) 297–343.

[170] A.P. Sutton, J. Chen, Philos. Mag. Lett. 61 (1990) 139–146.

[171] T.G. Gambu, U. Terranova, D. Santos-Carballal, M.A. Petersen, G. Jones, E. van Steen, N.H. de Leeuw, J. Phys. Chem. C 123 (2019) 20522–20531.

[172] Y. Kimura, Y. Qi, T.C. Ggn, W.A. Goddard III, Mater. Process Simul. Cent. (1998).

[173] P.J. Steinhardt, D.R. Nelson, M. Ronchetti, Phys. Rev. B 28 (1983) 784–805.

[174] P. Vanysek, CRC Handbook of Chemistry and Physics, 95th ed., CRC Press, 2014.

Appendix A: Model optimization

A1: Bulk optimization

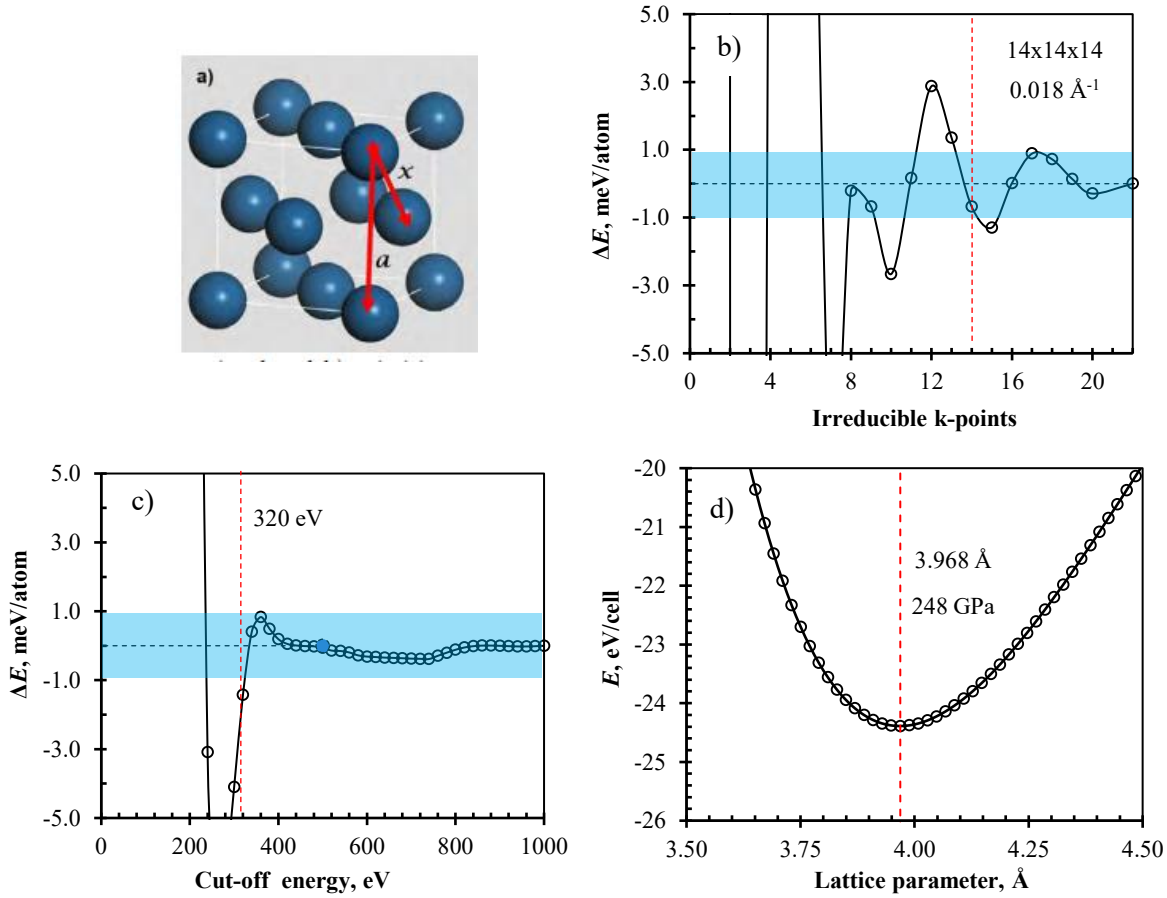

Figure A1.0.1: Parameter optimization fcc bulk platinum Pt; (a) conventional unit cell of fcc bulk Pt, (b) k-point grid optimization, (c) kinetic cutoff energy optimization and (d) lattice parameter optmization.

A2: Slab optimization

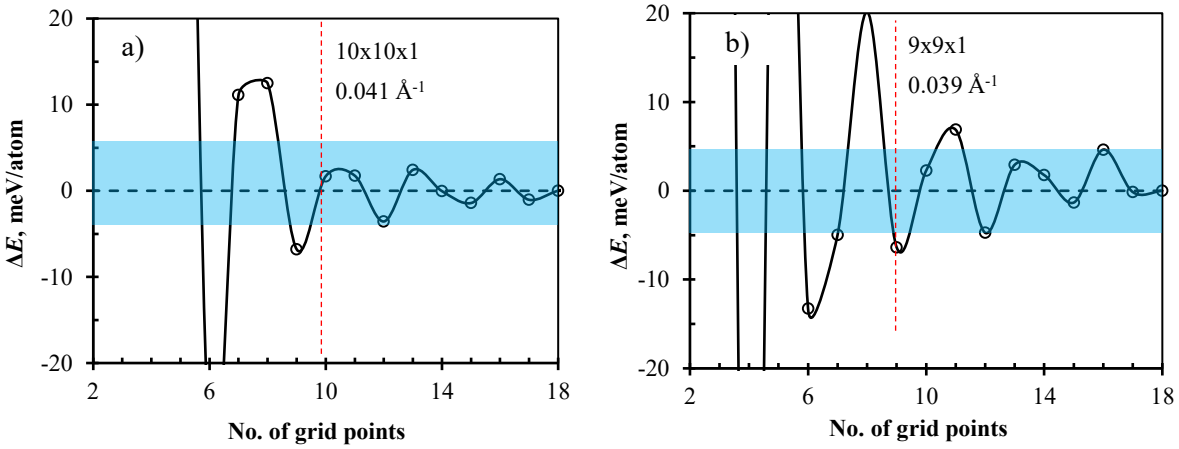

Figure A2.1: Optimization of the k-point mesh density necessary for modeling the (a) Pt(111)-*p*(1x1) and (b) Pt(100)-*p*(1x1) slab surfaces; all energy differences are reported relative to an 18x18x1 k-point mesh; each slab has 5 atomic layers and a vacuum spacing of 12 Å.

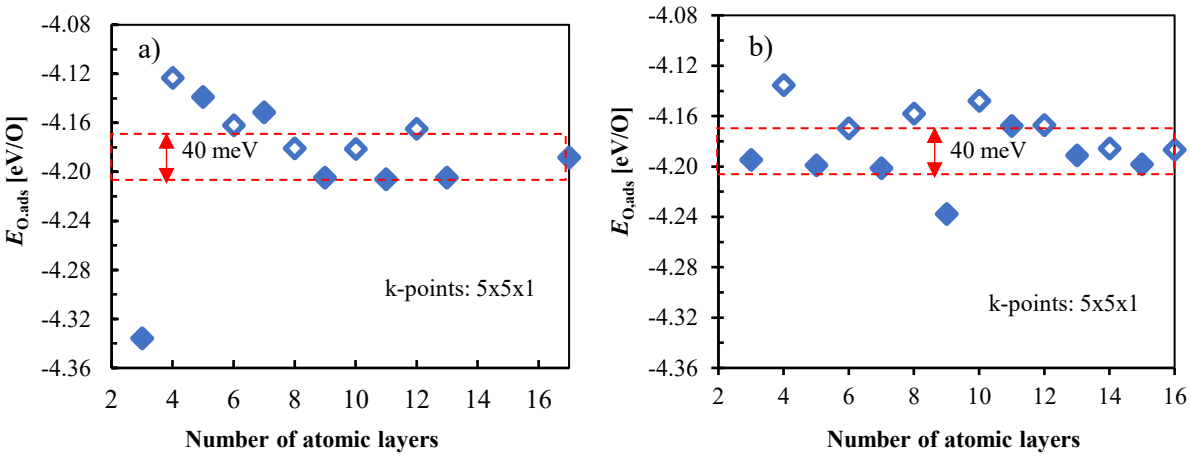

Figure A2.2: Slab thickness optimization (a) O(fcc)/Pt(111)-*p*(2x2) and (b) O(bridge)/Pt(100)-*p*(2x2); a 5x5x1 k-point grid, 12 Å vacuum gap and 3 relaxed layers [1].

Table A2.1: Number of relaxed layers optimization;(a) 6 layered Pt(111)-*p*(2x2) slab with O on fcc site, 5x5x1 k-point grid, 400 eV cut-off energy and 3 layers relaxed; (b) 6 layered Pt(100)-*p*(2x2) slab with O on bridge site, 5x5x1 k-point grid, 400 eV cut-off energy and 3 layers relaxed

No. layers relaxed	**Pt(111)-*p*(2x2)** / O(fcc) Thickness: 6 layers; k-points: 5x5x1 Cut-off energy: 400 eV;	**Pt(100)-*p*(2x2)** / O(bridge) Thickness: 6 layers; k-points: 5x5x1 Cut-off energy: 400 eV;	**Pt(100)-*p*(2x2)** / O(bridge) Thickness: 5 layers; k-points: 5x5x1 Cut-off energy: 400 eV;
	$E_{O,ads}$ [eV/½O_2]	$E_{O,ads}$ [eV/½O_2]	$E_{O,ads}$ [eV/½O_2]
1	-1.087		-0.651
2	-1.130	-0.760	-0.769
3	-1.130	-0.774	-0.784
4		-0.778	-0.799
5		-0.780	

A3: Nanowire optimization

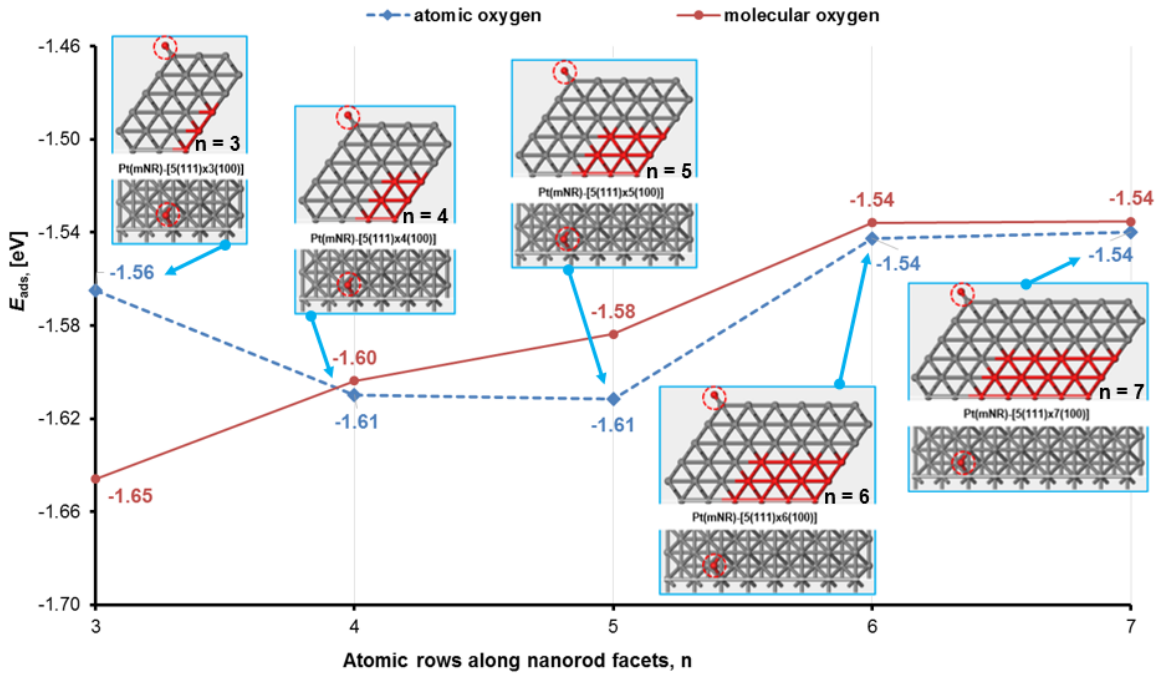

Figure A3.1: Adsorption energy of oxygen on a NW edge-bridge site as a function of the Pt{100} terrace length

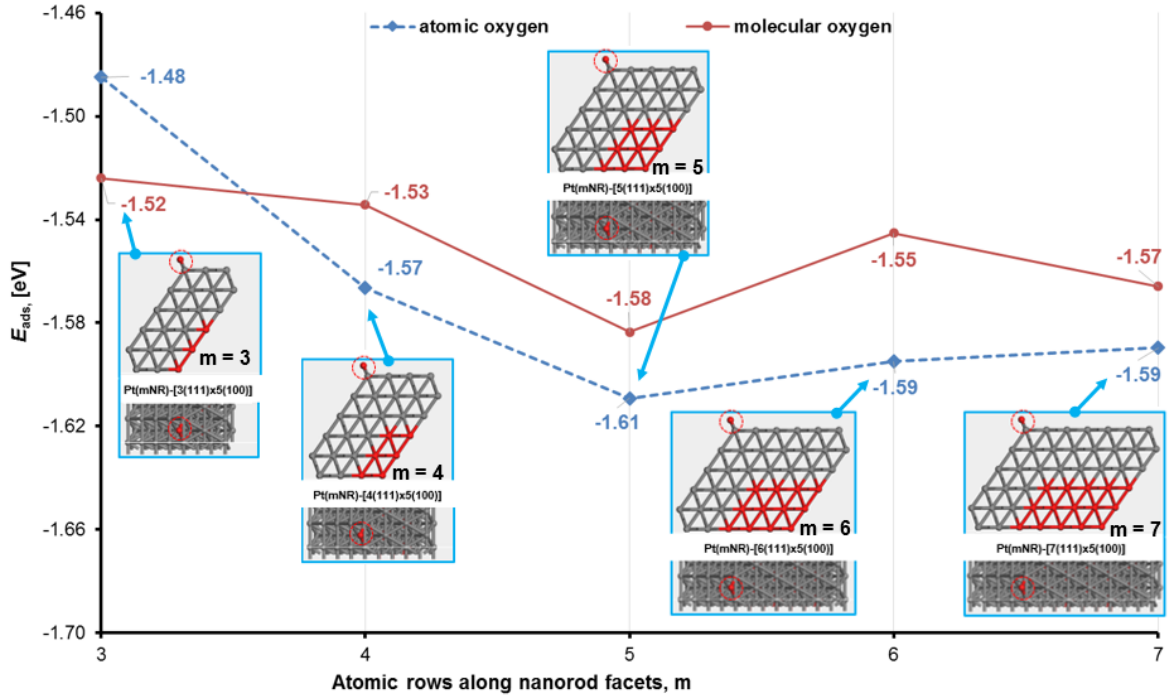

Figure A3.2: Adsorption energy of oxygen on a NW edge-bridge site as a function of the Pt{111} terrace length

Appendix B: Adsorption, Diffusion and Lateral interactions

B1: Additional adsorption structures on Pt surfaces

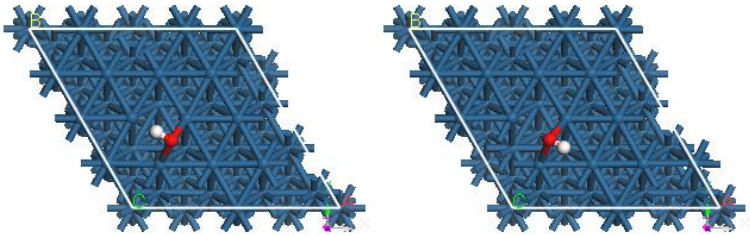

Figure B1.1: Microstates for OH* adsorption above b(1) sites

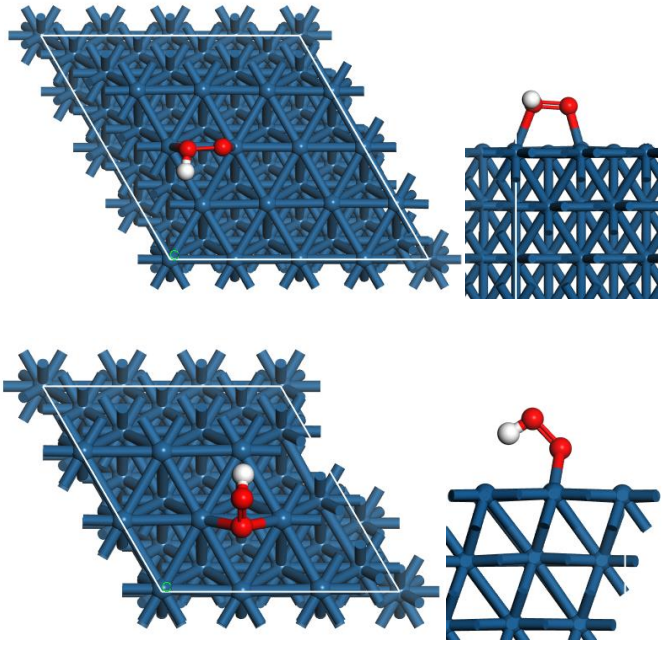

Figure B1.2: Microstates for OOH* adsorption above b(1) sites

B2: Diffusion over surfaces

Table B2.1: Calculated reaction (ΔE [eV]) and activation (E_{diff}) energies for diffusion of ORR intermediates over Pt(111)-p(4x4) and Pt(100)-p(3x3) surfaces

step		ΔE	E_{diff}	ν **[cm^{-1}]**
Pt(111)-p(4x4)				
O_2*	$f^{(1)}\rightarrow b^{(1)}$	0.008	0.103	850.7, 520.5, 392.4, 246.5, 213.3, -71.6
	$b^{(1)}\rightarrow h^{(1)}$	0.201	0.206	813.3, 498.2, 350.9, 298.2, 201, 95.8
O*	$f^{(1)}\rightarrow h^{(1)}$	0.415	0.597	495.6, 408.0, -112.6
H*	$f^{(1)}\rightarrow t^{(1)}$	0.040	0.152	2018.2, -128.9, -421.6
	$t^{(1)}\rightarrow h^{(1)}$	0.014	0.131	2004.7, -255.4, -420.6
	$t^{(1)}\rightarrow t^{(1)}$	0.000	0.108	2046.9, 261.6, -450.3
OH*	$b^{(1)}\rightarrow t^{(1)}$	0.077	0.15	3637.5, 880.4, 484.5, 355.8, 135.0, -91.7
	flip	0.012	0.306	3700.1, 688.9, 370.3, 197.9, 192.5, -405.8
	rotation	0.000	0.002	not calculated no barrier
H_2O*	$t^{(1)}\rightarrow t^{(1)}$	0.000	0.166	3802.3, 3680.7, 1579.1, 201.4, 162.5, 121.8, 53.8, 34.5, -79.8
	rotation	0.000	0.002	not calculated/no barrier
Pt(100)-p(3x3)				
O_2*	$b^{(0)}\rightarrow b^{(0)}$	n/a	n/a	** converges to its dissociated state
O*	$b^{(0)}\rightarrow b^{(0)}$	0.000	0.271	486.2, 351.4, *21.1*
H*	$b^{(0)}\rightarrow t^{(0)}$	0.218	0.221	2201.4, 227.8, -218.6
OH*	$b^{(0)}\rightarrow b^{(0)}$	0.000	0.545	3668.9, 886.9, 536.2, 128.5, 92.7, 40.3
	flip	0.000	0.386	3775.3, 794, 407.1, 358.5, 150, -629.2
	rotation	0.000	n/a	**PES relatively flat for top adsorbed OH*
H_2O*	$t^{(0)}\rightarrow t^{(0)}$	0.000	0.170	3794.1, 3669.4, 1570.3, 292.8, 193.8, 150.5, 70.6, 49.8, -105.6
	rotation	0.000	0.021	**PES relatively flat for top adsorbed OH*

B3: Pair interactions on Pt(111)-*p*(4x4)

This study has considered pairwise interactions between A* and B* adsorbates on Pt(111)-*p*(4x4) surfaces. The following Tables present a selected list of pair-interactions calculated on this surface. Microkinetic models consider some of these structures to account for coverage effect on both adsorption and activation energies (see Section 2.4). In the Tables below a * next an interaction energy indicates that adsorbates in a cell interact equally with their periodic images as a result the energy has been halved.

H – H		
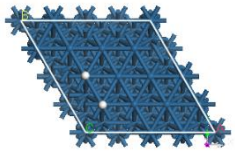	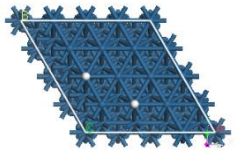	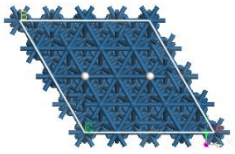
0.019	0.006	0.004*

H – O		
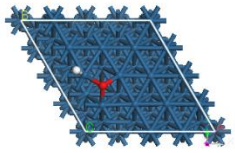	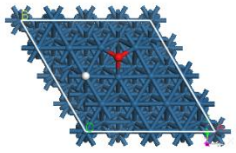	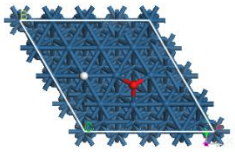
0.287	0.043	0.034

H – O_2				
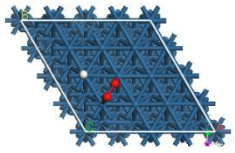	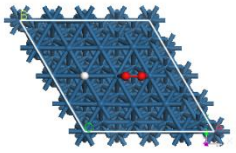	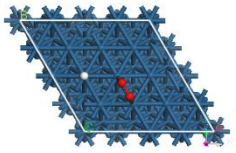	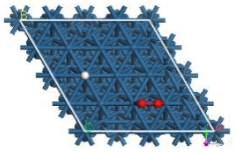	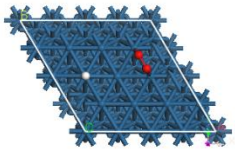
0.087	0.024	0.030	0.009*	0.017*

H – OH				
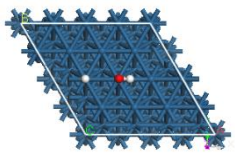	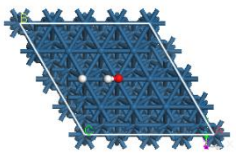	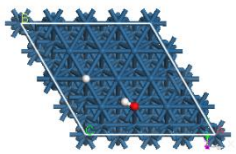	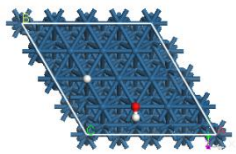	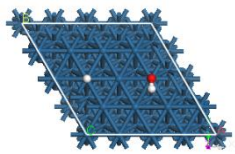
0.016	0.015	0.007	0.004	0.007*

H – H_2O				
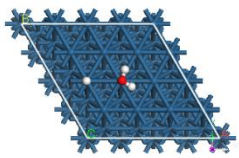	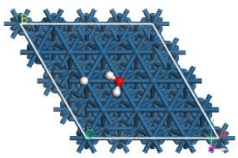	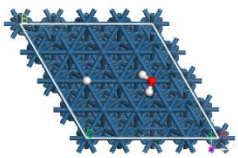	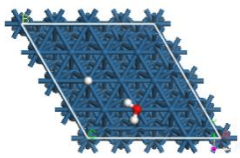	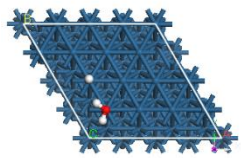
0.023	0.024	0.013*	0.014	0.019

H – OOH			
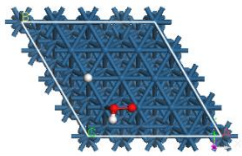	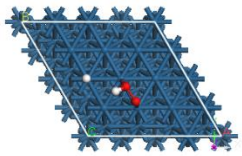	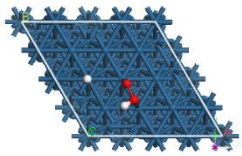	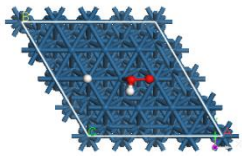
0.022	0.027	0.031	0.026
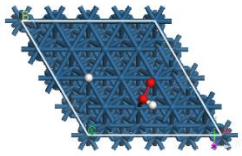	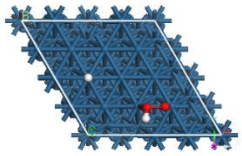	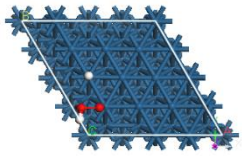	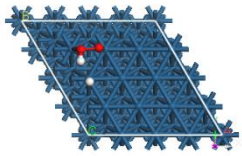
0.040	0.007*	0.080	0.057

O – O		
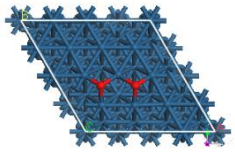	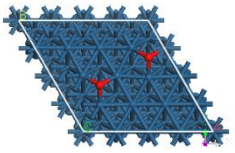	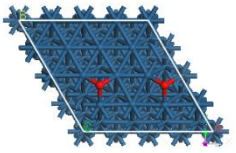
0.257	0.097*	0.022*

O – O_2			
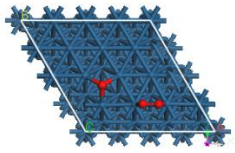	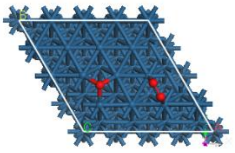	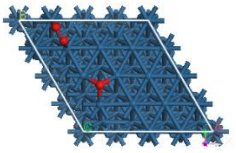	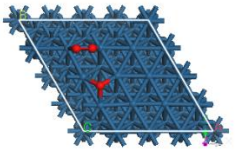
0.083	0.091	0.030*	0.148

O – OH				
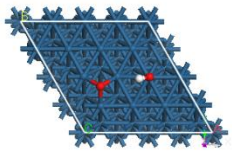	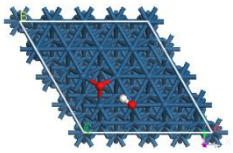	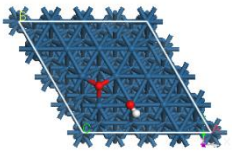	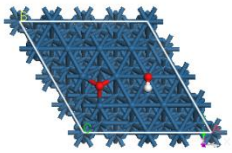	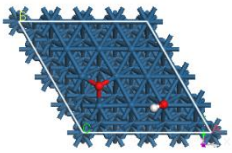
0.052	0.013	0.012	0.045	0.027*

O – H_2O				
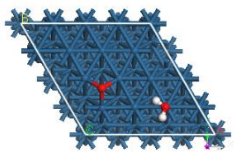	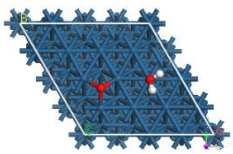	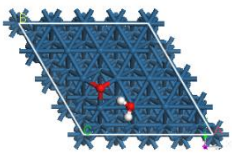	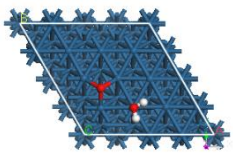	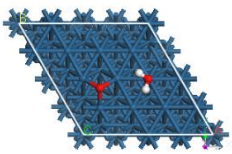
0.014*	0.033	-0.042	-0.007	0.035

O - OOH				
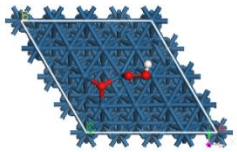	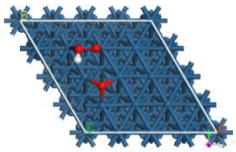	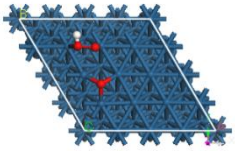	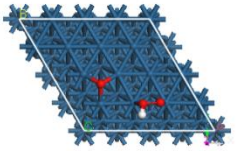	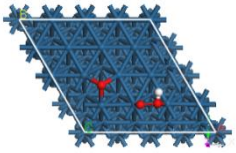
0.344	0.068	0.072	0.068	0.066

OH – OH			
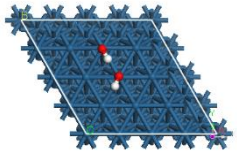	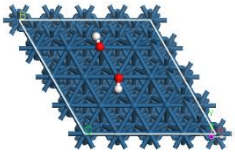	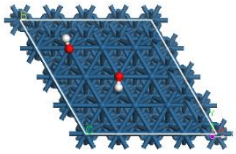	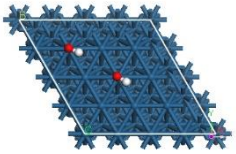
-0.221	0.037	0.018	-0.005

OH – O_2				
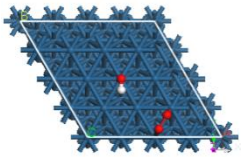	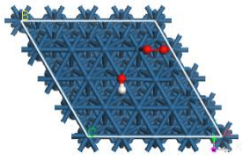	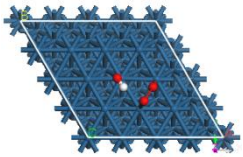	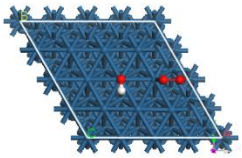	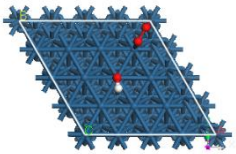
0.066	0.003	0.060	0.011	0.011

OH – H_2O			
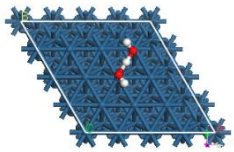	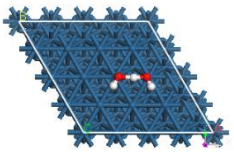	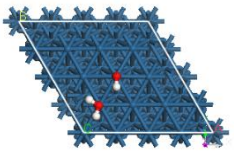	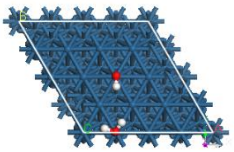
-0.607	-0.590	-0.048	0.043
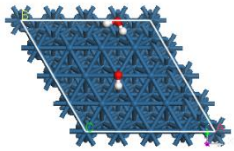	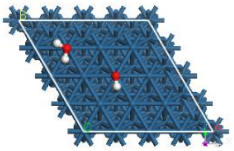	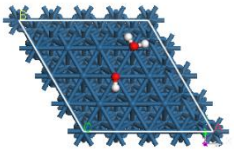	
-0.032	-0.006	0.003	

OH – OOH		
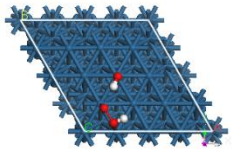	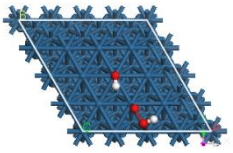	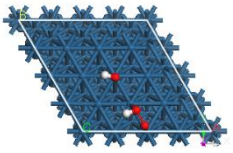
-0.061	-0.009	-0.018
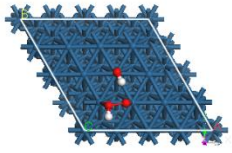	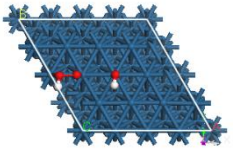	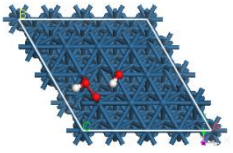
-0.036	-0.003	-0.036

$O_2 - O_2$			
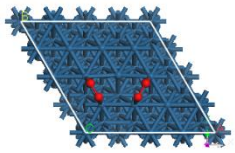	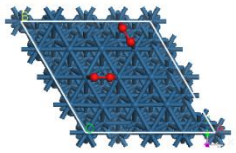	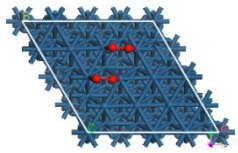	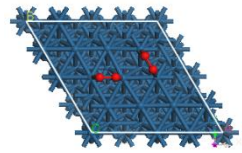
0.176	0.109	0.110	0.107

$O_2 - H_2O$			
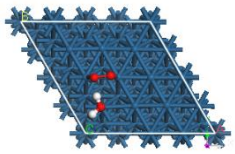	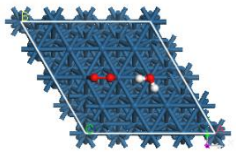	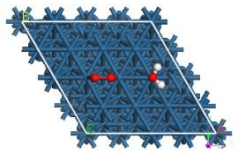	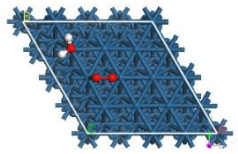
-0.114	-0.003	0.005*	0.001
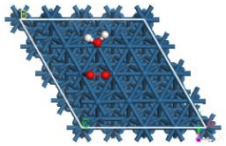	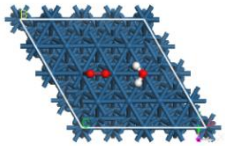	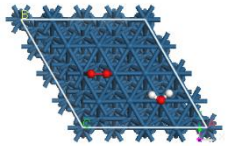	
0.035	-0.002	0.004*	

O_2 - OOH				
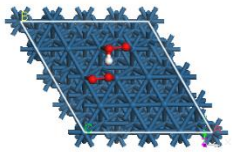	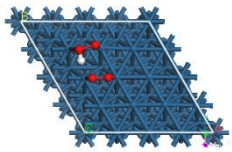	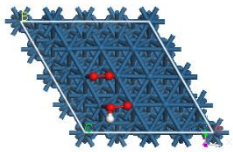	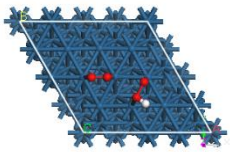	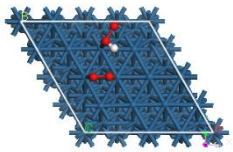
-0.144	0.014	0.085	0.057	0.050
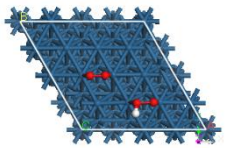	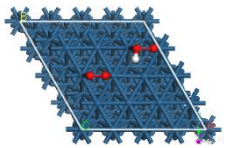	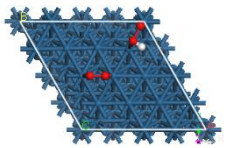	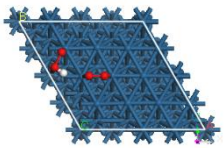	
0.052	0.052	0.060	0.069	

B4: Pair interactions on Pt(100)-*p*(3x3)

The interaction energy between various pairs over a Pt(100)-*p*(3x3) surface are reported below. These have also been used to describe coverage effects in microkinetic models.

H – H			
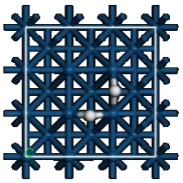	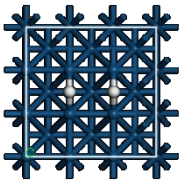	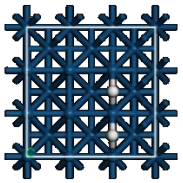	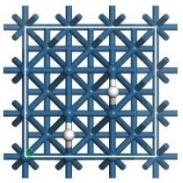
0.033	0.005	0.013	-0.001

H – O			
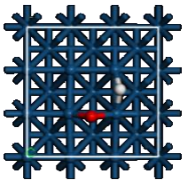	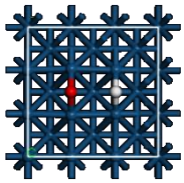	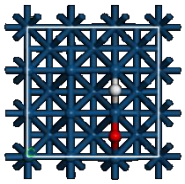	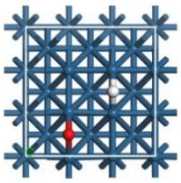
0.248	0.007	0.154	0.014

H – O_2			
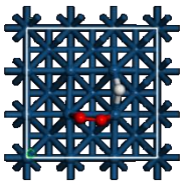	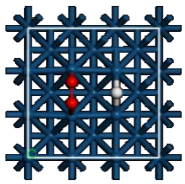	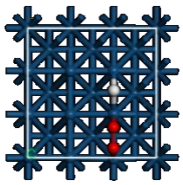	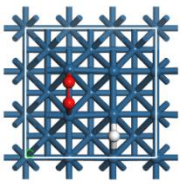
0.309	0.024	0.179	0.001

H – OH			
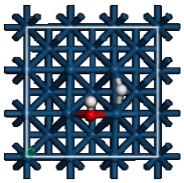	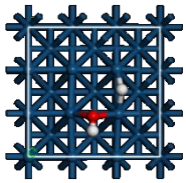	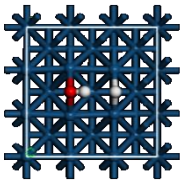	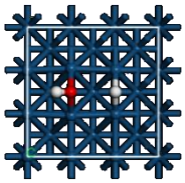
0.174	0.141	0.003	0.003
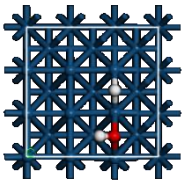	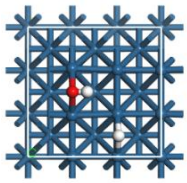	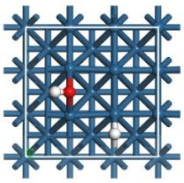	
0.105	0.002	0.002	

H – H_2O			
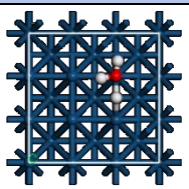	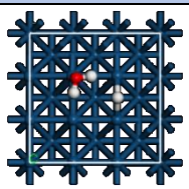	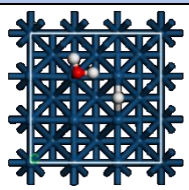	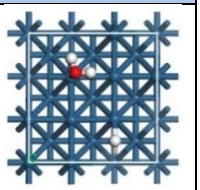
0.108	-0.002	-0.016	-0.008*

O – O			
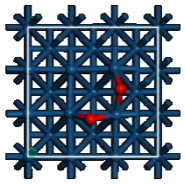	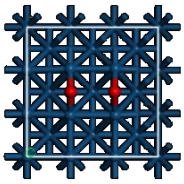	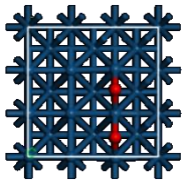	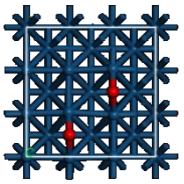
0.619	0.055	0.423	0.082

O – O_2		
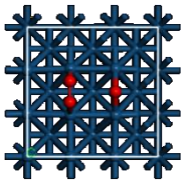	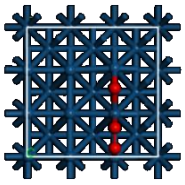	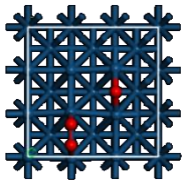
0.057	0.520	0.058

O – OH			
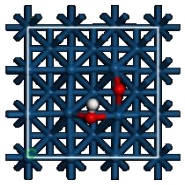	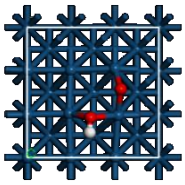	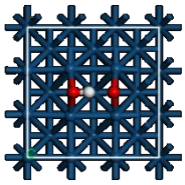	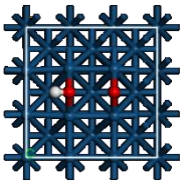
0.324	0.414	-0.217	0.000
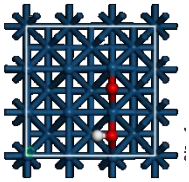	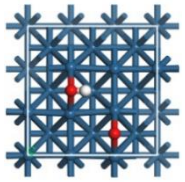	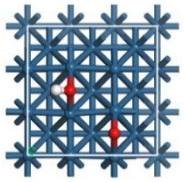	
0.328	0.033	0.026	

O – H_2O					
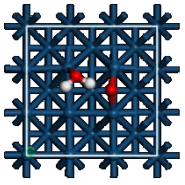	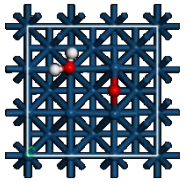	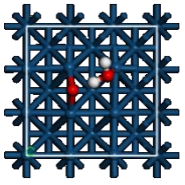	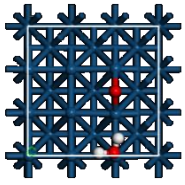	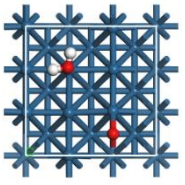	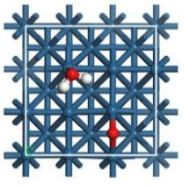
-0.306	-0.008	-0.282	0.028*	-0.003*	-0.017*

O_2 – O_2		
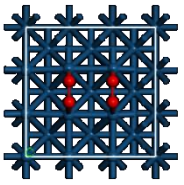	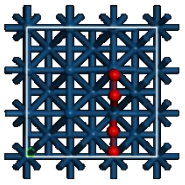	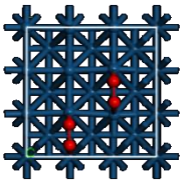
0.057	0.980	0.051

O_2 – OH			
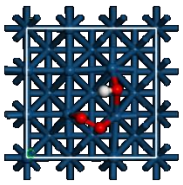	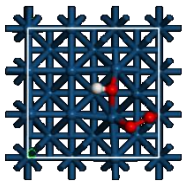	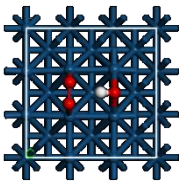	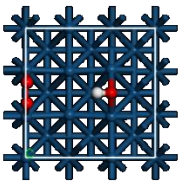
0.586	0.592	0.005	0.024
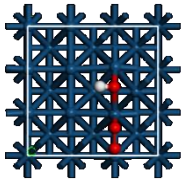	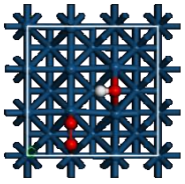	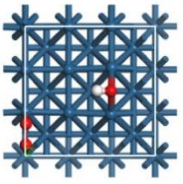	
0.472	0.021	0.014	

O_2 – H_2O		
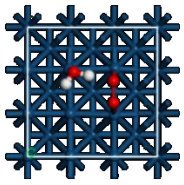	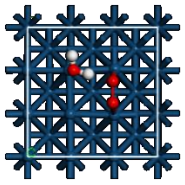	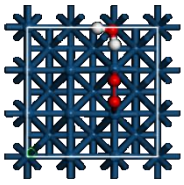
-0.210	-0.203	-0.040

OH – OH					
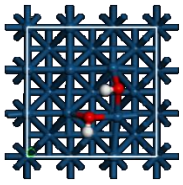	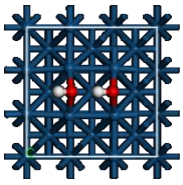	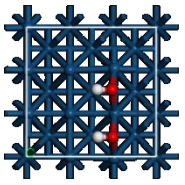	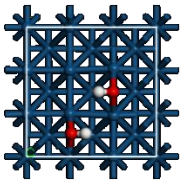	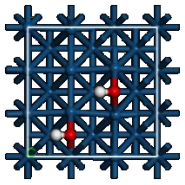	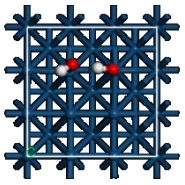
0.245	-0.137	0.334	0.052	0.026	-0.233

OH – H_2O				
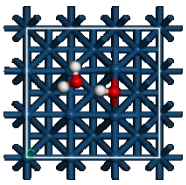	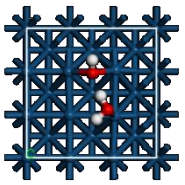	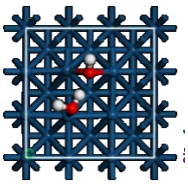	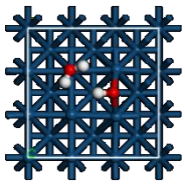	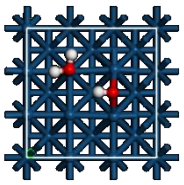
-0.140	-0.157	-0.151	0.205	-0.005
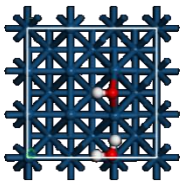	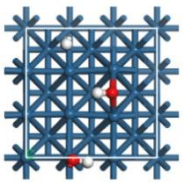	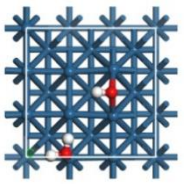	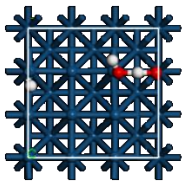	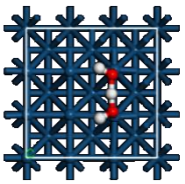
0.049*	0.015*	0.013*	-0.606	-0.590

H_2O – H_2O					
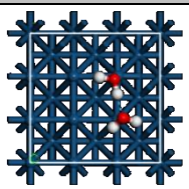	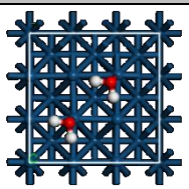	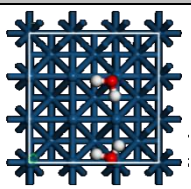	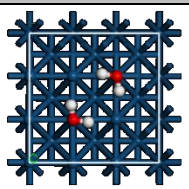	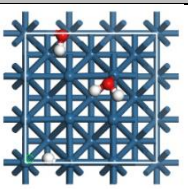	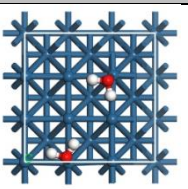
-0.280	0.036	0.049*	0.186	0.028*	0.027*

B5: Pair interactions on Pt NW edge sites

Interaction energies between edge adsorbed pairs are presented in Table 5.1 and a corresponding structure example given in Figure 5.2. The different structures will not be shown here given that they are rather straight forward structures involving co-adsorption between edge-bridge adsorbed intermediates as illustrated in Figure 5.2. Edge-edge interactions on modified edges is assumed to be the same as equivalent interactions on pure Pt NW edge sites. Given the very low edge coverage over these modified surfaces/edges, this assumption is rather reasonable.

Appendix C: Calculated Reaction Energetics

C1: Vibrational analyses

Table C1.3: Vibrational modes for initial, transtion and final states of different ORR elementary reaction over the Pt(111)-p(3x3) surface

	O_2* + * → 2O*											
IS	808.8,	489.2,	356.0,	314.2,	232.5,	138.2						
TS	625.1,	490.5,	343.1,	222.9,	126.3,	**254.4*i***						
FS	438.5,	418.0,	385.8,	368.9,	366.5,	349.7						
	O* + H* → OH* + *											
IS	2271.2,	419.8,	402.7,	383.2,	379.0,	365.7						
TS	1570.2,	614.3,	482.1,	339.8,	239.4,	**803.6*i***						
FS	3599.2,	766.6,	711.8,	386.8,	232.8,	180.0						
	OH* + H* → H_2O* + *											
IS	3672.3,	2286.0,	926.7,	518.1,	389.3,	369.9,	141.1,	108.9,	84.6			
TS	3656.4,	1657.8,	872.0,	673.9,	473.3,	368.9,	286.6,	128.4,	**376.6*i***			
FS	3731.1,	3621.7,	1563.5,	539.2,	513.8,	174.1,	100.0,	94.2,	75.2			
	2OH* → H_2O* + O*											
IS	3701.9,	2244.5,	1259.1,	1178.0,	876.7,	480.3,	450.9,	430.0,	287.1,	279.6,	159.9,	136.5
TS	3700.9,	1544.5,	1362.7,	835.5,	675.7,	585.9,	499.1,	421.8,	322.9,	178.7,	154.3,	**581.3*i***
FS	3742.0,	3629.1,	1575.5,	565.9,	489.3,	413.2,	369.1,	354.0,	171.7,	151.7,	99.9,	87.7
	O_2* + H* → OOH* + *											
IS	2275.1,	904.4,	541.5,	436.0,	370.0,	357.2,	226.8,	194.8,	130.5			
TS	1376.9,	861.5,	801.7,	509.3,	359.6,	314.5,	207.8,	159.2,	**736.1*i***			
FS	3486.6,	1225.9,	681.3,	571.3,	484.5,	296.4,	135.7,	117.4,	109.5			
	OOH* + * → OH* + H*											
IS	3520.9,	1230.3,	693.8,	550.0,	484.1,	290.1,	133.9,	107.6,	93.8			
TS	3584.0,	970.7,	700.7,	550.8,	395.1,	232.6,	156.8,	109.4,	**285.1*i***			
FS	3660.4,	927.6,	521.6,	424.3,	383.4,	375.1,	155.9,	124.5,	81.8			

Table C1.4: Vibrational modes for initial, transtion and final states of different ORR elementary reaction over the Pt(111)-p(3x3) surface

	O_2* + * → 2O*											
IS	885.4,	558.2,	428.7,	272.7,	214.2,	96.0						
TS	807.0,	544.6,	404.8,	268.5,	175.5,	**92.1*i***						
FS	504.9,	497.1,	490.6,	484.2,	187.0,	158.6						
	O* + H* → OH* + *											
IS	1337.1,	1064.2,	505.8,	488.8,	427.5,	160.6						
TS	915.7,	481.4,	410.0,	343.9,	294.2,	**1147.1*i***						
FS	3597.1,	837.7,	711.5,	402.9,	332.1,	145.0						
	OH* + H* → (OH* + H*)											
IS	3594.1,	1312.4,	1056.3,	837.0,	730.0,	473.5,	403.3,	337.2,	162.2			
TS	3573.2,	2162.1,	849.1,	744.3,	404.6,	335.7,	318.6,	153.3,	**233.7*i***			
FS	3564.8,	2244.2,	850.6,	740.1,	403.7,	333.5,	258.7,	191.7,	152.1			
	(OH* + H*) → H_2O* + *											
IS	3564.8,	2244.2,	850.6,	740.1,	403.7,	333.5,	258.7,	191.7,	152.1			
TS	3658.9,	1956.0,	866.6,	509.1,	496.5,	285.9,	235.1,	98.1,	**162.2*i***			
FS	3705.1,	3602.0,	1561.4,	570.6,	545.0,	206.8,	101.8,	83.5,	78.0			
	2OH* → H_2O* + O*											
IS	3663.1,	3306.3,	1011.6,	957.1,	781.7,	693.6,	424.3,	378.5,	346.5,	300.8,	250.8,	176.0
TS	3689.3,	1542.2,	1269.3,	845.6,	670.2,	553.7,	492.6,	420.2,	374.6,	182.5,	132.5,	**653.6*i***
FS	3707.1,	2629.5,	1564.7,	991.6,	696.1,	495.3,	465.3,	430.9,	315.5,	232.5,	160.3,	114.5

C2: Diffusion of ORR intermediates on M/Pt NW surfaces

The diffusion pathways on modified Pt NWs remains closely similar to the pathways on unmodified Pt NWs edges. The difference is in the energetics rather than the pathway folllowed.

Appendix D: Development of a Microkinetic Model

D1: Construction of microkinetic models

The microkinetic model is constructed in a Python programming language (Python 3.7), utilising several libraries which include, NumPy, SciPy and Matplotlib, in an Anaconda distribution. Various scripts were generated to (a) read and interpret an input file, (b) calculate kinetic rate constants which are temperature and coverage dependent, (c) calculate interaction energies depending on the model applied, i.e. BWA or QCA, for SA interaction energy is set to zero, (d) calculate probability of finding pairs of neighbours for a given pair of sites in the QCA model, (e) calculate kinetic rates of each step in the mechanism given a surface coverage and gas composition and (f) integrate the set of ODEs given reaction rates at initial and intermediate coverage states. A Microkinetic class containing various functions/methods was defined.

The model details are presented in Chapter 2 and the implementation above is merely the computation of that description. Care needed to be taken given the stiffness of the system and inclusion of lateral interactions, especially within the QCA model, resulted increased numerical challenges in the form of instability. A beta version of the scripts can be made available on request to the author or supervisor.

Appendix E: Microkinetic Model Inputs

E1: Description of input structure

In a microkinetic model, each reaction has a number of attributes. These include the identity of the initial, transition and final state together with information that describes each state. Here, the input data for each reaction has been order into 6 lines each describing an aspect of the reaction, i.e. vibrational frequencies, activation energies, etc., and together describing the whole reaction. In the developed model, these 6 lines are preceded by a line containing only the string "***@!Reaction***". The 6 lines together with the preceding string makeup a reaction Subblock. A reaction Block contains an appropriate number of Subblocks separated by either an empty or comment (any line staring with '#' is considered to be a comment) or a combination of both. The following details describe the contents of each line.

Line 1: Reaction identity and energetics line

This line has a minimum of 5 cells (entries) separated by a semicolon (**;**):

Entry	***type (units)***	***symbol***	***description***
1	string	-	name of reaction (no space, e.g. O2_ads_surf_1)
2	integer	-	reaction number
3	integer	-	reaction type. Adsorption/desorption = 0, surface reaction = 1
4	real (eV)	$E_{a,f}$	activation energy for the forward reaction
5	real (eV)	$E_{a,r}$	activation energy for the reverse reaction

If entry 3 equals 0, i.e. for and adsorption/desorption reaction, an additional 7 cells (entries) are included. These are described below:

Entry	***type (units)***	***symbol***	***description***
6	real (m^2)	A_{site}	area of the adsorption site (geometric area of a catalytic sites)
7	real (-)	S_0	initial sticking probability
8	real ($g.mol^{-1}$)	M_w	molar mass of an adsorbing molecule
9	real (-)	σ	symmetry number of the adsorbing molecule
10	real ($kg^3.m^6$)	$I_A I_B I_C$	product of moments of inertia
11	integer	di	$di = 1$ for linear molecule and $di = 0$ for nonlinear molecule
12	real (Pa)	p_i	reference pressure, 10^5 Pa

Line 2: Reaction equation, stoichiometry line

e.g.

A* + B* +<>+ C* + D* | -1 -1 1 1

for a generic reaction: A* + B* ↔ C* + D*

Line 3: vibrational modes of the initial state (all) [cm^{-1}]

Line 4: vibrational modes of the transition state (excluding the imaginary model) [cm^{-1}]

Line 5: vibrational modes of the final state (all) [cm^{-1}]

Line 6: additional reaction information

This line has of 10 cells (entries) separated by a semicolon (**;**):

Entry	*type (units)*	*symbol*	*description*
1	real (-)	α_i	BEP scaling factor (proximity factor)
2	integer	-	QCA parameter: = 2 (dual site) and = 1 (single site), forward
3	integer	-	QCA parameter: = 2 (dual site) and = 1 (single site), forward
4 – 10	unassigned entries, always equal to 0		

E2: Pt(111) input data

@!Reaction											
O2_ads_111	1	0	0	0.714	6.82E-20	1	32	2	1.95E-46	1	1.00E+05
O2 + *1 +<>+ O2*1 | -1 -1 1											
1578.3											
0.0											
897.8	544.6	365.3	228.3	168.1	118.7						
0	1	1	0	0	0	0	0	0	0		

@!Reaction											
H2_ads_111	2	0	0	1.052	6.82E-20	1	2	2	4.60E-48	1	1.00E+05
H2 + *1 +<>+ H*1 | -1 -2 2											
4329.6											
0											
2283.8	375.8	365.9	2283.8	375.8	365.9						
0	2	2	0	0	0	0	0	0	0		

@!Reaction											
H2O_ads_111	3	0	0	0.222	6.82E-20	1	18	2	5.8E-141	0	1.00E+05
H2O + *1 +<>+ H2O*1 | -1 -1 1											
3861.3	3743.8	1593.1									
0.0											
3731.1	3621.7	1563.5	539.2	513.8	174.1	100.0	94.2	75.2			
0	1	1	0	0	0	0	0	0	0		

@!Reaction									
O2_diss_111	4	1	0.485	2.244					
O2*1 + *1 +<>+ O*1 | -1 -1 2									
897.8	544.6	365.3	228.3	168.1	118.7				
625.1	490.5	343.1	222.9	126.3					
425.3	381.6	380.4	425.3	381.6	380.4				
0.20	2	2	0	0	0	0	0	0	0

@!Reaction									
O_hyd_111	5	1	1.041	0.975					
O*1 + H*1 +<>+ OH*1 + *1 | -1 -1 1 1									
2271.2	419.8	402.7	383.2	379.0	365.7				
1570.2	614.3	482.1	339.8	239.4					
3599.2	766.6	711.8	386.8	232.8	180.0				
0.49	2	2	0	0	0	0	0	0	0

@!Reaction									
OH_hyd_111	6	1	0.215	0.779					
OH*1 + H*1 +<>+ H2O*1 + *1 | -1 -1 1 1									
3672.3	2286.0	926.7	518.1	389.3	369.9	141.1	108.9	84.6	
3656.4	1657.8	872.0	673.9	473.3	368.9	286.6	128.4		
3731.1	3621.7	1563.5	539.2	513.8	174.1	100.0	94.2	75.2	
0.18	2	2	0	0	0	0	0	0	0

@!Reaction												
OH_h-lis_111	7	1	0.630	0.000								
H2O*1 + O*1 +<>+ OH*1 | -1 -1 2												
3701.9	2244.5	1259.1	1178.0	876.7	480.3	450.9	430.0	287.1	279.6	159.9	136.5
3700.9	1544.5	1362.7	835.5	675.7	585.9	499.1	421.8	322.9	178.7	154.3	
3742.0	3629.1	1575.5	565.9	489.3	413.2	369.1	354.0	171.7	151.7	99.9	87.7
0.89	2	2	0	0	0	0	0	0	0		

@!Reaction									
O2_hyd_111	8	1	0.536	0.493					
O2*1 + H*1 +<>+ OOH*1 + *1 | -1 -1 1 1									
2275.1	904.4	541.5	436.0	370.0	357.2	226.8	194.8	130.5	
1376.9	861.5	801.7	509.3	359.6	314.5	207.8	159.2		
3486.6	1225.9	681.3	571.3	484.5	296.4	135.7	117.4	109.5	
0.46	2	2	0	0	0	0	0	0	0

@!Reaction									
OOH_diss_111	9	1	0.036	1.773					
OOH*1 + *1 +<>+ OH*1 + O*1 | -1 -1 1 1									
3520.9	1230.3	693.8	550.0	484.1	290.1	133.9	107.6	93.8	
3584.0	970.7	700.7	550.8	395.1	232.6	156.8	109.4		
3660.4	927.6	521.6	424.3	383.4	375.1	155.9	124.5	81.8	
0.02	2	2	0	0	0	0	0	0	0

E3: Pt(100) input data

@!Reaction											
O2_ads_100	1	0	0	1.244	7.87E-20	1	32	2	1.95E-46	1	1.00E+05
O2 + *0 +<>+ O2*0 | -1 -1 1											
1578.3											
0.0											
885.4	558.2	428.7	272.7	214.2	96.0						
0	1	1	0	0	0	0	0	0	0		

@!Reaction											
H2_ads_100	2	0	0	1.377	7.87E-20	1	2	2	4.60E-48	1	1.00E+05
H2 + *0 +<>+ H*0 | -1 -2 2											
4329.6											
0											
1347.9	1046.2	385.1	1347.9	1046.2	385.1						
0	2	2	0	0	0	0	0	0	0		

@!Reaction											
H2O_ads_100	3	0	0	0.294	7.87E-20	1	18	2	5.8E-141	0	1.00E+05
H2O + *0 +<>+ H2O*0 | -1 -1 1											
3861.3	3743.8	1593.1									
0.0											
3705.1	3602.0	1561.4	570.6	545.0	206.8	101.8	83.5	78.0			
0	1	1	0	0	0	0	0	0	0		

@!Reaction										
O2_diss_100	4	1	0.1429	1.587						
O2*0 + *0 +<>+ O*0 | -1 -1 2										
885.4	558.2	428.7	272.7	214.2	96.0					
807.0	544.6	404.8	268.5	175.5						
503.2	486.1	139.4	503.2	486.1	139.4					
0.09	2	2	0	0	0	0	0	0	0	

@!Reaction										
O_hyd_100	5	1	0.538	0.867						
O*0 + H*0 +<>+ OH*0 + *0 | -1 -1 1 1										
503.2	486.1	139.4	1347.9	1046.2	385.1					
915.7	481.4	410.0	343.9	294.2						
3597.1	837.7	711.5	402.9	332.1	145.0					
0.38	2	2	0	0	0	0	0	0	0	

@!Reaction										
OH_hyd_100	6	1	0.889	0.700						
OH*0 + H*0 +<>+ H2O*0 + *0 | -1 -1 1 1										
3597.1	837.7	711.5	402.9	332.1	145.0	1347.9	1046.2	385.1		
3658.9	1956.0	866.6	509.1	496.5	285.9	235.1	98.1			
3705.1	3602.0	1561.4	570.6	545.0	206.8	101.8	83.5	78.0		
0.50	2	2	0	0	0	0	0	0	0	

@!Reaction												
OH_h-lis_100	7	1	0.000	0.518								
H2O*0 + O*0 +<>+ OH*0 | -1 -1 2												
3663.1	3306.3	1011.6	957.1	781.7	693.6	424.3	378.5	346.5	300.8	250.8	176.0	
3689.3	1542.2	1269.3	845.6	670.2	553.7	492.6	420.2	374.6	182.5	132.5		
3707.1	2629.5	1564.7	991.6	696.1	495.3	465.3	430.9	315.5	232.5	160.3	114.5	
0.08	2	2	0	0	0	0	0	0	0			

E4: Pt NW input data

@!Reaction											
O2_ads_eb	1	0	0.000	1.621	7.35E-20	1	32	2	1.95E-46	1	1.00E+05
O2 + *e +<>+ O2*e | -1 -1 1											
1578.3											
0.0											
822.7	580.4	466.3	286.8	222.8	81.4						
0	1	1	0	0	0	0	0	0	0		

@!Reaction											
H2_ads_eb	2	0	0.000	1.495	7.35E-20	1	2	2	4.60E-48	1	1.00E+05
H2 + *e +<>+ H*e | -1 -2 2											
4329.6											
0											
1345.6	1044.3	382.9									
0	2	2	0	0	0	0	0	0	0		

@!Reaction											
H2O_ads_eb	3	0	0.000	0.360	7.35E-20	1	18	2	5.8E-141	0	1.00E+05
H2O + *e +<>+ H2O*e | -1 -1 1											
3861.3	3743.8	1593.1									
0.0											
3725.7	3426.7	1561.7	574.2	553.0	227.1	206.7	100.2	48.4			
0	1	1	0	0	0	0	0	0	0		

@!Reaction										
O2f(1e)-->O2b(e)	4	1	0.029	1.013						
O2*1 + *e +<>+ O2*e + *1 | -1 -1 1 1										
808.8	489.2	356.0	314.2	232.5	138.2					
833.6	506.0	379.9	231.3	223.2						
822.7	580.4	466.3	286.8	222.8	81.4					
0.5	1	1	0	0	0	0	0	0	0	

@!Reaction										
Of(1e)-->Ob(e)	5	1	0.646	1.069						
O*1 + *e +<>+ O*e + *1 | -1 -1 1 1										
425.3	381.6	380.4								
502.7	372.9									
541.6	468.6	148.6								
0.5	1	1	0	0	0	0	0	0	0	

@!Reaction										
Ob(e)-->Ob(0e)	6	1	0.626	0.311						
O*e + *0 +<>+ O*0 + *e | -1 -1 1 1										
541.6	468.6	148.6								
481.2	371.8									
503.2	486.1	139.4								
0.5	1	1	0	0	0	0	0	0	0	

@!Reaction										
Ht(1e)-->Hb(e)	7	1	0.195	0.416						
H*1 + *e +<>+ H*e + *1 | -1 -1 1 1										
2283.8	375.8	365.9								
1981.7	-170.3									
1345.6	1044.3	382.9								
0.5	1	1	0	0	0	0	0	0	0	

@!Reaction									
Hb(e)-->Hb(0e)	8	1	0.336	0.277					
H*e + *0 +<>+ H*0 + *e | -1 -1 1 1									
1345.6	1044.3	382.9							
2121.8	199.5								
1347.9	1046.2	385.1							
0.5	1	1	0	0	0	0	0	0	0

@!Reaction									
OHt(1e)-->OHb(e)	9	1	0.119	0.991					
OH*1 + *e +<>+ OH*e + *1 | -1 -1 1 1									
3664.7	934.0	525.6	167.4	111.0	77.2				
3637.0	878.3	478.0	375.3	144.9					
3669.2	800.9	693.5	419.9	314.3	137.3				
0.5	1	1	0	0	0	0	0	0	0

@!Reaction									
OHb(e)-->OHb(0e)	10	1	0.681	0.473					
OH*e + *0 +<>+ OH*0 + *e | -1 -1 1 1									
3669.2	800.9	693.5	419.9	314.3	137.3				
3651.0	858.3	508.3	342.8	106.1					
3597.1	837.7	711.5	402.9	332.1	145.0				
0.5	1	1	0	0	0	0	0	0	0

@!Reaction									
H2Ot(1e)-->H2Ot(e)	11	1	0.121	0.260					
H2O*1 + *e +<>+ H2O*e + *1 | -1 -1 1 1									
3731.1	3621.7	1563.5	539.2	513.8	174.1	100.0	94.2	75.2	
3781.6	3668.5	1578.6	200.5	150.6	70.3	61.1	13.4		
3725.7	3426.7	1561.7	574.2	553.0	227.1	206.7	100.2	48.4	
0.5	1	1	0	0	0	0	0	0	0

@!Reaction									
H2Ot(e)-->H2Ot(0e)	12	1	0.224	0.158					
H2O*e + *0 +<>+ H2O*0 + *e | -1 -1 1 1									
3731.1	3621.7	1563.5	539.2	513.8	174.1	100.0	94.2	75.2	
3781.6	3668.5	1578.6	200.5	150.6	70.3	61.1	13.4		
3725.7	3426.7	1561.7	574.2	553.0	227.1	206.7	100.2	48.4	
0.5	1	1	0	0	0	0	0	0	0

@!Reaction									
O2b(e)-->2Ob(e)	13	1	1.189	2.887					
O2*e + *e +<>+ O*e | -1 -1 2									
822.7	580.4	466.3	286.8	222.8	81.4				
687.7	661.4	187.5	86.4	66.5					
541.6	468.6	148.6	541.6	468.6	148.6				
0.5	1	1	0	0	0	0	0	0	0

@!Reaction									
O2b(e)-->Ob(e)+Ob(0e)	14	1	0.642	2.025					
O2*e + *0 +<>+ O*e + O*0 | -1 -1 1 1									
822.7	580.4	466.3	286.8	222.8	81.4				
770.1	516.8	389.2	268.1	170.3					
503.2	486.1	139.4	503.2	486.1	139.4				
0.5	1	1	0	0	0	0	0	0	0

@!Reaction									
O2b(e)-->Ob(e)+Of(1e)	15	1	1.123	2.399					
O2*e + *1 +<>+ O*e + O*1 | -1 -1 1 1									
822.7	580.4	466.3	286.8	222.8	81.4				
769.2	448.9	280.9	222.0	96.3					
541.6	468.6	148.6	425.3	381.6	380.4				
0.5	1	1	0	0	0	0	0	0	0

@!Reaction									
Ob(0e)+Hb(e)	16	1	0.664	0.845					
H*e + O*0 +<>+ *e + OH*0 | -1 -1 1 1									
1345.6	1044.3	382.9	503.2	486.1	139.4				
931.2	493.1	471.2	394.5	291.9					
3597.1	837.7	711.5	402.9	332.1	145.0				
0.5	1	1	0	0	0	0	0	0	0

@!Reaction									
Ob(e)+Hb(0e)	17	1	0.847	1.089					
O*e + H*0 +<>+ OH*e + *0 | -1 -1 1 1									
541.6	468.6	148.6	1347.9	1046.2	385.1				
948.9	491.1	404.0	268.2	196.0					
3674.9	816.2	706.0	422.5	322.6	129.5				
0.5	1	1	0	0	0	0	0	0	0

@!Reaction									
Ob(e)+Ht(1e)	18	1	0.685	1.069					
O*e + H*1 +<>+ OH*e + *1 | -1 -1 1 1									
541.6	468.6	148.6	2283.8	375.8	365.9				
1406.5	689.3	518.9	375.4	259.0					
3669.2	800.9	693.5	419.9	314.3	137.3				
0.5	1	1	0	0	0	0	0	0	0

@!Reaction										
Of(1e)+Hb(e)	19	1	1.385	1.026						
O*1 + H*e +<>+ *e + OH*1 | -1 -1 1 1										
1345.6	1044.3	382.9	425.3	381.6	380.4					
1592.5	537.2	492.4	295.5	215.9						
3664.7	934.0	525.6	167.4	111.0	77.2					
0.5	1	1	0	0	0	0	0	0	0	

@!Reaction									
OHb(e)+Ht(1e)->H2Ot(e)	20	1	0.922	0.753					
OH*e + H*1 +<>+ H2O*e + *1 | -1 -1 1 1									
3669.2	800.9	693.5	419.9	314.3	137.3	2283.8	375.8	365.9	
3659.5	1425.8	824.1	765.0	466.4	435.0	282.0	116.1		
3725.7	3426.7	1561.7	574.2	553.0	227.1	206.7	100.2	48.4	
0.5	1	1	0	0	0	0	0	0	0

@!Reaction									
OHt(1e)+Hb(e)->H2Ot(1e)	21	1	0.662	1.005					
OH*1 + H*e +<>+ *e + H2O*1 | -1 -1 1 1									
3664.7	934.0	525.6	167.4	111.0	77.2	1345.6	1044.3	382.9	
3656.7	1480.8	852.9	689.6	445.7	368.7	262.4	125.3		
3731.1	3621.7	1563.5	539.2	513.8	174.1	100.0	94.2	75.2	
0.5	1	1	0	0	0	0	0	0	0

@!Reaction									
OHb(e)+Hb(00e)->H2Ot(e)	22	1	1.619	1.271					
OH*e + H*0 +<>+ H2O*e + *0 | -1 -1 1 1									
3669.2	800.9	693.5	419.9	314.3	137.3	1347.9	1046.2	385.1	
3651.6	1900.3	898.4	550.2	446.3	190.8	100.5	47.4		
3725.7	3426.7	1561.7	574.2	553.0	227.1	206.7	100.2	48.4	
0.5	1	1	0	0	0	0	0	0	0

@!Reaction									
OHb(00e)+Hb(e)->H2Ot(0e)	23	1	1.049	0.801					
OH*0 + H*e +<>+ *e + H2O*0 | -1 -1 1 1									
1345.6	1044.3	382.9	3597.1	837.7	711.5	402.9	332.1	145.0	
3649.3	1712.6	865.0	602.4	493.3	293.5	239.9	98.6		
3705.1	3602.0	1561.4	570.6	545.0	206.8	101.8	83.5	78.0	
0.5	1	1	0	0	0	0	0	0	0

@!Reaction											
OHb(e)+OHb(00e)	24	1	0.657	0.000							
OH*e + OH*0 +<>+ H2O*e + O*0 | -1 -1 1 1											
3669.2	800.9	693.5	419.9	314.3	137.3	3597.1	837.7	711.5	402.9	332.1	145.0
3720.0	1553.9	1264.1	806.2	710.9	526.0	479.3	420.0	370.6	171.1	125.8	
3725.7	3426.7	1561.7	574.2	553.0	227.1	206.7	100.2	48.4	503.2	486.1	139.4
0.5	1	1	0	0	0	0	0	0	0		

@!Reaction											
OHb(e)+OHb(00e)	25	1	0.430	0.000							
OH*e + OH*0 +<>+ O*e + H2O*0 | -1 -1 1 1											
3669.2	800.9	693.5	419.9	314.3	137.3	3597.1	837.7	711.5	402.9	332.1	145.0
3713.4	1514.9	1277.2	855.3	655.6	538.1	499.4	415.4	365.2	165.0	132.7	
3705.1	3602.0	1561.4	570.6	545.0	206.8	101.8	83.5	78.0	541.6	468.6	148.6
0.5	1	1	0	0	0	0	0	0	0		

@!Reaction											
OHb(e)+OHt(1e)	26	1	0.439	0.315							
OH*e + OH*1 +<>+ H2O*e + O*1 | -1 -1 1 1											
3669.2	800.9	693.5	419.9	314.3	137.3	3664.7	934.0	525.6	167.4	111.0	77.2
3716.4	3463.7	959.1	841.0	675.5	484.3	435.4	360.9	249.8	144.5	104.1	
3725.7	3426.7	1561.7	574.2	553.0	227.1	206.7	100.2	48.4	425.3	381.6	380.4
0.5	1	1	0	0	0	0	0	0	0		

@!Reaction											
OHbe+OHt1e	27	1	0.000	0.181							
OH*e + OH*1 +<>+ O*e + H2O*1 | -1 -1 1 1											
3669.2	800.9	693.5	419.9	314.3	137.3	3664.7	934.0	525.6	167.4	111.0	77.2
3709.5	1528.1	1369.0	823.9	619.9	554.5	532.6	413.3	364.8	168.3	146.1	
3731.1	3621.7	1563.5	539.2	513.8	174.1	100.0	94.2	75.2	541.6	468.6	148.6
0.5	1	1	0	0	0	0	0	0	0		

@!Reaction									
OHb(1e)+Ob(e)	28	1	0.446	0.862					
OH*1 + O*e +<>+ O*1 + OH*e | -1 -1 1 1									
3664.7	934.0	525.6	167.4	111.0	77.2	541.6	468.6	148.6	
1404.9	1358.4	611.2	506.2	466.7	372.7	336.5	185.4		
425.3	381.6	380.4	3669.2	800.9	693.5	419.9	314.3	137.3	
0.5	1	1	0	0	0	0	0	0	0

@!Reaction									
OHb(e)+Ob(0e)	29	1	0.070	0.158					
OH*e + O*0 +<>+ O*e + OH*0 | -1 -1 1 1									
3669.2	800.9	693.5	419.9	314.3	137.3	503.2	486.1	139.4	
1350.1	1347.1	680.1	538.6	454.9	408.7	394.9	204.6		
3597.1	837.7	711.5	402.9	332.1	145.0	541.6	468.6	148.6	
0.5	1	1	0	0	0	0	0	0	0

E5: Au/Pt NW input data

@!Reaction											
O2_ads_eb	1	0	0.000	0.151	0.00E+00	1	32	2	1.95E-46	1	1.00E+05
O2 + *e +<>+ O2*e | -1 -1 1											
1578.3											
0.0											
822.7	580.4	466.3	286.8	222.8	81.4						
0	1	1	0	0	0	0	0	0	0		

@!Reaction											
H2_ads_eb	2	0	0.000	0.314	0.00E+00	1	2	2	4.60E-48	1	1.00E+05
H2 + *e +<>+ H*e | -1 -2 2											
4329.6											
0											
1345.6	1044.3	382.9									
0	2	2	0	0	0	0	0	0	0		

@!Reaction											
H2O_ads_eb	3	0	0.000	0.205	0.00E+00	1	18	2	5.8E-141	0	1.00E+05
H2O + *e +<>+ H2O*e | -1 -1 1											
3861.3	3743.8	1593.1									
0.0											
3725.7	3426.7	1561.7	574.2	553.0	227.1	206.7	100.2	48.4			
0	1	1	0	0	0	0	0	0	0		

@!Reaction									
O2f(1e)-->O2b(e)	4	1	0.564	0.000					
O2*1 + *e +<>+ O2*e + *1 | -1 -1 1 1									
808.8	489.2	356.0	314.2	232.5	138.2				
833.6	506.0	379.9	231.3	223.2					
822.7	580.4	466.3	286.8	222.8	81.4				
0.5	1	1	0	0	0	0	0	0	0

@!Reaction										
O2b(e)-->O2b(00e)	5	1	0.000	1.094						
O2*e + *0 +<>+ O2*0 + *e | -1 -1 1 1										
541.6	468.6	148.6								
0.0	0.0									
541.6	468.6	148.6								
0.5	1	1	0	0	0	0	0	0	0	

@!Reaction										
Of(1e)-->Ob(e)	6	1	1.335	0.193						
O*1 + *e +<>+ O*e + *1 | -1 -1 1 1										
425.3	381.6	380.4								
502.7	372.9									
541.6	468.6	148.6								
0.5	1	1	0	0	0	0	0	0	0	

@!Reaction									
Ob(e)-->Ob(0e)	7	1	0.118	1.368					
O*e + *0 +<>+ O*0 + *e | -1 -1 1 1									
541.6	468.6	148.6							
481.2	371.8								
503.2	486.1	139.4							
0.5	1	1	0	0	0	0	0	0	0

@!Reaction									
Ht(1e)-->Hb(e)	8	1	0.547	0.151					
H*1 + *e +<>+ H*e + *1 | -1 -1 1 1									
2283.8	375.8	365.9							
1981.7	-170.3								
1345.6	1044.3	382.9							
0.5	1	1	0	0	0	0	0	0	0

@!Reaction									
Hb(e)-->Hb(0e)	9	1	0.179	0.710					
H*e + *0 +<>+ H*0 + *e | -1 -1 1 1									
1345.6	1044.3	382.9							
2121.8	199.5								
1347.9	1046.2	385.1							
0.5	1	1	0	0	0	0	0	0	0

@!Reaction									
OHt(1e)-->OHb(e)	10	1	0.498	0.527					
OH*1 + *e +<>+ OH*e + *1 | -1 -1 1 1									
3664.7	934.0	525.6	167.4	111.0	77.2				
3637.0	878.3	478.0	375.3	144.9					
3669.2	800.9	693.5	419.9	314.3	137.3				
0.5	1	1	0	0	0	0	0	0	0

@!Reaction									
OHb(e)-->OHb(0e)	11	1	0.250	0.885					
OH*e + *0 +<>+ OH*0 + *e | -1 -1 1 1									
3669.2	800.9	693.5	419.9	314.3	137.3				
3651.0	858.3	508.3	342.8	106.1					
3597.1	837.7	711.5	402.9	332.1	145.0				
0.5	1	1	0	0	0	0	0	0	0

@!Reaction									
H2Ot(1e)-->H2Ot(e)	12	1	0.017	0.000					
H2O*1 + *e +<>+ H2O*e + *1 | -1 -1 1 1									
3731.1	3621.7	1563.5	539.2	513.8	174.1	100.0	94.2	75.2	
3781.6	3668.5	1578.6	200.5	150.6	70.3	61.1	13.4		
3725.7	3426.7	1561.7	574.2	553.0	227.1	206.7	100.2	48.4	
0.5	1	1	0	0	0	0	0	0	0

@!Reaction									
H2Ot(e)-->H2Ot(0e)	13	1	0.000	0.089					
H2O*e + *0 +<>+ H2O*0 + *e | -1 -1 1 1									
3731.1	3621.7	1563.5	539.2	513.8	174.1	100.0	94.2	75.2	
3781.6	3668.5	1578.6	200.5	150.6	70.3	61.1	13.4		
3725.7	3426.7	1561.7	574.2	553.0	227.1	206.7	100.2	48.4	
0.5	1	1	0	0	0	0	0	0	0

E6: Ag/Pt NW input data

@!Reaction											
O2_ads_eb	1	0	0.067	0.000	0.00E+00	1	32	2	1.95E-46	1	1.00E+05
O2 + *e +<>+ O2*e | -1 -1 1											
1578.3											
0.0											
822.7	580.4	466.3	286.8	222.8	81.4						
0	1	1	0	0	0	0	0	0	0		

@!Reaction											
H2_ads_eb	2	0	0.441	0.000	0.00E+00	1	2	2	4.60E-48	1	1.00E+05
H2 + *e +<>+ H*e | -1 -2 2											
4329.6											
0											
1345.6	1044.3	382.9									
0	2	2	0	0	0	0	0	0	0		

@!Reaction											
H2O_ads_eb	3	0	0.000	0.319	0.00E+00	1	18	2	5.8E-141	0	1.00E+05
H2O + *e +<>+ H2O*e | -1 -1 1											
3861.3	3743.8	1593.1									
0.0											
3725.7	3426.7	1561.7	574.2	553.0	227.1	206.7	100.2	48.4			
0	1	1	0	0	0	0	0	0	0		

@!Reaction									
O2f(1e)-->O2b(e)	4	1	0.782	0.000					
O2*1 + *e +<>+ O2*e + *1 | -1 -1 1 1									
808.8	489.2	356.0	314.2	232.5	138.2				
833.6	506.0	379.9	231.3	223.2					
822.7	580.4	466.3	286.8	222.8	81.4				
0.5	1	1	0	0	0	0	0	0	0

@!Reaction									
O2b(e)-->O2b(00e)	5	1	0.000	1.312					
O2*e + *0 +<>+ O2*0 + *e | -1 -1 1 1									
541.6	468.6	148.6	0.0	0.0	0.0				
0.0	0.0	0.0	0.0	0.0					
541.6	468.6	148.6	0.0	0.0	0.0				
0.5	1	1	0	0	0	0	0	0	0

@!Reaction									
Of(1e)-->Ob(e)	6	1	1.620	0.034					
O*1 + *e +<>+ O*e + *1 | -1 -1 1 1									
425.3	381.6	380.4							
502.7	372.9								
541.6	468.6	148.6							
0.5	1	1	0	0	0	0	0	0	0

@!Reaction									
Ob(e)-->Ob(0e)	7	1	0.007	1.701					
O*e + *0 +<>+ O*0 + *e | -1 -1 1 1									
541.6	468.6	148.6							
481.2	371.8								
503.2	486.1	139.4							
0.5	1	1	0	0	0	0	0	0	0

@!Reaction									
Ht(1e)-->Hb(e)	8	1	0.823	0.050					
H*1 + *e +<>+ H*e + *1 | -1 -1 1 1									
2283.8	375.8	365.9							
1981.7	-170.3								
1345.6	1044.3	382.9							
0.5	1	1	0	0	0	0	0	0	0

@!Reaction									
Hb(e)-->Hb(0e)	9	1	0.055	0.964					
H*e + *0 +<>+ H*0 + *e | -1 -1 1 1									
1345.6	1044.3	382.9							
2121.8	199.5								
1347.9	1046.2	385.1							
0.5	1	1	0	0	0	0	0	0	0

@!Reaction									
OHt(1e)-->OHb(e)	10	1	0.156	0.399					
OH*1 + *e +<>+ OH*e + *1 | -1 -1 1 1									
3664.7	934.0	525.6	167.4	111.0	77.2				
3637.0	878.3	478.0	375.3	144.9					
3669.2	800.9	693.5	419.9	314.3	137.3				
0.5	1	1	0	0	0	0	0	0	0

@!Reaction									
OHb(e)-->OHb(0e)	11	1	0.182	0.603					
OH*e + *0 +<>+ OH*0 + *e | -1 -1 1 1									
3669.2	800.9	693.5	419.9	314.3	137.3				
3651.0	858.3	508.3	342.8	106.1					
3597.1	837.7	711.5	402.9	332.1	145.0				
0.5	1	1	0	0	0	0	0	0	0

@!Reaction									
H2Ot(1e)-->H2Ot(e)	12	1	0.000	0.091					
H2O*1 + *e +<>+ H2O*e + *1 | -1 -1 1 1									
3731.1	3621.7	1563.5	539.2	513.8	174.1	100.0	94.2	75.2	
3781.6	3668.5	1578.6	200.5	150.6	70.3	61.1	13.4		
3725.7	3426.7	1561.7	574.2	553.0	227.1	206.7	100.2	48.4	
0.5	1	1	0	0	0	0	0	0	0

@!Reaction									
H2Ot(e)-->H2Ot(0e)	13	1	0.018	0.000					
H2O*e + *0 +<>+ H2O*0 + *e | -1 -1 1 1									
3731.1	3621.7	1563.5	539.2	513.8	174.1	100.0	94.2	75.2	
3781.6	3668.5	1578.6	200.5	150.6	70.3	61.1	13.4		
3725.7	3426.7	1561.7	574.2	553.0	227.1	206.7	100.2	48.4	
0.5	1	1	0	0	0	0	0	0	0

E7: Energetics Summary

Table E7.1: Sumary of ORR elementary reactions, rate expressions and energetics calcualted on a Pt(111)-*p*(3x3) surface model; energies at 0 K and without zero-point correction.

#	**Reaction**	**Rate eqn.**	$E_{a,f}$	$E_{a,r}$	α	S_0
1	$O_2 + * \leftrightarrow O_2*$	$k_{1f}\theta_{*h}p_{O_2}-k_{1r}\theta_{O_2h}$	0.0	0.714	0.0	1.0
2	$H_2 + 2* \leftrightarrow 2H*$	$k_{2f}\theta_{*h}^2p_{H_2}-k_{2r}\theta_{Hh}^2$	0.0	1.052	0.0	1.0
3	$H_2O + * \leftrightarrow H_2O*$	$k_{3f}\theta_{*h}p_{H_2O}-k_{3r}\theta_{H_2Oh}$	0.0	0.222	0.0	1.0
4	$O_2* + * \leftrightarrow 2O*$	$k_{4f}\theta_{O_2h}\theta_{*h}-k_{4r}\theta_{Oh}^2$	0.485;	2.244	0.20	
5	$O* + H* \leftrightarrow OH* + *$	$k_{5f}\theta_{Oh}\theta_{Hh}-k_{5r}\theta_{OHh}\theta_{*h}$	1.041;	0.975	0.49	
6	$OH* + H* \leftrightarrow H_2O* + *$	$k_{6f}\theta_{OHh}\theta_{Hh}-k_{6r}\theta_{H_2Oh}\theta_{*h}$	0.215;	0.779	0.18	
7	$OH* + OH* \leftrightarrow O* + H_2O*$	$k_{7f}\theta_{OHh}^2-k_{7r}\theta_{Oh}\theta_{H_2Oh}$	0.630;	0.000	0.89	
8	$O_2* + H* \leftrightarrow OOH* + *$	$k_{8f}\theta_{O_2h}\theta_{Hh}-k_{8r}\theta_{OOHh}\theta_{*h}$	0.536;	0.493	0.46	
9	$OOH* + * \leftrightarrow O* + OH*$	$k_{9f}\theta_{OOHh}\theta_{*h}-k_{9r}\theta_{Oh}\theta_{OHh}$	0.036;	1.773	0.02	

Table E7.2: Sumary of ORR elementary reactions, rate expressions and energetics calcualted on a Pt(100)-*p*(3x3) surface model; energies at 0 K and without zero-point correction

#	**Reaction**	**Rate eqn.**	$E_{a,f}$	$E_{a,r}$	α	S_0
1	$O_2 + * \leftrightarrow O_2*$	$k_{1f}\theta_{*s}p_{O_2}-k_{1r}\theta_{O_2s}$	0.0	1.244	0.00	1.0
2	$H_2 + 2* \leftrightarrow 2H*$	$k_{2f}\theta_{*s}^2p_{H_2}-k_{2r}\theta_{Hs}^2$	0.0	1.377	0.00	1.0
3	$H_2O + * \leftrightarrow H_2O*$	$k_{3f}\theta_{*s}p_{H_2O}-k_{3r}\theta_{H_2Os}$	0.0	0.294	0.00	1.0
4	$O_2* + * \leftrightarrow 2O*$	$k_{4f}\theta_{O_2s}\theta_{*s}-k_{4r}\theta_{Os}^2$	0.143	1.587	0.09	
5	$O* + H* \leftrightarrow OH* + *$	$k_{5f}\theta_{Os}\theta_{Hs}-k_{5r}\theta_{OHs}\theta_{*s}$	0.538	0.867	0.38	
6	$OH* + H* \leftrightarrow H_2O* + *$	$k_{6f}\theta_{OHs}\theta_{Hs}-k_{6r}\theta_{H_2Os}\theta_{*s}$	0.886	0.700	0.50	
7	$OH* + OH* \leftrightarrow O* + H_2O*$	$k_{7f}\theta_{OHs}^2-k_{7r}\theta_{Os}\theta_{H_2Os}$	0.000	0.518	0.08	
8	$O_2* + H* \leftrightarrow OOH* + *$	$k_{8f}\theta_{O_2s}\theta_{Hs}-k_{8r}\theta_{OOHs}\theta_{*s}$				
9	$OOH* + * \leftrightarrow O* + OH*$	$k_{9f}\theta_{OOHs}\theta_{*s}-k_{9r}\theta_{Os}\theta_{OHs}$				

Table E7.3: Sumary of ORR elementary reactions, rate expressions and energetics calcualted on mult-faceted Pt NW surfaces; energies at 0 K and without zero-point correction and have been corrected such that they represent a NW model with Pt(111) and Pt(100) facets instead of Pt{111} and Pt{100} facets. The h, s and e coverage subscripts in column 3 refere to coverage on {111}, {100} and edge sites, respectively.

#	**Reaction**	**Rate eqn.**	$E_{a,f}$	$E_{a,r}$	α	S_0
1	$O_2 + * \leftrightarrow O_2*$	$k_{1f}\theta_{*e}p_{O_2}$-$k_{1r}\theta_{O_2e}$	0	1.621	0.0	1.0
2	$H_2 + 2* \leftrightarrow 2H*$	$k_{2f}\theta_{*e}^2 p_{H_2}$-$k_{2r}\theta_{He}^2$	0	1.495	0.0	1.0
3	$H_2O + * \leftrightarrow H_2O*$	$k_{3f}\theta_{*e}p_{H_2O}$-$k_{3r}\theta_{H_2Oe}$	0	0.360	0.0	1.0
4-6	$O_2* + * \leftrightarrow 2O*$	$k_{4f}\theta_{O_2e}\theta_{*e}$-$k_{4r}\theta_{Oe}^2$	1.189	2.887	0.5	
		$k_{5f}\theta_{O_2e}\theta_{*s}$-$k_{4r}\theta_{Oe}\theta_{Os}$	0.642	2.025	0.5	
		$k_{6f}\theta_{O_2e}\theta_{*h}$-$k_{4r}\theta_{Oe}\theta_{Oh}$	1.123	2.399	0.5	
7-10	$O* + H* \leftrightarrow OH* + *$	$k_{7f}\theta_{Os}\theta_{He}$-$k_{7r}\theta_{OHs}\theta_{*e}$	0.664	0.845	0.5	
		$k_{8f}\theta_{Oe}\theta_{Hs}$-$k_{8r}\theta_{OHe}\theta_{*s}$	0.847	1.089	0.5	
		$k_{9f}\theta_{Oe}\theta_{Hh}$-$k_{9r}\theta_{OHe}\theta_{*h}$	0.685	1.069	0.5	
		$k_{10f}\theta_{Oh}\theta_{He}$-$k_{10r}\theta_{OHh}\theta_{*e}$	1.385	1.026	0.5	
					0.5	
11-14	$OH* + H* \leftrightarrow H_2O* + *$	$k_{11f}\theta_{OHe}\theta_{Hh}$-$k_{11r}\theta_{H_2Oe}\theta_{*h}$	0.922	0.753	0.5	
		$k_{12f}\theta_{OHh}\theta_{He}$-$k_{12r}\theta_{H_2Oh}\theta_{*e}$	0.662	1.005	0.5	
		$k_{13f}\theta_{OHe}\theta_{Hs}$-$k_{13r}\theta_{H_2Oe}\theta_{*s}$	1.619	1.271	0.5	
		$k_{14f}\theta_{OHs}\theta_{He}$-$k_{14r}\theta_{H_2Os}\theta_{*e}$	1.049	0.801	0.5	
15-18	$OH* + OH* \leftrightarrow O* + H_2O*$	$k_{15f}\theta_{OHe}\theta_{OHs}$-$k_{15r}\theta_{Os}\theta_{H_2Oe}$	0.657	0.000	0.5	
		$k_{16f}\theta_{OHe}\theta_{OHs}$-$k_{16r}\theta_{Oe}\theta_{H_2Os}$	0.430	0.000	0.5	
		$k_{17f}\theta_{OHe}\theta_{OHh}$-$k_{17r}\theta_{Oh}\theta_{H_2Oe}$	0.439	0.315	0.5	
		$k_{18f}\theta_{OHe}\theta_{OHh}$-$k_{18r}\theta_{Oe}\theta_{H_2Oh}$	0.000	0.181	0.5	
19-20	$OH* + O* \leftrightarrow O* + OH*$	$k_{19f}\theta_{OHh}\theta_{Oe}$-$k_{19r}\theta_{Oh}\theta_{OHe}$	0.446	0.862	0.5	
		$k_{20f}\theta_{OHe}\theta_{Os}$-$k_{20r}\theta_{Oe}\theta_{OHs}$	0.070	0.158	0.5	
					0.5	
21	$O_2* + * \leftrightarrow * + O_2*$	$k_{21f}\theta_{O_2h}\theta_{*e}$-$k_{21r}\theta_{*h}\theta_{O_2e}$	0.029	1.013	0.5	
22-23	$O* + * \leftrightarrow * + O*$	$k_{22f}\theta_{Oh}\theta_{*e}$-$k_{22r}\theta_{*h}\theta_{Oe}$	0.646	1.069	0.5	
		$k_{23f}\theta_{Oe}\theta_{*s}$-$k_{23r}\theta_{*e}\theta_{Os}$	0.626	0.311	0.5	
24-25	$H* + * \leftrightarrow * + H*$	$k_{24f}\theta_{Hh}\theta_{*e}$-$k_{24r}\theta_{*h}\theta_{He}$	0.195	0.416	0.5	
		$k_{25f}\theta_{He}\theta_{*s}$-$k_{25r}\theta_{*e}\theta_{Hs}$	0.336	0.277	0.5	
26-27	$OH* + * \leftrightarrow * + OH*$	$k_{26f}\theta_{OHh}\theta_{*e}$-$k_{26r}\theta_{*h}\theta_{OHe}$	0.119	0.991	0.5	
		$k_{27f}\theta_{OHe}\theta_{*s}$-$k_{27r}\theta_{*e}\theta_{OHs}$	0.681	0.473	0.5	
26-27	$H_2O* + * \leftrightarrow * + H_2O*$	$k_{26f}\theta_{H_2Oh}\theta_{*e}$-$k_{26r}\theta_{*h}\theta_{H_2Oe}$	0.121	0.260	0.5	
		$k_{27f}\theta_{H_2Oe}\theta_{*s}$-$k_{27r}\theta_{*e}\theta_{H_2Os}$	0.224	0.158	0.5	

Table E7.4: Sumary of ORR elementary reactions, rate expressions and energetics calcualted on Au modified mult-faceted Pt NW surfaces. Activation energies at 0 K and without zero-point correction and have been corrected such that they represent a NW model with Pt(111) and Pt(100) facets instead of Pt{111} and Pt{100} facets. To be used with data in Tables E7.1 and E7.2 in microkinetic analysis. The h, s and e coverage subscripts in column 3 refere to coverage on {111}, {100} and edge sites, respectively.

#	**Reaction**	**Rate eqn.**	$E_{a,f}$	$E_{a,r}$	α	S_0
1	$O_2 + * \leftrightarrow O_2*$	$k_{1f}\theta_{*e}p_{O_2}-k_{1r}\theta_{O_2e}$	0	0.151	0.0	1.0
2	$H_2 + 2* \leftrightarrow 2H*$	$k_{2f}\theta_{*e}^2p_{H_2}-k_{2r}\theta_{He}^2$	0	0.314	0.0	1.0
3	$H_2O + * \leftrightarrow H_2O*$	$k_{3f}\theta_{*e}p_{H_2O}-k_{3r}\theta_{H_2Oe}$	0	0.205	0.0	1.0
21	$O_2* + * \leftrightarrow * + O_2*$	$k_{21af}\theta_{O_2h}\theta_{*e}-k_{21ar}\theta_{*h}\theta_{O_2e}$	0.564	0.000	0.5	
		$k_{21bf}\theta_{O_2h}\theta_{*e}-k_{21br}\theta_{*h}\theta_{O_2e}$	0.000	1.094		
22-23	$O* + * \leftrightarrow * + O*$	$k_{22f}\theta_{Oh}\theta_{*e}-k_{22r}\theta_{*h}\theta_{Oe}$	1.335	0.193	0.5	
		$k_{23f}\theta_{Oe}\theta_{*s}-k_{23r}\theta_{*e}\theta_{Os}$	0.118	1.368	0.5	
24-25	$H* + * \leftrightarrow * + H*$	$k_{24f}\theta_{Hh}\theta_{*e}-k_{24r}\theta_{*h}\theta_{He}$	0.547	0.151	0.5	
		$k_{25f}\theta_{He}\theta_{*s}-k_{25r}\theta_{*e}\theta_{Hs}$	0.179	0.710	0.5	
26-27	$OH* + * \leftrightarrow * + OH*$	$k_{26f}\theta_{OHh}\theta_{*e}-k_{26r}\theta_{*h}\theta_{OHe}$	0.498	0.527	0.5	
		$k_{27f}\theta_{OHe}\theta_{*s}-k_{27r}\theta_{*e}\theta_{OHs}$	0.250	0.885	0.5	
26-27	$H_2O* + * \leftrightarrow * + H_2O*$	$k_{26f}\theta_{H_2Oh}\theta_{*e}-k_{26r}\theta_{*h}\theta_{H_2Oe}$	0.017	0.000	0.5	
		$k_{27f}\theta_{H_2Oe}\theta_{*s}-k_{27r}\theta_{*e}\theta_{H_2Os}$	0.000	0.089	0.5	

Table E7.5: Sumary of ORR elementary reactions, rate expressions and energetics calcualted on Ag modified mult-faceted Pt NW surfaces. Activation energies at 0 K and without zero-point correction and have been corrected such that they represent a NW model with Pt(111) and Pt(100) facets instead of Pt{111} and Pt{100} facets. To be used with data in Tables E7.1 and E7.2 in microkinetic analysis. The h, s and e coverage subscripts in column 3 refere to coverage on {111}, {100} and edge sites, respectively.

#	**Reaction**	**Rate eqn.**	$E_{a,f}$	$E_{a,r}$	α	S_0
1	$O_2 + * \leftrightarrow O_2*$	$k_{1f}\theta_{*_e}p_{O_2}-k_{1r}\theta_{O_{2e}}$	0.067	0.0	0.0	1.0
2	$H_2 + 2* \leftrightarrow 2H*$	$k_{2f}\theta_{*_e}^2p_{H_2}-k_{2r}\theta_{He}^2$	0.441	0.0	0.0	1.0
3	$H_2O + * \leftrightarrow H_2O*$	$k_{3f}\theta_{*_e}p_{H_2O}-k_{3r}\theta_{H_2Oe}$	0.0	0.319	0.0	1.0
					0.5	
21	$O_2* + * \leftrightarrow * + O_2*$	$k_{21f}\theta_{O_{2h}}\theta_{*_e}-k_{21r}\theta_{*_h}\theta_{O_{2e}}$	0.782	0.000	0.5	
		$k_{21bf}\theta_{O_{2h}}\theta_{*_e}-k_{21br}\theta_{*_h}\theta_{O_{2e}}$	0.000	1.312	0.5	
22-23	$O* + * \leftrightarrow * + O*$	$k_{22f}\theta_{Oh}\theta_{*_e}-k_{22r}\theta_{*_h}\theta_{Oe}$	1.620	0.034	0.5	
		$k_{23f}\theta_{Oe}\theta_{*_s}-k_{23r}\theta_{*_e}\theta_{Os}$	0.007	1.701	0.5	
24-25	$H* + * \leftrightarrow * + H*$	$k_{24f}\theta_{Hh}\theta_{*_e}-k_{24r}\theta_{*_h}\theta_{He}$	0.823	0.050	0.5	
		$k_{25f}\theta_{He}\theta_{*_s}-k_{25r}\theta_{*_e}\theta_{Hs}$	0.055	0.964	0.5	
26-27	$OH* + * \leftrightarrow * + OH*$	$k_{26f}\theta_{OHh}\theta_{*_e}-k_{26r}\theta_{*_h}\theta_{OHe}$	0.156	0.399	0.5	
		$k_{27f}\theta_{OHe}\theta_{*_s}-k_{27r}\theta_{*_e}\theta_{OHs}$	0.182	0.603	0.5	
26-27	$H_2O* + * \leftrightarrow * + H_2O*$	$k_{26f}\theta_{H_2Oh}\theta_{*_e}-k_{26r}\theta_{*_h}\theta_{H_2Oe}$	0.000	0.091	0.5	
		$k_{27f}\theta_{H_2Oe}\theta_{*_s}-k_{27r}\theta_{*_e}\theta_{H_2Os}$	0.018	0.000	0.5	

E8: Near-edge ORR energetics

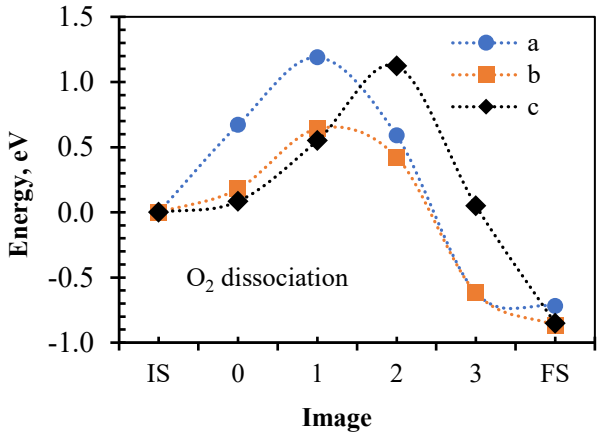

Figure E8.1: O_2 dissociation PES at edge and near-edge sites via (a) $O_2^{b(e)} \rightarrow 2O^{b(e)}$, (b) $O_2^{b(e)} \rightarrow 2O^{b(0e)}$ and (c) $O_2^{b(e)} \rightarrow O^{b(e)} + O^{f(1e)}$

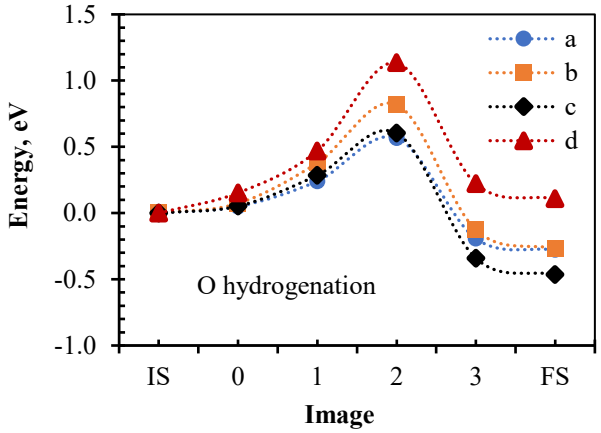

Figure E8.2: O hydrogenation PES at edge and near-edge sites via (a) $O^{b(00e)} + H^{b(e)} \rightarrow OH^{b(00e)}$, (b) $O^{b(e)} + H^{b(00e)} \rightarrow OH^{b(e)}$, (c) $O^{b(e)} + H^{t(1e)} \rightarrow OH^{b(e)}$ and (d) $O^{f(1e)} + H^{b(e)} \rightarrow OH^{b(1e)}$

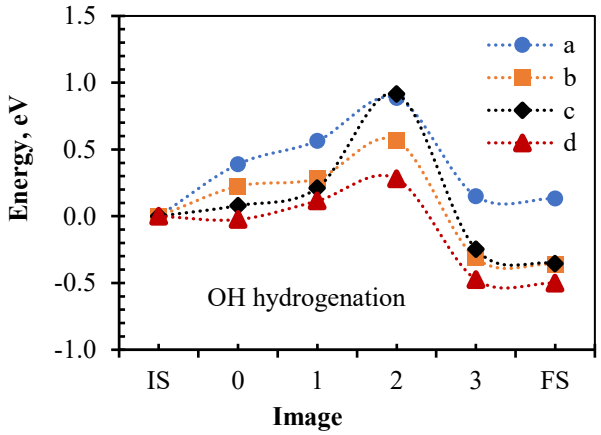

Figure E8.3: OH hydrogenation PES at edge and near-edge sites via (a) $OH^{b(e)} + H^{t(1e)} \rightarrow H_2O^{t(e)}$, (b) $OH^{t(1e)} + H^{b(e)} \rightarrow H_2O^{t(1e)}$, (c) $OH^{b(e)} + H^{b(00e)} \rightarrow H_2O^{t(e)}$ and (d) $OH^{b(00e)} + H^{b(e)} \rightarrow H_2O^{t(0e)}$

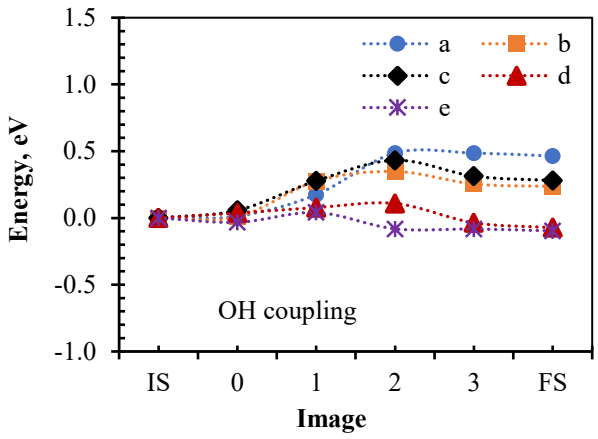

Figure E8.4: OH coupling (or reverse O hydrolysis) PES at edge and near-edge sites via (a) $OH^{b(e)} + OH^{b(00e)} \rightarrow H_2O^{t(e)} + O^{b(00e)}$, (b) $OH^{b(e)} + OH^{b(00e)} \rightarrow H_2O^{t(0e)} + O^{b(e)}$, (c) $OH^{b(e)} + OH^{t(1e)} \rightarrow H_2O^{t(e)} + O^{f(1e)}$, (d) $OH^{t(e)} + OH^{b(1e)} \rightarrow H_2O^{t(e)} + O^{f(1e)}$ and (e) $OH^{b(e)} + OH^{t(1e)} \rightarrow H_2O^{t(1e)} + O^{b(e)}$

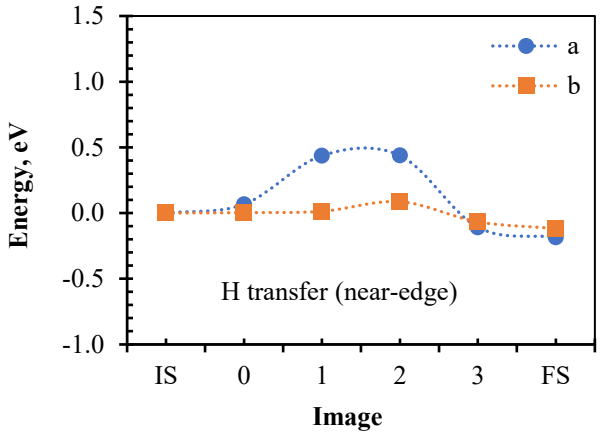

Figure E8.5: H transfer between edge and near edge O/OH intermediates PES at edge and near-edge sites via (a) $OH^{b(1e)} + O^{b(e)} \rightarrow O^{f(1e)} + OH^{b(e)}$ and (b) $OH^{b(e)} + O^{b(00e)} \rightarrow O^{b(e)} + OH^{b(00e)}$.

Appendix F: ORR on Pt surfaces

F1: ORR activity over Pt(111) and Pt(100)

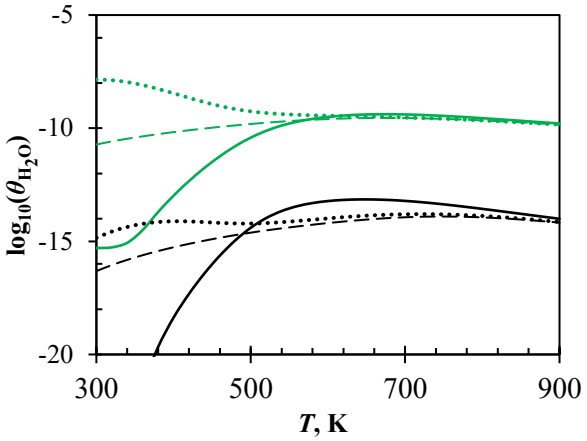

Figure F1.1: H_2O coverage on Pt(111) surface, black under dry conditions (H_2:O_2 = 2:1 and 1 bar) and green under moist conditions (H_2:O_2 = 2:1 and 1 bar + 0.46 bar H2O) by SA (—), BWA (− − −) and QCA (·····) microkinetic models at various temperatures.

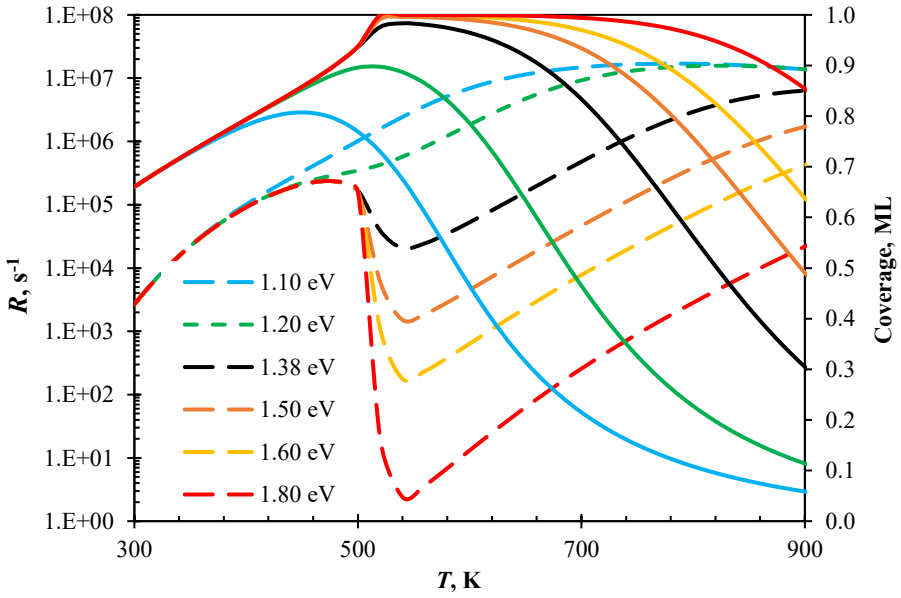

Figure F1.2: Effect of the adsorption energy of H_2 on the ORR rate (solid lines) and coverage of Pt(100) with H* adsorbates (dashed lines); black profiles correspond to the calculated case, i.e. -1.377 eV/H2. BWA model simulations under dry conditions (H_2:O_2 = 2:1 and 1 bar).

F2: ORR activity on multi-faceted Pt surfaces

F2.1 Effects of edge reaction events on ORR rate and pathway

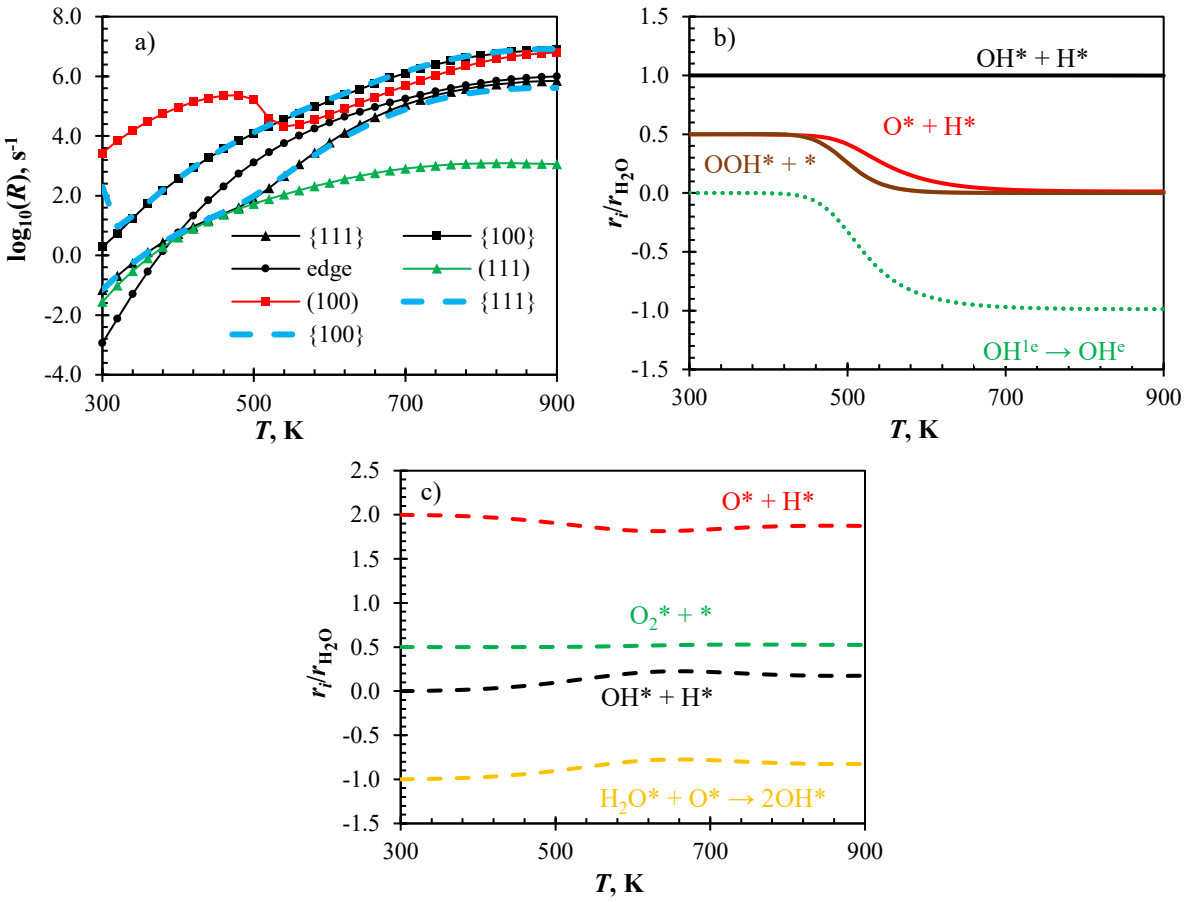

Figure F2.1: Effect of inter-facet diffusion only on the ORR rate (sky blue profile in (a)) and pathway on multifaceted Pt surfaces, (b) over Pt{111} facet and (c) over a Pt{100} facet. Based on a BWA and a $\chi_{edge}(1.00)$ model. (a) ORR rates (dashed blue line for diffusion only).

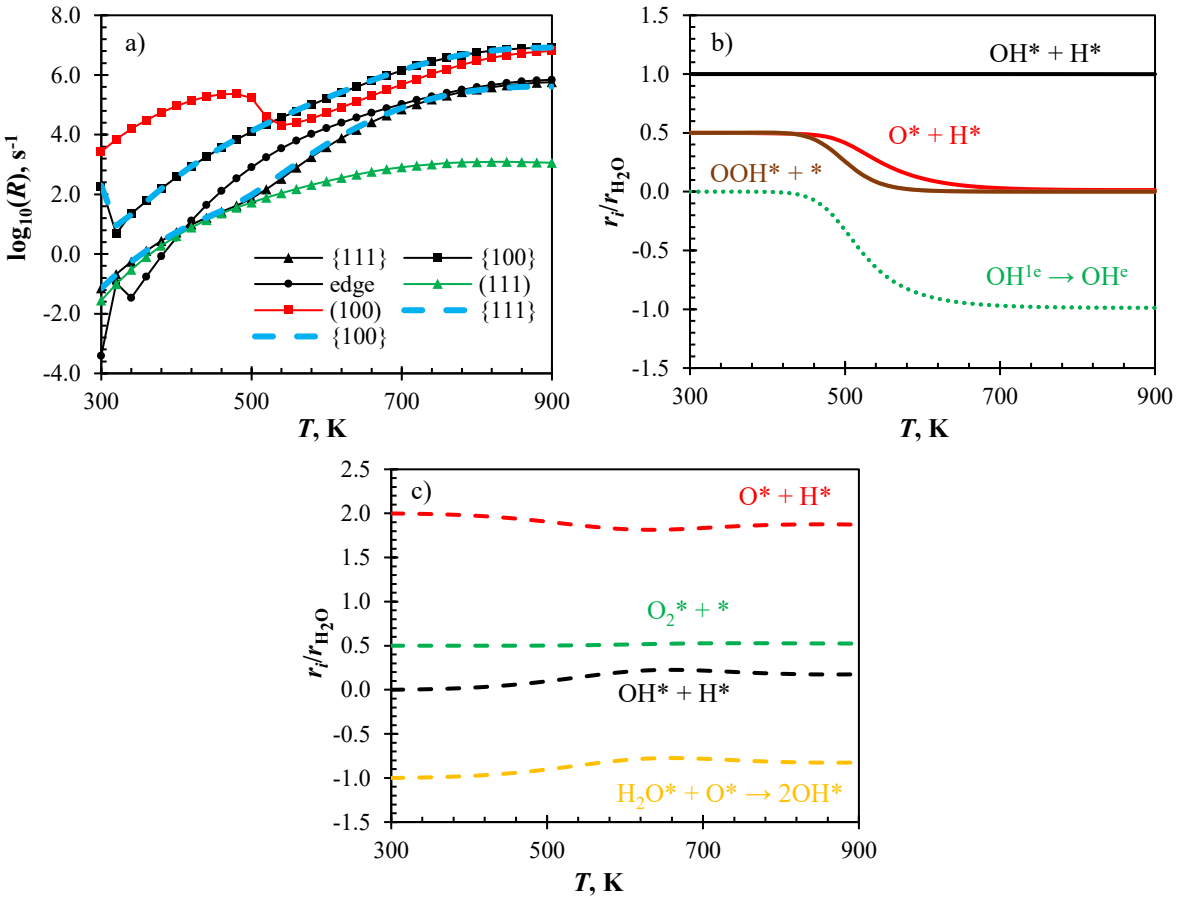

Figure F2.2: Effect of inter-facet diffusion only on the ORR rate (sky blue profile in (a)) and pathway on multifaceted Pt surfaces, (b) over Pt{111} facet and (c) over a Pt{100} facet. Based on a BWA and a $\chi_{edge}(0.34)$ model. (a) ORR rates (dashed blue line for diffusion only).

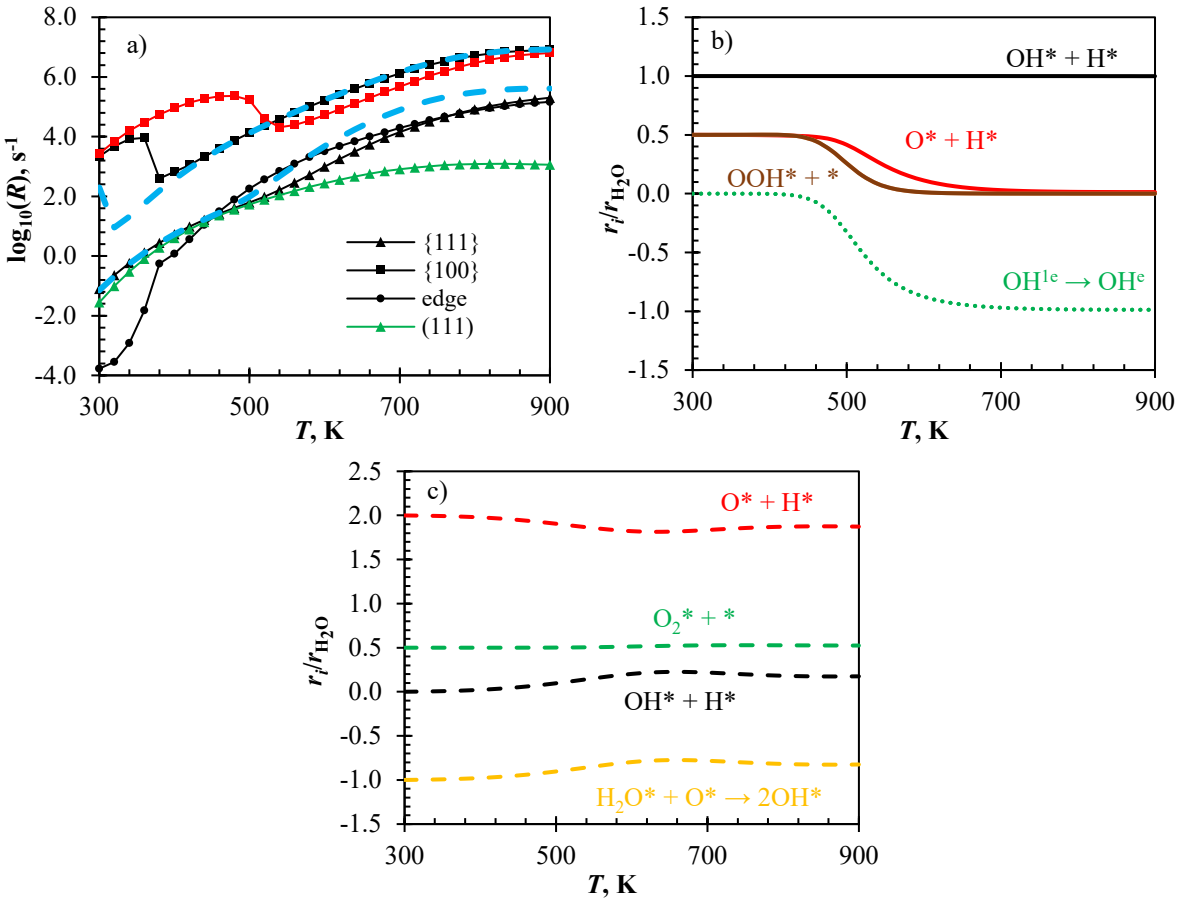

Figure F2.3: Effect of inter-facet diffusion only on the ORR rate (sky blue profile in (a)) and pathway on multifaceted Pt surfaces, (b) over Pt{111} facet and (c) over a Pt{100} facet. Based on a BWA and a $\chi_{edge}(0.04)$ model. (a) ORR rates (dashed blue line for diffusion only).

F2.2 Effects of edge sites fraction on ORR rate, surface coverage and pathway

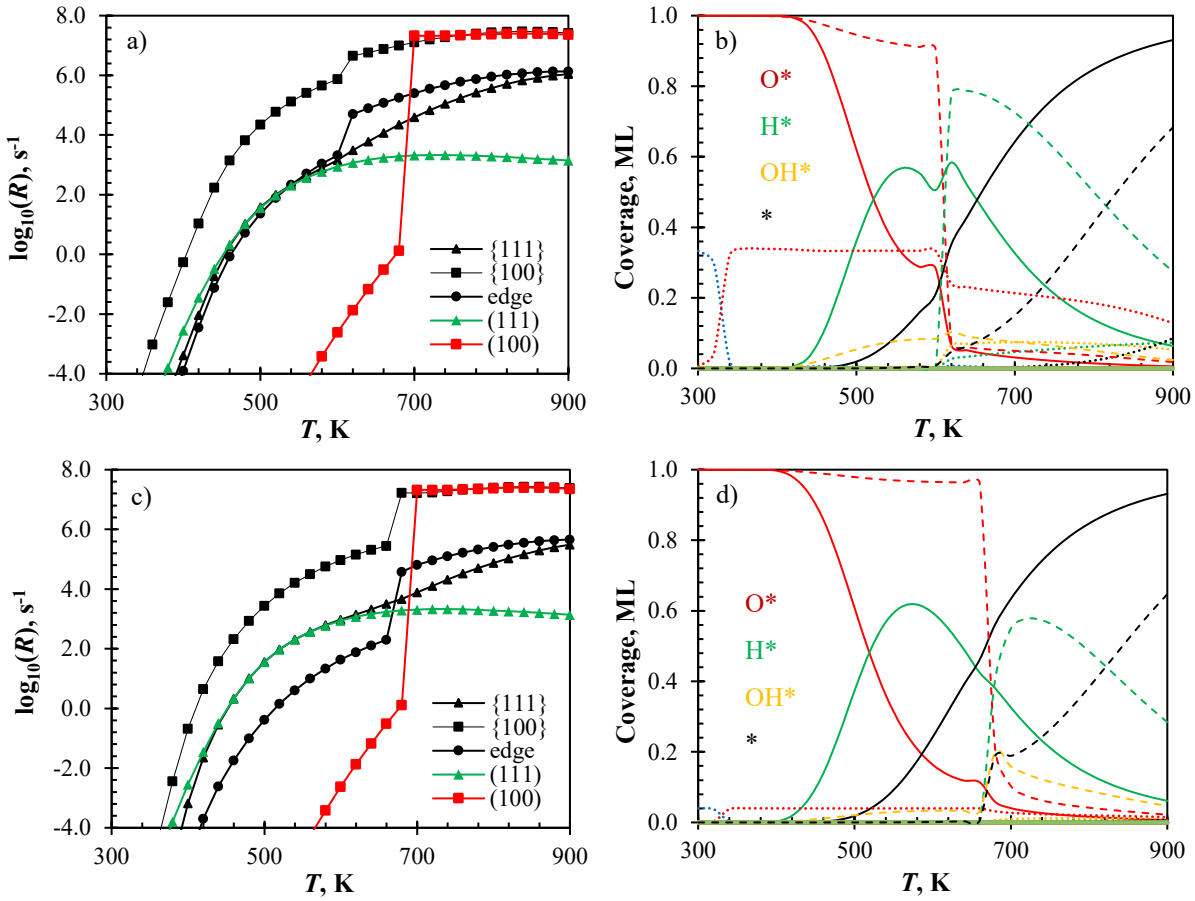

Figure F2.4: SA model predicted ORR activity over a multifaceted Pt surface, (a, c) H_2O evolution rates and (b, d) surface coverage over Pt{111} facet (—), Pt{100} facet (− − −) and edge sites (·····), for a $\chi_{edge}(0.34)$ model (a, b) and $\chi_{edge}(0.04)$ model (c, d).

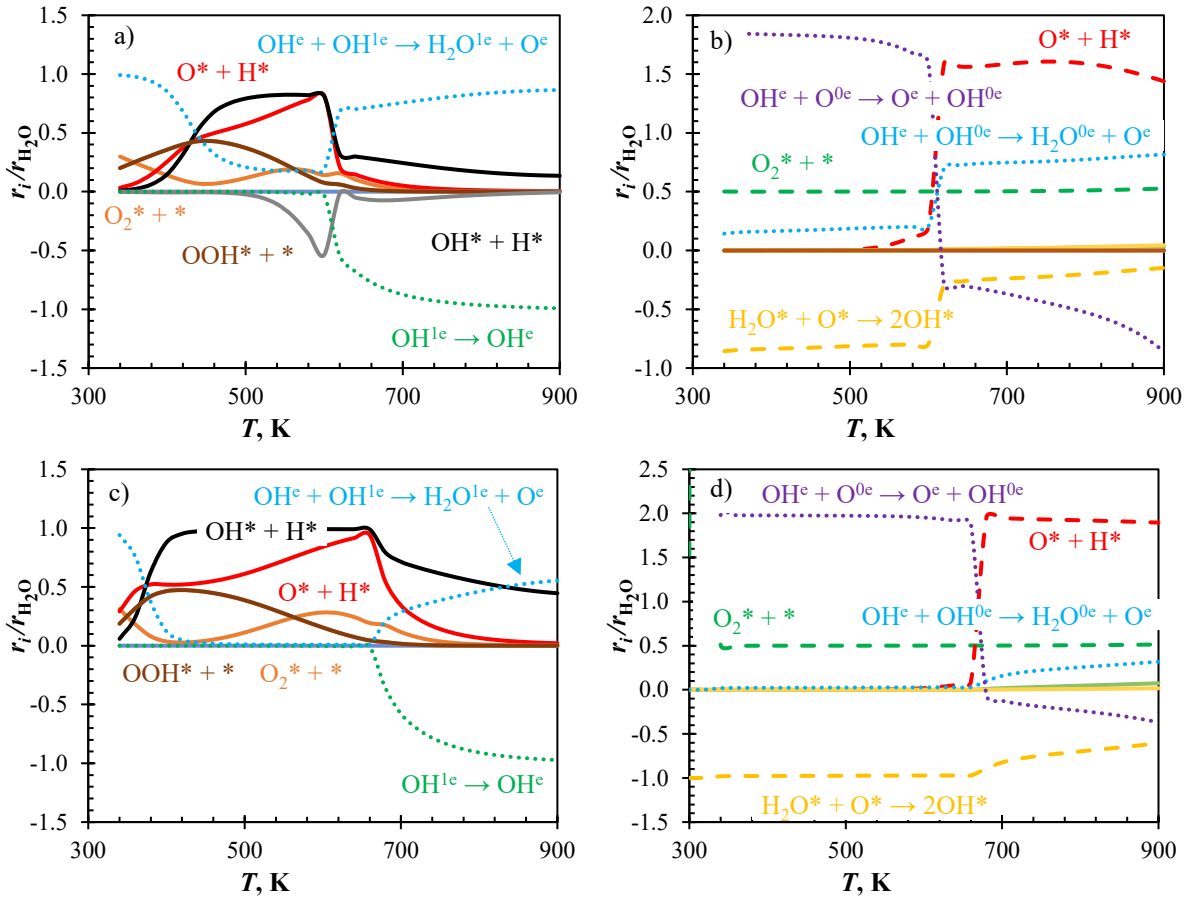

Figure F2.5: SA model predicted ORR pathway over a multifaceted Pt surface , (a, c) over Pt{111} facet and (b, d) Pt{100} facet; processes on Pt{111} facet (—), Pt{100} facet (− − −) and involving edge species (·····), for a $\chi_{edge}(0.34)$ model (a, b) and $\chi_{edge}(0.04)$ model (c, d). Negative values indicate that the reverse reaction contributes to the H2O evolution rate—(a,b) $\chi_{edge}(1.00)$, (c,d) $\chi_{edge}(0.34)$ and (e,f) $\chi_{edge}(0.04)$ models.

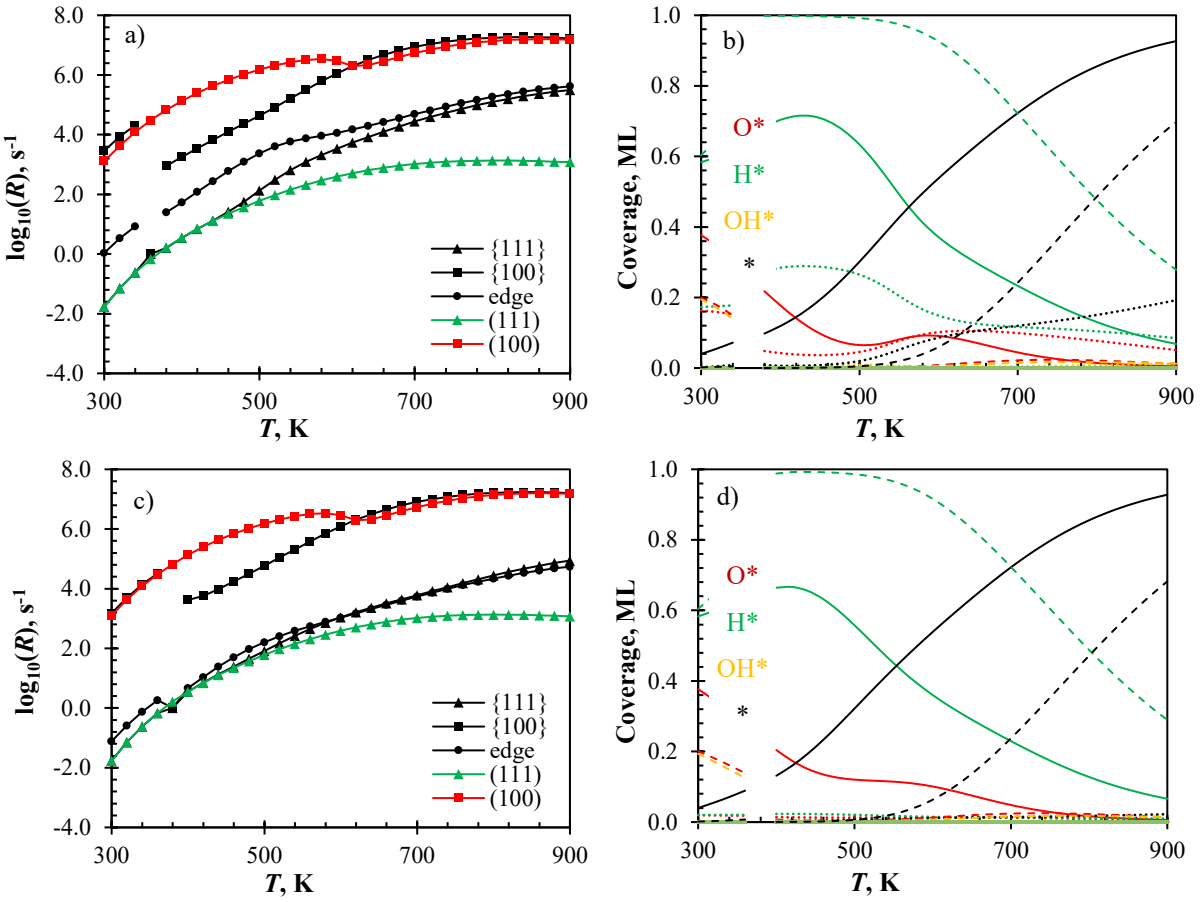

Figure F2.6: QCA model predicted ORR activity over a multifaceted Pt surface, (a, c) H_2O evolution rates and (b, d) surface coverage over Pt{111} facet (—), Pt{100} facet (– – –) and edge sites (·····), for a $\chi_{edge}(0.34)$ model (a, b) and $\chi_{edge}(0034)$ model (c, d).

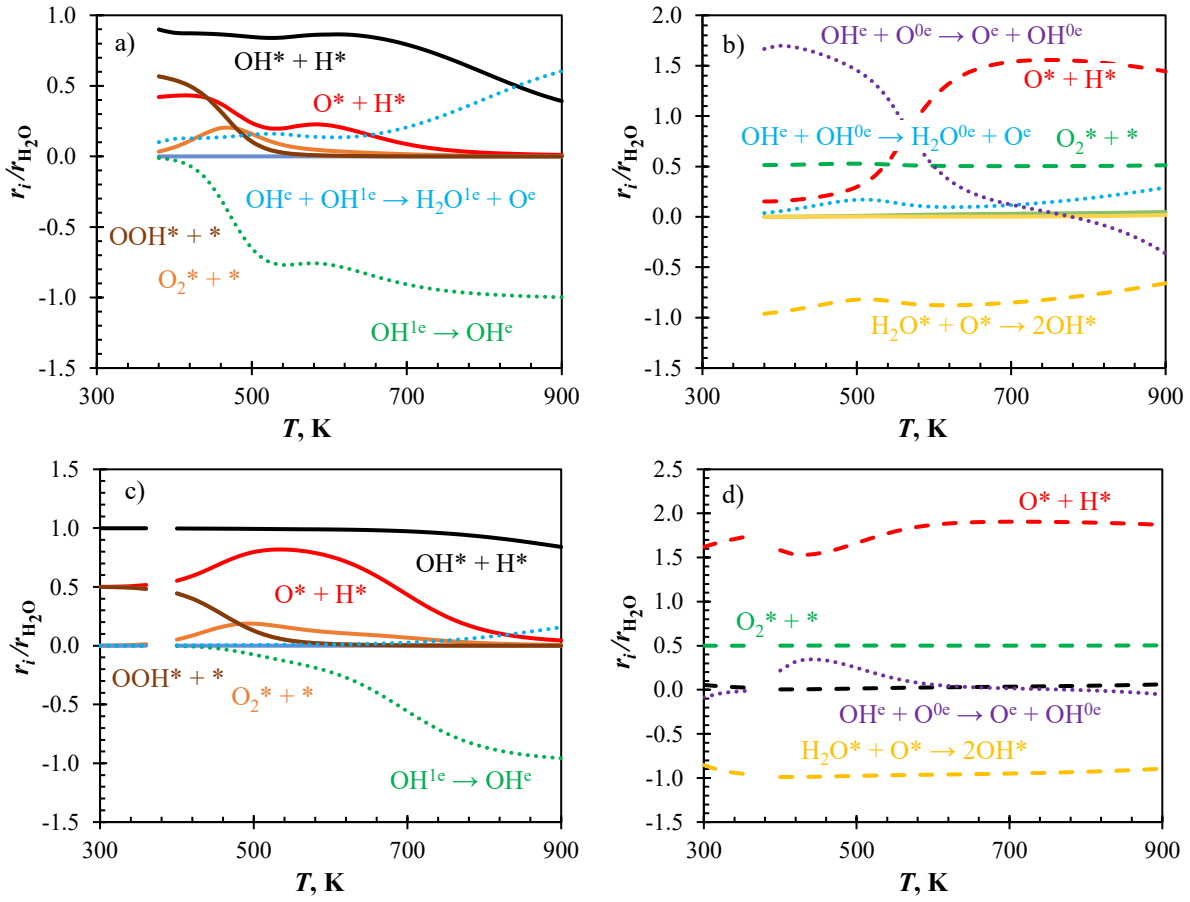

Figure F2.5: QCA model predicted ORR pathway over a multifaceted Pt surface , (a, c) over Pt{111} facet and (b, d) Pt{100} facet; processes on Pt{111} facet (—), Pt{100} facet (– – –) and involving edge species (·····), for a $\chi_{edge}(0.34)$ model (a, b) and $\chi_{edge}(0.04)$ model (c, d). Negative values indicate that the reverse reaction contributes to the H_2O evolution rate—(a,b) $\chi_{edge}(1.00)$, (c,d) $\chi_{edge}(0.34)$ and (e,f) $\chi_{edge}(0.04)$ models.

Appendix G: ORR on modified multi-faceted Pt surfaces

G1: Energetics

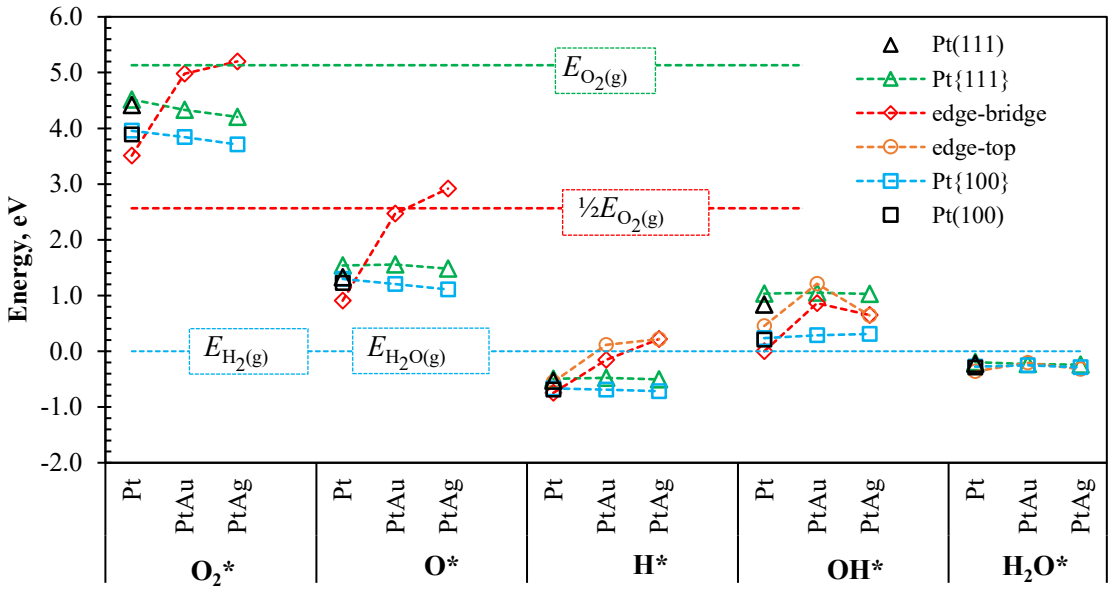

Figure G1.1: Adsorption energies of O_2*, O*, H*, OH* and H_2O* on modified and unmodified Pt NW surfaces; energies are reported relative to H_2O and H_2 gases.

Table G1.1: Comparison between adsorption energy of O on edge-bridge sites of modified and unmodified Pt NWs at different edge coverages.

	Ag (mod.)		**Au (mod.)**		**Pt (un-mod.)**	
Coverage ML	1xO/4x Ag 0.25	1xO/2x Ag 0.50	1xO/4x Au 0.25	1xO/2x Au 0.50	1xO/4x Pt 0.25	1xO/2x Pt 0.50
Clean [eV]	-751.95	-376.73	-753.61	-381.75	-763.55	-381.66
O/EB [eV]	-756.59	-375.89	-758.68	-380.47	-770.17	-388.25
E_{ads} [eV/½O_2]	0.28	0.35	-0.14	-0.09	-1.69	-1.66

G2: ORR activity and pathway analysis (QCA model) on Au/Pt NW

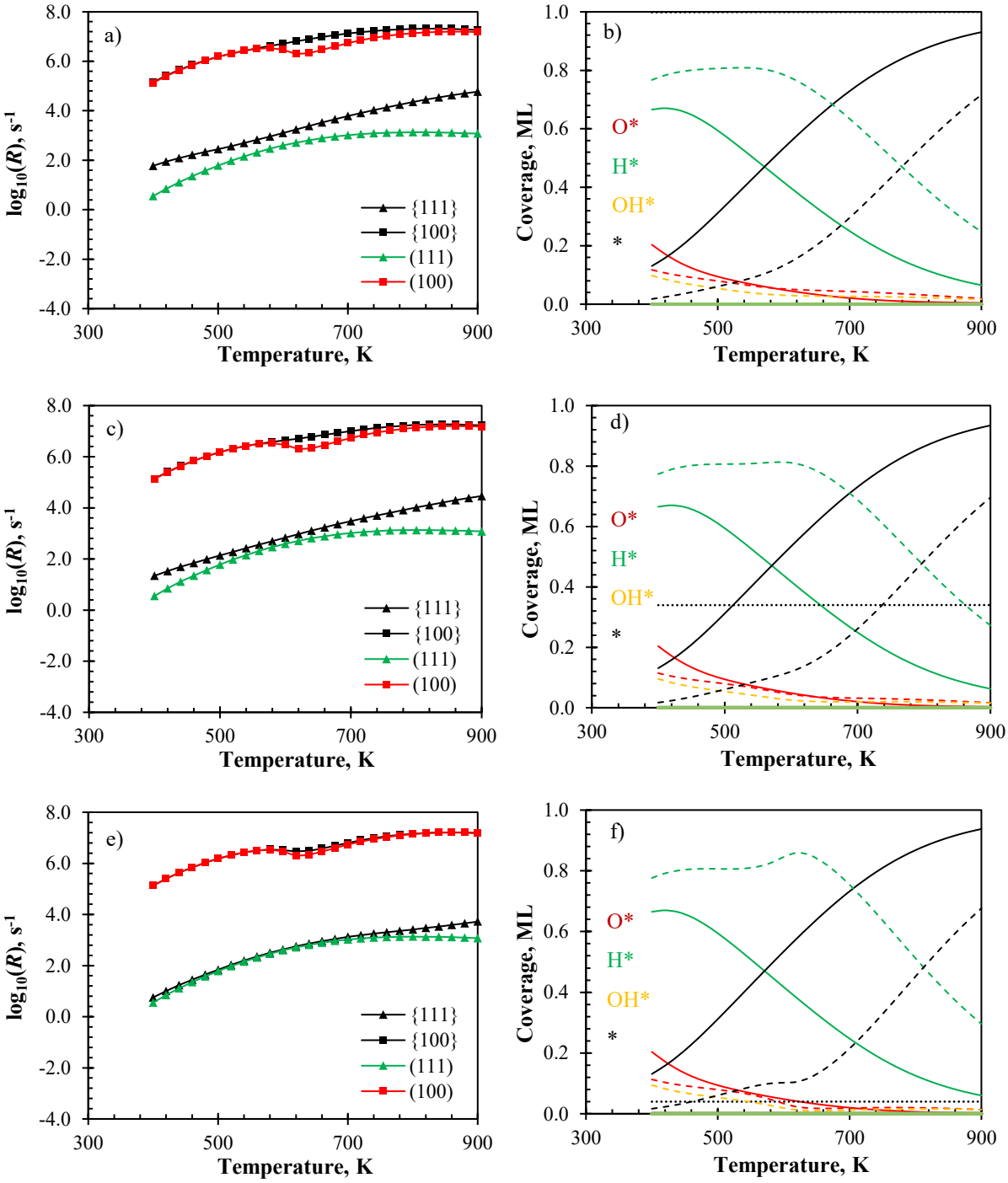

Figure G2.1: QCA model predicted ORR activity over a multifaceted Au/Pt surface, (a, c, e) H_2O evolution rates and (b, d, f) surface coverage over Au/Pt{111} facet (—), Au/Pt{100} facet (– – –) and edge sites (·····), for a $\chi_{edge}(1.00)$ model (a, b), $\chi_{edge}(0.34)$ model (c, d) and $\chi_{edge}(0.04)$ model (e, f).

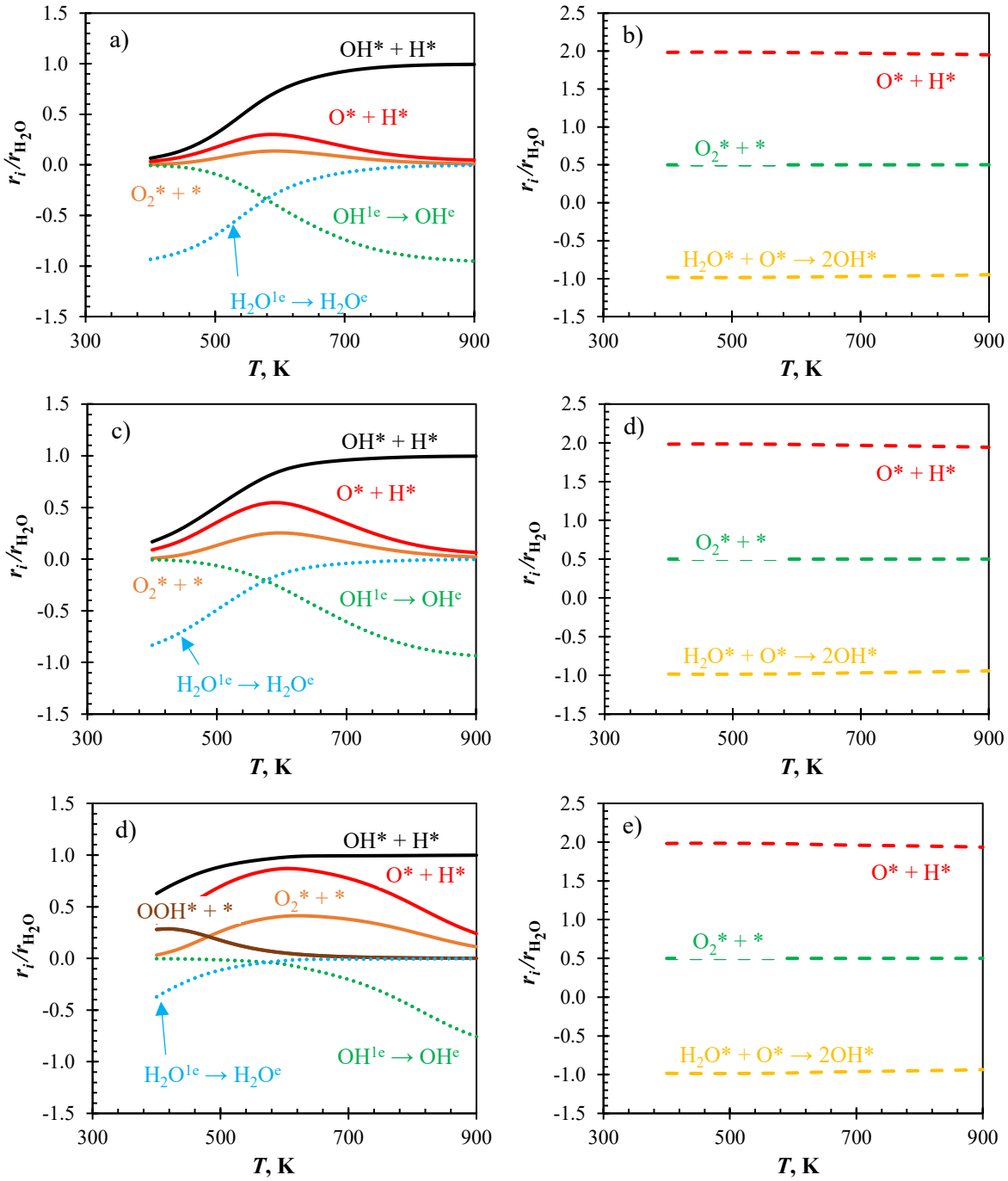

Figure G2.2: QCA model predicted ORR pathway over a multifaceted Au/Pt surface , (a, c, e) over Au/Pt{111} facet and (b, d, f) Au/Pt{100} facet; processes on Au/Pt{111} facet (—), Au/Pt{100} facet (– – –) and involving edge species (·····). Negative values indicate that the reverse reaction contributes to the H_2O evolution rate—(a,b) $\chi_{edge}(1.00)$, (c,d) $\chi_{edge}(0.34)$ and (e,f) $\chi_{edge}(0.04)$ models.

G3: ORR activity and pathway analysis (QCA model) on Ag/Pt NW

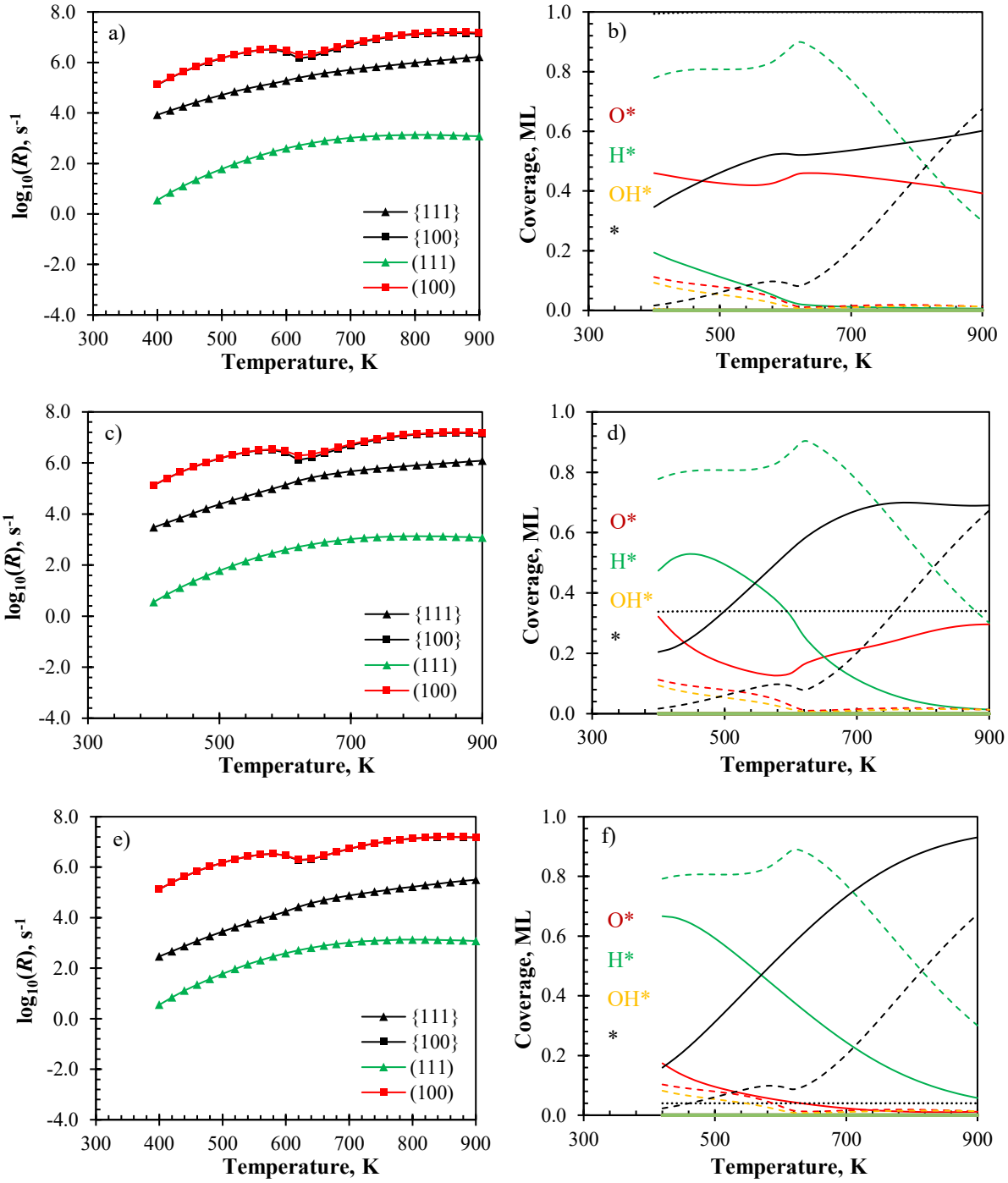

Figure G3.1: QCA model predicted ORR activity over a multifaceted Ag/Pt surface, (a, c, e) H_2O evolution rates and (b, d, f) surface coverage over Ag/Pt{111} facet (—), Ag/Pt{100} facet (– – –) and edge sites (·····), for a $\chi_{edge}(1.00)$ model (a, b), $\chi_{edge}(0.34)$ model (c, d) and $\chi_{edge}(0.04)$ model (e, f).

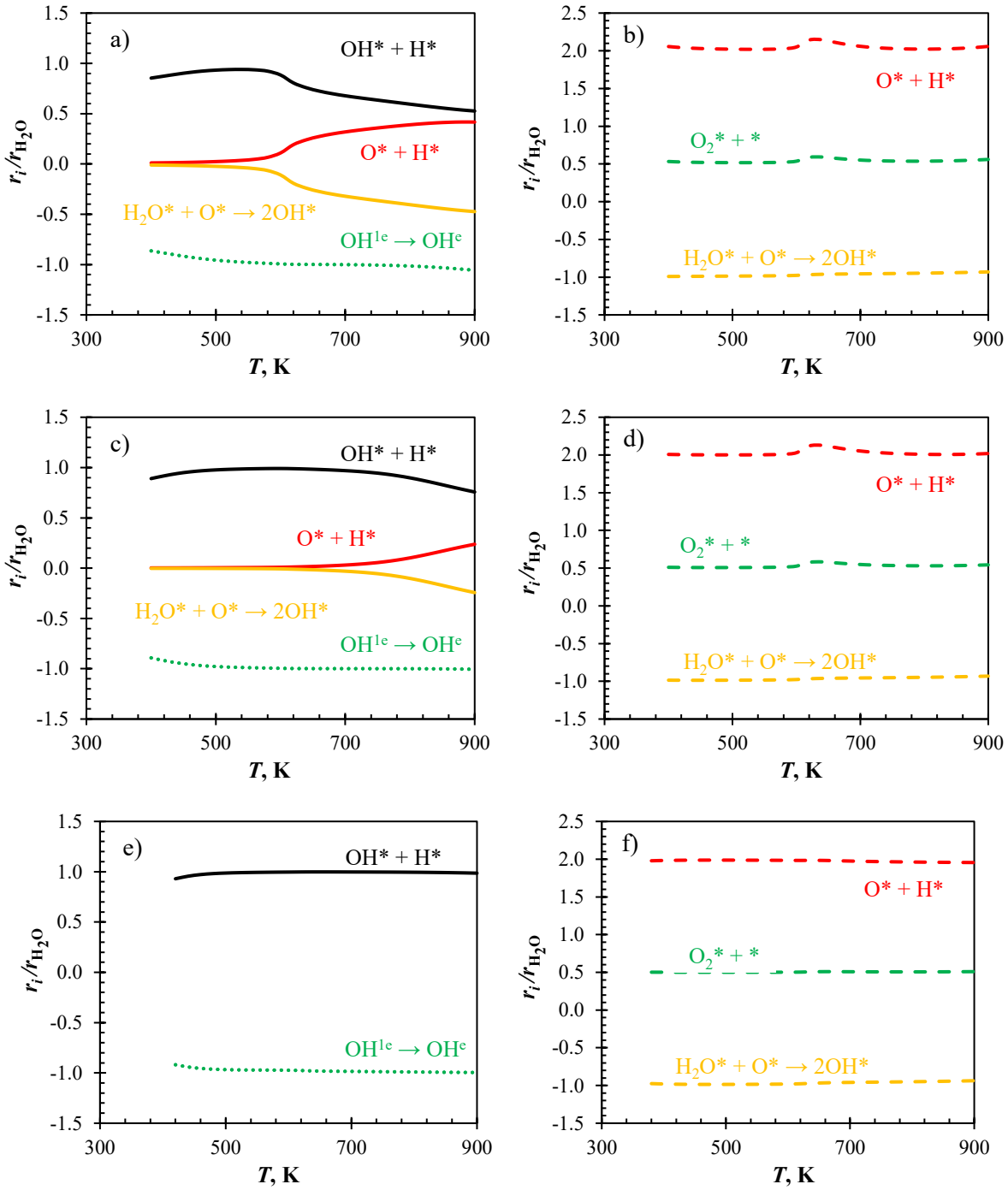

Figure G3.2: QCA model predicted ORR pathway over a multifaceted Ag/Pt surface , (a, c, e) over Ag/Pt{111} facet and (b, d, f) Ag/Pt{100} facet; processes on Ag/Pt{111} facet (—), Ag/Pt{100} facet (– – –) and involving edge species (·····). Negative values indicate that the reverse reaction contributes to the H_2O evolution rate—(a,b) $\chi_{edge}(1.00)$, (c,d) $\chi_{edge}(0.34)$ and (e,f) $\chi_{edge}(0.04)$ models.

G4: Overall ORR analysis comparison of different surfaces.

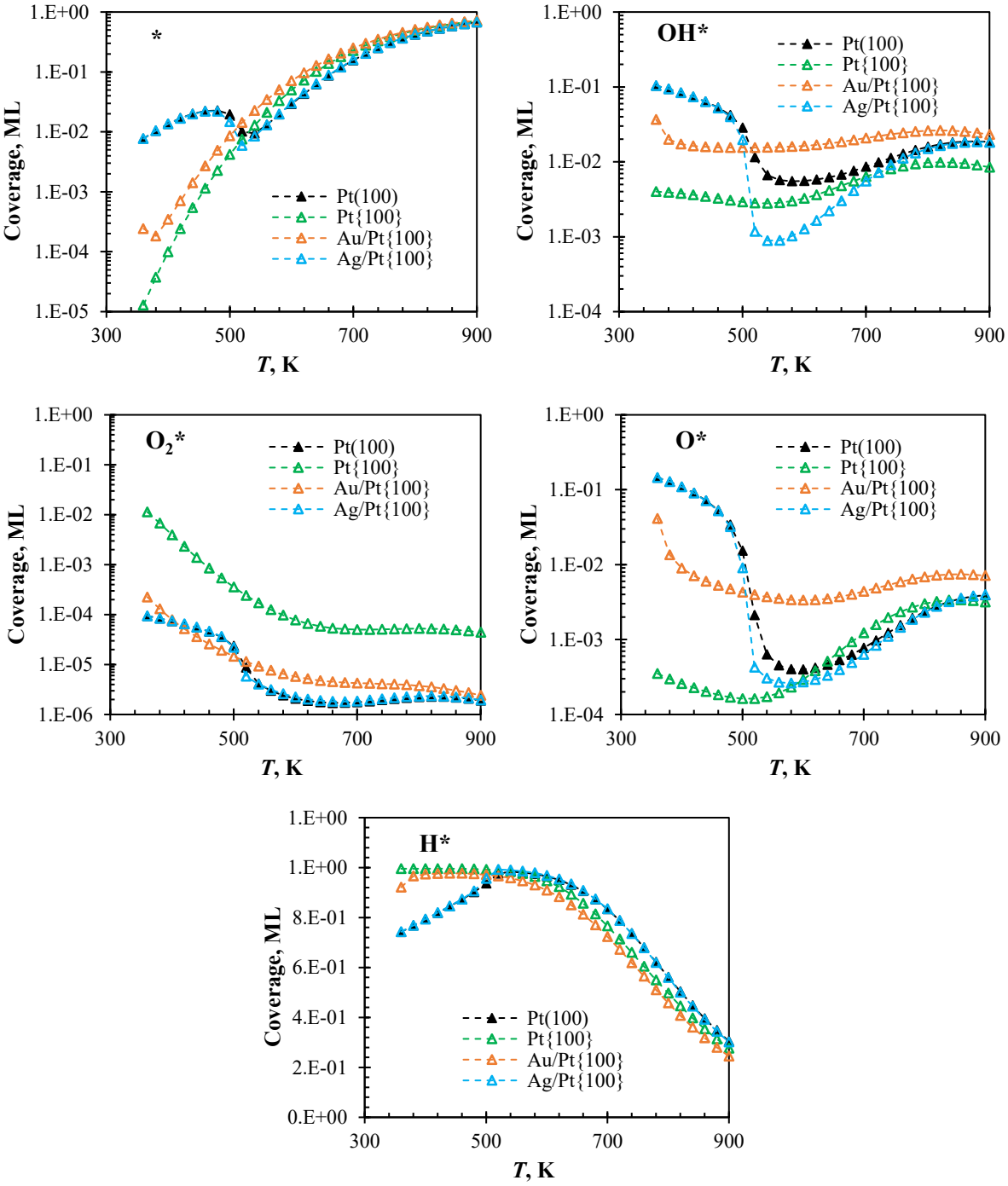

Figure G4.1: Comparison of the surface coverage predicted by the BWA model on different surface models of the $\chi_{edge}(1.00)$ model.

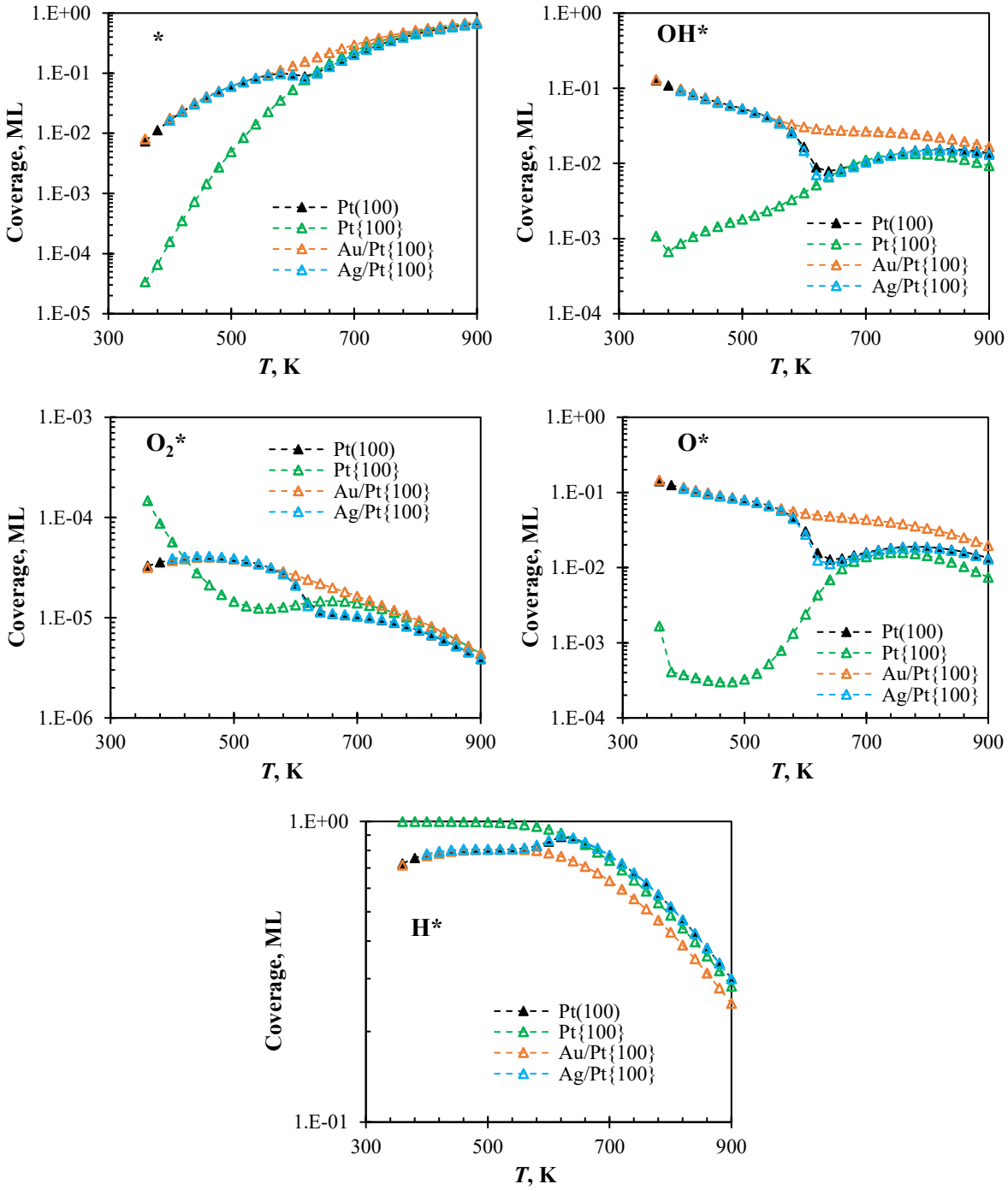

Figure G4.2: Comparison of the surface coverage predicted by the QCA model on different surface models of the $\chi_{edge}(1.00)$ model.

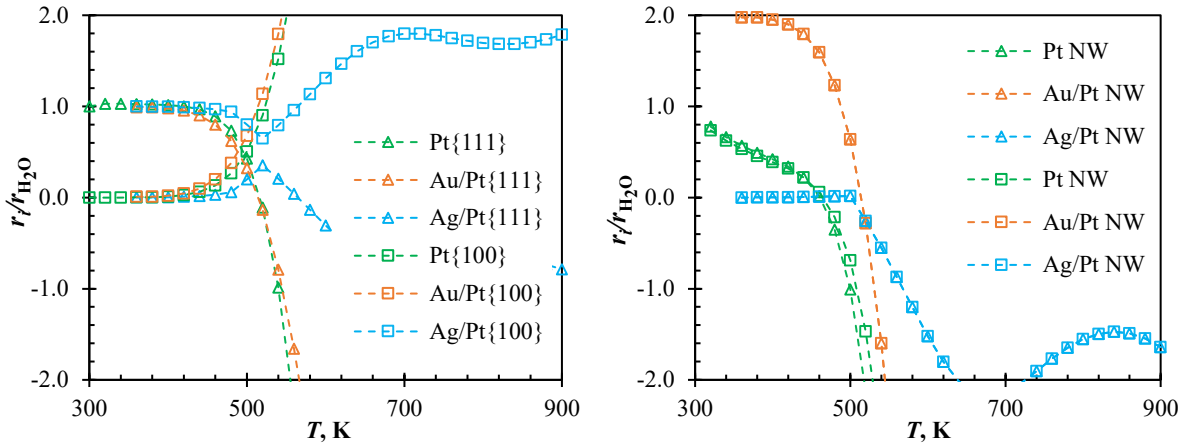

Figure G4.3: Ratio of the (a) H_2 adsorption rates on {111} facet (triangles) and {100} facet (squares), and the (b) H* diffusion rates from {111} → edge (triangles) and edge → {100} (squares) to the net desorption rate of H_2O over the $\chi_{edge}(1.00)$ model based on BWA simulations.

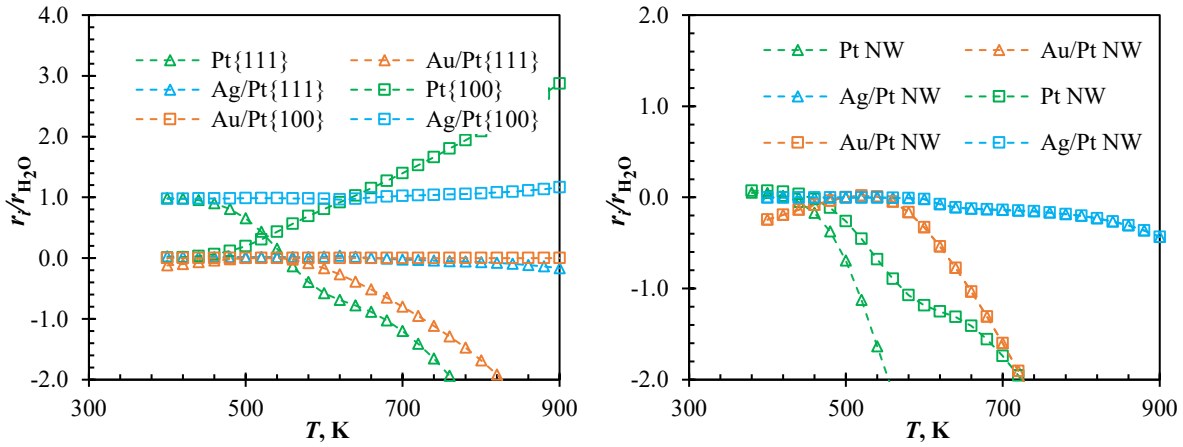

Figure G4.4: Ratio of the (a) H_2 adsorption rates on {111} facet (triangles) and {100} facet (squares), and the (b) H* diffusion rates from {111} → edge (triangles) and edge → {100} (squares) to the net desorption rate of H_2O over the $\chi_{edge}(1.00)$ model based on QCA simulations.

Appendix H: kinetic Monte Carlo model

H1: ORR from Pt(111) and Pt(100) surfaces

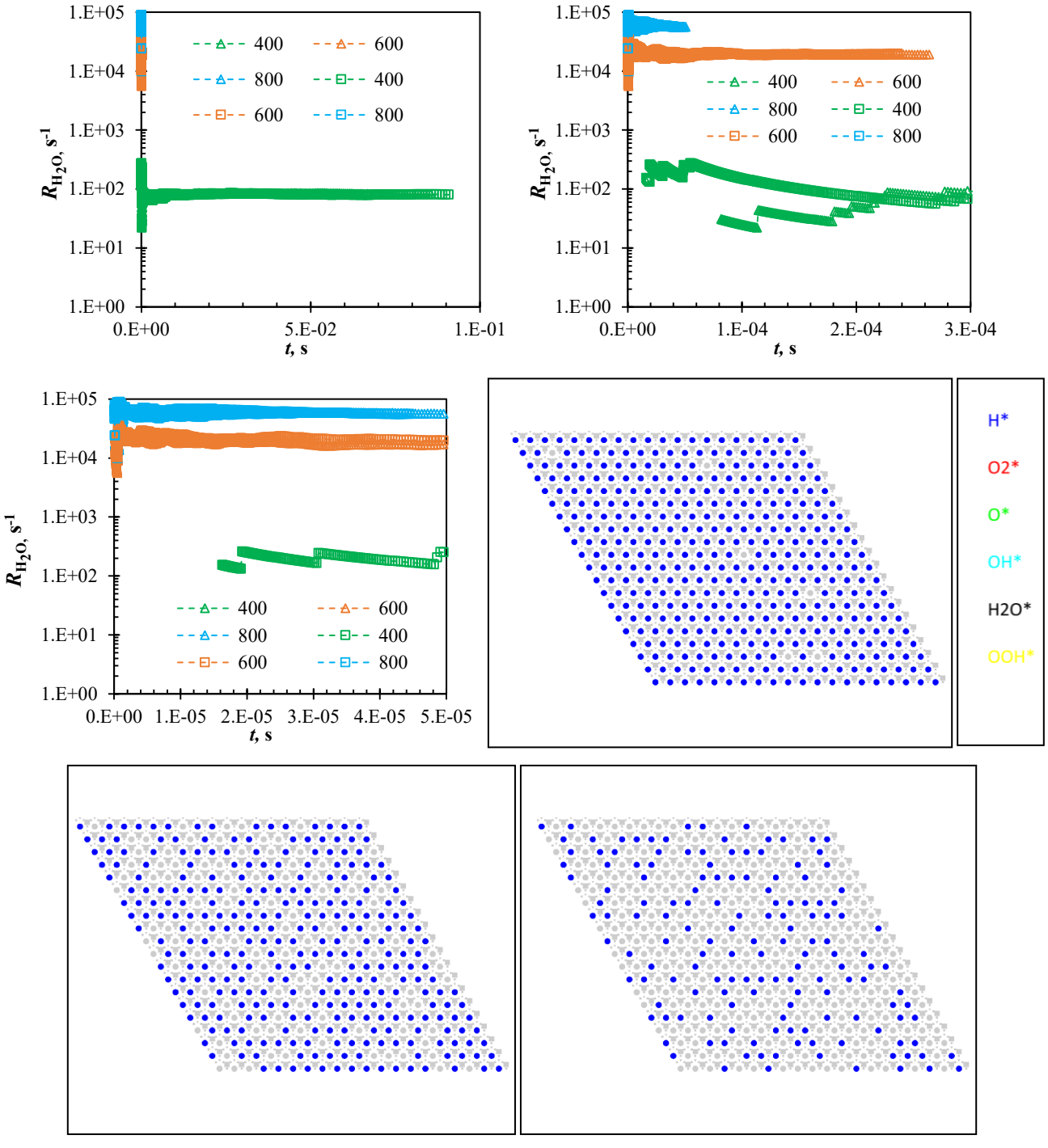

Figure H1.1: kinetic Monte Carlo simulations of the ORR from Pt(111)-(20x20) cell at 1 bar (H_2:O_2 = 2:1) dry conditions and random number generator seeding constants of 135 and 246. (a-c) ORR rate convergence with time at 400 K, 600 K and 800 K. And also napshots of last lattice state at (d) 400 K, (e) 600 K and (f) 800 K.

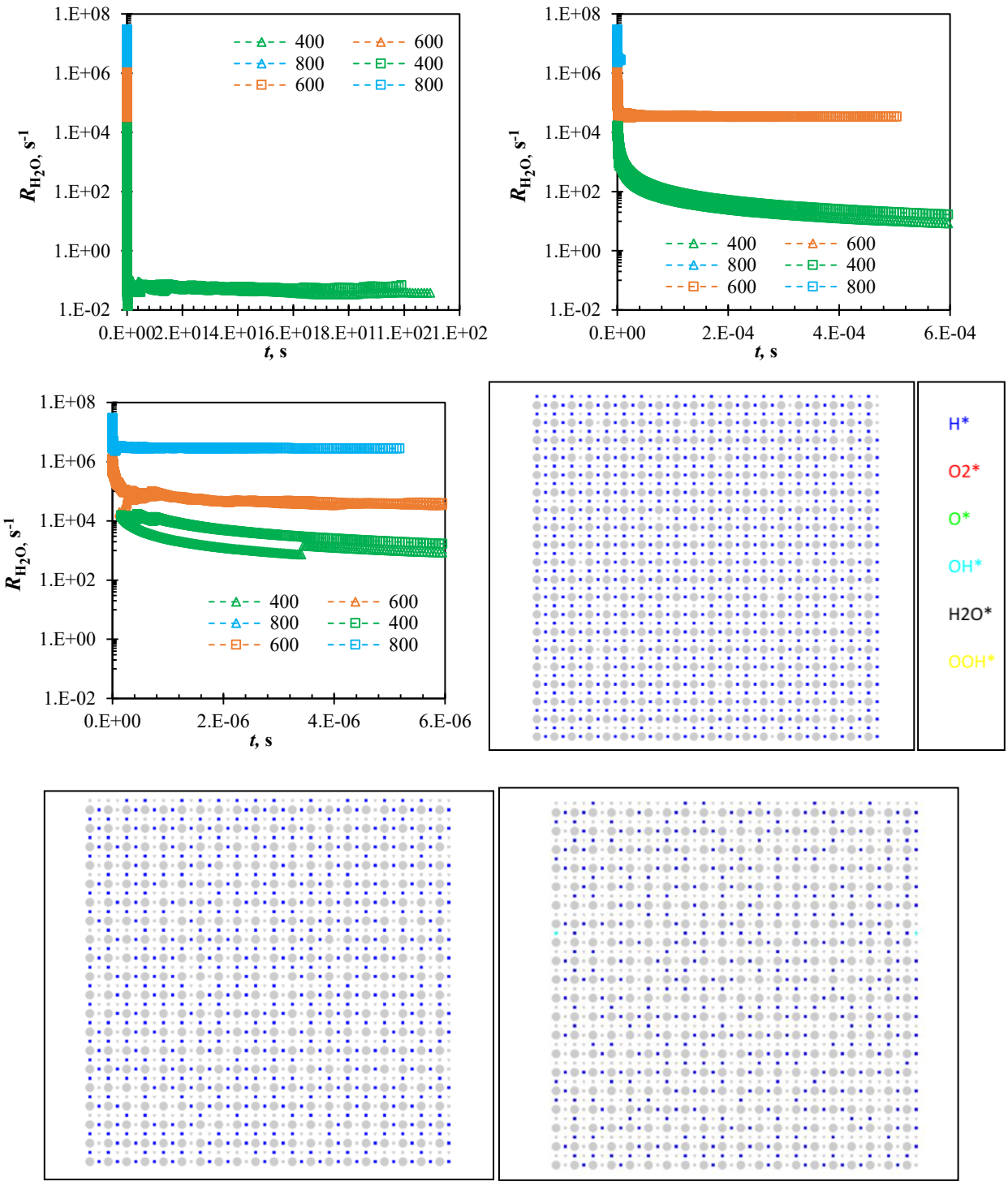

Figure H1.2: kinetic Monte Carlo simulations of the ORR from Pt(100)-(20x20) cell at 1 bar (H_2:O_2 = 2:1) dry conditions and random number generator seeding constants of 135 and 246. (a-c) ORR rate convergence with time at 400 K, 600 K and 800 K. And also napshots of last lattice state at (d) 400 K, (e) 600 K and (f) 800 K.

Appendix I: Molecular Dynamics Simulations

Table *5*: Sutton-Chen potential parameters[52]

	ϵ (meV)	a (Å)	*n*	*m*	*c*
Pt -Pt	19.768	3.920	10	8	34.428
Au – Au	12.896	4.080	10	8	34.428
Ag – Ag	2.533	4.090	12	6	145.658
Pd - Pd	4.126	3.890	12	7	108.526

Glossary

All symbols and scripts are described before and immediately after use. Below is a limited list of some of the acronyms and terms appearing in this work. All terms are discussed/described least once, on first appearance.

GHG	Green House Gas
PEMFCs	Proton Exchange Membrane Fuel Cells
ORR	Oxygen Reduction Reaction
HOR	Hydrogen Oxidation Reaction
Polarisation	Deviation of cell potential from theoretical potential
Overpotential	difference between operating potential and theoretical potential
NWs	Nanowires
NPs	Nanoparticles
Mesoporous	submicron pore structures
RDE	Rotating Disk Electrode
MEA	Membrane Electrode Assembly
*OCS**	Oxygen-Containing-Species adsorbed on a catalyst surface
DFT	Density Functional Theory
Inter-facet exchange	transport of reaction intermediates between difference/adjacent facets
Intra-facet exchange	transport/mobility of reaction intermediates within a given facet
Multifaceted	with multiple surface types
TISSE	Time independent Schrodinger Equation
HF	Hatree-Fock
a priori	known from theory
LDA	Local Density Approximation

GGA	Generalised Gradient Approximation
SCF	*self-consistent-field* loop (iterative procedure)
PES	potential energy surface
MKM	microkinetic model
TOF	turn over frequency umber of molecules consumed per second per site
SA	Single site approximation, coverage independent microkinetic model
BWA	Bragg-Williams-Approximation
QCA	Quasi-Chemical Approximation
Lateral interactions	repulsion/attraction between co-adsorbed intermediates
kMC	kinetic Monte Carlo
DMC	dynamic Monte Carlo
LG	Lattice gas
BEP	Brønsted–Evans–Polanyi principle, describes the scaling between activation and reaction energy
ML	monolayer
near-edge sites	sites adjacent to the edge but not on the edge row
edge sites	sites along the edge atomic row
terrace sites	sites not immediately adjacent to the edge atomic row but on the terraces
DRC	degree of rate control
CHE	chemical hydrogen electrode
SHE	standard hydrogen electrode
RHE	relative hydrogen electrode
MD	molecular dynamics